Dosimetry of preclinical and clinical case studies of ^{18}F-radiopharmaceuticals using Positron Emission Tomography and Computed Tomography: Methods of quantification, their improvement and considerations of critical exposures

Florian Bretin

University of Liège

Maastricht University

A thesis submitted for the degree of

Doctor of Philosophy

Liège, 2014

Abstract

Computed tomography (CT) and positron emission tomography (PET) are routinely used in (pre)clinical research and practice. The radiation burden inflicted on subjects from both modalities needs to be addressed to keep exposures as low as possible. While the focus in literature is on human dosimetry, few studies investigate the animal dosimetry in preclinical studies. This doctoral thesis aimed to quantify the radiation burden imposed on subjects by CT and PET in clinical and especially preclinical case studies using both experimental data and Monte Carlo simulations.

We derived the biodistribution of three ^{18}F-radiopharmaceuticals (^{18}F-UCB-H, 6-[^{18}F]fluoro-L-DOPA and 2-[^{18}F]fluoro-L-Tyrosine) in mice using the gold standard method organ harvesting, as well as dynamic microPET imaging and the new technique of hybrid imaging, where microPET activities are cross-calibrated with the activity remaining in post-scan harvested organs. The radiation dosimetry in humans was calculated and results of all methods were compared. For the newly developed tracer ^{18}F-UCB-H, a first-in-human clinical study was conducted and the radiation dosimetry was compared to preclinically obtained data. Additionally, the preclinically obtained human dosimetry of 6-[^{18}F]fluoro-L-DOPA was compared to clinical values available in the literature. The derived biodistributions of the three tracers were also applied to mouse S-factors to calculate absorbed doses in mice. Furthermore, the radiation dosimetry of the small animal microCT GE eXplore 120 was experimentally investigated *ex vivo* in a custom built phantom and *in vivo* in rats. A model of the imaging system was built using Monte Carlo simulations to further investigate the radiation dosimetry non-invasively.

The preclinical study of the three ^{18}F-radiopharmaceuticals in mice showed that hybrid imaging produces equivalent results compared to labour intensive organ harvesting while being more efficient from an ethical, economical, and scientific point of view. Sole dynamic microPET imaging produced poor results due to partial volume effects and quantification errors in small volumes. Clinically and preclinically derived data of ^{18}F-UCB-H and 6-[^{18}F]fluoro-L-DOPA agreed roughly regarding total-body absorbed dose and effective dose, but significant differences were revealed in

organ absorbed doses for both tracers. The experimentally derived radiation dosimetry of microPET and microCT imaging in mice showed that animals are exposed to significant amounts of radiation in preclinical studies. Monte Carlo simulations of the GE eXplore 120 were in good agreement with experimental results and provided a deeper insight into the spatial dose distribution.

Based on our analysis, hybrid imaging could serve as a replacement for the current gold standard of organ harvesting in preclinical dosimetry. Preclinically obtained estimates of human dosimetry showed relatively poor accuracy and should be used with caution for the calculation of injection limits in first-in-human studies. We demonstrated that excessive radiation doses are inflicted on small animals in preclinical imaging, especially in dual-modality longitudinal studies. The radiation should be addressed in advance to avoid critical exposures that might compromise the outcome of the study.

List of Publications

This thesis is based on the following papers, which are referred to in the text by their Roman numerals:

I. **Preclinical radiation dosimetry for the novel SV2A radiotracer [^{18}F]UCB-H**
Bretin F., Warnock G., Bahri MA., Aerts J., Mestdagh N., Buchanan T., Valade A., Mievies F., Giacomelli F., Lemaire C., Luxen A., Salmon E., Seret A. and Plenevaux A.
EJNMMI Research 3(1):35, 2013

II. **Hybrid MicroPET Imaging for Dosimetric Applications in Mice: Improvement of Activity Quantification in Dynamic MicroPET Imaging for Accelerated Dosimetry Applied to 6-[^{18}F]Fluoro-l-DOPA and 2-[^{18}F]Fluoro-l-Tyrosine**
Bretin F., Mauxion T., Warnock G., Bahri MA., Libert L., Lemaire C., Luxen A., Bardiés M., Seret A. and Plenevaux A.
Molecular Imaging and Biology 16(3):383-394, 2014

III. **Absorbed doses to mice for three [^{18}F]-tracers calculated from experimental data and Monte Carlo simulations**
Bretin F., Mauxion T., Bahri MA., Luxen A., Plenevaux A., Bardiés M. and Seret A.
Manuscript, submitted for Marie Curie Award at EANM conference 2013 in Lyon, France; Reached Top 5

IV. **Biodistribution and radiation dosimetry for the novel SV2A radiotracer [^{18}F]UCB-H: First-in-human study**
Bretin F., Bahri MA., Bernard C., Warnock G., Aerts J., Mestdagh N., Buchanan T., Otoul C., Koestler F., Mievis F., Giacomelli F., Degueldre C., Hustinx R., Luxen A., Seret A., Plenevaux A.* and Salmon E.*
Manuscript

V. **Performance evaluation and x-ray dose quantification for various scanning protocols of the GE eXplore 120 micro-CT**
Bretin F., Warnock G., Luxen A., Plenevaux A., Seret A. and Bahri MA.
IEEE Transactions on Nuclear Science 5(60):3235-3241, 2013

VI. **Monte Carlo Simulations of the dose from imaging with GE eXplore 120 micro-CT using GATE**
Bretin F., Bahri MA., Luxen A., Phillips C., Plenevaux A. and Seret A.
Manuscript

* Contributed equally

Contents

List of Figures

List of Tables

Glossary

18F-FDG 2-deoxy-2-[^{18}F]fluoro-D-glucose. 1

18F-FDOPA 6-[^{18}F]Fluoro-l-DOPA. 7

18F-FTYR 2-[^{18}F]Fluoro-l-Tyrosine. 7

18F-UCB-H [^{18}F]UCB-H. 7

CERN Conseil Européen pour la Recherche Nucléaire. 24

CT Computed tomography. 1

CTDI Computed tomography dose index. 33

FDA Food and Drug Administration. 6

FOV Field of view. 50

FWHM Full width half maximum. 50

GATE Geant4 Application to tomographic emission. 8

HVL Half-value layer. 53

ICRP International Committee of Radiation Protection. 3

MCS Monte Carlo simulation. 8

mFOV Multiple field of view. 50

microCT Micro computed tomography. 1

microPET Micro positron emission tomography. 1

microSPECT Micro single photon emission computed tomography. 2

MIRD Medical Internal Radiation Dose. 29

MOSFET Metal oxide semiconductor field-effect transistor. 33

MRI Magnetic resonance imaging. 28

MSAD Multiple scan average dose. 33

PDF Probability density function. 17

PET Positron emission tomography. 1

PMMA Poly(methyl methacrylate). 33

PVE Partial volume effect. 11

sFOV Single field of view. 50

TAC Time activity curve. 26

TLD Thermoluminescent dosimetry chip. 33

VOI Volume of interest. 38

CHAPTER 1

Introduction

1.1 Motivation

In the last two to three decades the use of computed tomography (CT) and positron emission tomography (PET) increased constantly and they are now essential for routine clinical use, as well as preclinical and clinical research [1, 2], e.g. in oncology [3]. Due to advances in technology in the past decade, stand-alone PET scanners have almost disappeared from modern hospitals and have been substituted for the dual-imaging modality PET/CT [3]. The combined system exhibits several advantages, such as intrinsically spatially co-registered images as well as faster and qualitatively better transmission scans for attenuation correction [4]. The main clinical applications of PET/CT imaging are staging, restaging and assessment of tumor response in oncological applications [3], with 2-deoxy-2-[^{18}F]fluoro-D-glucose (18F-FDG) being the currently most used radiopharmaceutical [5]. Other applications consist of the target volume definition for highly accurate radio therapy treatment [6], the assessment of myocardial viability and perfusion in cardiology [7, 8], and the diagnosis of neurological pathologies such as Alzheimer's [9], epilepsy [10], and Parkinson's [11]. One common application of preclinical micro positron emission tomography (microPET) imaging, which is often combined with micro computed tomography (microCT) imaging for anatomical referencing, is in the field of drug development as it allows for dynamic, pharmacological, longitudinal observations on the same animal [12]. Using suitable radiopharmaceuticals microPET imaging enables researchers to non-invasively monitor biological processes, disease progression and therapy response in small animals providing a potential translational model for human medicine [13]. Because of the widespread use of PET/CT and the ever-increasing number of applications, the radiation exposure of subjects undergoing a single PET or CT imaging session and especially a combined PET/CT scan needs to

be addressed to keep the radiation burden as low as possible. The focus of past dosimetric considerations in the literature has mainly been human applications. With the emergence of preclinical microPET and microCT of small animals in the last decade, however, there is a need for further investigations into the radiation burden of animals. Since longitudinal studies are commonly conducted in preclinical imaging and often involve dual-modality microCT/microPET or micro single photon emission computed tomography (microSPECT) scans [14, 15], the radiation exposure needs to be quantified to rule out any influence on the outcome of the study [16].

1.2 Units of radiation and biological effects

The amount of radiation received by any subject from any type of ionizing radiation in nuclear medicine and radiology is quantified using the absorbed dose (D). It is defined as the energy absorbed per unit mass of any material [17]

$$D = \frac{d\varepsilon}{dm}, \tag{1.1}$$

where $d\varepsilon$ is the mean deposited energy induced by the ionizing radiation to the matter in the volume element of mass dm. In radiology the term absorbed dose is used interchangeably with the term dose, however, in nuclear medicine as dose could possibly refer to other quantities D is always referred to as absorbed dose. Physical processes caused by ionizing radiation depositing the energy within matter will be described in Section 2.4. The SI unit of the absorbed dose is gray (Gy) with 1 Gy being equal to $1\frac{J}{kg}$. Other units for the same quantity exist but are outdated and $\frac{erg}{g}$ or rad will not be used here. In diagnostic nuclear medicine and radiology it is under all circumstances the aim to keep the absorbed dose as low as possible to avoid any biological effects in living tissue. Nonetheless, the overall aim is to acquire diagnostically useful images and the subject should not be exposed to radiation unnecessarily.

Radiobiology differentiates between two types of effects caused by ionizing radiation: stochastic effects and deterministic effects. Stochastic effects resulting from exposure to ionizing radiation are carcinogenesis and hereditary effects, whose severity are independent of the received absorbed dose and may, or may not, manifest many years or even decades after exposure [18, 19]. However, their probability of occurrence increases with the absorbed dose. Deterministic (or non-stochastic) effects occur only above a certain threshold of radiation exposure and are usually not of concern in diagnostic imaging opposed to radiation therapy (nuclear medicine

or external beam), which aims at producing deterministic effects in pathological tissue [19]. Below this threshold deterministic effects do not manifest, but beyond the threshold their severity increases with the absorbed dose. Because of inter-individual differences the threshold may vary. Manifestations of deterministic effects after acute exposure are i.e. erythema (reddening of the skin), epilation (loss of hair), depression of bone marrow cell division, NVD (nausea, vomiting, diarrhea), central nervous system damage, and damage to unborn children. However, in diagnostic imaging patients, whether in nuclear medicine or radiology, only stochastic effects are of concern due to the low absorbed doses.

Since the absorbed dose does not take into account the type of radiation or the type of target material, there is the need for other quantities in medical dosimetry as different materials, especially biological tissues, are more radiosensitive to different types of radiation than others [17, 19]. The International Committee of Radiation Protection (ICRP) publishes regularly recommendations on radiation protection and has defined the quantity of the effective dose [20], which is a sex, age, and dose rate (delivered dose over time) independent quantity. It is a measure of the resulting stochastic risk to a subject by a non-uniform radiation. As the effective dose is applicable to many situations (i.e. medical imaging including patient and practitioner, aviation exposures, etc.) one must account for different types of radiation and biological tissues. Before giving the definition of the effective dose the equivalent dose (or radiation-weighted dose) is to be considered. The equivalent dose is accounting for the different types of radiation (i.e. photons, electrons/positrons, neutrons, protons etc.) and their relative biological effectiveness in producing biological damage. Therefore, the equivalent dose H to a specific tissue or organ T is the weighted sum of all absorbed doses produced by each species of radiation [17, 19, 20]

$$H_T = \sum_R w_R D_{T,R}, \tag{1.2}$$

where w_R is the weighting factor for the radiation type R and $D_{T,R}$ the absorbed dose to tissue T from that particular radiation. The weighting factors were published first in ICRP publication 26 [21], and were most recently updated in ICRP publication 103 [20] in 2007. As the weighting factor w_R for radiations produced in diagnostic nuclear medicine and radiology are equal to unity, the equivalent dose can be interpreted as the physical absorbed dose in photons or electrons that has the same biological effect to an organ or tissue. However, since the quantity is committee-defined, the unit was assigned to be sievert (Sv) instead of gray (Gy). Heavier particles like protons, alpha particles or neutrons have higher weighting

factors as they are more potent in producing biological damage. In order to estimate the stochastic risk to a subject from any given ionizing imaging modality, all types of radiation must be known and therefore the equivalent dose H to all tissues. Additionally, the respective radiosensitivity of all tissues must be taken into account, as they vary for different organs and tissues. Their intrinsic radiosensitivity is reflected in the tissue weighting factor w_T, which allows for calculation of the effective dose E (also in sievert) to any organ or tissue T with a known weighting factor as

$$E = \sum_T w_T H_T. \tag{1.3}$$

The weighting factors w_T were first published in ICRP publication 26 [21] and were updated twice in ICRP 60 [22] and the most recent publication 103 [20]. The first weighting factors from ICRP 26 reflected mortality risk only, but due to the advancement in knowledge of radiosensitivity, the weighting factors of ICRP 60 and 103 reflect the following quantities: probability of attributable fatal cancer, weighted probability of attributable non-fatal cancer, weighted probability of severe hereditary effects, and relative amount of time lost [19]. The sum of all tissues / organs (with a known weighting factor) results in the effective dose for the whole body, which is commonly used in diagnostic nuclear medicine to assess the exposure risk. According to the EANM dosimetry committee the most recent weighting factors from ICRP 103 should not be applied yet, as they are phantom specific (male and female, published in [23]) and specific absorbed fractions for those phantoms were not published at the moment this manuscript was prepared [24]. Controversially, many studies apply the tissue weighting factors from ICRP 103 to effective dose calculations based on the standard hermaphroditic phantom [25–29] as was requested by reviewers during the publication process of Paper I in Appendix A. The effective dose based on ICRP 103 was also added in Paper II in Appendix B. We were made aware of that widely spread misconception during the review of Paper IV in Appendix D and therefore the reader is advised to focus on effective doses based on tissue weighting factors from ICRP 60, which are displayed exclusively in Chapter 3 to 5. The use of the effective dose for assessing radiation risk from medical exposures is contentious anyway, as the value is averaged over sex and age, and neglects the impact of absorbed dose rate [19, 30]. Many still recommend the use of absorbed doses for patient specific dosimetry as it only reflects deposited energy per mass [30, 31].

1.3 Typical clinical and preclinical exposures

Typical radiation exposures of patients undergoing PET imaging highly depend on the administered radiopharmaceutical, the amount of activity necessary to obtain a diagnostically useful image and partially on the scanners sensitivity towards signal detection. Therefore, every newly developed radiopharmaceutical needs to be investigated regarding its radiation burden to the subject. In CT imaging however, it depends exclusively on the technical properties of the scanner itself, such as beam geometry, collimation, detector size and sensitivity, and the noise reduction techniques applied in image reconstruction [32]. Mettler et al. published in 2008 a literature review on effective doses in radiology and nuclear medicine [33] based on over 150 peer-reviewed scientific publications. They reported average effective doses for several types of clinical CT examinations including head CT (2 mSv, range 0.9 to 4 mSv), chest CT (7 mSv, range 4 to 18 mSv), and coronary angiography (16 mSv, range 5 to 32 mSv). For PET imaging using 18F-FDG they stated an average effective dose of 14.1 mSv based on an administered activity of 740 MBq, however, injected activities are less using high sensitivity state of the art PET/CT scanners. Brix et al. studied the radiation exposure of patients undergoing whole-body dual-modality 18F-FDG PET/CT examinations in four different German hospitals using their hospital specific routine protocols and arrived at the conclusion of an average effective dose of 25 mSv (range of 23.7 to 26.4 mSv) [34]. Another study conducted by Huang et al. presented the radiation dosimetry of whole-body PET/CT scanning using different CT protocols and an injected activity of 370 MBq of 18-FDG. They reported an effective dose of 13.45 mSv to 31.91 mSv depending on the chosen CT imaging protocol [35]. There are far fewer studies published about the radiation dosimetry of small animals in either single PET or CT scans, or in dual-imaging PET/CT and SPECT/CT. Taschereau et al. published two separate studies on microCT [36] and microPET imaging in mice [37], reporting an average whole body absorbed dose of 93 mGy from microCT and an average whole body absorbed dose of 106 mGy for an injection of 7.4 MBq 18F-FDG from microPET. Since there are no existing radiation or tissue weighting factors for mice, absorbed doses can only be reported. Absorbed doses from preclinical microCT scanners tend to be much higher than clinically used CT scanners due to the trade-off that has to be made between the resolution (typically 50 to 100 μm) and the X-ray dose to achieve a sufficient signal-to-noise ratio in images [38].

1.4 Regulations for new radiopharmaceuticals

When planning a first-in-human clinical trial with a newly developed radiopharmaceutical, assessing the dosimetry preclinically in animals first is a prerequisite in order to rule out any overexposure of the subjects [39–41]. First injection limits projected from preclinically derived dosimetry data can be estimated and aim to keep the radiation exposure of subjects in clinical trials in acceptable ranges, while still producing diagnostically useful images. The regulations for the maximum allowed radiation burden to voluntary subjects in clinical trials for new radiopharmaceuticals depend on the country and agency. In Europe, guidelines adopted from ICRP publication 62 [42, 43], suggest different radiation exposures depending on the benefit of the radiopharmaceutical used compared with the detriment caused by the involved radiation. In other words, the more substantial the benefit is, the higher the allowed radiation burden to the subject might be, which is summarized in risk categories [40]. Their radiation exposure limits are based on the effective dose, neglecting any specific organ absorbed doses [43]. For a radiopharmaceutical with a minor level of expected societal benefit, which is categorized as simply increasing knowledge of e.g. a disease, an effective dose below 0.1 mSv is allowed with the risk category being trivial (1 in a million have a direct consequence linked to the radiation burden) [42]. When the expected level of societal benefit of the radiopharmaceutical is substantial, radiations above 10 mSv are allowed and direct consequences (such as cancer) for 1 out of 1000 are considered to be acceptable. However, the radiation must be kept below deterministic thresholds except for therapeutic experiments. In the United States of America the agency describing the radiation limits for research studies is the Food and Drug Administration (FDA). They follow a different approach and use specific organ doses limiting the maximum injectable dose based on the equivalent dose and specify a single scan and an annual limit. For the whole body, blood forming organs, lens of the eye, and gonads 30 mSv should not be exceeded per scan with the annual limit being 50 mSv. For all other organs 50 mSv per scan and an annual limit of 150 mSv should not be exceeded [43, 44].

1.5 Specific aims

The primary goal of this doctoral thesis was to assess the radiation burden inflicted on subjects in clinical and preclinical case studies involving newly developed PET radiopharmaceuticals. These case studies involve PET imaging and often CT imaging

for localisation and/or for attenuation correction of PET data. Therefore the focus was on the quantification of the radiation exposure of both imaging modalities. Specifically, several aims were defined:

I. **Preclinically derived human radiation dosimetry of newly developed (or unpublished) radiopharmaceuticals in PET imaging.** The well-known methodology of biodistribution assessment in small animals using organ harvesting and dynamic microPET imaging was experimentally applied towards radiopharmaceuticals. A newly developed compound [^{18}F]UCB-H (18F-UCB-H) with a presently unknown biodistribution and radiopharmaceuticals, whose preclinically derived radiation dosimetry was not available in literature (6-[^{18}F]Fluoro-l-DOPA (18F-FDOPA) and 2-[^{18}F]Fluoro-l-Tyrosine (18F-FTYR)) at the time, were studied . A third method of activity quantification, which aims to combine the advantages of organ harvesting and dynamic microPET imaging while possibly eliminating their disadvantages, was applied for the first time to mice experiments. Human radiation dosimetry calculations based on the preclinicially derived data using all three methods were performed and presented for the first time.

II. **Clinically derived human radiation dosimetry of 18F-UCB-H and comparison to preclinical results.** The human radiation dosimetry for the newly developed radiopharmaceutical 18F-UCB-H was derived for the first time based on a clinical study conducted within the frame of this thesis. The results were compared to preclinically derived results.

III. **Small animal radiation dosimetry of newly developed (or unpublished) radiopharmaceuticals in microPET imaging.** The experimentally obtained kinetic biodistributions were used to calculate the radiation dosimetry for all three radiopharmaceuticals in mice. The results, presented for the first time for the three specific tracers, and based on the different methods for assessing the biodistribution, were compared and discussed.

IV. **Experimental X-ray dose quantification of the GE eXplore 120 microCT.** The radiation dose delivered by several relevant imaging protocols of the GE eXplore 120 micro CT was quantified for the first time. It was assessed *ex vivo* using a custom built phantom and *in vivo* in sacrificed rats. The dosimetry was presented in the standard clinical measure of computed tomography dose index and organ doses inflicted on the animal.

V. **Simulation of X-ray dose of the GE eXplore 120 microCT using Monte Carlo simulations.** The X-ray source and the geometry of the GE eXplore 120 microCT was modelled in the Monte Carlo simulation (MCS) software package Geant4 Application to tomographic emission (GATE) and the energy deposition of the radiation was quantified in the same custom built phantom used in the experiments. Additionally the dose was derived for rats and mice and compared to the experimental results.

1.6 Structural outline

Chapter 2 provides the basic scientific background for readers unfamiliar with the topic to fully comprehend the published / unpublished publications this thesis is based on. A brief insight into medical imaging (PET and CT), radiopharmaceuticals, radiation transport in matter, and absorbed dose quantification techniques is given. References to in-depth information on each topic for the interested reader are suggested as covering all topics in detail is far beyond the scope of this manuscript. In Chapter 3 and subsections all performed studies dealing with one of the specific aims mentioned in Section 1.5 are introduced, their results are briefly discussed and links are established between the different studies. The full detailed (published / unpublished) manuscripts are provided as Appendix A to F for the interested reader. They offer in-depth descriptions of all involved methods, results and their discussion. Chapter 4 consists of a comprehensive discussion of all results and their impact on the field of preclinical and clinical dosimetry. Conclusions drawn from the discussion are summarized in Chapter 5.

CHAPTER 2

Scientific background

In this chapter a basic overview of the involved imaging techniques is presented with the focus on their respective production of ionizing radiation leading to the absorbed dose in matter. A basic physical overview of radionuclides and their radioactive decay, photon interactions with matter, the subsequent energy deposition due to interactions of charged particles with matter and ways of quantifying it, is covered. The mathematical basics of absorbed dose calculations in radiology and nuclear medicine are presented to provide the necessary background to comprehend the journal publications involved in this manuscript.

2.1 Positron Emission Tomography

PET imaging exploits the positron emission for imaging purposes, which is part of the radioactive decay of the isotope bound to a radiopharmaceutical. The subsequent annihilation of the positron with an electron is followed by the emission of two almost opposite photons [45]. The interactions of all emitted particles with matter inside the subject cause the radiation burden, which will be described in Section 2.4. The detection of the two opposing photons is called coincidence detection, which represents a line of response as the photons emitted under approximately 180° originate from an annihilation event on the straight line between the opposite detectors. The first coincidence detection technique with positron emitters was reported in 1951 by Wrenn et al. [46] for localization of brain tumors. There are a broad variety of radiopharmaceuticals available for use in e.g. oncology, neurology or cardiology and an overview of common radiopharmaceuticals, their use and production can be obtained here [5]. The radiopharmaceutical, which is often an analog to a natural occurring compound in the human body, is introduced to the blood circulation of the subject by injection (or inhalation for special tracers [47]) and distributes inside

the organism according to its physiological task making PET imaging a functional imaging technique. Since the radioactive isotope used for labelling of the tracer constantly decays, the coincidence detection can be used to spatially quantify the dynamic distribution of the isotope inside the subject as every detected event can be related to a nuclear disintegration. The PET scanner consists of a cylindrical detector array located around the subject, which dynamically detects the coincidence events in its field of view. The detected photons are considered a coincidence event, if they fulfil certain requirements. They need to be detected in both detectors within a certain timing window to ensure they originate from the same annihilation event and with an energy corresponding to the energy window of the detectors. There are several events that can lead to a coincidence event detection, i.e. the "true", the "scatter", the "random" and the "multiple" [48]. Only a true event is a correctly detected line of response, where two photons are detected originating from a single annihilation located on the line of response between the two opposite detectors. The scatter, random and multiple events are falsely detected lines of response due to scattering, absorption of photons or annihilation events at the same time (for details see [45, 48]). In order to obtain quantitative data from PET imaging, one has to account for these falsely detected lines of response during data processing. With increasing amount of radioactivity inside the field of view, the dead time of the detectors (non-responsiveness during and after detecting an event) play an important role in quantification as well, which needs to be corrected for. Since the annihilation events occur inside matter that attenuates photons, only a fraction of the emitted photons reach the detector. In order to account for the attenuation and to allow for accurate quantification, an attenuation scan is performed before (or sometimes after) the PET emission scan. In older clinical PET stand-alone systems (or preclinical stand-alone systems) the attenuation scan is performed by acquiring a blank scan without the object present and the transmission scan with the object present using a rotating source of a gamma or positron emitter (^{57}Co or ^{68}Ge). The ratio between blank and transmission scan results in the attenuation correction factors to correct the emission data [48]. In state of the art PET/CT systems, the attenuation correction factors are derived from the CT scan [49]. For details on image reconstruction the reader is referred to [48], with special focus on the filtered back projection [48] and the iterative list mode time-of-flight algorithm [50], since they were used for reconstruction in the presented publications. For most applications of PET imaging, especially dosimetry, accurate quantification of the radiopharmaceutical is essential. However, the spatial resolution of the imaging system is limited by physical effects

related to the radioactive isotope [51], the physics of the detection process [52] and the image reconstruction process [53], which impairs the quantification in small objects [54]. The finite spatial resolution, generally described by the system's point spread function, results in the partial volume effect (PVE) altering the intensities of voxels inside the image, which is more apparent in small objects and boundaries between adjacent structures having different intensities [53]. Additionally, due to the image representation in a spatially finite voxel grid, two structures could be present within the same voxel forming an average intensity of the two distinct structures. Accounting for these impairments of quantification is essential in dosimetry.

2.2 Computed Tomography

After the first publication of a clinical head scan using an EMI head scanner by Hounsfield and Ambrose in 1972 [55], CT gradually became indispensable in clinical routine. It was the first imaging technique to produce images of the inside of the human body without falsification through superposition of anatomical structures as present in radiography, which produces a planar projected 2D image. CT and radiography both image a structure using X-rays, which are of electromagnetic nature with a wavelength approximately between 10^{-8} m and 10^{-13} m (photon energies of 100 eV to 10 MeV). In diagnostic medicine, X-ray quanta with energies between 40 and 140 keV are used. Due to their short wavelength and high energy they penetrate matter as first observed by Wilhelm Conrad Roentgen in 1895, who received the Nobel Prize for Physics in 1901 for his discovery. X-rays are produced inside an X-ray tube. Electrons are accelerated in a vacuum towards a rotating solid metal anode by applying a high voltage between the anode and a wire filament acting as a cathode. After entering the anode the electrons interact with matter and two physical effects lead to the emission of photons in the energy range of X-rays. These effects will be explained more detailed in following chapters and can be found here [19, 56]. Briefly, in one effect the electrons interact with the Coulomb field of the atoms inside the anode material and consequently are slowed down. The deceleration of the charged particle creates an electric dipole emitting electromagnetic waves in the range of X-rays with a continuous energy spectrum called Bremsstrahlung. The other effect occurs during the direct interaction of the fast electron with an atomic electron of the anode material. If the atomic shell electron is removed from the shell by the collision, the atom is ionized and an electron from a higher energetic shell fills the vacant position. The energy difference between the shells is emitted as X-ray radiation,

leading to a characteristic energy spectrum with peaks according to the difference in energy of the specific shells, which is singular to the material(s) of the anode. Both spectra superimposed lead to the specific energy spectrum of the X-ray tube. In Figure 2.1 typical X-ray emission spectra are displayed (all produced with the X-ray spectrum simulator provided by Siemens, Link to X-ray toolbox). Figure 2.1a represents unfiltered spectra of materials and tube voltages used in mammography, and Figure 2.1b displays filtered spectra of tungsten as used in CT. The sharp peaks in all spectra can be related to the characteristic energy spectrum of the respective material and the underlying continuous spectrum to Bremsstrahlung.

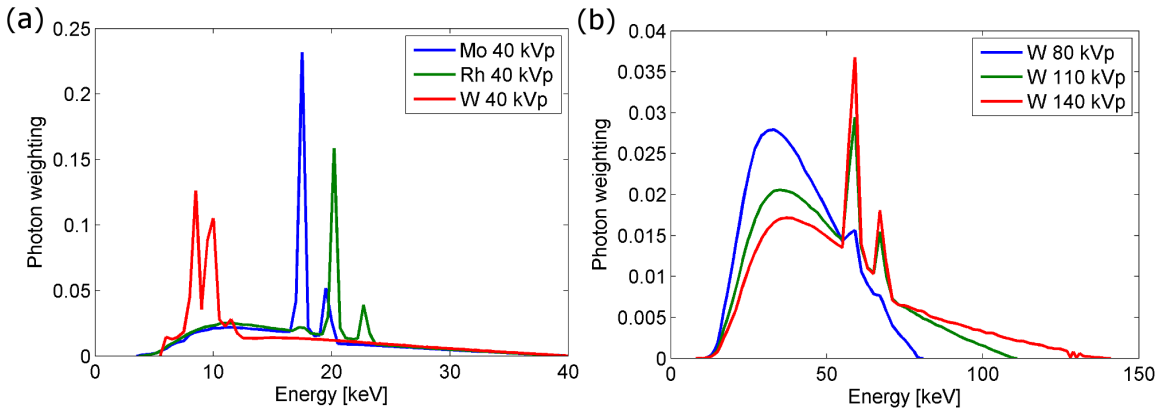

Figure 2.1: X-ray emission spectra of (a) Molybdenum (Mo), Rhodium (Rh) and Tungsten (W) at 40 kVp and (b) of W at 80, 110 and 140 kVp

The exposure of the subject to X-ray radiation and the subsequent interaction of the photons with matter of the subject cause the radiation burden as will be described later. In medical imaging the energy spectrum is usually filtered before the exposure of the patient to remove low energy X-ray quanta, which reduces the dose, and artifacts due to the energy dependence of the X-ray attenuation in the image reconstruction. The fact that X-ray absorption inside matter depends on their energy and atomic number Z of the material can be exploited to acquire the image of the inside of an object by exposing it to X-rays. In CT the X-ray source and a detector array at fixed geometry and distance rotate around the subject and collect spatially dissolved X-ray attenuation data of the subject at every angle referred to as projections. These projections plotted over all angles represent the sinogram of the respective axial image slice, which is ultimately the raw data that is used for reconstructing a 2D image of the X-ray attenuation inside the slice of the subject, i.e. a tomogram. Reconstructing an image out of projection data is an inverse problem

and involves complex physics, mathematics and computer science, which is far out of scope of this manuscript. The basics of image reconstruction in CT imaging can be found here [56] as well as a more detailed description of the whole CT imaging technique. All CT images presented in this manuscript have been reconstructed using Feldkamp's filtered backprojection [57].

2.3 Radionuclides

In this section the physical basics of radioactive nuclei used in diagnostic nuclear medicine, their decay scheme including the emitted particles and radiations are covered. Since every radiopharmaceutical used throughout this manuscript was labelled with the same isotope, the decay scheme of ^{18}F is explained only. Knowledge of the emitted particles, the resulting radiation and the interaction of both with matter are essential for dosimetric calculations. There are several ways for an unstable nucleus to decay depending on the type of nucleus. For therapeutic and diagnostic nuclear medicine only α, β and γ decay are of particular interest, however, there are also internal conversion, spontaneous emission of a single proton or neutron, and spontaneous fission. As ^{18}F is a β particle emitter, specifically a β^+ emitter, only the β^+ decay scheme will be discussed. ^{18}F is a proton enriched isotope of fluorine having an excessive number of protons and consequently an excessive neutral electric charge for its mass. It will try to reach a more energetically favourable state by making a transition to another nuclear state or nucleus. This transition, i.e. nuclear decay, can take place as two different decays, the positron decay and the electron capture. In case of the positron decay the following takes place on an atomic level [19, 48]

$$ {}^{\mathrm{A}}_{\mathrm{Z}}\mathrm{X} \rightarrow {}^{\mathrm{A}}_{\mathrm{Z-1}}\mathrm{Y} + {}^{0}_{1}\beta^{+} + \nu + Q(+e^{-}). \tag{2.1} $$

The proton enriched parent nucleus X decays into the energetically more favourable daughter nucleus Y by emitting the positron β^+ and a neutrino ν, which has a very small mass and no charge. After the nuclear transition described in 2.1, the daughter nucleus Y has an atomic number $Z-1$, which is one less than the parent nucleus X. In order to keep the electrical charge balanced, an orbital electron of the daughter nucleus must be ejected from the atom, which is achieved by a process called internal conversion. The nucleus supplies energy $(Q(+e^-))$ to overcome the binding energy of the orbital electron, which can leave the atom with residual kinetic energy to

balance charge. On a subnuclear spatial level the decay can be described as the conversion of a proton into a neutron n, a positron β^+, and a neutrino ν

$$ {}^{1}_{1}\mathrm{p} \rightarrow {}^{1}_{0}\mathrm{n} + {}^{0}_{1}\beta^+ + \nu. \tag{2.2} $$

Since during the positron decay a positron is ejected from the nucleus and an electron from the atom to keep the electrical charge balanced, the requirement for the positron decay to take place is that the parent atom must be heavier at least by double the electron/positron rest mass of $2m_e$ (1.022 MeV) than the daughter nucleus.

The competing process to positron decay is electron capture, which is possible due to the spatial overlap between the nuclear volume and the wavefunction of an orbital electron, especially the K-orbital of high-A nuclei due to their larger nuclear radii. The process takes place as follows on an atomic level

$$ {}^{\mathrm{A}}_{\mathrm{Z}}\mathrm{X} + e^{-} \rightarrow {}_{\mathrm{Z}-1}{}^{\mathrm{A}}\mathrm{Y} + \nu_e. \tag{2.3} $$

The proton-rich parent nucleus X absorbs an inner atomic electron e^- thereby changing a proton to a neutron and emitting a neutrino. Since the proton is changed into a neutron, the atomic mass remains unchanged while the number of protons decreases transforming the parent nucleus into the daughter nucleus Y. The missing electron on the K-shell is replaced by an electron from a higher orbital, which results in the emission of the difference in binding energy of both shells in form of X-ray radiation. Electron capture is possible when the parent nucleus is heavier than the daughter nucleus, however, when the mass difference exceeds 1.022 MeV, β^+ decay becomes possible. For ^{18}F electron capture occurs only 3.1% of the time, the remaining decay is ruled by positron decay. The branching ratio (or branching fraction) represents the fraction of particles which decay by an individual decay mode with respect to the total number of decaying particles. Therefore, the branching ratio of ^{18}F is 0.969, since decay by positron emission occurs 96.9% of the time.

After emission of the positron from the nucleus to reach the energetically more favourable nuclear state, the positron will have an initial energy with a dynamic distribution up to a maximum value. The particle will lose kinetic energy along its travelling path by different types of interactions with other nuclei. These types of interactions will be described in detail in a later section. In general, there are four different types of interactions: inelastic collision with atomic electrons, elastic scattering with atomic electrons, inelastic scattering with a nucleus, and elastic scattering with a nucleus. For elastic scattering kinetic energy and momentum are

conserved, but for inelastic scattering the kinetic energy of the positron is reduced. The particle is deflected by every interaction making an estimation of the travelling range of the positron difficult.

Eventually, after the kinetic energy is sufficiently reduced, the positron combines with an electron when both are essentially at rest leading to the annihilation event. The event sends off electromagnetic radiation in the form of two photons of the energy of 0.511 MeV, which is equal to the rest mass of each particle. The particles are emitted under an angle of 180° to conserve the momentum, however, due to the momentum being only close to zero and not strictly zero, many pairs are emitted with a slightly smaller angle in accordance to momentum preservation laws.

In PET imaging the measured signal consists of the coincidence detection of the photon pair with opposed directions. Usually one is interested in the distribution of the radiopharmaceutical inside the human body. However, due to the travelling path of the positron outside of the atom, the location of the annihilation process is not equal to the location of the positron emitting atom, which produces an uncertainty between the signal detection in PET imaging and the true localization of the radiopharmaceutical. The positron range increases with the initial energy of the positron as it may take longer for the kinetic energy to be reduced sufficiently for the annihilation process to take place. The positrons emitted by the β^+-decay of ^{18}F have with a mean energy of 249.8 keV (maximum energy of 633.5 keV) a relatively low energy and the isotope has a favourable half-life time of 109.8 min. The travelling path of the positron in water has a mean of only 0.6 mm (max. of 2.4 mm for ^{18}F; in contrast ^{11}C has max of 4.1 mm and mean of 1.1 mm) and the relatively long half-life makes an on-site cyclotron redundant. Additionally, the fluorine atom has a similar atomic radius to hydrogen and a high electronegativity, allowing it to closely mimic the behaviour of a carbon-hydrogen bond in an organic molecule when bound to carbon [5]. These properties make ^{18}F the ideal positron emitting candidate for PET tracer development, handling of the tracer, and resulting image resolution.

The probability of the occurrence of the nuclear transition in form of positron emission with subsequent annihilation in the time interval dt is proportional to λdt. The proportionality constant (or physical decay constant) λ is singular to the specific nuclear species and to the respective decay mode with units of reciprocal time. The probability of the transition occurring is equal to the proportion of radioactive decays in an ensemble of N identical radioactive nuclei

$$\frac{dN}{N} = -\lambda dt. \tag{2.4}$$

By integrating with initial conditions of N_0 as the number of nuclei at time $t = 0$, the number of remaining un-decayed nuclei at time t can be calculated as

$$N(t) = N_0 e^{-\lambda t}. \tag{2.5}$$

By rearranging 2.5 it becomes apparent that the transition rate $\frac{dN}{dt}$ is proportional to the number of radioactive nuclei

$$N(t) = \lambda N(t). \tag{2.6}$$

The absolute value of the transition rate (the number of decays per unit time) is called activity, $A(t)$, which has the unit of Becquerel (Bq). Substituting 2.5 into 2.6 (with $A_0 \equiv \lambda N_0$) yields the function of activity, which lets one calculate the activity of the nuclide after a time t

$$A(t) = A_0 e^{-\lambda t}. \tag{2.7}$$

The physical decay constant λ is related to the nucleus stability and the half-life $T_{1/2}$ is the time point at which half of the initially available radioactive nuclei have disintegrated

$$T_{1/2} = \frac{\ln 2}{\lambda} = \frac{0.693}{\lambda}. \tag{2.8}$$

As one is interested in the temporally dynamic distribution of a radiopharmaceutical in living organisms in nuclear dosimetry, the distribution will not be exclusively ruled by the physical half-life of the radioactive nucleus, but also by biological processes resulting in the washout or the clearance of the radiopharmaceutical from the tissue / organism. Therefore, one can define the effective half-life describing the temporal activity distribution inside an organ, assuming the biological process can be described by an exponential function as well

$$\lambda_{eff,i} = \lambda_{phys} + \lambda_{biol,i}, \tag{2.9}$$

with λ_{phys} being the physical decay constant and $\lambda_{biol,i}$ being the biological rate constant of the biological process i.

To be able to calculate the absorbed dose to a certain organ in nuclear dosimetry one is interested in the total number of disintegration in a source region, which is equal to the time-integrated activity in the source region (formerly referred to as cumulated activity) [58], and can be calculated from the time-activity distribution $A(t)$ having the unit of $Bq * s$ as

$$\tilde{A} = \int_0^\infty A(t)dt. \tag{2.10}$$

Although being a pure number, $Bq * s$ is currently used as unit for this quantity. This usage is based on practical considerations when making the various calculations leading to the absorbed dose.

2.4 Particle interactions with matter

The reason for radiation depositing energy inside matter, which is the definition of the absorbed dose as previously described, is the interaction of particles with the matter it is traversing. There are various interaction processes that can take place depending on the type of particle, its energy and the physical properties of the medium. All interactions are of stochastic nature, allowing for the interactions to be described by probability density functions (PDFs), the so called cross-sections of interaction and energy transfer, which are important for radiation transport and energy deposition calculations. The particles to be considered in PET and CT imaging are photons, electrons and positrons. They can be divided into uncharged particles, i.e. the photon, whose interaction mechanisms are described in Section 2.4.1, and charged particles, i.e. the electron and the positron, whose interactions with matter are covered in Section 2.4.2. A brief summary is provided here, for more detailed mathematical derivations the reader is referred to [19, 59, 60].

2.4.1 Photon interactions

When photons travel through matter of any kind, they will discretely interact with atoms and nuclei of the medium. There are elastic interactions and inelastic interactions with the former transferring no energy leading only to a deflection of the photon. The latter leads to a partial or full energy transfer to an atomic electron, since the electrons subsequently impart energy to the matter. Since photons are electrically neutral, they are far more penetrating than charged particles and can travel a significant distance inside matter. The type of photon-electron interaction depends fully on the photon energy, the polarization and the atomic and nuclear properties of the medium. In this section, the basic physical mechanisms of the interactions will be discussed. Since the photon energies in radiology and diagnostic PET imaging using ^{18}F are limited to the range between 1 keV and 511 keV, the mechanisms relevant for image formation and dosimetry in this energy window will be discussed only.

2.4.1.1 Rayleigh or Thomson scatter

Rayleigh or Thomson scatter is an elastic scattering event between an incident photon, considered as an electromagnetic wave, and an electron (Thomson) or an ensemble of electrons (Rayleigh), transferring no energy to the matter. Since there is no energy transferred to the electron, only the direction of the incident electromagnetic wave is changed after the interaction while the wavelength is preserved. It can be observed if the wavelength of the incident radiation is large compared with the diameter of the scattering nucleus. The electric field of the incoming beam sets a strongly bound electron into oscillation creating a dipole. Due to the acceleration during oscillation the electron radiates electromagnetic energy with the same frequency of the incident wave with the angular distribution of an electric dipole [56]. The effect is never dominating throughout the relevant energies in nuclear medicine or radiology but occurs the most in low and high Z materials between 10 keV and 100 keV.

2.4.1.2 Compton Scattering

Compton scattering of a photon is the incoherent scatter of a photon with a loosely bound electron, i.e. bound on an outer shell of the atom. The incident photon is deflected by an angle θ_γ with reduced energy (increase in wavelength), while the electron recoils at an angle θ_e having a kinetic energy of the difference between incident and scattered photon following the laws of momentum and energy conservation. This effect is important in dosimetric calculations, as the recoil electron subsequently deposits energy inside matter. The maximum energy transfer to the recoil electron occurs for a backscattered photon with an angle $\theta_\gamma = 180°$. The probability of the occurrence of Compton scattering depends on the energy of the incident photon, the scattering angles and is given by the Klein-Nishina equation [48]. However, as the formulas were derived under the assumption of the electron being at rest and free, i.e. no momentum and no binding energy, the formula only yields accurate results for photons with incident energy of above 1 MeV and for low-atomic number materials. In reality electrons have a momentum distribution and are bound (even if loosely) to the atom prior to the interaction with the photon, which alters the scattering angle and the transferred energy. Depending on Z of the traversing medium, Compton scattering becomes the dominant effect in photon attenuation above approximately 40 keV in carbon and 700 keV in lead.

2.4.1.3 Photoelectric absorption

In the photoelectric absorption process a bound atomic electron absorbs the incident photon and is subsequently ejected. The photons energy k, minus the binding energy and the kinetic energy of the recoil nucleus, is transferred to the kinetic energy of the electron. The photoelectric absorption has a strong dependence on the atomic number of the medium (Z^5) and on the incident photon energy ($k^{-7/2}$). If the incident photon energy k is below the binding energy $(E_B)_K$ of the K-orbital, photoelectric absorption in the K-orbital cannot take place and the energy transfer is essentially negligible except for high Z materials. For low Z materials like carbon photoelectric absorption is the dominant effect to photon energies of up to 40 keV and up to 700 keV in high Z materials like lead. Due to the ejection of the atomic electron from the atom, a vacancy in the specific shell where the absorption took place is created, leaving the atom in an excited state. Thus, an atomic electron from a higher orbital fills the vacancy to remove the excess of energy, while the difference between the electron binding energies of the orbitals is emitted as X-ray radiation. This can entail a cascade of subsequent vacancies including their filling by electrons from higher orbitals and emission of photons if the radiation energy is large enough. This effect is responsible for the characteristic X-ray emission spectrum of any material, as it possesses an X-ray peak at the specific energies corresponding to the difference of binding energies between the orbitals. However, the excess of energy that is produced by the ejection of the electron from the atom can also be directed to eject one or more atomic electrons from outer orbits. This non-radiative process is called Auger effect and the ejected electron is called the Auger electron. Both effects contribute to dosimetry, as the emitted X-ray radiation will be absorbed or the Auger electron will be slowed down along its respective travelling path and therefore both will deposit energy in the medium.

2.4.1.4 Attenuation coefficient

The overall probability, so the combination of all interaction cross-sections, of a photon undergoing an interaction per unit distance travelled by any of the above processes is expressed by the linear attenuation coefficient μ in $\frac{1}{cm}$, which depends on the energy of the incident photon and the density of the medium. The mass attenuation coefficient equals the linear attenuation coefficient divided by the mediums density and its unit is $\frac{cm^2}{g}$. As one is interested in the energy transfer in dosimetry, the energy transfer cross-sections of Compton effect and photoelectric absorp-

tion are added up to form the total mass energy-transfer coefficient. Some of the energy, transferred from the incident photons to the atomic electrons, is carried away by subsequent radiative relaxation processes. The subtraction of the radiative relaxation processes from the total mass energy-transfer coefficient leads to the mass energy-absorption coefficient, which quantifies the total amount of energy transferred to atomic electrons enabling the calculation of the amount of energy imparted to the matter. In Figure 2.2 the mass attenuation coefficient and the mass energy-absorption coefficient are displayed for carbon, oxygen, soft tissue and bone (material definitions from ICRP and tabulated data taken from NIST Standard Reference Database 126, Link NIST data).

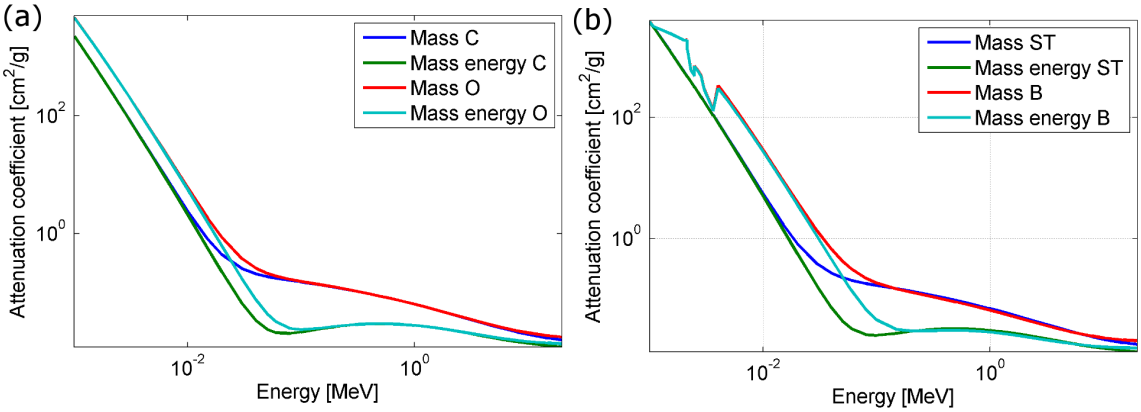

Figure 2.2: Mass attenuation coefficient (Mass) and mass energy-absorption coefficient (Mass energy) of (a) carbon (C) and oxygen (O) and (b) soft tissue (ST) and bone (B)

2.4.2 Charged particle interactions

Moving charged particles, originating from either the radioactive decay described in Section 2.3 or the interaction of photons with matter as described in the previous Section, are the cause of the absorbed dose. As in PET and CT imaging only light particles like electrons and positrons are of concern, heavy particles like protons and ions will not be discussed. The energy deposition of heavy particles is due to their increased mass slightly different to those of light particles and their path inside matter is different due to less scattering. When charged particles travel through matter, they transfer energy to the medium by coulombic interactions with atomic electrons and nuclei. In contrast to photons, which can travel a significant distance before interacting discretely leading to partial or total energy transfer to an atomic

electron, charged particles undergo far more discrete interactions and slow down faster due to coulombic interactions making them less penetrating than photons.

The particular way and amount of energy transferred to the medium by charged particles is described by the total stopping power, which is subdivided into collisional and radiative stopping power with both having the unit of $\frac{MeV}{m}$. Both describe the energy loss of charged particles along a unit path length. The quantity of interest for dosimetry is the mass stopping power in $\frac{MeV*m^2}{kg}$, which is equal to the stopping power divided by the density of the medium. For mathematical descriptions and a more detailed picture the reader is referred to [19, 59, 60], as only a brief summary will be provided within the manuscript.

The collisional mass stopping power describes the coulombic interaction of the incident electron with atomic electrons. It combines the contributions from two types of collisions, which depend on the perpendicular distance b between the trajectory of the charged particle and the radius of the scattering atom. If the distance is large ($b \gg r_{atom}$), the particle will interact with the atom as a whole, which is referred to as a soft collision. The probability of the event is high, however, the net energy transfer per interaction is small leading to a temporal polarization or excitation of an atomic electron into empty quantum states. If the distance is approximately as small as the radius of the atom ($b \approx r_{atom}$), the charged particle will interact with a single atomic electron, being referred to as a hard collision. The probability is lower than for a soft collision, but the net energy transfer is substantially higher, leading to an approximately equal energy transfer from both, soft and hard collision, from a global point of view. The hard collision with an atomic electron can result in ionization of the atom including subsequent radiative relaxation processes as previously described for photoelectric absorption. The ejected electron, which is called a $\delta-$ray, can carry energy a significant distance away from its origin, making this an important feature for dosimetry considerations. The collisional mass stopping power is below an energy of 0.5 MeV antiproportional to energy, i.e. the slower the incident electron the higher the energy deposition, while it flattens out for higher energies and becomes approximately independent for higher energies. It is largely independent of Z. However, higher Z materials have greater binding energies for inner shell electrons, leading to an increased excitation energy, which in turn decreases the collisional mass stopping power for higher Z materials slightly.

If the distance is smaller than the atomic radius ($b \ll r_{atom}$), the charged particle will interact with the nucleus of the atom, leading to a strong deflection of the particle's path or to complete deceleration. The deceleration of the charged particles

creates an electric dipole emitting electromagnetic waves in the frequency range of X-rays known as Bremsstrahlung. The maximum bremsstrahlung photon energy is equal to the kinetic energy of the incident charged particle resulting from the full stop of the particle and conversion of the complete kinetic energy into radiation. This effect is summarized in the radiative mass stopping power, which is not contributing to the locally deposited energy, as the energy is carried away by radiation. The radiative mass stopping power is in general proportional to Z^2 and the energy of the charged particle. In Figure 2.3 the collision, radiative and total mass stopping power of electrons in soft tissue and compact bone (material definitions from ICRP and tabulated data taken from NIST Standard Reference Database 124, Link NIST data) are displayed.

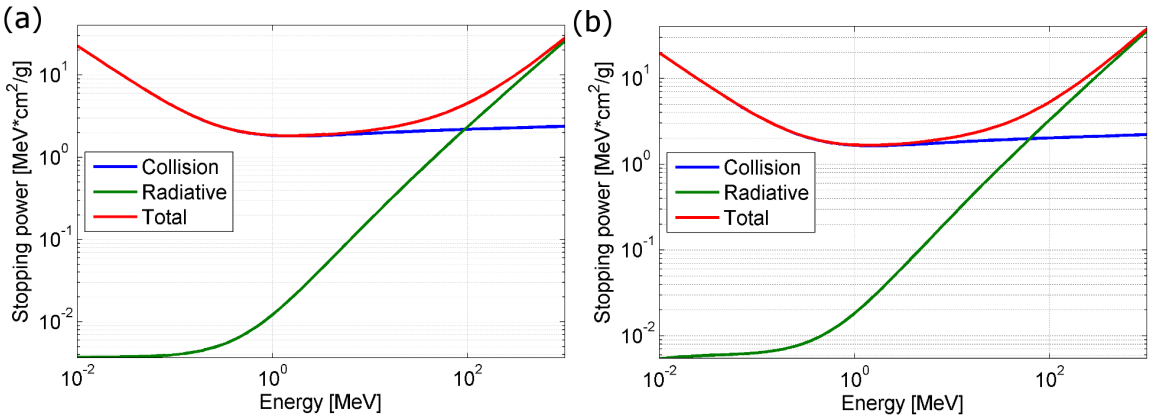

Figure 2.3: Collision, radiative and total mass stopping power of electrons in (a) soft tissue and (b) bone

In general, positrons and electrons are assumed to show similar behaviour regarding collisional and radiative stopping power, since they have the same mass but opposite charge. This however holds only true for high energies. The collisional stopping power of positrons is slightly greater below energies of 0.5 MeV and less above that threshold. The radiative stopping power of positrons is significantly different to electrons at low energies. The ratio of the radiative stopping power of electrons and positrons is unity at about 10 MeV but only 0.5 at 10 keV [19].

In summary, the collisional mass stopping power is the predominant contributor to the total mass stopping power at low energies and becomes essentially independent of energy at about 0.5 MeV. For high Z materials like lead, the collisional mass stopping power is approximately lower by a factor of 2 compared to water. The radiative mass stopping power is negligible at low energies compared to the collisional

mass stopping power and only becomes the dominant energy transfer mechanism at about 10 MeV in lead and 100 MeV in water, which are energies far outside of the medical diagnostic energy window. However, the radiative mass stopping power is proportional to Z^2 and energy. Another important quantity for dosimetry is the electron range, i.e. how far electrons travel inside a medium in order to be able to predict the position of the energy deposition. Since the energy loss of a charged particle due to collisions is a stochastic process, the energy distribution of a monoenergetic electron beam after traversing a certain depth of medium is varying and consequently the range of the electron. This effect is called energy and range straggling.

2.5 Monte Carlo simulations in medical physics

This section aims to introduce the method of Monte Carlo simulations (MCS), their purpose in medical physics and the specific application of radiation dosimetry will be discussed. The numerical method known as MCS can be described as a statistical simulation method involving sequences of random numbers to solve problems of stochastic nature [61]. MCS is useful in medical physics because of the stochastic nature of radiation emission, its transport and detection, since deterministic methods and experimental measurements are infeasible. However, the applications of this method varied greatly and its use for medical physics increased only after the review paper by Raeside [62] in 1976. The method will be described only briefly, as a detailed description of the mathematics involved can be obtained elsewhere [62–64].

2.5.1 General concept

The most common, very simple example to explain the basic idea of MCS is the problem of Buffon's needle, based on the following question: What is the probability (P) of a thin needle of length d being randomly thrown onto an array of equally spaced parallel lines, which are separated by a distance D (with $d < D$), to intersect with one of the lines? The probability P for the needle hitting a line is equal to $\frac{2d}{\pi D}$, which can be derived by the two probability density functions for the distance of the needle centre to the parallel lines and the orientation angle between lines and the needle. If the needle is randomly thrown N times (N being a large number), and n intersections are observed, π is approximated by $\frac{2D}{D}\frac{N}{n}$. The idea that π can be

approximated with a large enough N can serve as the basis for a Monte Carlo computation. When putting that into relation with medical imaging, it becomes clear that three inputs for MCS are essential [61]. One input is the PDFs of all possible particle interactions (cross-sections of interactions) in matter for all involved particles of the particular imaging process. The other important input is the random numbers in the interval [0, 1] to sample from the PDFs. All random number generators (RNG) used in MCS are based on mathematical algorithms. Since they are created deterministically, they are pseudo-random, which is defined as appearing random but exhibiting a repeatable pattern. As many as 10^7 to 10^{12} random numbers are used in a typical simulation and even slight patterns or correlations could alter the outcome of the simulation [65]. There are many RNGs that have been suggested for the use in MCS and will not be discussed further, however, summaries of available pseudorandom number generators were published [66]. The last important input parameter is the sampling rules, i.e. how to sample from the pdfs. Therefore, in an oversimplified way, by using a large amount of random numbers (N) to sample from the PDFs one can reach a solution to a specific physical problem such as energy deposition in a complex system.

2.5.2 GATE package

The dedicated medical imaging Monte Carlo package GATE was first publicly released in 2004 [67], and combines a wide and accurate physics modelling ability with a user-friendly way of modelling complex scanner geometry and imaging configurations [68]. It is based on the Geant4 libraries written in C++, which were developed by Conseil Européen pour la Recherche Nucléaire (CERN) to simulate interactions of particles with matter over a very wide energy range for i.e. the Large Hadron Collider [69]. GATE encapsulates the libraries to achieve a modular, widely applicable and scripted simulation toolkit focused on medical imaging applications. The end-user of GATE does not have to perform any C++ coding, every simulation can be defined and run using script language. The user can freely define the source of radiation, the scanner geometry, the detectors, the phantom (voxellized images are also possible) and can set the various physical phenomena involved. For the physical processes to be simulated, the user can choose several sets of cross-sections in form of PDFs depending on the energy window and the involved physics.

2.5.3 PET dosimetry using Monte Carlo simulations

Although not performed in the frame of this work, Monte Carlo simulations are essential for dosimetry in PET imaging. Assuming two cubic sources filled with a homogeneous amount of ^{18}F, radiation transport of emitted particles and their subsequent energy deposition in each of them can be simulated. The knowledge of how much energy per nuclear disintegration is deposited in each of the cubes can be used to calculate the absorbed dose for any given amount of activity in this specific static geometrical arrangement. Replacing the simple cubic arrangement by the much more complex geometry of a biological body, one is able to calculate for each organ, being a source of activity, the energy that is imparted to the source organ itself (self-radiation) and the surrounding organs (cross-radiation). Figure 2.4 represents a simple example of the two cubes filled with ^{18}F. Both cubes act as a source and a target at the same time. Black arrows symbolize the self-radiation of source 1 and green arrows the self-radiation in source 2. Red and pink arrows represent the cross-radiation from source 1 to target 2 (pink arrows) and from source 2 to target 1 (red arrows).

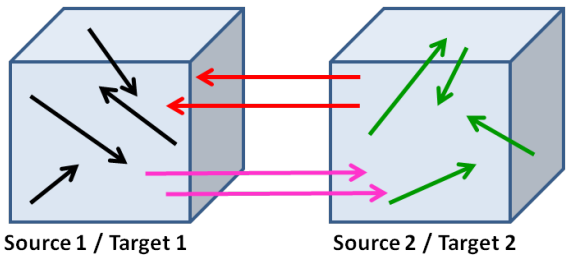

Figure 2.4: Self- and cross-radiation in a cubical arrangement

Due to the additive nature of the absorbed dose, it is possible to derive factors, called *absorbed dose rate per unit activity* or simply S-factor, for all sets of organs allowing for the calculation of absorbed doses for a static geometry. Since the calculation of these S-factors is computationally very expensive, a population averaged phantom with precalculated S-factors is used for absorbed dose calculations in clinical routine instead of patient specific dosimetry. For human dosimetry calculations performed in the frame of this work, the commercially available software package OLINDA/EXM [70] was used, which includes the phantom of Cristy and Eckerman [71] and S-factors released by Stabin et al. [72]. The software also provides a urinary excretion module, as obtaining experimental data including voiding of the bladder and activity data over several hours is often not feasible. The module was used for

the calculation of the urinary bladder wall absorbed dose (self-irradiation) and the contribution of the activity to surrounding organs (cross-radiation). Inputs for the model are the amount of activity, a voiding interval and the biological half-life of the activity inside the body. For mouse absorbed dose calculations the MOBY phantom developed by Segars et al. [73] was used in combination with the S-factors derived recently by Mauxion et al. [74].

2.5.4 CT dosimetry using Monte Carlo simulations

In CT dosimetry the energy deposition inside the subject only depends on the energy spectrum produced by the X-ray tube (therefore the properties such as tube voltage, tube current and anode material) and the exposure times of the applied protocol. Consequently, precalculated factors cannot be directly derived, since the dosimetry is not only subject dependent but also machine dependent. However, Monte Carlo simulations can be used to simulate the photon transport of the emitted X-ray quanta of the specific X-ray tube and the subsequent interactions and energy deposition inside the subject. The implemented setup of the GE eXplore 120 microCT, the derived dosimetry, and the comparison to experimentally obtained data will be presented in Section 3.6.

2.6 Methods of assessing the kinetic biodistribution of radiopharmaceuticals

In nuclear dosimetry one is interested in the time integrated activity (cumulated activity) of the radiopharmaceutical inside a particular source organ or tissue. It is equal to the integration of the time-dependent activity $A(t)$ (see 2.10) yielding the total amount of nuclear disintegrations inside the source organ or tissue [75]. The quantitatively accurate determination of the time activity curve (TAC) $A(t)$ in all activity bearing tissues is required for correct absorbed dose calculations. The TAC is characterized by the uptake and the retention of the radiopharmaceutical and includes the radioisotope specific physical half-life and the tissue specific biological half-life describing the washout velocity of the radiopharmaceutical by biological processes [76].The activity is quantified in serial measurements post administration of the radiopharmaceutical by quantitative imaging (non-invasive), tissue sampling (invasive) or excreta counting [75]. The temporal sampling frequency of the measurement is of utter importance in order to accurately reconstruct the time-activity

profile, as especially due to the administration via the blood stream the initial uptake of the radiopharmaceutical can be a fast process and a low sampling frequency could lead to a falsification of the TAC (aliasing). For subsequent absorbed dose calculations it is vital that all activity that was administered to the studied subject is accounted for in order to consider the total amount of energy deposited inside matter. In the following sections, the methods used in the conducted experiments to derive the TAC in various organs in a preclinical and / or clinical setup will be explained.

2.6.1 Organ harvesting

The preclinical technique of tissue sampling or organ harvesting is a widely used method of time-dependent activity quantification in small animals for dosimetry purposes [41, 77–80]. The TAC is established by sacrificing several animals at different time points post injection of the radiopharmaceutical. At each time point animals are sacrificed, dissected, and their organs are harvested to subsequently quantify the activity present in a specific organ using a gamma well counter. Usually three to five animals are used per time point to provide a mean value at each point to account for intraspecies differences. Animals are kept under anaesthesia from injection to sacrificing by decapitation. For a detailed description of the organ harvesting methods the reader is referred to the respective publications (Appendix A, B and C) in this manuscript. The method is labour intensive, requires an extensive amount of animals per study and is slow regarding data acquisition. However, every organ / tissue independent of size and function can be harvested.

2.6.2 Dynamic PET imaging

Another way of assessing the time-dependent distribution of the radiopharmaceutical post injection inside the body is dynamic PET imaging, which is used in clinical [28, 81–83] as well as preclinical studies [84–88]. The subject is imaged for a longer period of time (between 100 and 300 minutes, depending on tracer's kinetics) directly after the administration of the radiopharmaceutical with the possibility of dividing the total scanning duration into time frames of arbitrary length. This allows for the reconstruction of the TAC of each region of interest within the scanners field of view with a high temporal sampling frequency. If the subject exceeds the field of view, multiple axial sections are acquired per frame to form a dynamic full-body

image at the expense of temporal sampling frequency due to fewer frames. For accurate organ delineation and/or the attenuation correction functional PET imaging is often complemented by anatomical CT imaging for segmentation (or structural magnetic resonance imaging (MRI) if available). For detailed information on the scanners used, the time-framing of the dynamic acquisitions, segmentation of the complementary and co-registered CT scan and other methodical details the reader is referred to the publications (Appendix A to D). In a preclinical setup, dynamic microPET imaging has advantages over organ harvesting, since the number of animals required can be drastically reduced (to around 5 per study compared to 30). The full biodistribution inside each subject can be derived with a much higher temporal resolution. However, imaging limitations such as the previously mentioned PVE need to be addressed.

2.6.3 Hybrid imaging

Both previously explained methods of assessing the kinetic biodistribution (organ harvesting and dynamic PET imaging) have advantages and disadvantages in preclinical dosimetry, which will be addressed more detailed in chapter 4. Hybrid imaging, which combines organ harvesting and imaging, aims to overcome the limitations of both methods and it was first applied by Kesner et al. [41] towards dosimetry derived from rat data. The small animals are scanned dynamically from injection of the radiopharmaceutical to sacrificing and are dissected afterwards. The activity remaining in organs is quantified using a gamma well counter, and the ratio between the *ex vivo* measured activity and the *in vivo* measured activity of the last time point of the dynamic PET scan is used to scale the TAC of the PET image. The method reduces the number of animals to be sacrificed compared to the organ harvesting method, while overcoming the imaging limitations of pure dynamic microPET imaging. Whether the method can be applied in much smaller species such as mice needs to be addressed.

2.7 Extrapolation from preclinical to clinical data

Before a first-in-human study can be conducted with any new radiopharmaceutical, it is, according to national regulations [40, 44], a prerequisite to derive the human dosimetry preclinically to prevent any over-exposure of human subjects. Consequently, the derived animal data has to be extrapolated to human data, since

the data cannot be directly applied to the human case due to anatomical and/or metabolic differences. One extrapolation method is the percentage kilogram per gram method after Kirshner [89], which is widely used in literature [41, 88, 90–95]. It assumes proportionality based on the weight difference between organ and body mass of the respective species allowing for the extrapolation of the activity level in percentage of injected dose per gram of tissue from any species to another if organ and body weights are available,

$$[\frac{\%}{g_{organ}} \times (kg_{TBweight})_{animal}] \times (\frac{g_{organ}}{kg_{TBweight}})_{human} = (\frac{\%}{organ})_{human}. \tag{2.11}$$

Although neglecting metabolic differences between species, the simple approach of the percentage kilogram per gram method is the prevailing method for extrapolation from animal data to human data. There are various methods for additional metabolic scaling, since it is known that species with a greater body mass usually have a slower metabolic rate, which are described here [19]. There are publications discussing the effectiveness of the different extrapolation methods and their combinations [96], but a conclusion, which method is superior, could not be reached [17, 19]. However, as the simple method of Kirshner is widely applied in dosimetry literature, it was used in all relevant publications in the frame of this work.

2.8 MIRD scheme for dosimetry in nuclear imaging

The estimation of internal radiation dosimetry of a radiopharmaceutical in diagnostic nuclear medicine requires knowledge of the following physical or physiological properties:

- The radiation decay scheme of the involved radionuclide (discussed in Section 2.3)
- The kinetic biodistribution of the radiopharmaceutical labelled with the specific radionuclide (discussed in Section 2.6) in a certain anatomy
- The radiation transport and energy deposition of the emitted particles in this anatomy (discussed in Section 2.5)

The Medical Internal Radiation Dose (MIRD) scheme incorporates the above mentioned physical entities and allows for calculation of the absorbed dose to any anatomy as long as all three properties are known. It was developed by the MIRD

committee, which is part of the American Society of Nuclear Medicine and periodically publishes dosimetry papers and guidelines in the Journal of Nuclear Medicine with their first set of instructions being published in 1968 [97]. The MIRD scheme provides a way to calculate the absorbed dose to a target region from a source region containing a dynamic distribution of activity. Since the absorbed dose is additive by nature, the contribution from each source region to a target region can be calculated separately and summed up to obtain the total absorbed dose to a target region from all contributing source regions [17, 76]. The main MIRD equation, describing the time-dependent rate of the deliverance of the absorbed dose to a target region r_T from ionizing radiation emitted by a source region r_S at time t after administration, is

$$\dot{D}(r_T, t) = \sum_{r_S} A(r_S, t) S(r_T \leftarrow r_S, t). \tag{2.12}$$

Here $A(r_s, t)$ is referred to as the time-dependent activity in the source region r_S and $S(r_T \leftarrow r_S, t)$ is commonly described as the radionuclide-specific S-factor mentioned in Section 2.5. It represents the mean absorbed dose rate received by the target region r_T from the source region r_S at time t after administration per unit activity as previously mentioned. There are two types of S-factors to be considered: one is the case where target and source region are two spatially separated regions (referred to as cross-radiation), and the case where target and source region are the identical physical object (referred to as self-irradiation). In ordinary diagnostic nuclear medicine dosimetry calculations the S-factor is precalculated for a specific radionuclide including its decay scheme and a static set of target and source region. However, in theory the volume of any region can vary over time with special physiological cases being the bladder, the lung and the heart. Their volume fluctuates constantly due to their physiological task inside the live organism, which will be neglected throughout this manuscript and the static case is considered only. For time-dependent considerations of the S-factor the reader is referred to [58]. As the mean absorbed dose to the target region r_T is the summation over all source organs r_S contributing radiation, the total absorbed dose can be written as a sum, already neglecting the time dependency of the S-factor to consider fixed volumes for r_T and any r_S only,

$$D(r_T, T_D) = \sum_{r_S} \tilde{A}(r_S, T_D) S(r_T \leftarrow r_S, t). \tag{2.13}$$

The time-integrated activity $\tilde{A}$ over dose-integration period T_D in source region r_S is empirically determined by means of activity quantification as described in Section

2.6 and can is given by (same as 2.10, but restricted to T_D and r_S)

$$\tilde{A}(r_S, T_D) = \int_0^{T_D} A(r_S, t)dt. \tag{2.14}$$

It is quite common to provide dosimetry results as absorbed dose coefficients $d(r_t, T_D)$ (although still referred to as absorbed dose in most literature publications), which is the absorbed dose normalized per unit administered activity in $\frac{Gy}{Bq}$. Therefore, the time-integrated activity $\tilde{A}$ is given as the fraction of total injected activity A_0 having the unit (Bq*s/Bq) [58, 75]

$$\tilde{a}(r_S, T_D) = \frac{1}{A_0} \int_0^{T_D} A(r_S, t)dt. \tag{2.15}$$

The quantity is referred to as the time-integrated activity coefficient (formerly the residence time). However, both terminologies are still used in various publications. The S-factor represents the fraction of energy deposited in r_T released from a single radioactive decay inside r_S and is normalized to the mass m_{r_T}. When not confined to a fixed radionuclide, static volumes, masses and distances between them (r_T and r_S), the S-factor is dependent on all mentioned parameters. However, in the following chapters all S-factors are precalculated using fixed parameters representing a static case for the radionuclide ^{18}F. Therefore the S-factor can be defined based on the previous description as

$$S(r_T \leftarrow r_S) = \frac{\sum_i E_i Y_i \phi(r_T \leftarrow r_S; E_i)}{m_{r_T}}. \tag{2.16}$$

Here the summation occurs over all nuclear decay channels i having the energy E_i, which is the released energy of a photon or kinetic energy in case of a β particle, and the yield Y of the particular channel i. ϕ is the absorbed fraction of the energy E_i of the decay channel i emitted in r_S absorbed in r_T and m_{r_T} is the fixed mass of the target region. By substituting E_i and Y_i one can rewrite the expression as

$$S(r_T \leftarrow r_S) = \frac{\sum_i \triangle_i \phi(r_T \leftarrow r_S; E_i)}{m_{r_T}}, \tag{2.17}$$

with $\triangle_i = E_i Y_i$ being the mean energy emitted by each i^{th} nuclear transition. To further simplify one can express the specific absorbed fraction, which is the ratio of the absorbed fraction and the target mass,

$$\Phi(r_T \leftarrow r_S; E_i) = \frac{\phi(r_T \leftarrow r_S; E_i)}{m_{r_T}}. \tag{2.18}$$

Combining the expressions 2.17 and 2.18 and substituting the expressions in 2.13 the formula of the mean absorbed dose can be written as

$$D(r_T, T_D) = \sum_{r_S} \sum_{i} \triangle_i \Phi(r_T \leftarrow r_S; E_i) \int_0^{T_D} A(r_S, t) dt. \tag{2.19}$$

If the absorbed dose coefficient $d(r_T, T_D)$ normalized to the total injected activity A_0 is used, which is more common in dosimetry publications, one can write

$$d(r_T, T_D) = \sum_{r_S} \sum_{i} \triangle_i \Phi(r_T \leftarrow r_S; E_i) \frac{1}{A_0} \int_0^{T_D} A(r_S, t) dt. \tag{2.20}$$

When using the MIRD scheme to calculate the mean absorbed dose received by a target region in diagnostic nuclear medicine a few limitations hold true. The activity within a source organ might vary dynamically but is assumed to have a spatially homogeneous distribution inside the whole volume. Additionally, all regions, whether target or source region, have a homogeneous mass distribution, i.e. the density of the region is homogeneous as well. As earlier described in this chapter, the geometry of source and target regions is assumed fixed over time when using precalculated S-factors for a certain representative phantom, so no physiological movement of organs during the presence of the radiopharmaceutical takes place. Therefore, the absorbed doses calculated using the MIRD scheme (when assumptions apply) in combination with the previously described phantom and S-factors (see Section 2.5.3) remain estimations for a hermaphroditic, age- and geometry averaged static phantom.

2.9 Dosimetry in CT imaging

In this section, a brief overview of how the dose in CT imaging is calculated will be provided. With the evolution from planar 2D radiography to rotational 3D CT, new concepts for dose quantification were required. In CT imaging, as opposed to radiography, the X-ray source rotates around the subject to acquire projections from all angles for a specific axial length (depending on detector array, X-ray source and type of CT) leading to a more homogeneous dose distribution with significant higher exposure. Although the X-ray beam and therefore the exposure area is confined to the axial length to be acquired by collimation of the beam, the axial dose profile is not a rectangular function limited to the scan length. Due to scattering, energy is deposited outside of the collimated area forming tales on each side of the respective

axial dose profile. Additionally, depending on the type of CT scanner and imaging protocol, several axial sections with overlapping dose distributions to obtain a full body scan are acquired, further increasing the radiation burden to the subject. A concept introduced by Shope et al. in 1981 [98], the computed tomography dose index (CTDI), accounts for the scattered radiation outside of the collimated X-ray beam by relating the total amount of dose deposited to the acquired axial image section. The general formula for the CTDI measured in Gy, in continuous from, is [56, 99]

$$CTDI = \frac{1}{d}\int_{-\infty}^{\infty} D(z)dz. \tag{2.21}$$

Here, d represents the nominal slice thickness or the total axial length to be imaged and $D(z)$ denotes the function of dose along the axial direction z. The axial dose profile $D(z)$ is routinely measured for clinical CTs inside a standardized poly(methyl methacrylate) (PMMA) phantom in different transaxial positions using an ionization chamber [99, 100]. However, the radiation dose can be measured discretely using thermoluminescent dosimetry chip (TLD) [101] or metal oxide semiconductor field-effect transistor (MOSFET) sensors [102]. The standardized $CTDI_{100}$, which is used for characterizing the dose of a single axial image section including the dose profile over 100 mm, is given by

$$CTDI_{100} = \frac{1}{NT}\int_{-50mm}^{50mm} D(z)dz, \tag{2.22}$$

where N is the number of simultaneously acquired image slices during one full tube rotation and T is the slice thickness in (mm). The CTDI depends on the CT system and the protocol specific settings of tube voltage, tube current and exposure time per projection. For comparison of the radiation burden between different CT systems the normalized CTDI value is often used, which is normalized to the current-time product making the value device specific at a fixed tube voltage,

$$CTDI_n = \frac{CTDI}{it}, \tag{2.23}$$

with i being the applied tube current and t the total exposure time over all projections of the specific protocol. If multiple axial image sections are acquired, the dose increases due to overlapping dose profiles and each single dose profile contributes to the dose deposition in the next acquired image section. The dose can then be characterized by the multiple scan average dose (MSAD), calculated as [99]

$$MSAD = \frac{1}{I}\int_{-I/2}^{I/2} D_{N,I}(z)dz. \tag{2.24}$$

Here, I refers to the central scan interval or image width, where the dose is quantified, and $D_{N,I}(z)$ to the axial dose profile incorporating N adjacent single dose profiles. There are several slightly different representations of the CTDI and MSAD depending on the CT system used and the regulatory agency involved, which can be found in the literature [56, 99]. However, the CTDI represents an averaged dose over a volume inside a PMMA phantom or air (depending on which CTDI is used) specific to a CT system and should not be regarded as a patient specific dose [103]. In the following Chapters the term CTDI will always refer to the CTDI_{100}, which was used exclusively.

CHAPTER 3

Publications & studies

3.1 Preclinical radiation dosimetry for [^{18}F]UCB-H

3.1.1 Overview

In this section the preclinical radiation dosimetry of a novel radiopharmaceutical published in the European Journal of Nuclear Medicine and Molecular Imaging Research is briefly discussed [80]. For detailed information on the performed experiments and in-depth results the reader is referred to the Paper I in Appendix A. The radiotracer 18F-UCB-H, newly developed by UCB Pharma (UCB Pharma Ltd., Slough, Berkshire, UK) and the Cyclotron Research Centre of the University of Liège, was investigated in collaboration between UCB Pharma and the Cyclotron Research Centre of the University of Liège. The compound shows a nanomolar affinity for the human SV2A protein [104] which is believed to play a role in epilepsy as the antiepileptic drug levetiracetam targets the same protein [105]. However, since the specific mechanism of levetiracetam is not fully understood, the new compound may provide a deeper insight into epilepsy and other diseases of the central nervous system. As required by research guidelines in the EU and the United States of America [40], we derived the human radiation dosimetry of the radiopharmaceutical for the first time from mice before any first-in-human use. Traditionally, the preclinical dosimetry is obtained by *ex vivo* organ harvesting (see Section 2.6.1), but the method is time consuming, requires many animals to be sacrificed, and the data acquisition has to be spread over several days for one tracer depending on staff and facilities available. Another promising approach is *in vivo* dynamic microPET imaging (see Section 2.6.2), which might overcome several disadvantages of the traditional *ex vivo* organ harvesting. The data acquisition is much faster, since the complete kinetic biodistribution of the tracer over time can be derived from one animal in one microPET scanning session. Consequently, fewer animals need to be sacrificed and less staff and fewer

lab days are required per investigation. The study aimed at acquiring the preclinical radiation dosimetry of 18F-UCB-H using both methodologies and to compare their results. In this study we injected twenty-four male mice under isoflurane anaesthesia with a bolus of the newly developed radiopharmaceutical 18F-UCB-H followed by decapitation at 6 different time points for organ harvesting experiments (n=4 at 2, 5, 10, 30, 60 and 120 min). Following dissection of the animal the activities remaining in organs were quantified with a gamma well counter. Dynamic microPET imaging over 120 min including microCT imaging for segmentation was performed on five separate mice. Two types of segmentation techniques were used; the laborious full-organ segmentation and fast sphere segmentation, where spheres are placed in the centre of each organ (see Figure 3.1). The obtained TACs, extrapolated to human values as in Kirshner et al. [89] (see Section 2.7), were used for absorbed dose calculations performed with the human dosimetry software OLINDA/EXM [70]. Different urinary excretion scenarios were modelled using the dynamic bladder module implemented in the dosimetry software [106], including two voiding scenarios and different fractions being excreted via the urinary pathways.

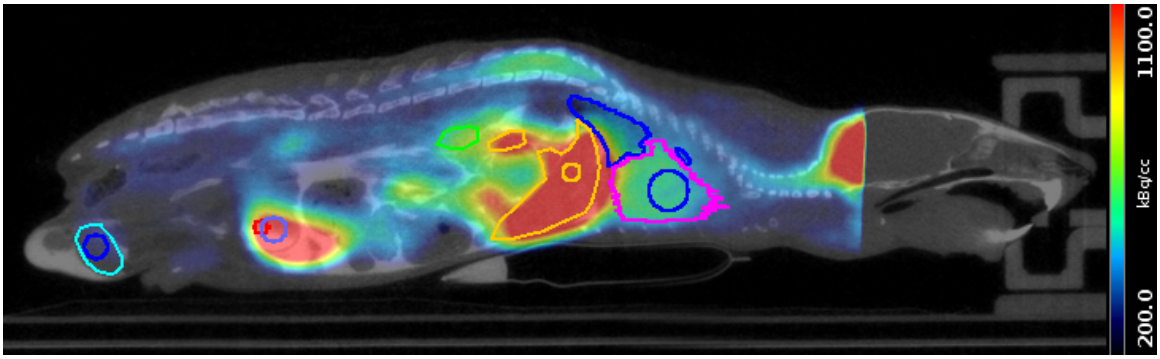

Figure 3.1: Representative PET/CT image including VOIs (full organ segmentation and sphere segmentation); due to the limited axial field of view of the microPET the brain could not be included in imaging analysis

The TACs over 120 min derived by organ harvesting and dynamic microPET imaging are displayed in Figure 3.2. Biological clearance of the radiopharmaceutical from organs was neglected after 120 min and only physical decay was assumed till 10h post injection.

The computed absorbed doses of major organs in humans and the resulting effective dose based on the tissue weighting factors from ICRP publication 60 [22] are shown in Figure 3.3. For a more detailed list of absorbed doses the reader is referred to Paper I in Appendix A. A correlation of r=0.96 ($p < 0.0001$) was found

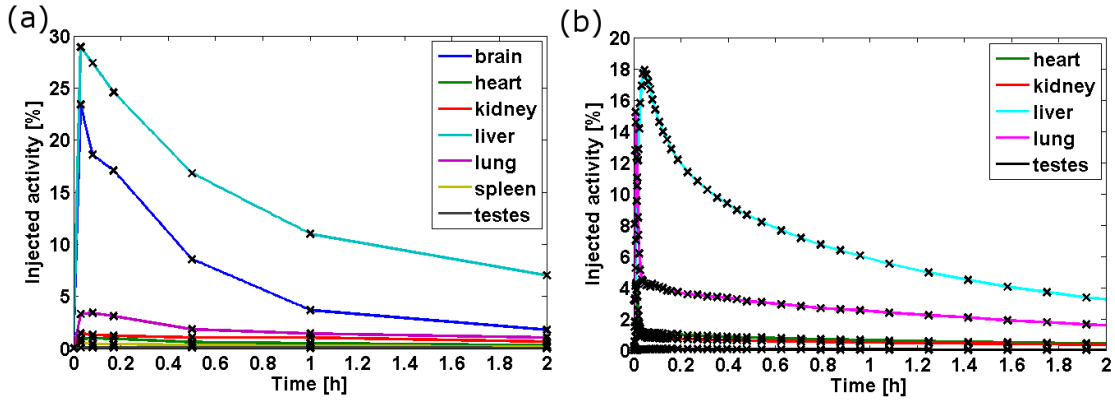

Figure 3.2: TAC derived by (a) organ harvesting and (b) dynamic microPET imaging (sphere segmentation); adopted from [80]

between datasets of absorbed doses (full datasets only shown in Paper I in Appendix A) derived by organ harvesting and dynamic microPET imaging.

The effective dose derived by organ harvesting was 2.18E-02 ± 5.50E-04 mSv/MBq and 2.15E-02 ± 2.88E-04 mSv/MBq derived by dynamic microPET imaging (single sphere segmentation). The highest absorbed dose was received by the urinary bladder wall (1.54E-01 ± 5.00e-04 mGy/MBq derived by organ harvesting) followed by the liver (5.84E-02 ± 7.35E-03 mGy/MBq derived by organ harvesting). The derived urinary bladder wall absorbed dose was calculated using a theoretical model with a fraction of 0.5 of all injected activity leaving via the urinary excretion system with voiding every 4h. With the assumption of a smaller fraction of 0.3 the absorbed dose would be decreased to 9.67E-02 ± 5.50E-04 mGy/MBq.

3.1.2 Discussion

The comparison of the labour intensive *ex vivo* organ harvesting and the fast dynamic microPET imaging showed that despite the numerous advantages of microPET imaging, the method does not provide accurate quantification in small animals. The result agrees with findings by Constantinescu et al. [90], who also reported poor correlation between microPET activities and activities in post-scan harvested organs. Significant over-/underestimations were revealed in time-integrated activity coefficients (former residence times, see Section 2.8) of major organs in comparison to organ harvesting with ratios of both values ranging from 2.3 (largest underestimation in microPET; liver) to 0.53 (largest overestimation in microPET; lung) based

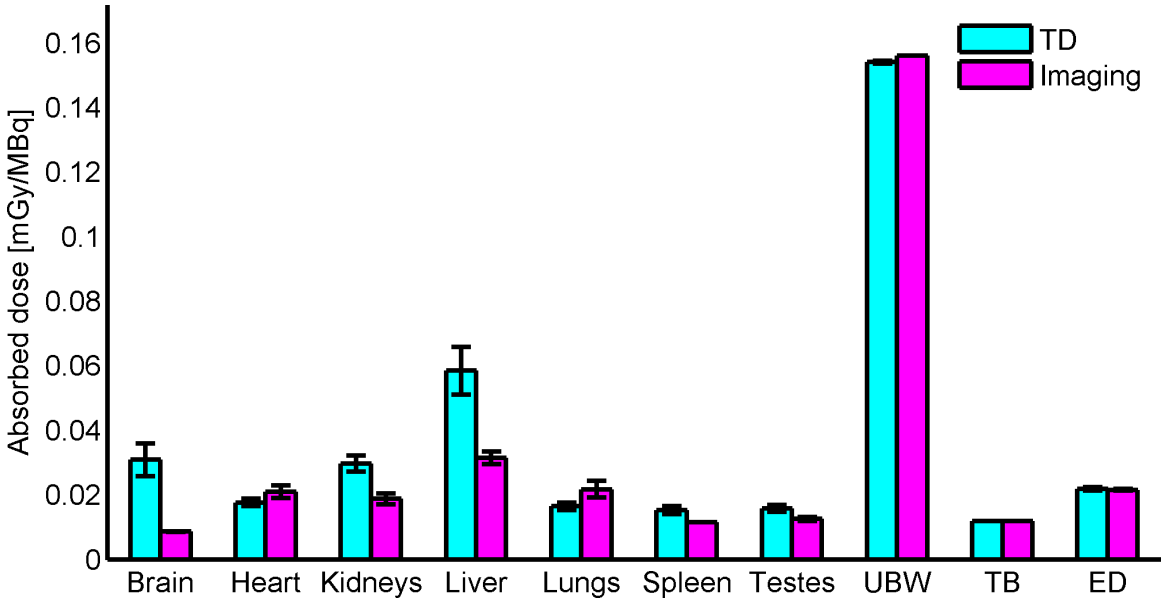

Figure 3.3: Absorbed doses of main organs derived by organ harvesting (TD) and dynamic imaging (imaging) with sphere segmentation; UBW = urinary bladder wall, TB = total body and ED = effective dose in mSv/MBq based on tissue weighting factors from ICRP 60

on full organ segmentation. The effect causing the differences in activity quantification between organ harvesting and dynamic microPET imaging is the well known imaging artifact PVE / spill over effect (see Section 2.1). It is especially present on boundaries of structures having different activities and decreases with object size. The main cause of the effect is the finite spatial resolution of microPET imaging, which is limited by detector sizes and the physical nature of the positron emission. We attempted to minimize the effect by decreasing the size of the volume of interest (VOI) created in images used for extraction of the TAC from organs. Spheres of 2 mm radius were positioned in the centre of organs to avoid PVEs on boundaries between structures, but only a slight improvement was observed and ratios of time-integrated activity coefficients of organs in the range of 2.04 (largest underestimation in microPET; liver) to 0.64 (largest overestimation in microPET; lung) remained. Although a correlation of above r=0.96 ($p < 0.0001$) was achieved between all dosimetry estimates and the resulting effective dose deviated by only 2%, ratios of absorbed doses for some organs were in the range of 3.58 (brain) to 0.76 (lung). However, the brain was only derived by organ harvesting explaining the large difference because only cross-radiation was taken into account in dosimetry estimates derived by microPET imaging (2^{nd} largest overestimation was the liver with

a ratio of 1.86). Projected maximum single injection doses according to research regulations were 325 MBq in the USA and 459 MBq in the EU (both values based on organ harvesting, bladder fraction of 0.5 and ICRP 60 values in case of EU limit). We demonstrated, that 18F-UCB-H meets standard regulations regarding radiation dosimetry for use in human clinical trials and its radiation burden is comparable or less than the most widely used clinical tracer 18F-FDG with reported values between 2.1E-02 mSv/MBq and 2.9E-02 mSv/MBq [107]. Since preclinically derived radiation dosimetry estimates are the basis for calculations of safe injection limits for first-in-human use, it is of great importance to achieve accurate quantification to prevent over-exposure of subjects in clinical studies. Therefore, ways of improving dynamic microPET imaging for dosimetric purposes in mice, specifically the impact of PVE, were sought. Kesner et al. [41] applied a method to improve quantification in rats involving a cross-calibration between organ harvesting and dynamic microPET imaging for radiation dosimetry. Since PVEs are object size dependent, success of this method for dosimetry in mice was uncertain and it was applied to a study of two different radiopharmaceuticals presented in the following Chapter.

3.2 Hybrid microPET imaging in mice for accelerated dosimetry

In this Section the radiation dosimetry of 18F-FDOPA and 18F-FTYR as published in Molecular Imaging and Biology is briefly summarized [108]. For in-depth information the reader is referred to Paper II in Appendix B. 18F-FDOPA and 18F-FTYR were selected for this study, since no radiation dosimetry estimates were available in literature for 18F-FTYR and for 18F-FDOPA only clinical values were published. The radiation dosimetry of both tracers was derived from mice by organ harvesting and dynamic microPET imaging as was for 18F-UCB-H in Section 3.1. Additionally, we applied a method we refer to as hybrid imaging for the first time in mice in order to address the impaired quantification of pure microPET imaging revealed in the preclinical study of 18F-UCB-H. TACs are cross-calibrated with activity measurements from post scan dissected organs, which aims at combining the advantages of microPET imaging of fast and efficient data acquisition involving far fewer animals and the advantages of accurate quantification of organ harvesting. The preclinically derived human radiation dosimetry of 18F-FDOPA was compared to the published clinically derived values by Brown et al. [109] and the human radiation dosimetry of 18F-FTYR was presented for the first time in literature. Additionally, the mouse

radiation dosimetry of both tracers was calculated using S-factors recently published by Mauxion et al. [74]. However, since a separate manuscript investigating the animal radiation dosimetry was prepared for all tracers used throughout this work, the mouse dosimetry data is summarized and presented in Section 3.3. After bolus injection of 18F-FDOPA, thirty anaesthetized mice in total were sacrificed by decapitation at 6 different time points (n=5 at 2, 5, 10, 30, 60 and 120 min) for organ harvesting and four separate mice were scanned dynamically over 120 min with microPET. Supplemental microCT images were acquired for image segmentation. Co-registered 3D representations of microCT and averaged microPET images are displayed in Figure 3.4. VOIs based on the co-registered microCT images were used for data extraction from dynamic microPET images (full organ segmentation and sphere segmentation). Every mouse undergoing dynamic microPET imaging was dissected afterwards and the activity remaining in organs was quantified using the same approach as in organ harvesting. A cross-calibration factor, the ratio between the activity derived from the dissected organ and the activity at the last time point in dynamic microPET in the same organ, was obtained and applied to scale TACs derived from microPET imaging. For 18F-FTYR eighteen mice were sacrificed for organ harvesting (n=3 at 2, 5, 10, 30, 60 and 120 min) and processed in the same manner. However, mice used for the final time point (120 min) of organ harvesting were scanned dynamically for 120 min instead of using separate subjects. The obtained TACs were processed in the same way as for 18F-FDOPA. Time-integrated activity coefficients were calculated from derived TACs for both tracers and used for calculating human dosimetry estimates with OLINDA/EXM. All derived TACs extrapolated to human data are displayed in Figure 3.5. Only data derived by sphere segmentation is presented here.

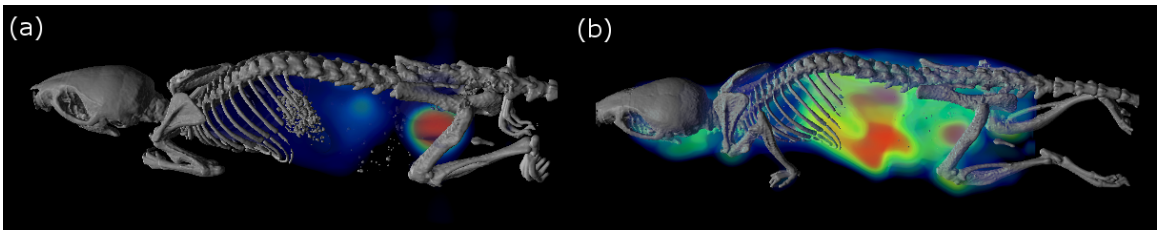

Figure 3.4: 3D representation of co-registered microCT and averaged microPET image of representative subjects with (a) 18F-FDOPA and (b) 18F-FTYR

The correlation between time-integrated activity coefficients derived by organ harvesting and pure imaging was improved by the cross-calibration of hybrid imag-

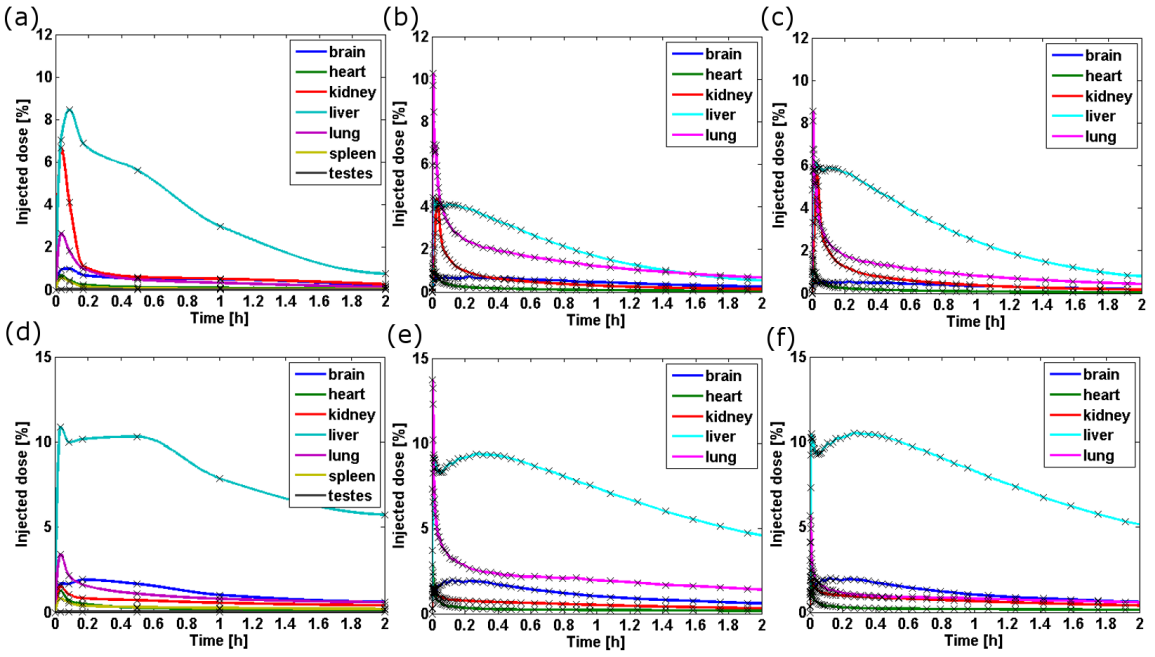

Figure 3.5: 18F-FDOPA TACs: (a) organ harvesting, (b) imaging, (c) hybrid imaging, and 18F-FTYR: (d) organ harvesting, (e): imaging, (f) hybrid imaging [108]

ing from r=0.69 ($p < 0.1995$) to r=0.95 ($p < 0.0149$) for 18F-FDOPA and from r=0.98 ($p < 0.0034$) to r=0.99 ($p < 0.0001$) for 18F-FTYR (data only shown in Paper II in Appendix B). The highest time-integrated activity coefficient was obtained for the urinary bladder wall (theoretical value, fraction of 0.5) and the liver for 18F-FDOPA and the liver followed by the urinary bladder wall (theoretical value, fraction of 0.2 due to evidence of less activity accumulation in the bladder) for 18F-FTYR. Faster sphere segmentation resulted in time-integrated activity coefficients closer to values derived by organ harvesting than values obtained using laborious manual full organ segmentation. In Figure 3.6 the calculated absorbed doses of major organs and the resulting effective dose of both tracers is displayed for all three methods. The correlation between the sets of absorbed doses derived by organ harvesting and pure imaging was marginally improved by hybrid imaging and correlation values of above r=0.995 ($p < 0.0001$) were achieved. The effective dose (using the tissue weighting factors from ICRP 60) of 18F-FDOPA was 1.97E-02 $\pm$ 1.00E-04 mSv/MBq derived by organ harvesting (2.02E-02 $\pm$ 1.12E-04 mSv/MBq by imaging / 2.00E-02 $\pm$ 7.07E-05 mSv/MBq by hybrid imaging). The highest absorbed dose was received by the liver followed by the osteogenic cells (organ harvesting). The effective dose of 18F-FTYR was 1.64E-02 $\pm$ 2.50E-04 mSv/MBq obtained by organ harvesting (1.70E-

02 ± 2.36E-04 mSv/MBq by imaging / 1.63E-02 ± 1.70E-04 mSv/MBq by hybrid imaging). The liver received the highest radiation burden followed by the kidneys (organ harvesting).

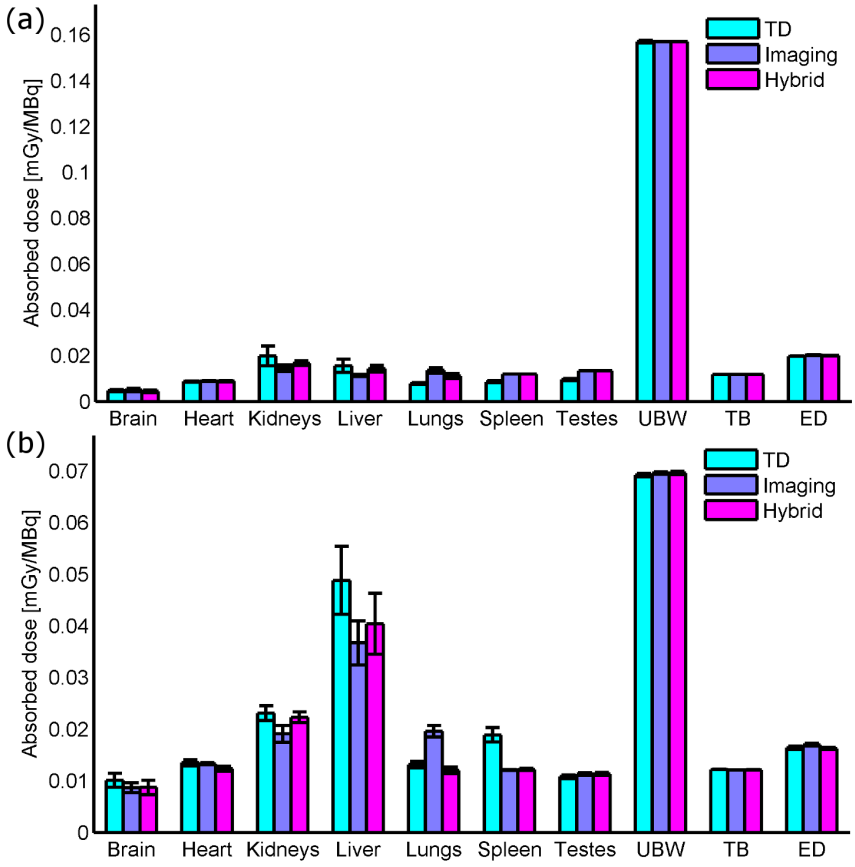

Figure 3.6: Absorbed doses of main organs derived by organ harvesting (TD) and dynamic imaging (imaging) and hybrid imaging for (a) 18F-FDOPA and (b) 18F-FTYR; UBW = urinary bladder wall, TB = total body and ED = effective dose in mSv/MBq based on tissue weighting factors from ICRP 60

3.2.1 Discussion

Applying hybrid imaging towards dynamic microPET imaging for dosimetric purposes has increased the accuracy of radiation dosimetry estimates for both radiopharmaceuticals. The fast small sphere segmentation produced more accurate results making laborious full organ segmentation unnecessary as it is more prone to PVE. Absolute errors in time-integrated activity coefficients and the resulting absorbed doses were reduced by hybrid imaging for most organs in both tracers as can be

seen in Figure 3.6. This is of special concern in radiation dosimetry as preclinical estimates are used to calculate injection limits for first-in-human clinical trials and underestimations could result in over-exposure of human subjects. Although for some organs slight differences remained between organ harvesting and hybrid imaging, they can be explained by methodological differences (such as the blood removal from organs in organ harvesting) and remaining PVEs. In the microPET attenuation scan (acquired at low resolution using a ^{57}Co point source) PVEs on organ boundaries cause additional overestimations in the reconstructed emission scan, especially on boundaries with large density differences (i.e. on lung boundaries). Using a modern combined PET/CT system might improve quantification accuracy. Smaller remaining differences could be explained by only using the last time point of microPET imaging for cross-calibration. PVE is a dynamic problem in imaging, as it depends on the activity inside the region of interest as well as the activity in the background [53]. Since conditions are changing constantly in the dynamic biodistribution, the calibration factor might change dynamically as well. The comparison of the preclinically derived radiation dosimetry of 18F-FDOPA in humans to the clinically derived values by Brown et al. [109] showed that correlations of above r=0.99 ($p < 0.0001$) were achieved with all three methods. The total body absorbed dose and the effective dose were estimated with an error of 10% and 2%, respectively. However, ratios between the preclinically derived absorbed dose values and the clinical values from Brown et al. for 18F-FDOPA from 0.61 (underestimation in kidney; hybrid imaging) to 1.30 (overestimation in muscle; hybrid imaging) were found for organ absorbed doses. Additionally, the critical organ was misinterpreted by our preclinically derived values as the uterus was estimated to receive the highest dose, whereas Brown et al. showed that the kidney is the critical organ. In conclusion, we demonstrated that the new method hybrid imaging in mice yields comparable results to organ harvesting, while involving fewer resources, radiopharmaceuticals and substantially fewer animals. The full biodistribution of each animal can be acquired with a much higher time resolution with less intraspecies differences compared to organ harvesting, where multiple animals are used for each derived time point. We also showed that time-consuming whole-organ delineation is unnecessary and can be replaced by the much faster sphere segmentation, which counteracts PVE on organ boundaries further. We derived for the first time in literature the radiation dosimetry of 18F-FTYR and determined the effective dose to be 1.64E-02 mSv/MBq $\pm$ 2.50E-04 mSv/MBq with the liver being the most exposed organ (based on organ

harvesting). The revealed differences in human organ absorbed doses between preclinically derived estimates and clinically derived estimates for 18F-FDOPA suggest that preclinically derived radiation dosimetry estimates should nevertheless be used with care when calculating injection doses for first-in-human studies.

3.3 Absorbed doses to mice for three [^{18}F]-tracers

3.3.1 Overview

In this Section the animal radiation dosimetry of 18F-FDOPA, 18F-FTYR and 18F-UCB-H (for details see Paper III in Appendix C) in mice is briefly summarized. The manuscript was submitted for the Marie Cure Award at the EANM conference in Lyon, France, and was considered as one of the best 5 of all submitted abstracts. Since small animals are commonly used as translational models for human clinical research, they often have to undergo longitudinal studies involving several consecutive microPET scans [15, 110]. The cumulative received absorbed dose of the animals might be considerably large, which is often neglected in preclinical studies. It might have a significant impact on the animal's physiology and consequently could compromise the outcome of the study. A single entrance absorbed dose of above 6 Gy is considered lethal to a mouse [111]. The biological effects of low-level radiation, however, will vary with type of radiation, dose delivered, delivery rate, type of tissue, and animal strain [112]. Consequently, it is of great importance to be able to predict the amount of radiation in various study setups. The aim of this investigation was to quantify the radiation burden animals are exposed to by microPET imaging in a typical preclinical setup and to project the data from single injections to longitudinal studies, where animals have to undergo several consecutive scans. The experimentally obtained biodistributions of the tracers were taken from the preclinical study presented in Section 3.1 and the preclinical study presented in Section 3.2. The TACs derived with several methods (organ harvesting, dynamic imaging and hybrid imaging) were applied to the MOBY phantom [73] and using the S-factors recently derived by Mauxion et al. [74] the mouse dosimetry was calculated for the first time for the three ^{18}F radiopharmaceuticals. A 3D representation of co-registered images from microCT and averaged microPET images of all tracers for representative subjects are displayed in Figure 3.7.

Absorbed doses of major organs in mice are shown in Figure 3.8 for all three tracers. The total body absorbed dose was 14.04 $\pm$ 0.03 mGy/MBq derived by organ

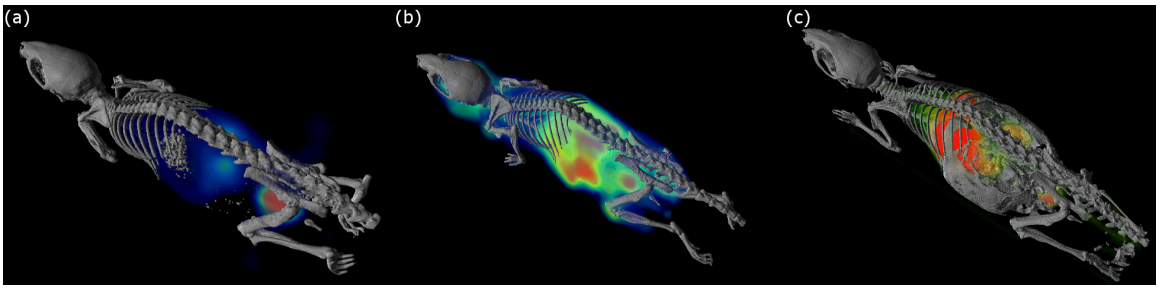

Figure 3.7: 3D representation of representative subject of averaged PET/CT image for (a) 18F-FDOPA, (b) 18F-FTYR and (c) 18F-UCB-H

harvesting for 18F-FDOPA, 14.23 ± 0.05 mGy/MBq for 18F-FTYR and 14.38 ± 0.06 mGy/MBq for 18F-UCB-H. The average total body absorbed dose across all methods and tracers was 14.19 ± 0.10 mGy/MBq. The largest absorbed dose was received by the urinary bladder wall for 18F-FDOPA (value not included in Figure 3.8, 660.8 ± 276.88 mGy/MBq), and the liver for 18F-FTYR (48.23 ± 6.27 mGy/MBq) and 18F-UCB-H (65.14 ± 8.47 mGy/MBq).

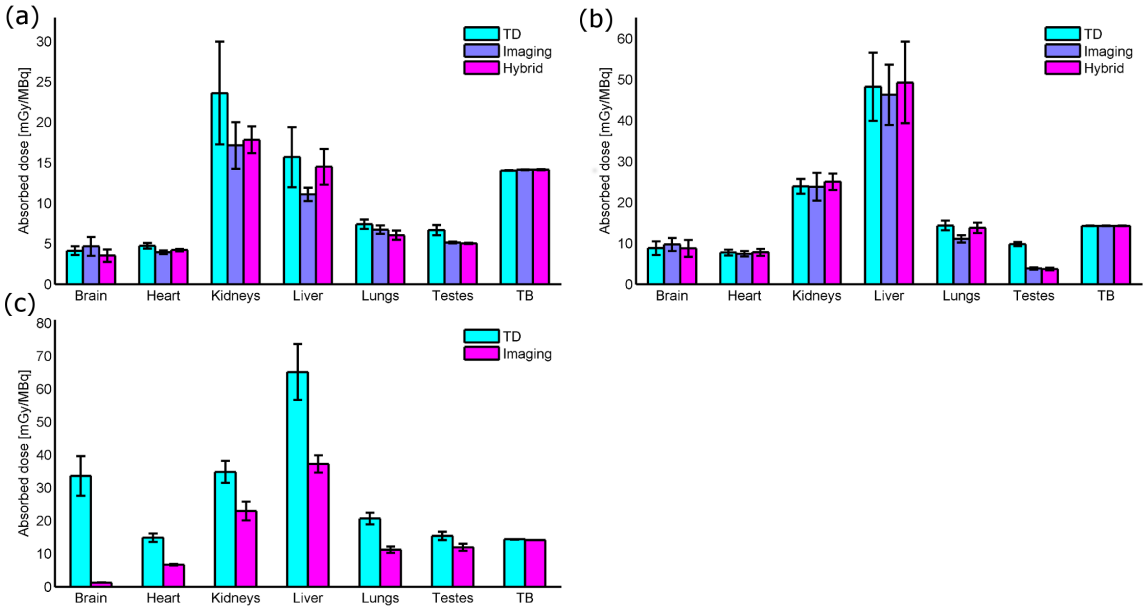

Figure 3.8: Absorbed doses in mice derived by organ harveting (TD), dynamic imaging (Imaging) and hybrid imaging (Hybrid) from (a) 18F-FDOPA, (b) 18F-FTYR and (c) 18F-UCB-H. TB = total body

3.3.2 Discussion

Applying hybrid imaging led to an improvement of activity quantification in most organs for 18F-FDOPA and 18F-FTYR (hybrid imaging not applied to 18F-UCB-H) in mouse dosimetry analogous to the extrapolated human dosimetry. The calculation of the mouse dosimetry has shown that the animals receive a significant amount of radiation from a single microPET scan. When considering a standard injection of 10 MBq per animal per scan, absorbed organ doses can vary between 100 and 400 mGy with the urinary bladder wall for 18F-FDOPA receiving the highest amount of radiation of above 6 Gy per single scan. However, the urinary bladder wall absorbed dose was derived without voiding assuming a static organ volume and therefore might be overestimated. The total body absorbed dose (effective dose cannot be derived as there are no weighting factors for animal tissues) was calculated as approximately 140 mGy per scan per animal for all tracers, which is in agreement with published data for other ^{18}F-tracers in mice [37]. The organ receiving the highest radiation for 18F-UCB-H and 18F-FTYR was the liver. Assuming five consecutive scans in a longitudinal study with injections of 10 MBq each, the cumulative total body absorbed dose from microPET amounts to 0.7 Gy. Single organ absorbed doses might reach 3.25 Gy for the liver using 18F-UCB-H or 30 Gy for the bladder wall using 18F-FDOPA. This significant exposure might alter the physiology and thus have an impact on the results of the study or even introduce stochastic / deterministic effects. In most longitudinal studies, subjects undergo for each microPET scan an additional microCT scan, which further increases the radiation burden. Researchers should always consider the amount of radiation delivered and keep it as low as possible by limiting the injected activity and the number of scans while still producing the desired images. In order to be able to estimate the total received radiation in a dual modality imaging setup, the dose inflicted on animals from microCT was investigated and is presented in Section 3.5 and 3.6.

3.4 Radiation dosimetry for [^{18}F]UCB-H: First-in-human study

3.4.1 Overview

In this section the clinically derived human radiation dosimetry of 18F-UCB-H is briefly discussed. For detailed information on the conducted experiments and in-depth results the reader is referred to Paper IV in Appendix D. The investigated

radiotracer is the same as in Section 3.1 and targets the human SV2A protein. Following the preclinical investigation of the radiation dosimetry, the safety of the radiopharmaceutical for administration in humans has to be confirmed according to national regulations by a first-in-human trial. The aim of the study was to determine the biodistribution and the whole body radiation dosimetry of 18F-UCB-H for the first time in 5 male subjects using dynamic PET imaging. Injection limits according to European and American regulations in medical research, which keep the radiation burden below recommended thresholds, were derived and presented. Furthermore, since the same tracer was also investigated preclinically (see section 3.1), the radiation dosimetry results were compared to each other. Dynamic whole body PET/CT imaging was performed on five healthy volunteers over approximately 110 minutes. TACs were derived from segmented organs on co-registered CT images and the human radiation dosimetry was calculated using OLINDA/EXM [70]. The same urinary excretion scenarios as in the preclinical study (Appendix A / [80]) were implemented with voiding every 2h or 4h and fractions of injected activity leaving via urinary pathways of 0.3 to 0.5.

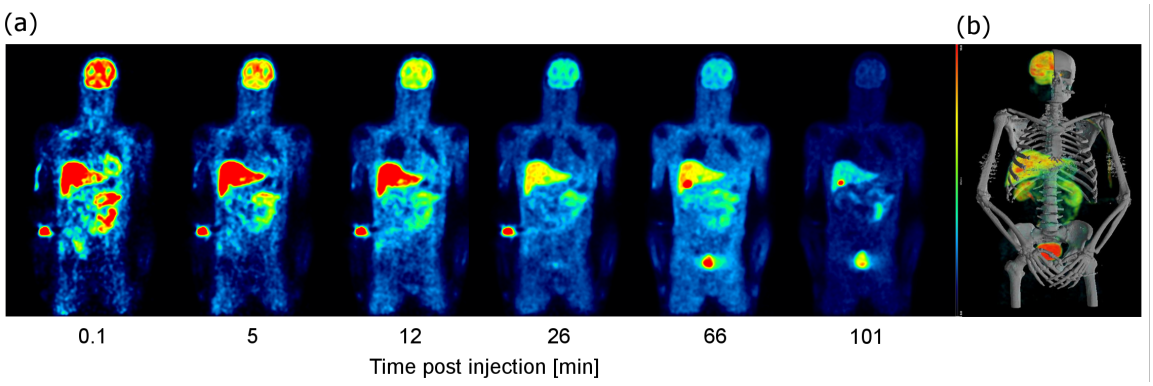

Figure 3.9: (a) Whole-body coronal image of representative subject at different time points post administration of 18F-UCB-H and (b) 3D representation of PET/CT image averaged over all frames

In Figure 3.9 a sequence of whole-body coronal images of a representative subject is displayed. High uptake could be observed in the brain, which is the tracer's main organ of interest, the liver, and the gallbladder. In Figure 3.10 the calculated absorbed doses and the effective dose based on the tissue weighting factors from ICRP publication 60 are presented along with their corresponding preclinically derived values from Section 3.1. The effective dose amounted to 1.98E-02 $\pm$ 1.30E-04 mSv/MBq and the highest radiation was received by the urinary bladder wall (not

included in Figure 3.10), followed by the gallbladder and the liver. However, the urinary bladder wall value was derived using the software module of OLINDA/EXM for urinary excretion in a rather conservative setup.

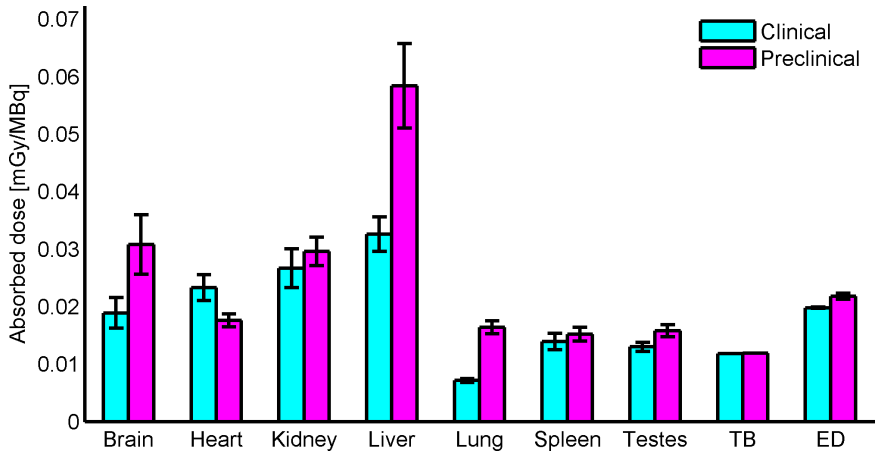

Figure 3.10: Preclinically and clinically derived absorbed dose estimates (both for urinary excretion scenario of voiding every 4h and 0.5 of injected activity leaving via urinary pathways), ED = Effective dose in [mSv/MBq]

3.4.2 Discussion

The biodistribution of 18F-UCB-H revealed a significant uptake of the tracer inside the brain emphasizing its potential for the investigation of the role of SV2A in the normal and pathological central nervous system. The effective dose based on tissue weighting factors from ICRP publication 60 resulting from an administration of 18F-UCB-H of 1.98E-02 $\pm$ 1.39E-04 mSv/MBq was determined to be less than reported values in literature for the most widely used clinical tracer 18F-FDG [107]. The injection limits according to American and European regulatory agencies were determined and showed, that single injections up to 321 MBq in the USA and 505 MBq in Europe result in equivalent doses (USA) and effective doses (EU) below limits of the respective agency. When comparing clinically derived results to preclinical results it becomes evident, that the effective dose and total body absorbed dose were estimated preclinically within a 10% error window of the clinically derived values. Despite the close estimations for total-body absorbed doses and a correlation value r=0.969 ($p < 0.0001$) between the datasets, some significant differences with ratios between clinical and preclinical values of 0.43 to 1.97 were found in single-organ absorbed doses (i.e. 0.43 for preclinical overestimation of lung absorbed dose and

1.97 for preclinical underestimation of gallbladder wall absorbed dose). They could be related to methodological differences (anaesthetized in animals vs. awake in humans) and interspecies differences in properties such as metabolic rate. Additionally, the injected activity per kilogram body mass is 100-fold higher in mice than in humans possibly resulting in higher blood activities increasing the absorbed dose in highly perfused organs (such as brain, liver and lung). Since preclinical estimates are only derived to project first injection doses to limit exposure of subjects in a first-in-human trial, errors in single absorbed doses might cause an over-exposure of the subject if the projections are not handled with care. However, most values were overestimated in preclinical estimates.

3.5 X-ray dose quantification of the GE explore 120 micro-CT

3.5.1 Overview

In the following Section the manuscript published in the IEEE Transactions on Nuclear Science about the dosimetry and the performance evaluation of the microCT GE eXplore 120 is discussed (for details the reader is referred to Appendix E / [113]). All experiments and analysis related to the performance evaluation were conducted by Dr. Mohamed Ali Bahri. However, since the focus of the manuscript is on dosimetry, the performance evaluation is only partially summarized. Since in most preclinical microPET studies a microCT scan is performed for anatomical information, additional radiation is received by the animal with each scan. MicroCTs are usually characterized by a very high spatial resolution of typically a few μm to 100 μm depending on the machine, its intended application and protocol settings. The high resolution and small detector sizes usually entail a high radiation dose (high photon flux) in order to keep signal-to-noise ratios above acceptable thresholds for image reconstruction. Therefore, in order to be able to predict total radiation received by animals in longitudinal studies involving microPET and microCT, the dosimetry of the microCT GE eXplore 120 microCT was investigated for the first time. The GE eXplore 120 microCT provides a set of pre-implemented protocols for the end user to apply in different situations. In order to choose the appropriate protocol for a specific study, the resulting image quality of each protocol like contrast and resolution should be considered. Additionally, the resulting dose to the animals should be known *a priori* in order to estimate the overall radiation

burden received by the subjects, especially in dual modality and/or longitudinal studies. Here we investigated the image quality and radiation burden of different implemented protocols to provide help in choosing the appropriate protocol for different studies and to clarify the dose inflicted on animals during microCT scans. The dose measurements were conducted using a mobileMOSFET dose verification system (BestMedical Canada, Canada) in four protocols that are regularly applied in live animal scans. The properties of the protocols (P1 to P4) are summarized in Table 3.1.

	Voltage (kV)	Current (mA)	Exposure time (ms)	Projections (Views)	Gantry rotation (°)	Voxel size (µm)
Fast scan 220 (P1)	70	32	16	220	193	100
Fast scan 360 (P2)	70	32	16	360	360	100
Soft tissue fast scan (P3)	70	50	32	220	193	50
Soft tissue step & shoot (P4)	80	32	16	220	193	100

Table 3.1: Properties of investigated microCT protocols

A custom-built PMMA phantom with several inlets for sensors was used to obtain dose profiles to calculate the $CTDI_{100}$ and MSAD (see Section 2.9 / [99]). The dose was also quantified *in vivo* in sacrificed rats of different size/weight to obtain organ doses and to assess the impact of the surrounding tissue. single field of view (sFOV) and multiple field of view (mFOV) scans were acquired and compared to the $CTDI_{100}$ and MSAD. Additionally, a scan with each protocol in each rat was performed with the QRM bar pattern phantom [114] inserted into the abdominal cavity to visually assess the *in vivo* image quality and its deterioration due to the amount of surrounding tissue. The determined $CTDI_{100}$ showed that the average radiation inside the centre position of the PMMA phantom varied approximately between 20 mGy (P1) and 56 mGy (P3). The MSAD was estimated by analytical superposition of the acquired sFOV dose profiles according to machine properties and amounted to approximately 28 mGy (P1) to 78 mGy (P3). Since the acquired field of view (FOV) (55 mm) is smaller than the full width half maximum (FWHM) (74.5 mm) of the dose profile, large tails at each side of the dose profile increase the $CTDI_{100}$ compared to the real measured *in vivo* point dose as can be seen in Figure 3.11.

When applying a factor accounting for the difference between the FOV and the FWHM, the measurements agree. No significant impact of the animal's weight

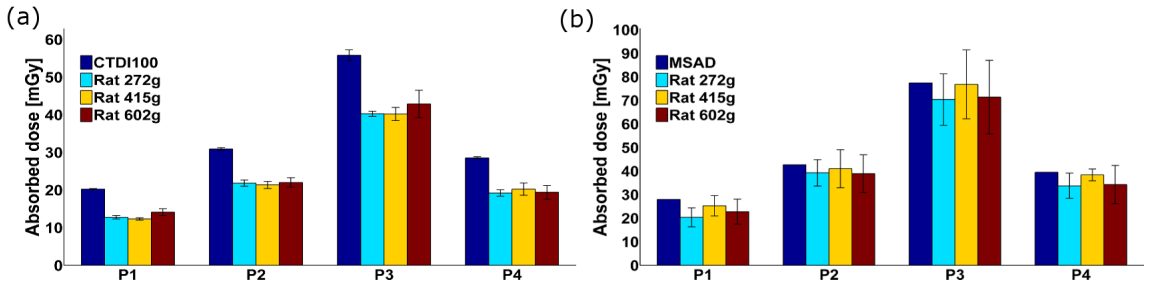

Figure 3.11: (a) $CTDI_{100}$ (single FOV measurement) (b) MSAD (multiple FOV measurement) each vs. *in vivo* averaged dose point measurements (brain, chest, abdomen, anal cavity) in rats of different size [113]

or the location of the sensor (brain, chest, abdomen and anal cavity) on the dose measurement was observed. However, when visually inspecting the *in vivo* scan of the bar pattern phantom in Figure 3.12, a clear impact can be observed regarding resolution and contrast.

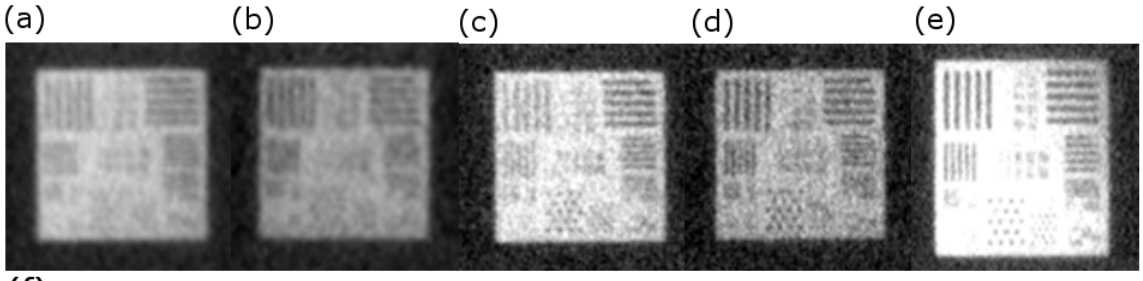

(f)

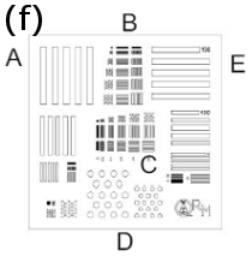

Block	linewidth (µm)	linepairs per pattern	points (µm)	points per pattern
A	5, 10, 25, 50, 100, 150	5		
B	5, 10, 15, 20, 25, 30	5	5, 10, 15, 20, 25, 30	18
C	5, 10, 15, 20, 25, 30	5	5, 10, 15, 20, 25, 30	18
D			5, 10, 25, 50, 100, 150	18
E	5, 10, 25, 50, 100, 150	5		

Figure 3.12: *In vivo* bar pattern scan using (a) P2 in rat 272g, (b) P2 in rat 602g, (c) P3 in rat 272g, (d) P3 in rat 602g, (e) P3 *ex vivo* in air and (f) technical sketch of phantom [114]. All images from -500 to 2000 HU [113]

3.5.2 Discussion

We demonstrated by deriving the $CTDI_{100}$ and the MSAD *ex vivo* using a phantom, that the GE eXplore 120 microCT delivers a significant amount of radiation per scan. *Ex vivo* measurements were confirmed by *in vivo* results obtained in sacrificed

rats. Depending on the protocol additional doses of 28 mGy to 78 mGy are inflicted on each animal per microCT scan when using mFOV acquisitions. Higher energy protocols such as P3 were able to confirm the *ex vivo* measured resolution of 100 μm independent of the rats weight, whereas low energy protocols could only achieve 150 μm in the smaller rat. The animal's weight had a clear impact on the contrast between the resolution plate and the filling material as can be seen in Figure 3.12c and Figure 3.12d. The larger the amount of surrounding tissue the less contrast is remaining between plate and filling material. In conclusion, a trade off between resolution/contrast and the delivered dose must be made. If contrast/resolution is of great importance, smaller animals seem more suitable for experiments. If the highest resolution is not necessary, low energy protocols should be used for dose reduction. Since the experimental setup only allows for dose point measurements, Monte Carlo simulations were performed to investigate the spatial dose distribution inside small animals further non-invasively. The results and their implications are presented in the following Section.

3.6 Monte Carlo simulations of the dose from the GE eXplore 120 microCT

3.6.1 Overview

In the following Section, the manuscript on Monte Carlo simulations (MCS) of the GE Explore 120 microCT using GATE is summarized. For in-depth information on the study the reader is referred to Paper VI in Appendix F. Small animal imaging has gained significant importance in preclinical studies due to the increasing use of small animals as translational models for clinical disease and treatment research [13]. Most studies investigating the dose delivered by microCTs rely upon experimental measurements in phantoms and sacrificed animals [101, 112, 113]. Organ doses are derived using MOSFET sensors or TLD chips, but both have a large geometry and provide only dose point measures. MCS are a useful tool to investigate the dose distribution within organs non-invasively [36, 115]. Bone doses, which are expected to be higher than organ doses due to their high density, cannot be derived experimentally since only surface entrance doses can be obtained. The aim of this study was to establish a model of the GE eXplore 120 microCT in the MCS package GATE [68] and to derive the dose delivered by the machine from several protocols that are regularly applied to live animals. Simulated data was compared

to experimentally derived results available in Appendix F and [113]. We modelled the built-in X-ray source of the GE eXplore 120 microCT, the PX1483GS from Dunlee (Subdivision of Philips Healthcare, Amsterdam, Netherlands), as a circular source of the size of the focal spot (diameter of 0.3 mm) and simulated X-ray spectra at 70, 80 and 100 kVp tube voltage using an online tool provided by Siemens based on the algorithm of Boone et al. [116]. The half-value layer (HVL) of the spectra, which represents the thickness of a material in the beam path to reduce the intensity of the radiation by half (in this case aluminium), was measured experimentally and simulated in order to validate the spectra. CT images of the PMMA phantom used in the experiments [113], a representative rat and mouse were implemented into the model as phantoms and material compositions of PMMA, carbon fiber, soft tissue, lung, air and bone were assigned to the respective regions of the three phantoms. We derived the $CTDI_{100}$ (from sFOV acquisitions) and the MSAD (mFOV acquisitions, see Section 2.9 for definitions) using the PMMA phantom and organ doses in mice and rats using the respective CT image phantom. Four protocols (P1 to P4) were investigated, which are displayed in Table 3.1. Only a fraction of the amount of emitted photons per second from the X-ray tube was simulated to keep computation times in an acceptable range. The ratio between the experimentally determined $CTDI_{100}$ and the $CTDI_{100}$ in the simulated dose maps of the PMMA phantom was used to scale the dose maps to exposures corresponding to the real amount of photons emitted by the X-ray tube (similar to Taschereau et al. [36]). In Figure 3.13a the simulated spectra at 70, 80 and 100 kVp are presented along with their corresponding HVL determined by experiments and simulation in Figure 3.13b. A slight error increase at higher tube voltages between simulated data and measured data was observed, however, data agreed within 7%.

In Table 3.2 results from the simulations using the PMMA phantom for all investigated protocols are displayed. The largest dose was delivered by the protocol P3 followed by P2. Large standard deviations were observed for the transaxial average of the $CTDI_{100}$ for P1, P3 and P4 compared to P2.

In Figure 3.14 a comparison of experimentally derived dose profiles inside the PMMA phantom and simulated dose profiles is displayed for sFOV acquisitions (Figure 3.14a) and mFOV acquisitions (Figure 3.14b). The $CTDI_{100}$ derived from the central position and all transaxial positions is compared in Figure 3.14c.

Simulation dose maps of the mouse and rat phantom showed large doses deposited in bone of 459.13 ± 96.37 mGy in mice and 298.69 ± 91.87 mGy in rats from the high energy protocol P3. All soft tissue organs showed similar average

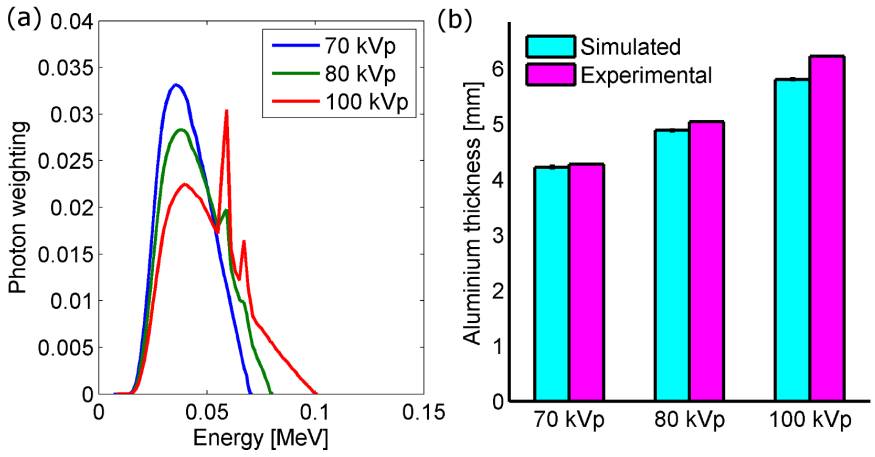

Figure 3.13: (a) Simulated spectra at respective tube voltage and (b) the corresponding HVL from simulation and experiments

	P1	P2	P3	P4
Scaling factor fc	9816.1	12642.0	13547.8	14228.1
$CTDI_{100}$ center [mGy]	20.25 ± 0.44	30.09 ± 0.29	55.81 ± 0.48	28.56 ± 7.41
$CTDI_{100}$ transaxial [mGy]	20.12 ± 2.59	30.94 0.19	55.58 ± 7.82	28.13 ± 3.71
MSAD center [mGy]	28.75 ± 1.32	-	-	-
MSAD transaxial [mGy]	28.76 ± 4.05	-	-	-

Table 3.2: Scaling factor (ratio between simulated and experimental $CTDI_{100}$), simulated $CTDI_{100}$, and transaxial average of $CTDI_{100}$ of all protocols and the simulated MSAD of P1

radiation exposures of 159.42 ± 43.92 mGy in mice (P3) and 128.02 ± 36.67 mGy in rats (P3). Mice received higher doses than rats due to their smaller mass with an average total body dose of 188.70 ± 112.05 mGy from P3 (rat: 118.89 ± 71.09 mGy P3).

3.6.2 Discussion

We established a valid Monte Carlo simulation model of the GE eXplore 120 microCT. The necessary X-ray spectra were simulated using a Siemens online tool. Their HVL values simulated using our Monte Carlo model agreed within a 7% error window with experimentally measured values. The error increase for higher tube voltages could be related to characteristic emission peaks from the PX1483GS, whose anode is made of tungsten and rhenium, while the spectra implemented in the simulations

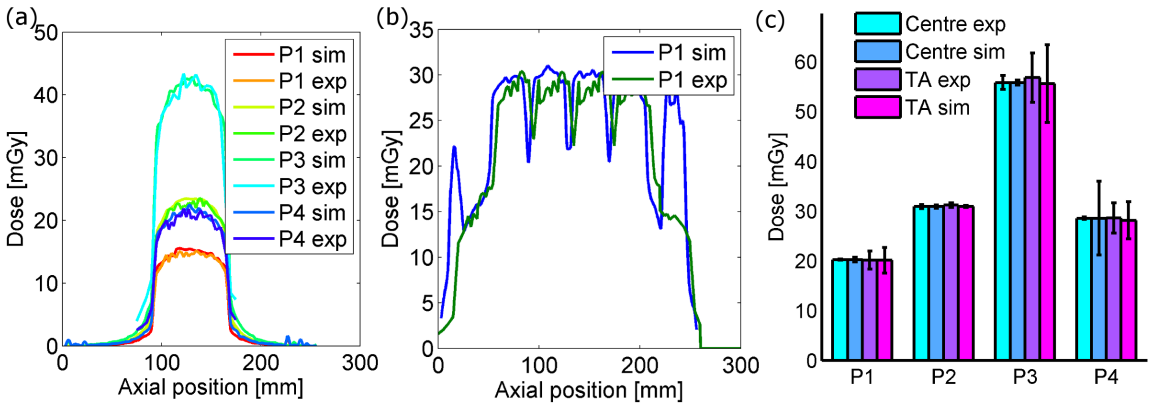

Figure 3.14: Dose profiles derived from the central position inside the PMMA phantom for (a) sFOV acquisition, (b) mFOV acquisitions and (c) the corresponding $CTDI_{100}$ including the transaxial average; exp= experimentally derived and sim= simulated

represented an anode fully made of tungsten. Characteristic emission peaks, which become more apparent at higher tube voltages (see Figure 3.13a) are unique to the respective material and might have caused a slight mismatch between experimentally determined and simulated HVL values. Simulated $CTDI_{100}$ and MSAD values confirmed experimental results with the highest radiation delivered by P3 followed by P2. Higher standard deviations in transaxial averages for P1, P3 and P4 compared to P2 can be related to 192° gantry rotation increasing the radiation exposure on one side of the phantom. The simulated mFOV acquisition dose profile compared to the experimental dose profile shown in Figure 3.14b revealed dose deposition peaks outside of the phantom boundaries in air, which are artifacts that might originate from the sharp density drop on each side of the phantom. Those edge effects might be related to scatter from inside the phantom. Further investigations need to be performed. However, the calculation of the MSAD from the simulated mFOV dose profile was not affected since only the central portion of the dose profile is taken into account. The simulated organ doses revealed high dose depositions in small animals that exceeded the estimations based on the MSAD from experimental values. Especially bones receive large amounts of radiation with doses of 459.13 ± 96.37 mGy in mice and 298.69 ± 91.87 mGy in rats using P3. A higher radiation burden in mice than in rats is a result of the lower mass / volume of the mouse, which is in agreement with results presented by Boone et al. [117], who derived the total body dose as a function of the diameter of the small animal present. The fact that a dose increase of only approximately 50% from rat to mouse was observed, although the

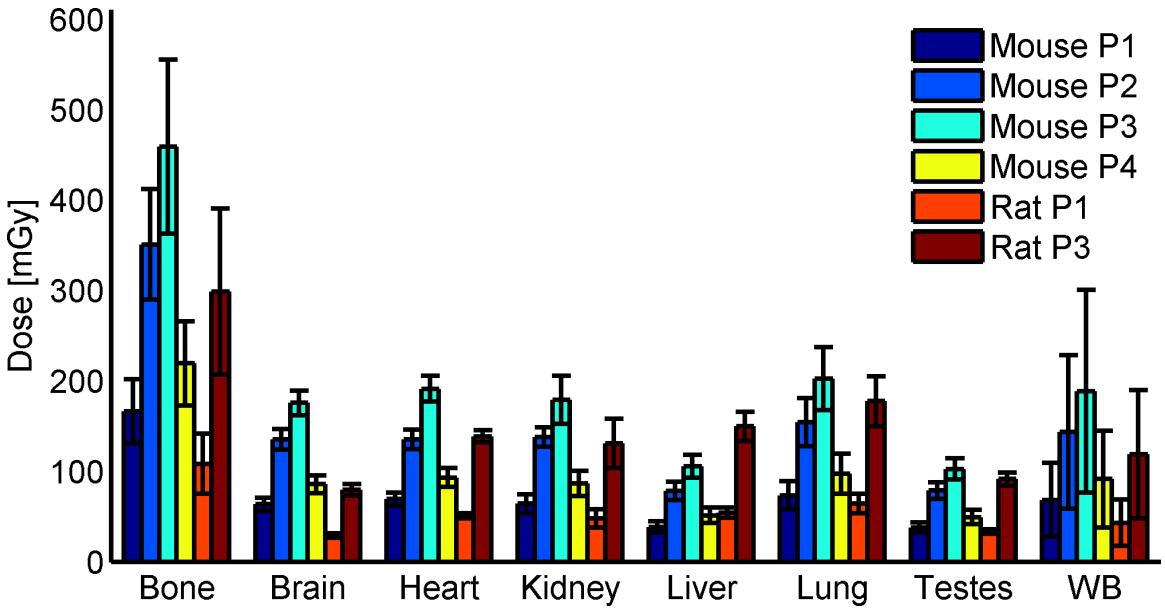

Figure 3.15: Organ doses derived from mFOV acquisitions in mice (3 sFOV, P1 to P4) and rats (5 sFOV, P1 and P3), WB=whole body

volume of the rat is 10-fold greater, explains why no clear trend was observed for experimental dose values in rats of different size (approximately 250g to 620g) in Section 3.5. Researchers need to take the significant additional radiation exposure from microCT into account especially when planning longitudinal dual-modality studies combined with microPET. Since even low level radiations might alter physiological processes [118, 119], the outcome of specific studies might be altered by radiation induced effects.

CHAPTER 4

Discussion

In this manuscript several studies were introduced aiming at the quantification of the radiation burden inflicted on small animals in a preclinical environment or on humans in clinical trials by PET and/or CT imaging. Methodological improvements especially regarding faster and more ethical data acquisition in preclinical radiation dosimetry of PET radiopharmaceuticals using mice were investigated and presented. Comparisons were made between clinically and preclinically derived radiation dosimetry estimates of the same radiopharmaceuticals. Furthermore, the dose received by animals from microCT imaging in preclinical studies was investigated both experimentally and through Monte Carlo simulations. In the introduction, several specific aims (see Section 1.5) were defined and each was addressed with a single study, summarized and discussed in Chapter 3 (see Appendix A to F for in-depth information). The current chapter aims to combine the separate studies into one comprehensive general discussion leading to the implications of the derived results for the field of preclinical and clinical dosimetry.

4.1 Methods of preclinically derived human radiation dosimetry

The human radiation dosimetry of 18F-UCB-H, 18F-FDOPA and 18F-FTYR was derived for the first time preclinically from the biodistribution of the radiopharmaceutical in mice (see Sections 3.1 and 3.2). The biodistributions were obtained using the traditional method of organ harvesting, dynamic microPET imaging, and the newly applied method hybrid imaging (18F-FDOPA and 18F-FTYR only), which combines imaging and organ harvesting.

In Table 4.1 a summary of advantages and disadvantages of all three methods is provided. While organ harvesting features accurate quantification and the possibility

	Advantages	Disadvantages
Organ harvesting	• Accurate quantification • Number of possible organs • Blood extraction	• Number of animals • Labour intensive • Statistics not straight forward • Low temporal resolution • Intraspecies variability
Dynamic imaging	• Whole biodistribution of each animal • High temporal resolution • Early blood peaks are detectable • Statistics straight forward • Low number of animals • Fast data acquisition	• Partial volume effects • Low contrast for segmentation when using microCT • Fewer organs can be derived • No blood extraction
Hybrid imaging	• Same as dynamic imaging • Improved quantification due to cross-calibration (reduced impact of PVE)	• Low contrast for segmentation when using microCT • Fewer organs can be derived • No blood extraction

Table 4.1: Advantages and disadvantages of activity quantification methods

to investigate all organs/tissues/fluids that can be extracted during a dissection, it also requires a substantial amount of animals to be sacrificed (depending on number of time-points and number of animals per time-point), which necessitates large animal housing facilities. The data acquisition is labour-intensive and has to be spread across several days depending on the staff and facilities present. This also entails the necessity of several tracer productions increasing the cost of the investigation. Since only a few time-points are usually investigated, the time-resolution is low and early blood peaks cannot be detected. Intraspecies variability is increased since every sample of each time point is obtained using a different animal, which complicates the derivation of statistics [41].

Dynamic microPET imaging features rapid and simplified data acquisition with a high time resolution enabling the detection of early blood uptake peaks that might contribute significantly to the radiation dosimetry. It involves very few animals, de-

creasing the cost of tracer production and animal housing. The complete dynamic biodistribution in each animal can be obtained for each microPET scan, reducing intraspecies differences and facilitating the derivation of statistics. However, as has been shown by using 18F-UCB-H ([80] / Appendix A), 18F-FDOPA and 18F-FTYR ([108] / Appendix B), and by other authors [90], microPET imaging in mice without further corrections lacks the accurate quantification necessary for dosimetry applications. Significant differences were found in time-integrated activity coefficients, and consequently, human absorbed dose estimates derived using organ harvesting and dynamic microPET imaging. Ratios of time-integrated activity coefficients (organ harvesting divided by microPET imaging full organ segmentation) of up to 0.53 (overestimation; lung) and 2.30 (underestimation; liver) were obtained in the preclinical study of 18F-UCB-H, 0.23 (overestimation; lung) to 1.88 (underestimation; kidney) using 18F-FDOPA and 0.30 (overestimation; lung) to 1.52 (underestimation; liver) using 18F-FTYR. However, when excluding the lung, overestimations were reduced to ratios of 0.73 for 18F-UCB-H, 0.63 for 18F-FDOPA and 0.9 for 18F-FTYR. The lung has a very high volume fluctuation due to movement during respiration and the VOI in the microCT image represents only one specific inflation state. Since neither microCT nor microPET images were gated to the respiration, the co-registration is prone to misalignments as the volume of the lung shown in either image is an average over the respective imaging time. Gating of both images to the same time point might improve the quantification but would reduce the signal-to-noise ratio significantly in microPET imaging as a high amount of coincidence counts is neglected.

Additionally, PVEs arising from the attenuation correction using a ^{57}Co point source further impair the quantification in the lung (in case of stand alone microPET like the Siemens Concorde Focus 120 microPET), which has been shown in the study of 18F-FDOPA and 18F-FTYR (Appendix B). Since the resolution of the attenuation scan is comparably low, PVEs occur on the boundary between lung and surrounding tissue. As the attenuation correction of the emission scan is a multiplication of the attenuation value and the detected coincidence signal, PVEs in the attenuation scan lead to a misinterpretation of the signal in the emission scan. This effect should be decreased when using newer dual modality microPET/microCT scanners, as the resolution of the microCT is higher. These PVEs arise on every transition between tissues of different density in the attenuation scan and between tissues of different activities in the emission scan, which leads to the large over-/underestimations using pure dynamic microPET imaging in most organs.

We found that it was possible to counteract these effects by altering the segmentation technique. By using small spheres that were placed in the centre of each organ, PVEs on the boundaries of organs were avoided and the accuracy of quantification was slightly improved in both studies. However, differences in values derived by organ harvesting remained in time-integrated activity coefficients and consequently human absorbed dose estimates. Total body absorbed doses and effective doses agreed within a 10% error window, but far larger differences in single organ absorbed doses remained (e.g. ratio of 2.05 between absorbed dose derived by organ harvesting and imaging for the liver in 18F-UCB-H study; underestimation in imaging). As has been stressed before, when using preclinically derived estimates to calculate injection limits for first human trials, large differences in absorbed organ doses might lead to significant over-exposures in subjects. The fact that the averaged effective dose is not significantly different while such large differences in single organ absorbed doses are present points out the weakness of using the effective dose for the estimation of injection limits. This issue will be addressed in Section 4.2.1.

Another disadvantage of using microCT and microPET in mice for dosimetric purposes was the low contrast in microCT images for segmentation. Automated segmentation techniques are technically not feasible and most authors rely upon manual full-organ segmentation [41, 88, 90, 120], which is subjective and time-consuming. Using the sphere segmentation increased the segmentation speed significantly, but the subjectivity of manual segmentation remains. Additionally, only major organs can be segmented due to the low contrast, decreasing the accuracy of the radiation dosimetry estimates. Recent developments in the field of preclinical MRI systems might provide a solution for the segmentation issue, as MRI imaging (depending on the sequence) provides a superior soft tissue contrast to CT imaging, possibly allowing for user independent and fast automated segmentation.

Hybrid imaging, which was applied to microPET imaging in mice for the first time, improved the quantification significantly as has been shown in the study of 18F-FDOPA and 18F-FTYR (Appendix B). The cross-calibration of microPET TACs using activity measures of post-scan dissected organs decreased differences found in derived time-integrated activity coefficients and consequently radiation dosimetry estimates between organ harvesting and imaging. Ratios of time-integrated activity coefficients between organ harvesting and hybrid imaging were improved to a range from 0.39 to 1.32 for 18F-FDOPA (0.23 to 1.88 between organ harvesting and imaging) and 0.94 to 1.12 for 18F-FTYR (0.30 to 1.52 between organ harvesting and imaging). This is also reflected in the slight improvement of correlation values

between the derived datasets of dosimetry estimates (18F-FDOPA: r=0.997 pure imaging / r=0.999 hybrid imaging; 18F-FTYR: r=0.985 pure imaging / r=0.996 hybrid imaging; all $p < 0.0001$). The combination of single-sphere segmentation and the cross-calibration of hybrid imaging proved an appropriate method to counteract the main disadvantage of microPET imaging, the impaired quantification.

Remaining differences can be explained by several points. The most obvious is that both methods involve large uncertainties. As pointed out before, organ harvesting lacks a high time resolution and incorporates many interspecies differences due to the vast amount of animals involved per study. If experiments are not conducted thoroughly, assumed time spans between injection and dissection are only approximated, as the blood circulation does not stop immediately after decapitation and the blood content in extracted organs may vary across subjects. In hybrid imaging the cross-calibration factor is derived using the last time point of the dynamic microPET imaging acquisition and the activity in the post-scan dissected organ. Since the PVE depends on several factors, some of which change dynamically in a dynamic system (see Section 2.1), a calibration factor derived at the end of the acquisition may not reflect the situation at the beginning, and could lead to remaining differences between TACs. There are other methods to correct for PVEs, such as the inversion of the geometric transfer matrix [121], but it requires the point spread function of the system, accurate anatomical information (ideally from MRI), and is computationally expensive. Previously mentioned disadvantages like segmentation issues and volume fluctuations in organs due to non-gated scanning still apply to hybrid imaging as well. However, the impact of PVEs were minimized by hybrid imaging reaching a satisfactory level of activity quantification for dosimetric applications using microPET. From an economic, ethical and scientific point of view, organ harvesting has become obsolete considering the similar results obtained using hybrid imaging and the uncertainties involved in both methods. The technique requires only a fraction of animals to be sacrificed and the data acquisition is faster and more efficient. A dosimetric study can in theory be conducted in one day (by a small team of two requiring only one tracer production, data analysis excluded).

4.2 Comparison of preclinically and clinically derived human dosimetry

In Section 3.2 and Section 3.4 the preclinically derived dosimetry of 18F-FDOPA and 18F-UCB-H were compared to the existing clinically derived dosimetry of 18F-FDOPA

[109] and to the herein conducted first-in-human study of 18F-UCB-H (Appendix D). Although the effective dose and total body absorbed dose were estimated within a 10% error window, significant differences were found in single-organ absorbed doses (preclinical values derived by organ harvesting). For 18F-FDOPA the highest difference was found for lungs and testes with ratios between absorbed doses of 1.63 and 1.55, respectively (both underestimated in preclinical data). In the comparison of 18F-UCB-H the largest difference was found for the gallbladder wall and the lung with ratios between absorbed doses of 1.97 and 0.43, respectively (underestimation for galbladder wall and overestimation for lung in preclincal data). For 18F-FDOPA the critical organ was misinterpreted in preclinical estimates possibly resulting in an over-exposure in clinical trials. The variation in data can be traced back to methodological differences and interspecies dissimilarities. In preclinical studies animals are anaesthetized (often using isoflurane or ketamine) and warmed, which might have an impact on the distribution of the radiopharmaceutical. This has been shown in mice for 18F-FDG by Fueger et al. [122]. They observed strong differences in the uptake in skeletal muscle and especially in brown adipose tissue and myocardium, depending on parameters such as fasting, type of anaesthesia, and temperature of the animal. In clinical studies subjects are awake during the scan possibly resulting in a slightly altered uptake scenario for some radiopharmaceuticals.

Another difference is the injected activity per body weight in comparison. As stated in the manuscript of the clinical study of 18F-UCB-H (Appendix D), the injected activity per kilogram body weight in mice is more than 100-fold the injected activity in humans (285 MBq/kg vs. 2 MBq/kg). This might provide an explanation for the deviation in large and highly perfused organs (i.e. liver), as the concentration of the activity in the blood stream is higher entailing a larger amount of radiation present in the organs. Extrapolation to human data is commonly based in literature on the ratio of organ mass to body mass in both species (see Section 2.7). An assumption is made that metabolic rates are similar in both species and only vary according to their weight differences [123]. But even monkeys used in preclinical studies, which are assumed to possess a high physical similarity to humans, were proven to poorly estimate radiation dosimetry in humans using radiopharmaceuticals labeled with ^{11}C [123]. As pointed out in Section 2.7, there are methods accounting for metabolic differences in species when extrapolating TACs, however, none prevail but the method based on the ratio of organ mass to body mass in both species. Sakata et al. [92] compared the clinically derived radiation dosimetry and the preclinically obtained radiation dosimetry in mice (by organ harvesting) from

five ^{11}C and one ^{18}F labelled tracer. Their radiation estimates, based on mice, also showed only a rough similarity for effective doses (ratios from 0.86 to 1.88), but especially significant differences for absorbed doses in single organs occurred and the critical organ was misinterpreted for two out of six tracers. The results derived within the study of 18F-UCB-H (Appendix A and D) and 18F-FDOPA (Appendix B) further underline that animal data extrapolated to humans is notoriously unreliable due to intraspecies and methodological differences. Since injection limits for first-in-human studies have to be based on preclinical estimates (the US follow FDA regulations and some countries of the EU follow recommendations from the ICRP), the safety of those regulations should be scrutinized.

Due to discrepancies between estimates based on preclinical data and results obtained in humans, over-exposures of subjects in first-in-human studies may occur. Therefore, it is recommended to use preclinical radiation dosimetry estimates with caution and keep the injected activity in first-in-human studies as low as possible while still obtaining images with sufficient signal-to-noise ratio for further investigation. It might even be safer, if preclinical studies were omitted and replaced by low activity first-in-human scans, as proposed by Zanotti et al. [39, 123], due to the large uncertainty of preclinical estimates. They reviewed a large amount of clinical dosimetry studies and concluded that the received effective dose across different ^{18}F and ^{11}C tracers varied but was in a narrow range and is therefore predictable for novel tracers. Low activity scans in humans, which are feasible due to the high sensitivity of modern scanners, should be the first approach used to detect critical organs and to estimate higher safe injection limits. This would remove the uncertainties involved in preclinical estimates minimizing the risk of over-exposing subjects in first-in-human studies. Another advantage would be, from an ethical point of view, the avoidance of animal experiments.

4.2.1 Absorbed dose vs. effective dose

As already described in Section 1.4, the EU follows recommendations of the ICRP limiting the effective dose per injection in clinical trials based on the expected health benefit of the radiopharmaceutical [39, 40]. The FDA in the USA provides limits for different organs based on the equivalent dose (which is equal to the absorbed dose for PET imaging as the radiation weighting factor is unity) [39]. It is contentious which quantity is more suitable for use in nuclear medicine. Several authors agree that the broad use of the effective dose as commonly done nowadays in radiology

and nuclear medicine is inappropriate [19, 30, 31]. The weighting factors reflecting the radiosensitivity of tissues are averaged over population, age, and sex. The risk of fatal cancer due to a uniform body exposure however, is a function of age and sex and decreases with age. The effective dose can only be related to a reference person and it should be used only for comparing the health detriment to a reference subject for different types of exposures. The widespread misconception already pointed out in Section 1.2 about the most recent tissue weighting factors from ICRP publication 103 and their erroneous use in literature creates additional uncertainty when basing injection limits on the effective dose.

The absorbed dose (or equivalent dose in PET imaging) reflects only the deposited energy per unit mass and might be a better quantity to limit the injection of the radiopharmaceutical. Risk assessment for individual patients in general should always be based on absorbed organ dose estimates accounting for stature, gender, and age. Especially when only a few radiosensitive organs receive a significant absorbed dose, as was the case for most radiopharmaceuticals investigated, it is more appropriate to use absorbed doses [30, 31]. Regarding preclinical radiation dosimetry estimates, the effective dose was estimated correctly within $\pm$ 10%, but absorbed doses of single organs showed much larger deviations. This might lead to over-exposures when using effective doses to calculate injection limits. However, even the absorbed dose (or equivalent dose) should be used carefully as many assumptions are made during the calculation of the quantity. The mathematical hermaphroditic phantom developed by Cristy and Eckerman [71] and the respective S-factors [124] only approximate the anatomical geometry of each subject. The distribution of the radiopharmaceutical inside each organ is assumed to be homogeneous and the organ itself has a uniform density. New computational phantoms were developed by the ICRP and ICRU [23], which will improve the accuracy of the radiation dosimetry once S-factors are published.

Martin [31] estimated the involved standard errors in absorbed dose calculations. The uncertainty in the measurement of the administered dose was determined as $\pm$ 10%. For the measurement of the uptake, distribution, and retention of the tracer it was $\pm$ 30% and the statistical error in the involved Monte Carlo simulations was $\pm$ 5%. These large standard deviations might explain the large inter-study differences for the same tracer that were found by Zanotti et al. [39]. This also further questions the validity and safety of using preclinical estimates for the calculation of first injection limits, when even clinically derived estimates vary for the same tracer, since preclinical estimates involve even more assumptions and uncertainties.

A standardized investigation protocol, as suggested by Eberlein et al. [24] and provided for clinical studies by Lassmann et al. [125], regarding image acquisition and absorbed dose calculations might reduce methodological differences and possibly provide safer radiation dosimetry estimates for the calculation of injection limits.

4.3 Exposure considerations in preclinical longitudinal studies

While the great majority of publications dealing with radiation dosimetry focus on human dosimetry for first-in-human studies and safe application of radiopharmaceuticals in a clinical environment, relatively few publications focus on the radiation received by animals in preclinical studies. Bearing in mind the ever increasing use of small animals as translational models for clinical research, however, the radiation dosimetry should be taken into account. This is especially important when conducting longitudinal studies with several consecutive microPET/microCT scans, which possibly introduce radiation levels that could compromise the outcome of the study. Due to the 100-fold amount of activity per bodyweight injected in mice for microPET studies compared to human studies, the absorbed doses from microPET are significantly higher than from regular PET imaging in humans, as was shown in Chapter 3.5. MicroCT imaging requires a high photon flux compared to clinical systems to achieve the very fine resolution while still maintaining an appropriate signal-to-noise ratio. It therefore delivers an additional considerable amount of radiation as was shown experimentally and using Monte Carlo simulations in Section 3.5 and 3.6.

A lethal level of radiation for mice is considered to be a single total body entrance dose of 6 Gy [111]. While it is unlikely that such an excessive amount of radiation is received during a dual modality scan especially as a single entrance dose, studies have shown that far lower radiations might have an impact on the animal's neurology or physiology [16, 118, 119]. The biological effects of low-level radiation, however, will vary with type of radiation, dose delivered, delivery rate, strain of mice, and type of tissue [112]. The herein derived radiation dosimetry in mice for 18F-UCB-H, 18F-FDOPA and 18F-FTYR revealed total body absorbed doses of approximately 14 mGy/MBq, which is in accordance with data published by other authors for other ^{18}F tracers [37]. Critical organs received far higher absorbed doses than other organs, with the urinary bladder wall for 18F-FDOPA being exposed to the excessive absorbed

dose of 660 mGy/MBq (liver with 65 mGy/MBq for 18F-UCB-H and liver with 49 mGy/MBq for 18F-FTYR).

In longitudinal microPET studies, which are commonly conducted in preclinical oncology studies to investigate tumour growth or inhibition by pharmaceuticals, up to five or six consecutive microPET/microCT scans [15, 126, 127] can be performed over several weeks. Most of the studies do not address the radiation burden inflicted on the animals or the possible impact on tumour growth. We created six theoretical scenarios of microPET/microCT imaging studies in mice (see Table 4.2) to project cumulative doses received in longitudinal dual modality imaging studies. We assumed 7 MBq injected activity per microPET scan, since this was the common amount of injected activity for mice in our conducted experiments. Each microCT protocol (P1 to P4) was implemented in a different 5 consecutive dual modality scan scenario (S1 to S4). Two rather excessive scenarios involving 10 consecutive scans were created to estimate the strong accumulation of absorbed doses, especially in local organs. The microCT protocols P1 and P3 were used, since P1 produces the lowest exposure and P3 provides the highest soft tissue contrast while resulting in the highest radiation burden.

Scenario	Tracer	Injected activity [MBq]	microCT protocol	# of scans
S1	18F-UCB-H	7	P1	5
S2	18F-FDOPA	7	P3	5
S3	18F-FTYR	7	P4	5
S4	18F-UCB-H	7	P2	5
S5	18F-UCB-H	7	P1	10
S6	18F-FTYR	7	P3	10

Table 4.2: Dual-modality imaging scenarios (for details on P1 to P4 see Table 3.1)

We used the absorbed doses in mice from the three radiopharmaceuticals presented in Section 3.3 and the microCT doses simulated using MCSs in Section 2.5 (for details see Appendix C and F). Single-modality doses per scan and the cumulative dose from both modalities for the respective longitudinal setup are displayed in Table 4.3.

Depending on the chosen microCT protocol and the radiopharmaceutical involved, cumulative total body doses of up to 1.4 Gy can be inflicted on mice in a 5 scan dual-modality longitudinal study. Cumulative organ or bone doses can reach

Scenario	Modality	Bone	Brain	Heart	Kidney	Liver	Lung	Testes	WB
	MicroPET dose [mGy]	65.6	235.4	104.2	243.9	456.0	144.8	107.9	100.7
S1	MicroCT dose [mGy]	166.4	63.6	69.2	64.2	38.5	73.5	37.6	68.4
	Cumulative dose [Gy]	***1.2***	***1.5***	***0.9***	***1.5***	***2.5***	***1.1***	***0.7***	***0.8***
	MicroPET dose [mGy]	39.2	24.6	29.5	124.9	101.5	42.4	35.4	99.0
S2	MicroCT dose [mGy]	459.1	175.8	191.3	178.9	105.6	202.3	102.5	188.7
	Cumulative dose [Gy]	***2.5***	***1.0***	***1.1***	***1.5***	***1.0***	***1.2***	***0.7***	***1.4***
	MicroPET dose [mGy]	38.3	61.1	54.5	175.1	345.0	96.2	26.0	99.7
S3	MicroCT dose [mGy]	219.4	85.8	93.0	86.5	51.3	97.4	49.3	91.3
	Cumulative dose [Gy]	***1.3***	***0.7***	***0.7***	***1.3***	***2.0***	***1.0***	***0.4***	***1.0***
	MicroPET dose [mGy]	65.6	235.4	104.2	243.9	456.0	144.8	107.9	100.7
S4	MicroCT dose [mGy]	351.0	135.4	135.5	137.6	78.0	154.3	78.6	143.8
	Cumulative dose [Gy]	***2.1***	***1.9***	***1.2***	***1.9***	***2.7***	***1.5***	***0.9***	***1.2***
	MicroPET dose [mGy]	93.7	336.3	148.8	348.4	651.4	206.8	154.2	143.8
S5	MicroCT dose [mGy]	166.4	63.6	69.2	64.2	38.5	73.5	37.6	68.4
	Cumulative dose [Gy]	***2.6***	***4.0***	***2.2***	***4.1***	***6.9***	***2.8***	***1.9***	***2.1***
	MicroPET dose [mGy]	54.7	87.3	77.8	250.2	492.8	137.4	37.2	142.4
S6	MicroCT dose [mGy]	459.1	175.8	191.3	178.9	105.6	202.3	102.5	188.7
	Cumulative dose [Gy]	***5.1***	***2.6***	***2.7***	***4.3***	***6.0***	***3.4***	***1.4***	***3.3***

Table 4.3: Cumulative doses from longitudinal dual-modality imaging scenarios; dose refers to absorbed dose

far higher levels with the liver being exposed to 2.7 Gy in S4 and bones to 2.5 Gy in S2. In the rather conservative scenarios S5 and S6 involving 10 consecutive dual modality scans cumulative total body doses of up to 3.3 Gy are reached with single organ doses of 6.9 Gy received by the liver. The cumulative exposure of several consecutive scans is probably sublethal in mice, since a single entrance dose of 6 Gy is considered lethal [111], but the radiation may be large enough to induce stochastic or deterministic effects in animals. The radiation could possibly alter physiological parameters [119, 128] and therefore have an impact on the outcome of a study if the respective parameter is involved. Cumulative doses in rats from dual-modality studies are expected to be lower, since it was shown that the microCT dose is a function of the volume of the animal. However, microPET absorbed doses in rats might reach an equivalent or higher level than in mice due to the high injected dose per kilogram (average of 385 MBq/kg in [104] or 400 Mbq/kg in [41]).

4.4 Future directions

National regulations requiring preclinical radiation dosimetry in small animals as a prerequisite for first-in-human studies should be reconsidered due to the large uncertainties involved in preclinical dosimetry. Modern PET scanners feature a high sensitivity, which makes low-activity human scans a viable option for detecting critically exposed organs. This may be an ethical and scientifically accurate alternative to preclinical animal testing. However, if preclinical radiation dosimetry in small animals has to be performed, the ethical and efficient method of hybrid imaging should be applied. Partial volume corrections in dynamic small animal imaging should be further investigated and the benefits of combining microPET and small animal MRI imaging should be explored. Replacing CT with MRI in small animal imaging would additionally mean a decrease of the radiation exposure. Researchers in preclinical imaging should be aware of the large radiation burden inflicted on animals and should consider its impact on their respective study. We derived microPET absorbed doses of three ^{18}F radiopharmaceuticals in mice and microCT doses in mice and rats. At the time this manuscript was prepared, rat models for internal dose calculations were available, but no absorbed doses for any radiopharmaceutical in rats were published to our knowledge. Since the injected activity per kilogram in rats in several studies is even larger than in mice, a significant radiation burden can be expected. Absorbed doses for several radiopharmaceuticals in rats should therefore be calculated and published to provide researchers with the possibility of assessing the dose inflicted on animals in their specific study setup. The same holds true for every new microCT machine available to researchers. The radiation dosimetry should be assessed in a similar way as proposed in this manuscript and published to provide every user with the information. Monte Carlo simulations proved to be a valuable tool for the non-invasive investigation of the microCT dose. Future improvements could be detailed computational phantoms and incorporating the exact amount of photons generated by the source.

CHAPTER 5

Conclusions

- By acquiring the biodistribution of three ^{18}F-tracers using traditional organ harvesting and dynamic microPET imaging we demonstrated that without appropriate corrections and precautions sole dynamic microPET imaging lacks the accurate quantification necessary for preclinical radiation dosimetry in mice.

- The method of hybrid imaging, which we applied to dynamic microPET imaging of mice for the first time, increased the accuracy of quantification and provided similar results to organ harvesting, while being more efficient from an ethical, economical, and scientific point of view.

- It was shown by comparing data of three ^{18}F-tracers that full organ segmentation for dosimetry is unnecessarily laborious and prone to errors due to PVE and the misinterpretation of boundaries. Simple sphere segmentation inside each organ produced more accurate results.

- We presented for the first time in literature the preclinically derived human radiation dosimetry of 18F-UCB-H, 18F-FDOPA and 18F-FTYR with effective doses based on tissue weighting factors from ICRP publication 60 of 2.18E-02 $\pm$ 5.5E-04 mSv/MBq, 1.97E-02 $\pm$ 1.00E-04 mSv/MBq and 1.64E-02 $\pm$ 2.50E-04 mSv/MBq, respectively.

- By conducting the first-in-human clinical dosimetry study of 18F-UCB-H we determined the effective dose to be 1.98E-02 $\pm$ 1.39E-04 mSv/MBq with the critical organs being the urinary bladder wall, the gallbladder, and the liver. We showed that the radiation burden of the tracer is similar or lower than that of widely used clinical tracers such as 18F-FDG and provided safe injection

doses according to research guidelines in the EU (single injection of 505 MBq) and USA (single injection of 321 MBq).

- We compared preclinically derived data and clinically derived data of 18F-UCB-H and 18F-FDOPA and showed that preclinically derived estimates roughly predicted total-body absorbed doses and the effective dose, but poorly predicted single-organ absorbed doses. In case of 18F-FDOPA the critical organ was misinterpreted in preclinical dose estimates. They should be used with care when estimating first injection limits for first-in-human studies.

- We calculated and presented for the first time the mouse radiation dosimetry of 18F-UCB-H, 18F-FDOPA and 18F-FTYR and demonstrated that mice receive highly significant amounts of radiation from microPET scanning. Total body absorbed doses of 14 mGy/MBq were calculated for all three tracers with critical organ exposures of 65 mGy/MBq for 18F-UCB-H (liver), 660 mGy/MBq for 18F-FDOPA (urinary bladder wall), and 48 mGy/MBq for 18F-FTYR (liver).

- The radiation dosimetry of the GE eXplore 120 microCT was experimentally derived in a PMMA phantom and presented. The single-field-of-view radiation ranged from 20.15 to 56.79 mGy ($CTDI_{100}$) and the multiple-field-of-view from 27.98 to 77.45 mGy (MSAD), depending on the chosen protocol. *In vivo* results acquired in sacrificed rats confirmed *ex vivo* phantom measurements.

- A Monte Carlo simulation model of the GE eXplore 120 microCT was established for the first time, validated, and used to further investigate the radiation dose non-invasively in mice and rats. It was shown that the skeleton receives far higher doses (average maximum of 459 mGy in mice using P3) than predicted by the $CTDI_{100}$ and MSAD.

- By deriving the radiation dosimetry from microPET and microCT we demonstrated that mice are exposed to significant amounts of radiation in dual modality studies. In longitudinal studies cumulative doses (of up to 3.3 Gy for total body and 6.9 Gy for single organs) could potentially induce stochastic/deterministic effects and alter the outcome of the investigation.

APPENDIX A

Paper I

Preclinical radiation dosimetry for the novel SV2A radiotracer [^{18}F]UCB-H

Bretin F., Warnock G., Bahri MA., Aerts J., Mestdagh N., Buchanan T., Valade A., Mievies F., Giacomelli F., Lemaire C., Luxen A., Salmon E., Seret A. and Plenevaux A.

EJNMMI Research 3(1):35, 2013

Bretin *et al. EJNMMI Research* 2013, **3**:35
http://www.ejnmmires.com/content/3/1/35

EJNMMI Research
a SpringerOpen Journal

ORIGINAL RESEARCH Open Access

Preclinical radiation dosimetry for the novel SV2A radiotracer [^{18}F]UCB-H

Florian Bretin[1], Geoffrey Warnock[1], Mohamed Ali Bahri[1], Joël Aerts[1], Nathalie Mestdagh[2], Tim Buchanan[3], Anne Valade[2], Frédéric Mievis[1], Fabrice Giacomelli[1], Christian Lemaire[1], André Luxen[1], Eric Salmon[1], Alain Seret[1] and Alain Plenevaux[1*]

Abstract

Background: [^{18}F]UCB-H was developed as a novel radiotracer with a high affinity for synaptic vesicle protein 2A, the binding site for the antiepileptic levetiracetam. The objectives of this study were to evaluate the radiation dosimetry of [^{18}F]UCB-H in a preclinical trial and to determine the maximum injectable dose according to guidelines for human biomedical research. The radiation dosimetry was derived by organ harvesting and dynamic micro positron emission tomography (PET) imaging in mice, and the results of both methods were compared.

Methods: Twenty-four male C57BL-6 mice were injected with 6.96 ± 0.81 MBq of [^{18}F]UCB-H, and the biodistribution was determined by organ harvesting at 2, 5, 10, 30, 60, and 120 min (n = 4 for each time point). Dynamic microPET imaging was performed on five male C57BL-6 mice after the injection of 9.19 ± 3.40 MBq of [^{18}F]UCB-H. A theoretical dynamic bladder model was applied to simulate urinary excretion. Human radiation dose estimates were derived from animal data using the International Commission on Radiological Protection 103 tissue weighting factors.

Results: Based on organ harvesting, the urinary bladder wall, liver and brain received the highest radiation dose with a resulting effective dose of 1.88E-02 mSv/MBq. Based on dynamic imaging an effective dose of 1.86E-02 mSv/MBq was calculated, with the urinary bladder wall and liver (brain was not in the imaging field of view) receiving the highest radiation.

Conclusions: This first preclinical dosimetry study of [^{18}F]UCB-H showed that the tracer meets the standard criteria for radiation exposure in clinical studies. The dose-limiting organ based on US Food and Drug Administration (FDA) and European guidelines was the urinary bladder wall for FDA and the effective dose for Europe with a maximum injectable single dose of approximately 325 MBq was calculated. Although microPET imaging showed significant deviations from organ harvesting, the Pearson's correlation coefficient between radiation dosimetry derived by either method was 0.9666.

Keywords: Dosimetry, Preclinical microPET, Organ harvesting, SV2

Background

Epilepsy is a chronic neurological disorder characterized by seizures and abnormal electroencephalographic activity. It affects people of all ages with more than 50 million cases worldwide. In contrast to other antiepileptic drugs, levetiracetam (Keppra®, UCB Pharma Ltd., Slough, Berkshire, UK) has a unique mechanism of action, binding to the neuronal synaptic vesicle protein 2A (SV2A) in the brain [1]. SV2 proteins are critical to proper nervous system function, and they have been demonstrated to be involved in vesicle trafficking. However, the specific role of SV2A in epilepsy remains unclear. The newly developed fluorine-18 radiolabelled positron emission tomography (PET) imaging agent [^{18}F]UCB-H shows a nanomolar affinity for the human SV2A protein and will be of great value in studying the function of SV2A in diseases of the central nervous system [2].

* Correspondence: alain.plenevaux@ulg.ac.be
[1]Cyclotron Research Centre, University of Liège, Allée du 6 Août, Building B30, Sart Tilman, Liège 4000, Belgium
Full list of author information is available at the end of the article

A prerequisite to the use of a novel radiotracer in human clinical trials and good clinical practice is a preclinical dosimetry study in animals. This enables the prediction of dose limits in humans that will keep radiation doses below harmful limits while still producing diagnostically beneficial images. Radiation estimates for humans derived from small animals are traditionally obtained by *ex vivo* tissue distribution (TD) studies, where organs are harvested post-injection at several time points to establish the biodistribution. However, dynamic imaging approaches in small animals using microPET are a promising alternative, because the complete biodistribution of the radiopharmaceutical can be obtained within a single *in vivo* scan with a much higher time resolution. The aims of this study were to predict the radiation dose given to humans based on the distribution of [^{18}F]UCB-H in mice and to determine the maximum injectable dose according to radiation guidelines in biomedical research. Additionally, the TD and microPET approaches to assess the biodistribution were investigated and compared.

Methods

Chemistry

[^{18}F]UCB-H was obtained in a four-step radiosynthesis. Briefly, this consisted of nucleophilic labeling of a pyridine precursor, reductive amination of the labeled product, and internal cyclisation. Specific activity was higher than 500 MBq/μg at the end of synthesis.

Animals

Male C57BL-6 mice were initially obtained at 5 weeks of age from Charles River Laboratories (Brussels, Belgium) and subsequently bred at the Animal Facility of the GIGA-University of Liège (BE-LA 2610359). The animals were housed under standard 12h:12h light/dark conditions with food and water available *ad libitum*. All experimental procedures and protocols used in this investigation were reviewed and approved by the Institutional Animal Care and Use Committee of the University of Liège.

Tissue distribution

The data acquisition and analysis were conducted in accordance with MIRD pamphlet no. 16 [3]. For the TD of [^{18}F]UCB-H, 24 male C57BL-6 mice (23.96 ± 1.31 g [20.6 to 26.1 g]) were injected with an iv bolus of 6.96 ± 0.81 MBq [5.18 to 8.06 MBq] [^{18}F]UCB-H via the tail vein under isoflurane anesthesia. Anesthesia was maintained until sacrificed by decapitation after 2, 5, 10, 30, 60, and 120 min (n = 4 for each time point). Blood samples were obtained (0.5 to 1 ml), and the following organs were harvested by dissection: the brain, bone (femur), liver (partial), kidney, heart, spleen, intestine (partial), pancreas, adrenals, testes, skin (partial), muscle (partial/thigh), stomach, lung, and bladder. All organs were weighed (NewClassic ML, Mettler Toledo, Switzerland), and the activity was quantified using a gamma well counter (Cobra II Auto-Gamma, Perkin-Elmer, Waltham, MA, USA), resulting in the average activity per gram of tissue in mice. The gamma well counter was calibrated measuring a known quantity of ^{18}F activity (quantified using a calibrated gamma spectrometer: high purity 30% germanium GR3020 from Canberra Industries, Meriden, CT, USA), thereby obtaining a calibration factor between real and measured activity. The measurement uncertainty was evaluated to be ±5%.

Dynamic microPET imaging

Dynamic microPET imaging was performed on five male C57BL-6 mice with an average weight of 29.72 ± 6.70 g [24.2 to 40.8 g]. 9.19 ± 3.40 MBq [3.84 to 14.20 MBq] [^{18}F]UCB-H was administered via the tail vein as bolus. All procedures were performed under isoflurane anesthesia. Co-registered micro-computed tomography (CT) images were acquired with an eXplore 120 microCT (Gamma Medica, USA/GE Healthcare, Sevenoaks, Kent, UK) [4] to obtain anatomical information for segmentation. An iodine-based contrast agent (1:10 dilution of iobitridol-XENETIX300, Guerbet, Roissy, France) was administered in the peritoneal cavity prior to microCT to aid full organ segmentation. All microCT images were reconstructed using Feldkamp's filtered backprojection algorithm [5] with a cutoff at the Nyquist frequency and an isotropic voxel size of 100 μm. The same MINERVE animal cell bed (Equipement Veterinaire Minerve, Esternay, France) was used in both imaging modalities to provide anesthesia, physiological control, monitoring of respiration, and simplified co-registration of the images. Dynamic microPET scans over 120 min were acquired using a Siemens Concorde Focus 120 microPET (Siemens, Munich, Germany) [6] and followed by transmission measurement with ^{57}Co point source. In order to obtain dynamic imaging data for as many organs as possible, the field of view of the scanner was positioned on the chest and lower body disregarding the brain. The list-mode data were histogrammed into three-dimensional (3D) sinograms by Fourier rebinning [7] and reconstructed by filtered backprojection with a ramp filter cutoff at the Nyquist frequency. Corrections for randoms, dead time, and attenuation were applied but not scatter correction, since it was shown by Bahri et al. [8] that no benefit for quantification is gained by applying scatter correction for the Focus-F120. No partial volume correction was performed on the acquired data. A set of 3D images was reconstructed in a 256 × 256 × 95 matrix with a pixel size of 0.4 × 0.4 × 0.8 mm. The dynamic time framing was as follows: 6 × 5 s, 6 ×

Bretin et al. EJNMMI Research 2013, 3:35
http://www.ejnmmires.com/content/3/1/35

10 s, 3 × 20 s, 5 × 30 s, 5 × 60 s, 8 × 150 s, 6 × 300 s, and 6 × 600 s, and all data were decay corrected to the beginning of each individual frame.

MicroCT and microPET images were co-registered using a landmark-based approach. Volumes of interest (VOIs) were drawn manually by a single observer on the microCT images using PMOD (Version 3.306, PMOD Technologies, Zurich, Switzerland). This allowed the delineation of the following organs: the heart, lung, liver, kidneys, and testes (referred to as 'dynamic whole'). The average organ activity per volume was obtained from the co-registered microPET images. Additionally, VOIs in the shape of spheres with a radius of 2 mm were placed in the center of the same organs to limit the impact of partial volume effects on the quantification and used for dosimetry (referred to as 'dynamic single'). For the heart, one VOI was positioned over the myocardium and parts of the chambers; for the liver, two VOIs were placed in the center of the organ; for lungs, kidneys, and testes, one VOI was placed in the center of each organ (i.e., left and right wing for lungs, left and right organ for kidneys and testes). MicroPET calibration for conversion of counts/pixel in Bq/ml was performed as recommended by the manufacturer. Accuracy of the technique has been reported to be better than 2% [8].

Dosimetry analysis

When using animal data to predict human dosimetry, an interspecies extrapolation is necessary to account for differences between animal and human. A commonly used method in preclinical imaging is that of Kirshner et al. [9], which is based on a linear scaling of the percent uptake in the animal by the ratio of the organ weights and total body weights in both species:

$$\left[\left(\frac{\%}{g_{organ}}\right)_{animal} \bullet \left(kg_{TBweight}\right)_{animal}\right] \bullet \left(\frac{g_{organ}}{kg_{TBweight}}\right)_{human} = \left(\frac{\%}{organ}\right)_{human}$$

The organ uptake in percentage of injected dose multiplied by the body weight in kilograms is assumed to be constant across species, allowing for the calculation of equivalent organ activities in humans from animal data. Since the organ-to-body weight ratio is necessary to extrapolate to humans and to create consistent time-activity curves from the obtained average organ activity per volume or gram of tissue, a 'standard mouse' was created using six C57BL-6 mice. This 'standard mouse' allowed both organ density and the ratio of organ weight to body weight to be calculated and a species average assumed. The mice were weighed and then dissected to determine the organ weight and density by microCT for volume quantification. The mean total body weight was 32.28 ± 3.98 g [28.6 to 39.8 g]. The following organs were harvested: the brain, liver, kidney, heart, spleen, testes, and lung. The organ volume was obtained from the microCT images by a threshold-based segmentation approach. All weights were finally scaled to a bodyweight of 35 g. Only data from organs where the ratio of organ weight to bodyweight was known were used for dosimetry.

Average organ activity per mass or volume was normalized for injected dose and multiplied by organ weights or organ volumes, respectively. Activity levels were linearly interpolated, and only physical decay was assumed after the last time point up to 10 h post-injection. Thus, a homogenous activity distribution within each organ was assumed, and biological clearance after 2 h post-injection was neglected, assuming the activity was 'trapped' within the source organ. The time-activity curves (TACs) were then extrapolated from animal values to human values using Equation 1. Human organ weights and body weight were taken from the standard 70-kg adult male hermaphroditic phantom implemented in the human dosimetry software OLINDA/EXM (version 1.1) [10] and animal organ weights from the standard mouse as described above. In addition, TACs that were calculated based only on animal organs (i.e., no extrapolation to human values) were used to calculate additional dose estimates to provide an estimation window for the human dosimetry (referred to as 'NE' for no extrapolation). Urine excretion data were modeled using the implemented dynamic voiding bladder module [11] in OLINDA/EXM. A voiding interval of 4 h was assumed, and fractions of 0.5 to 0.3 of total injected activity leaving the body via the urinary excretion system with a biological half-life of 3 h were defined and separately implemented. The same scenarios were implemented using a voiding interval of 2 h to provide data for the impact of a possible pre-scan hydration of the subject to decrease the bladder dose. The residence time for each organ, which is equal to the number of disintegrations within the source organ, was calculated by trapezoidal numerical integration of the TACs in MATLAB (version 7.12.0) as proposed in literature [3,12]. Activity from other organs that could not be extrapolated due to the unknown weight-to-body weight ratio was assigned together with all unaccounted for activity to the remainder, which is assumed to be homogenously distributed throughout the remaining body. OLINDA/EXM was used to calculate absorbed doses. The effective doses in the standard 70-kg male human based on the recent tissue weighting factors published in International Commission on Radiological Protection (ICRP) 103 [13] were calculated using Excel (version 2010, Microsoft, Albuquerque, NM, USA) and are presented in the 'Results' section. For comparison purposes with other tracers and previous works, the effective doses using old tissue weighting factors from ICRP 60 [14] were also calculated using OLINDA/EXM and were provided as additional files.

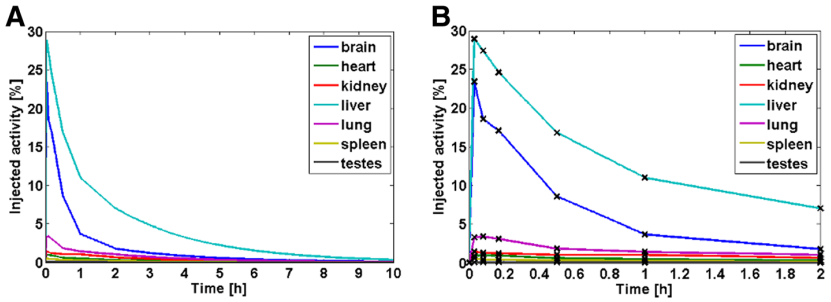

Figure 1 Mean human TACs derived by TD in mice (A: total, B: zoom in).

Since the TACs of the TD are derived from several time points in different animals, each individual time point has its own standard deviation (SD). Therefore, the SD of residence times derived from the TD was calculated as follows. Two additional animal TACs were constructed using mean ± 1 SD of each individual time point of the activity measurement. These two TACs were then extrapolated to human values as previously described, and the mean residence time corresponding to each TAC was computed [15-17]. This provided a residence time window which is expressed as a coefficient of variation in percent (%CV) from the mean value. The residence time window was used to calculate a minimum and maximum dose for the TD, resulting more in a best and worst case scenario as opposed to a real SD. The mean of best and worst case scenario was used as the error for the measured absorbed dose and reported as %CV of the mean value. For the statistics of the microPET imaging, every scan was treated separately, and mean and standard deviation expressed as %CV were regularly calculated across scans. Correlations between datasets were calculated by the Pearson product–moment correlation coefficient in MATLAB.

Results

Figures 1 and 2 illustrate the human biodistribution of [^{18}F] UCB-H derived from animal TD and from microPET imaging based on sphere segmentation (dynamic single), respectively. In both datasets, the highest initial activity uptake was obtained within the liver with 29% and 18%, respectively. However, brain data could not be derived from PET data, as the brain was outside the scanner's field of view. Furthermore, the spleen could not be accurately delineated in CT images in the absence of additional contrast agents. TACs from whole organ segmentation (dynamic whole) were provided as Additional file 1 (whole TACs) and Additional file 2 (zoom in).

The mean residence times obtained by the TD and dynamic microPET imaging with both segmentation methods are presented in Table 1. The highest level of disintegrations per organ occurred within the liver with 4.45E-01 h (TD), 1.93E-01 (dynamic whole), and 2.18E-01 h (dynamic single). Bladder values are theoretical values derived using the dynamic bladder module described above.

A cross section of all anatomical planes of the merged PET/CT image is illustrated in Figure 3. High uptake in liver, kidneys, bladder, and spinal cord can be observed.

The animal-derived dose estimations from the TD method (Table 2) predicted that the highest absorbed dose is received by the urinary bladder wall (modeled theoretical value) with 1.54E-01 ± 5.00E-04 mGy/MBq, followed by the liver with 5.84E-02 ± 7.35E-03 mGy/MBq and the brain with 3.08E-02 ± 5.15E-03 mGy/MBq. The effective dose

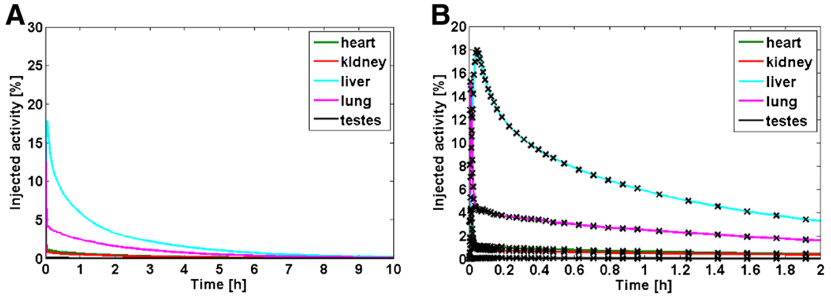

Figure 2 Mean human TACs derived by microPET imaging in mice (dynamic single) (A: total, B: zoom in).

Bretin et al. EJNMMI Research 2013, 3:35
http://www.ejnmmires.com/content/3/1/35

Table 1 Human residence times (h) (bladder fraction 0.5) derived by TD and dynamic imaging based on whole organ segmentation and single spheres

Organ	TD	%CV	Dynamic whole	%CV	Dynamic single	%CV
Bladder (theoretical)	3.08E-01	-	3.08E-01	0.0	3.08E-01	0.0
Brain	1.74E-01	18.1	-	-	-	-
Heart wall	1.79E-02	10.1	2.45E-02	11.6	2.39E-02	12.3
Kidneys	3.57E-02	10.5	1.67E-02	9.1	1.90E-02	13.2
Liver	4.45E-01	13.8	1.93E-01	6.7	2.18E-01	6.6
Lung	5.96E-02	9.8	1.13E-01	11.8	9.30E-02	14.8
Spleen	9.04E-03	13.6	-	-	-	-
Testes	2.11E-03	12.7	1.04E-03	12.1	1.12E-03	12.8
Remaining body	1.58E + 00	6.7	1.98E + 00	1.4	1.97E + 00	1.2

was 1.88E-02 ± 5.11E-04 mSv/MBq. The highest dose estimate, based on microPET imaging (dynamic single), was received by the urinary bladder wall with 1.56E-01 ± 0.00E-00 mGy/MBq, followed by the liver with 3.14E-02 ± 1.97E-03 mGy/MBq (brain was not imaged). The effective dose was 1.84E-02 ± 3.51E-04 mSv/MBq. Mean dose estimates based on whole organ segmentation are provided as Additional file 3 and effective doses for all three methods obtained using old weighting factors form ICRP 60 as Additional file 4.

In Table 3, the variation of the urinary bladder wall absorbed dose when using fractions of 0.3 to 0.5 as previously described is shown as well as its impact on the effective dose for both methods. When reducing the voiding interval to 2 h, the absorbed dose decreases to 9.21E-02 mGy/MBq (TD) for a bladder fraction of 0.5 and to 5.94E-02 mGy/MBq (TD) for a bladder fraction of 0.3.

Discussion

The tissue distribution of [^{18}F]UCB-H was obtained by traditional organ harvesting at several time points in mice as well as by dynamic microPET imaging to compare the results of both methods. Dynamic microPET imaging is an interesting alternative to organ harvesting. Organ harvesting requires many animals and can be labor intensive. In dynamic microPET imaging, the complete biodistribution can be obtained within a single scan. Furthermore, it allows sampling of the activity distribution with a much higher time resolution, thus catching early blood uptake peaks in organs that are well perfused. Such peaks could substantially contribute to organ radiation. However, when comparing the residence times obtained with all three techniques (Table 1), dynamic imaging (dynamic whole) alone significantly over- or underestimated the activity within organs. This effect could be explained by known imaging limitations in very small volumes such as partial volume effect or spill over from nearby organs. Low activity organs (i.e., the heart and lung) were overestimated by 36 to 89% in the microPET images presumably due to spill over from neighboring high activity organs (i.e., the liver). All other organs were underestimated in microPET images by 43 to 50%, which could be related to partial volume effect. Deriving TACs from small sphere VOIs in the center of organs (dynamic single) should have reduced the impact of partial volume effect and slightly improved quantification. However, underestimations of 49 to 53 % and overestimations of 33 to 55% remained. A further improvement in quantification might have been achieved

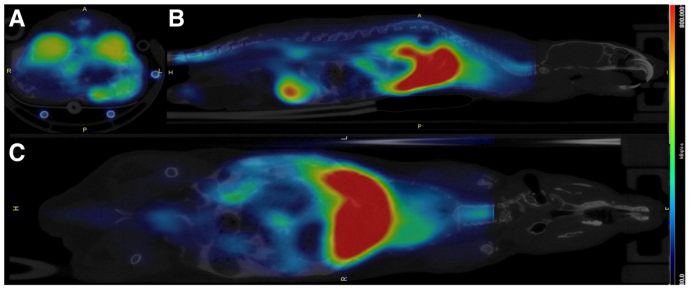

Figure 3 Transverse (A), sagittal (B), and coronal (C) planes of merged average PET/CT image of a representative subject. PET image was averaged across all frames and smoothed using a Gaussian kernel of 1 × 1 × 2 mm in PMOD. The color scale was set to the range 80 to 800 kBq/cc in all planes (Brain outside FOV).

Table 2 Human absorbed dose (mGy/MBq) and effective dose (mSv/MBq)

Target Organ	TD	%CV	TD NE	Dynamic single	%CV	Dynamic single NE
Adrenals	1.43E-02	1.7	1.65E-02	1.36E-02	1.0	1.44E-02
Brain	3.08E-02	16.7	2.05E-02	8.61E-03	1.1	8.27E-03
Breasts	7.71E-03	2.9	7.18E-03	8.88E-03	0.7	8.36E-03
Gallbladder wall	1.86E-02	4.3	2.26E-02	1.56E-02	1.7	1.75E-02
LLI wall	1.36E-02	4.0	1.28E-02	1.55E-02	0.8	1.52E-02
Small intestine	1.24E-02	3.2	1.22E-02	1.37E-02	0.5	1.37E-02
Stomach wall	1.11E-02	2.3	1.11E-02	1.20E-02	0.4	1.20E-02
ULI wall	1.25E-02	2.4	1.27E-02	1.34E-02	0.6	1.36E-02
Heart wall	1.76E-02	6.5	1.77E-02	2.09E-02	9.2	1.26E-02
Kidneys	2.96E-02	8.4	7.07E-02	1.87E-02	9.1	4.06E-02
Liver	5.84E-02	12.6	8.40E-02	3.14E-02	6.3	4.32E-02
Lungs	1.64E-02	6.7	1.11E-02	2.17E-02	12.0	1.23E-02
Muscle	9.82E-03	3.1	9.42E-03	1.10E-02	0.4	1.08E-02
Ovaries	1.38E-02	4.0	1.30E-02	1.57E-02	0.7	1.54E-02
Pancreas	1.40E-02	0.7	1.55E-02	1.37E-02	0.7	1.43E-02
Red marrow	9.71E-03	2.0	9.41E-03	1.04E-02	0.4	1.03E-02
Osteogenic cells	1.39E-02	3.6	1.26E-02	1.57E-02	0.8	1.53E-02
Skin	7.22E-03	3.7	6.73E-03	8.17E-03	0.7	8.00E-03
Spleen	1.52E-02	7.9	1.50E-02	1.15E-02	0.5	1.16E-02
Testes	1.58E-02	6.6	1.13E-01	1.25E-02	5.1	6.41E-02
Thymus	9.26E-03	3.5	8.39E-03	1.09E-02	0.8	1.01E-02
Thyroid	8.86E-03	4.1	7.62E-03	1.01E-02	0.9	9.63E-03
Urinary bladder wall	1.54E-01	0.3	1.54E-01	1.56E-01	0.0	1.56E-01
Uterus	1.90E-02	2.9	1.82E-02	2.09E-02	0.5	2.06E-02
Total body	1.19E-02	0.0	1.21E-02	1.18E-02	0.4	1.19E-02
Effective dose (mSv/MBq)	1.88E-02	2.7	2.72E-02	1.84E-02	1.9	2.19E-02

Human absorbed dose (mGy/MBq) and effective dose for ICRP 103 weighting factors (mSv/MBq) derived by animal tissue distribution (TD) and dynamic imaging based on single sphere segmentation (both bladder fraction 0.5) for the standard 70-kg male phantom including no extrapolation (NE) estimation based on pure animal data.

by applying partial volume correction based on the inversion of geometric transfer matrix [18], but it requires the point spread function of the system and accurate anatomical information (ideally from MRI). Another, simpler approach to overcome these limitations that could be useful is a combined method where animals are sacrificed after dynamic imaging, and the activity of the harvested organs is quantified with a gamma well counter to cross-calibrate organ activity measured with microPET. Kesner et al. applied this approach to dosimetry in rats [15]. An investigation of this approach in mice, where size dependent effects are more eminent than in rats, will be part of future studies. Furthermore, movement artifacts arising due to rapid respiration and heart motion could be avoided by gated scanning [19]. However, it should be noted that gating decreases signal to noise ratios and leads to longer and fewer frames. An iodine-based contrast agent was used to aid organ delineation in the microCT scans. Although of great use in organ delineation, this contrast agent is most likely cleared via the same pathways as the tracer and might thus have altered uptake in liver and kidneys. The effect of IP contrast agent on residence times in the TD method will be considered in future studies.

Table 3 Influence of bladder fraction on urinary bladder wall dose (UBW) and effective dose (ED)

Dose		TD	Dynamic single
Bladder fraction 0.3	UBW	9.67E-02	9.85E-02
	ED	1.66E-02	1.63E-02
Bladder fraction 0.4	UBW	1.26E-01	1.28E-01
	ED	1.77E-02	1.74E-02
Bladder fraction 0.5	UBW	1.54E-01	1.56E-01
	ED	1.88E-02	1.84E-02

Variation of UBW absorbed dose in mGy/MBq and ED for ICRP 103 weighting factors (mSv/MBq) for different bladder fractions and a voiding interval of 4 h.

Bretin et al. EJNMMI Research 2013, 3:35
http://www.ejnmmires.com/content/3/1/35

The correlation between the extrapolated dose estimates derived by TD and dynamic single was $r = 0.9666$ ($p < 0.0001$) and $r = 0.9603$ ($p < 0.0001$) between TD and dynamic whole. The largest absolute differences in absorbed dose were found in brain, liver, and kidneys, which were underestimated in dynamic imaging by 72% (expressed as percentage of absorbed dose derived by organ harvesting), 46% and 37%, respectively. Since the brain data in dynamic imaging were derived from the remainder, the large deviation in absorbed dose for brain is a logical consequence of the methodology, as opposed to liver and kidneys, which were clearly derived by both methods. However, the effective dose deviated by only approximately 2%.

In comparison to the effective dose for 18F-FDG using the 70-kg adult male phantom, [^{18}F]UCB-H remained below the reported effective dose for FDG of 2.1E-02 to 2.9E-02 mSv/MBq [20] with values (based on ICRP 103) of 1.88E-02 mSv/MBq (TD) and 1.84E-02 mSv/MBq (dynamic single). Based on the old tissue weighting factors from ICRP 60, the effective dose was 2.18E-02 mSv/MBq (TD) and 2.15E-02 mSv/MBq (dynamic single). These values are also well below the limits given by the ICRP [21]. When assuming a smaller bladder fraction of 0.3, the effective dose based on TD is decreased to an average of 1.66E-02 mSv/MBq (dynamic single 1.63E-02 mSv/MBq, both ICRP 103) for the standard 70-kg male. Assuming a shorter voiding interval (pre-scan hydration of the subject) of 2 h, the effective dose further decreases to 1.65E-02 mSv/MBq (TD and ICRP 103; 1.61E-02 mSv/MBq for dynamic single) for a bladder fraction of 0.5 and 1.53E-02 mSv/MBq (TD and ICRP 103; 1.49E-02 mSv/MBq for dynamic single) for a bladder fraction of 0.3.

The dose limits described by the US Food and Drug Administration (expressed in equivalent dose, equal to absorbed dose in this case, radiation weighting factor equal to 1) state that 30 mSv per scan should not be exceeded, or an annual dose of 50 mSv for whole body, blood forming organs, lens of the eye and gonads. The limits for all other organs are 50 mSv (single scan) and 150 mSv (annual) [22]. Therefore, for research in the USA, the maximum single injected dose of [^{18}F]UCB-H allowed (assuming a bladder fraction of 0.5 and ICRP 103 factors) is 325 MBq, while the maximum annual dose is 974 MBq, with the urinary bladder being the critical organ for both (values derived from TD; dynamic imaging yields very similar values of 321 and 962 MBq). When decreasing the bladder fraction to 0.3, the critical organ remains the urinary bladder, but the single and annual doses increase to 517 MBq for single injection and 1,551 MBq for annual injection (508 MBq/1,523 MBq dynamic imaging). European regulations propose that the effective dose should not exceed 10 mSv per scan [21]. Based on this more stringent criterion, the maximum injectable dose per scan derived by organ harvesting would be 532 MBq per subject (543 MBq dynamic single). If the bladder fraction is only 0.3, the maximum injectable dose is 601 MBq (614 MBq dynamic single). However, the presently derived injection limits represent a worst case scenario due to assumptions made, such as physical decay only after the last measured time point or the relatively high fraction of injected activity cleared via urinary pathways. First human clinical trials are indispensable for confirming injection limits.

In displacement studies, subjects are injected at least twice in a short time interval in order to detect the baseline state and the activation state, or displacement [23]. Therefore, a limit of 300 MBq per scan will keep radiation exposure below harmful limits with an annual limit of three injections for practice in the USA. However, based on the high amount of activity reaching the brain [2], the injection of 200 MBq per scan ought to be sufficient to provide diagnostically useful images with [^{18}F]UCB-H.

Conclusions

In this study, it was shown that the novel SV2A radiotracer [^{18}F]UCB-H meets the standard regulations regarding radiation dose for use in human clinical trials. A maximum single injectable dose of approximately 325 MBq per scan was estimated based on the classical organ harvesting technique. Dynamic imaging results by microPET showed significant deviations from organ harvesting results for single-organ absorbed doses, indicating that accurate quantification in such small volumes as mice organs is limited. However, the effective dose derived by microPET deviated by only 2% from the classical organ harvesting result.

Additional files

Additional file 1: TACs (dynamic whole). Time-activity curves derived by whole organ segmentation.

Additional file 2: TACs (dynamic whole). Time-activity curves derived by whole organ segmentation (zoom in).

Additional file 3: Mean doses (dynamic whole). Mean absorbed doses in mGy/MBq including effective dose in mSv/MBq (ICRP 103) from whole organ segmentation.

Additional file 4: Effective doses (ICRP 60). Mean effective doses from old tissue weighting factors from ICRP 60.

Competing interests

All authors declare that they have no competing interests.

Authors' contributions

FB carried out the experiments, participated in the design of the study, and drafted the manuscript. GW carried out the experiments and participated in the design of the study. MAB participated in the design of the study and interpretation of data. JA carried out radiochemistry. NM, TB, FM, and AV revised the manuscript for important intellectual content. FG and CL helped carrying out radiochemistry. AL and ES revised the manuscript for important intellectual content. AS and AP participated in the design of the study, interpretation of data, and revised the manuscript for important intellectual content. All authors read and approved the final manuscript.

Acknowledgments
This work was funded by the Walloon Region Public Private Partnership NEUROCOM, with University of Liège and UCB Pharma as partners. FB is supported by Marie Curie Initial Training Network (MCITN) *Methods in Neuroimaging* under grant no. #MC-ITN-238593. MAB is a 'collaborateur logistique,' and AP is a senior research associate from FRS-FNRS Belgium. We would like to thank the reviewers for their constructive and helpful remarks.

Author details
[1]Cyclotron Research Centre, University of Liège, Allée du 6 Août, Building B30, Sart Tilman, Liège 4000, Belgium. [2]UCB Pharma, NewMedicines-Neurosciences Discovery Research, Braine-l'Alleud 1420, Belgium. [3]UCB Pharma, NewMedicines-Neurosciences Discovery Medicine, Braine-l'Alleud 1420, Belgium.

Received: 7 March 2013 Accepted: 20 April 2013
Published: 7 May 2013

References

1. Lynch BA, Lambeng N, Nocka K, Kensel-Hammes P, Bajjalieh SM, Matagne A, Fuks B: **The synaptic vesicle protein SV2A is the binding site for the antiepileptic drug levetiracetam.** *Proc Natl Acad Sci USA* 2004, **101:**9861.
2. Warnock G, Aerts J, Bahri M, Bretin F, Buchanan T, Klitgaard H: **Characterization of a novel radiotracer targeting synaptic vesicle protein 2A (SV2A).** *World Mol Imag Conf* 2012:134.
3. Siegel JA, Thomas SR, Stubbs JB, Stabin MG, Hays MT, Koral KF, Robertson JS, Howell RW, Wessels BW, Fisher DR: **MIRD pamphlet no. 16: techniques for quantitative radiopharmaceutical biodistribution data acquisition and analysis for use in human radiation dose estimates.** *J Nucl Med* 1999, **40:**37S–61S.
4. Bahri MA, Warnock G, Plenevaux A, Choquet P, Constantinesco A, Salmon E, Luxen A, Seret A: **Performance evaluation of the General Electric eXplore CT 120 micro-CT using the vmCT phantom.** *Nucl Instrum Methods Phys Res, Sect. A* 2011, **648:**S181–S185.
5. Feldkamp L, Davis L, Kress J: **Practical cone-beam algorithm.** *JOSA A* 1984, **1:**612–619.
6. Laforest R, Longford D, Siegel S, Newport DF, Yap J: **Performance evaluation of the microPET® - FOCUS-F120.** *IEEE Trans Nucl Sci* 2007, **54:**42–49.
7. Defrise M, Kinahan P, Townsend DW, Michel C, Sibomana M, Newport D: **Exact and approximate rebinning algorithms for 3-D PET data.** *IEEE Trans Med Imag* 1997, **16:**145–158.
8. Bahri MA, Plenevaux A, Warnock G, Luxen A, Seret A: **NEMA NU4-2008 image quality performance report for the microPET Focus 120 and for various transmission and reconstruction methods.** *J Nucl Med* 2009, **50:**1730–1738.
9. Kirshner A, Ice R, Beierwaltes W: **Radiation dosimetry of 19-iodocholesterol [I31I]: the pitfalls of using tissue concentration data (reply).** *J Nucl Med* 1975, **16:**248–249.
10. Stabin MG, Sparks RB, Crowe E: **OLINDA/EXM: the second-generation personal computer software for internal dose assessment in nuclear medicine.** *J Nucl Med* 2005, **46:**1023–1027.
11. Cloutier RJ, Smith SA, Watson EE, Snyder WS, Warner GG: **Dose to the fetus from radionuclides in the bladder.** *Health Phys* 1973, **25:**147.
12. Stabin MG: *Fundamentals of Nuclear Medicine Dosimetry.* New York: Springer; 2008.
13. Valentin J: *Icrp: The 2007 Recommendations of the International Commission on Radiological Protection.* Elsevier Health Sciences; 2008.
14. Protection ICoR: 1990: *Recommendations of the International Commission Radiological Protection*, Adopted by the Commission in November 1990; 1991:60.
15. Kesner AL, Hsueh WA, Czernin J, Padgett H, Phelps ME, Silverman DHS: **Radiation dose estimates for [18 F] 5-fluorouracil derived from PET-based and tissue-based methods in rats.** *Mol Imaging Biol* 2008, **10:**341–348.
16. Vesselle H, Grierson J, Peterson LM, Muzi M, Mankoff DA, Krohn KA: **18F-fluorothymidine radiation dosimetry in human PET imaging studies.** *J Nucl Med* 2003, **44:**1482–1488.
17. Mankoff DA, Peterson LM, Tewson TJ, Link JM, Gralow JR, Graham MM, Krohn KA: **[18F] fluoroestradiol radiation dosimetry in human PET studies.** *J Nucl Med* 2001, **42:**679–684.
18. Rousset OG, Ma Y, Evans AC: **Correction for partial volume effects in PET: principle and validation.** *J Nucl Med* 1998, **39:**904–911.
19. Yang Y, Rendig S, Siegel S, Newport DF, Cherry SR: **Cardiac PET imaging in mice with simultaneous cardiac and respiratory gating.** *Phys Med Biol* 2005, **50:**2979.
20. Deloar HM, Fujiwara T, Shidahara M, Nakamura T, Watabe H, Narita Y, Itoh M, Miyake M, Watanuki S: **Estimation of absorbed dose for 2-[F-18] fluoro-2-deoxy-D-glucose using whole-body positron emission tomography and magnetic resonance imaging.** *Eur J Nucl Med* 1998, **25:**565–574.
21. Verbruggen A, Coenen HH, Deverre JR, Guilloteau D, Langstrom B, Salvadori PA, Halldin C: **Guideline to regulations for radiopharmaceuticals in early phase clinical trials in the EU.** *Eur J Nucl Med Mol Imaging* 2008, **35:**2144–2151.
22. Code of Federal Regulations - Drugs for human use, Title 21, Volume 5: http://www.accessdata.fda.gov/scripts/cdrh/cfdocs/cfcfr/CFRSearch.cfm?fr=361.1.
23. Carson RE, Herscovitch P, Daube-Witherspoon ME: *Quantitative Functional Brain Imaging with Positron Emission Tomography.* Amsterdam: Elsevier Science; 1998.

doi:10.1186/2191-219X-3-35
Cite this article as: Bretin *et al.*: Preclinical radiation dosimetry for the novel SV2A radiotracer [^{18}F]UCB-H. *EJNMMI Research* 2013 **3**:35.

APPENDIX B

Paper II

Hybrid MicroPET Imaging for Dosimetric Applications in Mice: Improvement of Activity Quantification in Dynamic MicroPET Imaging for Accelerated Dosimetry Applied to 6-[^{18}F]Fluoro-l-DOPA and 2-[^{18}F]Fluoro-l-Tyrosine

Bretin F., Mauxion T., Warnock G., Bahri MA., Libert L., Lemaire C., Luxen A., Bardiés M., Seret A. and Plenevaux A.

Molecular Imaging and Biology 16:383-394, 2014

MOLECULAR IMAGING AND BIOLOGY

Mol Imaging Biol (2014) 16:383–394
DOI: 10.1007/s11307-013-0706-z

Published Online: 19 November 2013

World Molecular Imaging Society

RESEARCH ARTICLE

Hybrid MicroPET Imaging for Dosimetric Applications in Mice: Improvement of Activity Quantification in Dynamic MicroPET Imaging for Accelerated Dosimetry Applied to 6-[^{18}F] Fluoro-L-DOPA and 2-[^{18}F]Fluoro-L-Tyrosine

F. Bretin,[1] T. Mauxion,[2] G. Warnock,[1] M. A. Bahri,[1] L. Libert,[1] C. Lemaire,[1] A. Luxen,[1] M. Bardiès,[2] A. Seret,[1] A. Plenevaux[1]

[1]*Cyclotron Research Centre, University of Liege, Allée du 6 Août, Building B30, Sart Tilman, 4000 Liege, Belgium*
[2]*Inserm UMR 1037 INSERM/UPS, Centre de Recherche en Cancérologie de Toulouse, 31062 Toulouse, France*

Abstract

Purpose: Dynamic microPET imaging has advantages over traditional organ harvesting, but is prone to quantification errors in small volumes. Hybrid imaging, where microPET activities are cross-calibrated using post scan harvested organs, can improve quantification. Organ harvesting, dynamic imaging and hybrid imaging were applied to determine the human and mouse radiation dosimetry of 6-[18 F]fluoro-L-DOPA and 2-[18 F]fluoro-L-tyrosine and compared.

Procedures: Two-hour dynamic microPET imaging was performed with both tracers in four separate mice for 18 F-FDOPA and three mice for 18 F-FTYR. Organ harvesting was performed at 2, 5, 10, 30, 60 and 120 min post tracer injection with $n=5$ at each time point for 18 F-FDOPA and $n=3$ at each time point for 18 F-FTYR. Human radiation dosimetry projected from animal data was calculated for the three different approaches for each tracer using OLINDA/EXM. S-factors for the MOBY phantom were used to calculate the animal dosimetry.

Results: Correlations between dose estimates based on organ harvesting and imaging was improved from $r=0.997$ to $r=0.999$ for 18 F-FDOPA and from $r=0.985$ to $r=0.996$ ($p<0.0001$ for all) for 18 F-FTYR by using hybrid imaging.

Conclusion: Hybrid imaging yields comparable results to traditional organ harvesting while partially overcoming the limitations of pure imaging. It is an advantageous technique in terms of number of animals needed and labour involved.

Key words: 18 F-FDOPA, 18 F-FTYR, MicroPET, Dosimetry, Quantification

Introduction

According to most governmental research guidelines for the use of newly developed radiopharmaceuticals in humans, the biodistribution and the radiation dosimetry must be determined preclinically in advance of any clinical application in order to eliminate the chance of excess radiation exposure. *Ex vivo* measurement of the biodistribution over time using harvested organs has long been considered the gold-standard technique. Organs are harvested from small to mid-size animals such as mice or dogs at several time points post administration of the

Correspondence to: A. Plenevaux; *e-mail:* Alain.Plenevaux@ulg.ac.be

radiopharmaceutical and the behaviour of the tracer extrapolated to human data [1–3]. However, organ harvesting is labour intensive and many animals are required to establish the biodistribution. Additionally, due to the low time resolution, early blood peaks in organs cannot be detected. In primates or larger animals dynamic PET is increasingly common in radiation dosimetry due to its high time resolution and time efficient procedure [4–6]. However, animal husbandry for larger species is complex and costly. The development of microPET imaging allows determination of the complete *in vivo* biodistribution in small rodents, which are easier to handle and widely used in other preclinical applications. However, microPET is prone to partial volume effects (PVE) in small volumes with subsequent quantification errors [7] and hence dosimetry errors, which in the worst case could lead to overexposure of subjects in the clinic. A simple method of correcting for PVE is scaling of the extracted time–activity curve (TAC). This scaling is based on the ratio between measured activity from PET and the post scan harvested organ activity (measured with a gamma well counter). This method, sometimes referred to as hybrid imaging, was applied in rats by Kesner et al. [8] with a resultant improvement in the correlation between dose estimates derived by organ harvesting, imaging and hybrid imaging. PVE and spill-over are size dependent and thus more prevalent in smaller animals (an average mouse weighs approximately ten times less than an average rat). Thus, the hybrid approach may be of even more value in mice. The aim of this study was to apply the hybrid technique in mice and to compare the absorbed dose values obtained after extrapolation to humans with this technique to those obtained using the widely accepted organ harvesting. The compounds used in this study were 6-[^{18}F]fluoro-L-DOPA (18 F-FDOPA) and 2-[^{18}F]fluoro-L-tyrosine (18 F-FTYR). The radiation dosimetry of 18 F-FDOPA in humans (with carbidopa pretreatment) was derived by Brown et al. [9] and will be compared to the results derived in this study. To the best of our knowledge, the radiation dosimetry of 18 F-FTYR is not available in literature and will be presented for the first time. Additionally, we present the dosimetry in mice calculated using the MOBY phantom [10] and S-factors derived using Monte Carlo Simulations (GATE) [11].

Materials and Methods

Animals

Male C57BL/6 mice were obtained from Charles River Laboratories (Brussels, Belgium) and subsequently bred at the Animal Facility of the GIGA-University of Liege (BE-LA 2610359). All animals were housed under standard 12 h:12 h light/dark conditions with food and water available *ad libitum*. All protocols and experimental procedures used in this investigation were reviewed and approved by the Institutional Animal Care and Use Committee of the University of Liege.

Radiochemistry

6-[^{18}F]fluoro-L-DOPA was synthesized as described by Libert et al. [12]. 2-[^{18}F]fluoro-L-Tyrosine was prepared using a similar methodology but with 2-formyl-5-methoxy-*N*,*N*,*N*-trimethylbenzenaminium trifluoromethanesulfonate as the starting chemical. The tracers were obtained at the NCA level and therefore with the highest specific activity ever achieved for these tracers (540 GBq/μmol).

Study Protocol

All data acquisition and analysis was performed in accordance to MIRD pamphlet no. 16 [13]. Anesthesia was induced with 4.5 % isoflurane (in oxygen) and maintained after tail vein tracer injection by inhalation of 1–2 % isoflurane. After sacrifice by decapitation brain, liver, kidney, heart, spleen, testes and lung were harvested. The tissues were weighed (NewClassic ML, Mettler Toledo, Switzerland) and activities were quantified by radioassay using a gamma well counter (Cobra II Auto-Gamma; Perkin-Elmer, USA) resulting in the average activity per g of tissue at each time point.

For 18 F-FDOPA, organ harvesting was performed in 30 mice (average weight 23.51±1.75 g) after an average i.v. bolus of 8.47±1.45 MBq. Five mice per time point were sacrificed by decapitation after 2, 5, 10, 30, 60, and 120 min. Dynamic PET images were acquired for 120 min after i.v. bolus injection of 7.66±1.62 MBq 18 F-FDOPA via the tail vein in four separate mice (average bodyweight 22.10±1.21 g). Organs were harvested post scan and activity per gram of tissue was determined as described above.

For 18 F-FTYR, dynamic imaging and organ harvesting were performed in the same experiment. 18 mice (average weight 27.63 ±1.97 g) received 8.08±1.21 MBq and were sacrificed by decapitation after 2, 5, 10, 30, 60 and 120 min, with n=3 at each time point. The three mice to be sacrificed at 120 min post injection were also scanned dynamically from injection to sacrifice.

Dynamic microPET images were acquired using a Siemens Concorde Focus 120 microPET (Siemens, Germany) [14] and followed by transmission measurement using the rotating ^{57}Co point source of the scanner. The list-mode data were histogrammed into 3D sinograms using Fourier rebinning [15] and reconstructed using filtered backprojection (FBP) with a ramp filter cutoff at the Nyquist frequency. Corrections for randoms, dead-time and attenuation were applied but not for scatter, since it was shown that there is no significant improvement by applying the scatter correction for the Focus 120 microPET [16]. A set of 3D images were reconstructed in a 256×256×95 matrix with a pixel size of 0.4×0.4×0.8 mm. The dynamic time framing consisted of the following frames: 6×5, 6×10, 3×20, 5×30, 5×60, 8×150, 6×300, 6×600 s, and all data were decay corrected to the beginning of each individual frame. Micro-CT images were also acquired with an eXplore 120 micro-CT (Gamma Medica, USA/GE Healthcare, UK) to obtain anatomical information for segmentation. All CT images were reconstructed using Feldkamp's FBP algorithm [17] with a cut-off at the Nyquist frequency and an isotropic voxel size of 100 μm. In both imaging modalities, the MINERVE animal cell bed (Bioscan, USA) was used which provided anesthesia, physiological control and monitoring of respiration. Micro-CT and microPET images were manually co-registered using the commercially available research software PMOD (Version 3.306, PMOD

Technologies, Switzerland). The frame-averaged microPET image was matched by rigid transformations to the microCT image, as for both tracers skull and spine showed significant uptake, which was sufficient for registration to microCT images. Two types of volume of interest (VOI) were drawn by a single observer (F.B.) on the micro-CT images. Full organ segmentation was performed (brain, heart, liver, lung and kidneys) and spheres of 2-mm radius were placed in organs (two VOIs in liver, kidneys and lung, single VOIs otherwise) to decrease the impact of PVE and average activity per volume were derived. Results based on both segmentation techniques were compared. MicroPET calibration for conversion of counts/pixel to Bq/ml was performed as recommended by the manufacturer. The accuracy of this calibration has been reported to be better than 2 % in our laboratory [16].

CT images displayed in the Results section were filtered with an isotropic 3D Gaussian kernel of $0.2\times0.2\times0.2$ mm^3 and the PET image with a 3D Gaussian kernel of $1\times1\times2$ mm^3. The PET image was averaged over all dynamic frames and scaled from 0 to 1,200 kBq/ml.

For each tracer three different TAC were derived: organ harvesting only (will be referred to as organ harvesting), dynamic PET imaging only (imaging) and hybrid dynamic PET imaging (hybrid imaging), where the activity measured with PET was scaled by a factor derived from the ratio between PET activity at the end of the image acquisition and the quantified post scan activity from harvested organs of the same animal.

Organ weights and volumes were taken from a standard C57BL/6 mouse of 35 g created from five male mice, whose organs were weighed and the volume quantified using microCT. Organ activities per gram or volume from organ harvesting or microPET images were then normalized for injected activity and organ weight or volume of the standard mouse, respectively. For hybrid dynamic PET imaging, the TAC was then scaled as described above. All TACs were interpolated with piecewise cubic Hermite interpolation between time points and then extrapolated to human values as described by Kirshner et al. [18]. The method is based on the ratio of organ weight to body weight using animal organ weights from the standard mouse created and human organ weights from the standard 70 kg standard hermaphroditic male phantom [19] implemented in OLINDA/EXM (Version 1.1) [20]. In all TACs, physical decay only was assumed after 120 min neglecting any biological clearance from the organs. All numbers of disintegrations in an organ (cumulated activity) were calculated as area under the curve, which is mathematically equal to the residence time, using trapezoidal numerical integration in Matlab. Urinary excretion was theoretically modeled using the urinary bladder module [21] implemented in OLINDA/EXM for human dose estimates. For 18 F-FDOPA,a fraction of 0.5 of the injected activity was assumed to be cleared via the urinary pathway with a biological half-life of 3 h and voiding was assumed to occur every 4 h. For 18 F-FTYR the same scenario was used, but with a fraction of only 0.2 due to evidence of much reduced accumulation of activity in the bladder. The absorbed doses in major human organs and the effective dose based on the old tissue weighting factors from ICRP 60 [22] were calculated with OLINDA/EXM using the three different TACs for each tracer. Effective doses based on the more recent tissue weighting factors from ICRP 103 [23] were calculated using the absorbed doses from OLINDA/EXM in Microsoft Excel.

Since the TACs derived by organ harvesting consist of numerous time points in different animals, every individual time point has its own standard deviation (SD). Hence, the SD of residence times derived by organ harvesting could not be calculated directly and was calculated as follows. Two additional animal TACs were calculated using the mean±1SD of each individual time point of the activity measurement, which were then extrapolated to human values and the residence times corresponding to each TAC was computed [24]. This residence time window was expressed as a coefficient of variation in percent (%CV) from the mean value. These residence times (mean±1SD) were used to calculate a minimum and maximum absorbed dose for organ harvesting resulting in a best and worst case scenario rather than a real SD. The mean of best and worst case scenario was used as the error for the absorbed dose expressed as %CV of the mean absorbed dose value obtained using the mean TAC. For the statistics of imaging and hybrid imaging every scan was treated separately and mean±1SD expressed as %CV were calculated across scans as usual. Correlations between datasets were calculated using Pearson product–moment correlation coefficient in MATLAB.

Mouse Dosimetry

S-factors were derived for the MOBY phantom [10] using GATE v6.1 [25]. The method used to generate the MOBY dataset and S-factors has been previously described [11]. The biodistribution data acquired for both tracers was processed in the same way as for the human dosimetry but without final extrapolation. Also, organ weights and volumes were not taken from our created standard mouse but from the MOBY phantom, as S-factors are geometry dependent. No bladder model was used, but the bladder activity acquired from the dynamic microPET scans using a 2-mm-radius spherical VOI on the coregistered microCT image was assigned to the bladder of the MOBY phantom. The absorbed doses for organs with derived S-factors and the total body absorbed dose were calculated. SDs for organ harvesting were derived as described above.

Results

The biodistribution for both 18 F-FDOPA and 18 F-FTYR was acquired using organ harvesting, imaging and hybrid imaging. Results based on sphere segmentation are described below, whole organ segmentation data are provided as electronic supplemental material 1 (ESM 1). A representative co-registered PET/CT image for each tracer is illustrated in Fig. 1.

Mean human TACs, normalized for injected activity and organ weight/size, for both radiopharmaceuticals were calculated for all three techniques and are displayed in Fig. 2.

Residence times based on the TACs for organ harvesting, imaging and hybrid imaging were calculated and are displayed in Table 1 for 18 F-FDOPA and in Table 2 for 18 F-FTYR. Pearson's product–moment correlation coefficient r and the significance value p for imaging and hybrid imaging to organ harvesting were calculated for the set of residence times obtained with all three approaches (i.e., brain, heart, kidney, liver, lung). Correlation between datasets for 18 F-FDOPA was improved from $r=0.6875$

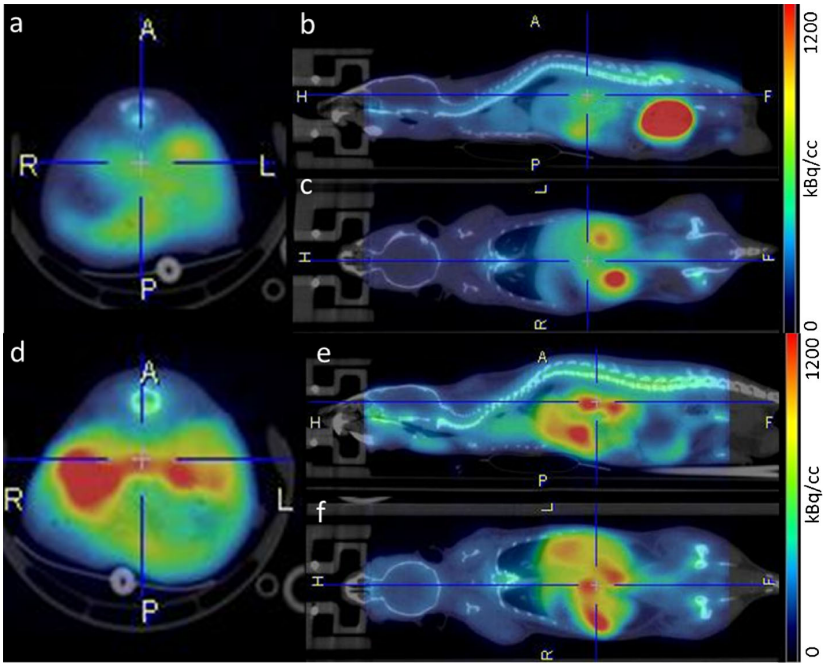

Fig. 1 18 F-FDOPA PET/CT image: **a** transversal, **b** sagittal, **c** coronal image plane, and 18 F-FTYR PET/CT image: **d** transversal, **e** sagittal, **f** coronal image plane.

(p=0.1995) for imaging to r=0.9460 (p=0.0149) for hybrid imaging. The highest number of disintegrations per organ occurred in the urinary bladder followed by the liver for all three methods.

For 18 F-FTYR the correlation was improved from r=0.9801 (p=0.0034) to r=0.9999 (p<0.0001). The largest residence time derived for 18 F-FTYR was in the liver, followed by the bladder.

When assuming the organ harvesting residence time to be the reference value, a recovery coefficient defined as the ratio between residence times derived by organ harvesting and imaging can be calculated. These recovery coefficients

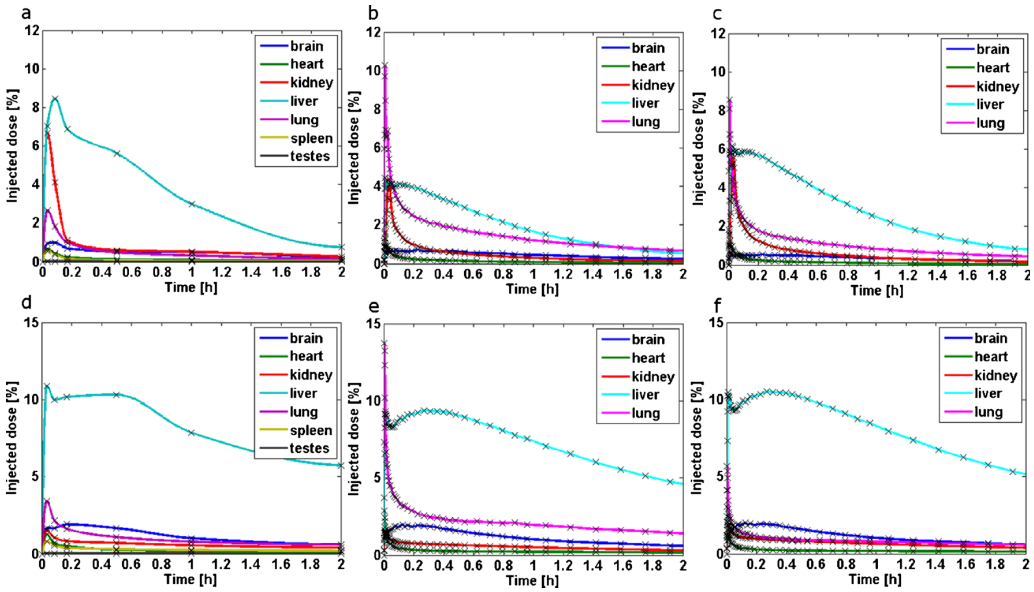

Fig. 2 18 F-FDOPA TACs: **a** organ harvesting, **b** imaging, **c** hybrid imaging, and 18 F-FTYR TACs: **d** organ harvesting, **e** imaging, **f** hybrid imaging.

Table 1. Human residence times and %CV for 18 F-FDOPA obtained with organ harvesting, imaging and hybrid imaging

18 F-FDOPA	TD	%CV	Imaging	%CV	Hybrid Imaging	%CV
Brain[a]	1.38E−02	20.5	1.54E−02	28.0	1.17E−02	26.6
Heart[a]	3.41E−03	15.6	3.49E−03	8.6	3.56E−03	13.7
Kidney[a]	2.19E−02	31.8	1.32E−02	17.2	1.66E−02	9.5
Liver[a]	8.86E−02	27.4	5.33E−02	7.1	7.77E−02	15.9
Lung[a]	1.25E−02	13.1	4.72E−02	15.5	3.22E−02	20.9
Spleen	2.12E−03	16.6				
Testes	2.90E−04	41.8				
Bladder	3.08E−01	0.0	3.08E−01	0.0	3.08E−01	0.0
Remainder	2.18E+00	1.7	2.19E+00	0.5	2.18E+00	0.3
Pearson's r	–	–	0.6875		0.9460	
Significance (p)	–	–	0.1995		0.0149	

[a]Experimentally derived by all three methods and used for calculation of correlation

are shown in Table 3. Applying hybrid imaging improved quantification for most organs, except for brain and heart using 18 F-FDOPA and for heart using 18 F-FTYR. Large overestimations occurred for the lung with imaging for both tracers. Human dose estimates projected from animal data derived by organ harvesting, imaging and hybrid imaging are displayed in Table 4 (18 F-FDOPA) and Table 5 (18 F-FTYR). The Correlation for 18 F-FDOPA was marginally improved from $r=0.9974$ ($p<0.0001$) between organ harvesting and imaging to $r=0.9988$ ($p<0.0001$) between organ harvesting and hybrid imaging. The organ receiving the highest absorbed dose was the urinary bladder wall for all three datasets. The second highest absorbed dose received for all three methods was in the uterus.

For 18 F-FTYR, the correlation was increased from $r=0.9852$ ($p<0.0001$) to $r=0.9962$ ($p<0.0001$). The highest absorbed dose was received by the urinary bladder wall, followed by the liver, for all three methods.

Mouse absorbed dose estimates for both tracers calculated from organ harvesting, imaging and hybrid imaging are displayed in Tables 6 and 7. For 18 F-FDOPA the organ receiving the highest absorbed dose was the kidney for organ harvesting and the bladder for imaging and hybrid imaging. For 18 F-FTYR the critical organ was the liver for all three methods.

Discussion

The biodistribution and radiation dosimetry (human and mouse) of 6-[18 F]fluoro-L-DOPA and 2-[18 F]fluoro-L-tyrosine were obtained using not only the well-established gold-standard technique of organ harvesting, but also using a conventional imaging technique and sophisticated hybrid imaging technique. Differences between (human) residence times derived by organ harvesting and conventional imaging were found for both radiopharmaceuticals (Table 3), most likely resulting from deficiencies in quantification in microPET. Constantinescu et al. also reported a poor correlation between post scan harvested organ activities and final microPET measurements [26].

For 18 F-FDOPA, the brain, heart and lung were overestimated in conventional imaging, whereas kidney and liver were underestimated with pure imaging. The brain overestimation is a result of high tracer uptake in the skull compared to the brain tissue itself, causing a spill over into the brain VOI. The heart uptake from imaging combines counts from blood and myocardium. This highlights a limitation of microPET for this purpose, compared to *ex vivo* harvesting, where blood is mostly removed from organs before activity quantification. Thus, despite PVE the heart activity is slightly overestimated in imaging. The substantial overestimation of activity in the lung is a combination of

Table 2. Human residence times and %CV for 18 F-FTYR obtained by organ harvesting, imaging and hybrid imaging

18 F-FTYR	TD	%CV	Imaging	%CV	Hybrid Imaging	%CV
Brain[a]	3.86E−02	22.2	3.81E−02	15.7	3.83E−02	22.6
Heart[a]	8.78E−03	9.1	9.21E−03	3.0	7.86E−03	9.4
Kidney[a]	2.24E−02	8.7	1.87E−02	13.5	2.38E−02	8.4
Liver[a]	3.05E−01	18.1	2.60E−01	13.6	2.92E−01	16.8
Lung[a]	3.42E−02	8.8	7.80E−02	7.9	3.19E−02	11.1
Spleen	1.06E−02	13.3	–	–	–	–
Testes	9.51E−04	12.8	–	–	–	–
Bladder	1.23E−01	0.0	1.23E−01	0.0	1.23E−01	0.0
Remainder	2.08E+00	3.6	2.14E+00	8.0	2.19E+00	7.0
Pearson's r	–	–	0.9801	–	0.9999	–
Significance (p)	–	–	0.0034	–	<0.0001	–

[a]Experimentally derived by all three methods and used for calculation of correlation

Table 3. Ratios between human residence times derived by organ harvesting and imaging techniques

	18 F-FDOPA		18 F-FTYR	
Organ	Imaging	Hybrid imaging	Imaging	Hybrid imaging
Brain	1.11	0.85	0.99	0.99
Heart	1.02	1.04	1.05	0.89
Kidney	0.60	0.76	0.83	1.06
Liver	0.60	0.88	0.85	0.96
Lung	3.77	2.57	2.28	0.93

spill over from the high activity organs (liver and heart) in its vicinity and limitations in attenuation correction resulting from PVE and the lack of resolution in the attenuation map. Fig. 3 displays a representative microCT image and corresponding co-registered PET attenuation map obtained with the rotating ^{57}CO point source. Overestimation of the attenuation value is especially apparent on the boundaries of the microCT VOI. Using a combination of the low resolution attenuation map for attenuation correction and high resolution microCT images for segmentation in the lung leads to an overestimation of average activity. However, using the microCT VOI to manipulate the attenuation map proved impossible due to proprietary file format issues (PMOD and Siemens file formats). The manufacturer's software (ASIpro) (S*iemens* Medical Solutions USA, Inc.) could be used for lung segmentation based on the attenuation map and to improve attenuation correction, but the accuracy of segmentation proved very low due to poor contrast and resolution in the attenuation map. As such, the resulting difference in lung residence times was negligible. The use of a combined PET/CT system would overcome this limitation.

For 18 F-FDOPA, hybrid imaging appeared to increase the accuracy for almost every organ by partially compensating for the errors described above. However, the lung was still overestimated by a factor of 2.57 and the kidney was underestimated by a factor of 0.76 (Table 3). The agreement between brain and heart residence times for the quantification methods was slightly decreased for 18 F-FDOPA (compared to 18 F-FTYR). For 18 F-FTYR, using hybrid imaging slightly decreased the accuracy of quantification in the heart as described above, but the agreement between organ harvesting and imaging was increased or equal for every other organ after cross calibration. On the whole, hybrid imaging tends to slightly underestimate organ activity in comparison to organ harvesting, with the largest underestimation in the kidney for 18 F-FDOPA. Improved residence time correlations for 18 F-FTYR compared to 18 F-FDOPA might be an effect of using the same animals for organ harvesting at 120 min and dynamic scanning, due

Table 4. Human dose (mGy/MBq) estimates and %CV for 18 F-FDOPA using organ harvesting, imaging and hybrid imaging

Target organ	Organ harvesting	Imaging	Hybrid imaging	%CV organ harvesting	%CV imaging	%CV hybrid imaging
Adrenals	1.27E−02	1.25E−02	1.27E−02	2.0	0.0	0.9
Brain[a]	4.69E−03	4.96E−03	4.34E−03	9.1	14.2	12.1
Breasts	8.86E−03	9.03E−03	8.96E−03	1.0	0.4	0.3
Gallbladder wall	1.39E−02	1.32E−02	1.37E−02	2.5	0.3	1.6
LLI wall	1.68E−02	1.69E−02	1.68E−02	1.2	0.3	0.3
Small intestine	1.46E−02	1.46E−02	1.46E−02	1.0	0.3	0.0
Stomach wall	1.24E−02	1.24E−02	1.24E−02	0.4	0.0	0.0
ULI wall	1.40E−02	1.39E−02	1.40E−02	0.4	0.3	0.3
Heart Wall[a]	8.63E−03	8.87E−03	8.85E−03	4.1	1.3	3.1
Kidneys[a]	1.99E−02	1.45E−02	1.67E−02	21.9	9.7	5.9
Liver[a]	1.56E−02	1.14E−02	1.43E−02	18.6	4.0	10.5
Lungs[a]	7.81E−03	1.35E−02	1.11E−02	4.2	9.0	9.9
Muscle	1.16E−02	1.16E−02	1.16E−02	0.9	0.4	0.0
Ovaries	1.69E−02	1.69E−02	1.69E−02	1.2	0.4	0.0
Pancreas	1.33E−02	1.32E−02	1.33E−02	0.8	0.4	0.6
Red marrow	1.08E−02	1.08E−02	1.08E−02	0.9	0.0	0.0
Osteogenic cells	1.69E−02	1.70E−02	1.69E−02	1.2	0.3	0.3
Skin	8.74E−03	8.77E−03	8.75E−03	1.2	0.3	0.2
Spleen	8.59E−03	1.20E−02	1.20E−02	5.0	0.0	0.0
Testes	9.56E−03	1.34E−02	1.33E−02	4.3	0.4	0.0
Thymus	1.09E−02	1.11E−02	1.10E−02	0.9	0.4	0.8
Thyroid	1.09E−02	1.10E−02	1.09E−02	1.8	0.4	0.4
Urinary bladder wall	1.57E−01	1.57E−01	1.57E−01	0.3	0.0	0.0
Uterus	2.22E−02	2.22E−02	2.22E−02	0.9	0.3	0.2
Total body	1.17E−02	1.17E−02	1.17E−02	0.0	0.0	0.0
Effective dose ICRP 60 (mSv/MBq)	1.97E−02	2.02E−02	2.00E−02	0.5	0.5	0.7
Effective dose ICRP 103 (mSv/MBq)	1.60E−02	1.68E−02	1.67E−02	1.0	0.9	0.7
Pearson's r		0.9974	0.9988			
Significance (p)		<0.0001	<0.0001			

[a]Experimentally derived by all three methods

Table 5. Human dose (mGy/MBq) estimates and %CV for 18 F-FTYR using organ harvesting, imaging and hybrid imaging

Target organ	Organ harvesting	Imaging	Hybrid imaging	%CV organ harvesting	%CV Imaging	%CV hybrid imaging
Adrenals	1.48E−02	1.45E−02	1.48E−02	2.4	1.4	1.6
Brain[a]	8.74E−03	8.67E−03	8.70E−03	15.6	10.9	15.9
Breasts	9.14E−03	9.36E−03	9.17E−03	1.4	0.8	1.2
Gallbladder wall	1.79E−02	1.71E−02	1.77E−02	4.7	3.1	4.3
LLI wall	1.39E−02	1.40E−02	1.40E−02	2.9	1.9	2.2
Small intestine	1.39E−02	1.38E−02	1.39E−02	1.8	1.4	1.2
Stomach wall	1.29E−02	1.28E−02	1.29E−02	0.8	0.7	1.0
ULI wall	1.39E−02	1.37E−02	1.39E−02	0.7	0.7	0.9
Heart wall[a]	1.29E−02	1.33E−02	1.23E−02	4.7	1.5	3.9
Kidneys[a]	2.16E−02	1.91E−02	2.23E−02	6.7	8.6	4.8
Liver[a]	4.20E−02	3.67E−02	4.04E−02	15.7	11.7	14.6
Lungs[a]	1.24E−02	1.96E−02	1.20E−02	5.2	5.8	5.3
Muscle	1.11E−02	1.11E−02	1.11E−02	1.8	1.3	1.5
Ovaries	1.43E−02	1.44E−02	1.44E−02	2.4	1.8	2.1
Pancreas	1.51E−02	1.47E−02	1.49E−02	1.3	0.8	0.8
Red marrow	1.07E−02	1.07E−02	1.07E−02	0.9	0.9	0.9
Osteogenic cells	1.65E−02	1.67E−02	1.66E−02	2.1	1.6	1.9
Skin	8.50E−03	8.55E−03	8.57E−03	2.1	1.5	1.7
Spleen	1.74E−02	1.21E−02	1.22E−02	8.0	0.8	1.5
Testes	1.05E−02	1.13E−02	1.13E−02	3.3	2.3	2.5
Thymus	1.11E−02	1.14E−02	1.11E−02	1.8	1.1	1.3
Thyroid	1.07E−02	1.08E−02	1.08E−02	2.8	1.6	2.2
Urinary bladder wall	6.94E−02	6.96E−02	6.96E−02	0.5	0.4	0.4
Uterus	1.64E−02	1.64E−02	1.65E−02	2.1	1.4	1.9
Total body	1.21E−02	1.21E−02	1.21E−02	0.4	0.0	0.4
Effective dose ICRP 60 (mSv/MBq)	1.64E−02	1.70E−02	1.63E−02	1.5	1.4	1.0
Effective dose ICRP 103 (mSv/MBq)	1.43E−02	1.50E−02	1.42E−02	2.2	1.9	1.5
Pearson's *r*		0.9852	0.9962			
Significance (*p*)		<0.0001	<0.0001			

[a]Experimentally derived by all three methods

Table 6. Mouse dose (mGy/MBq) estimates and %CV for 18 F-FDOPA using organ harvesting, imaging and hybrid imaging

Target organ	Organ harvesting	Imaging	Hybrid imaging	%CV organ harvesting	%CV imaging	%CV hybrid imaging
Skin	6.41	5.79	5.68	2.8	5.4	6.9
Heart total	4.74	3.94	4.21	7.1	5.6	3.6
Heart tissue	4.49	3.77	3.97	4.7	5.7	3.6
Heart blood	4.84	4.00	4.30	7.9	5.5	3.7
Body	17.64	16.28	15.95	2.9	4.4	6.1
Liver	15.70	11.08	14.50	23.6	7.4	15.3
Gallbladder	6.35	4.66	5.85	20.2	6.6	12.8
Total lung	7.40	6.72	6.05	7.9	7.8	9.3
Right lung	7.55	6.85	6.20	7.6	7.5	8.9
Left lung	7.34	6.69	5.99	8.0	8.0	9.5
Stomach total	2.73	2.33	2.44	4.7	4.8	3.0
Stomach wall	5.99	5.04	5.25	3.7	5.7	3.8
Stomach content	2.18	1.88	1.97	5.1	4.4	2.7
Pancreas	3.60	3.04	3.17	7.4	5.5	3.3
Total kidney	23.61	17.13	17.84	26.9	16.9	9.3
Right kidney	23.32	16.96	17.58	26.9	16.9	9.4
Left kidney	24.10	17.45	18.23	26.9	16.9	9.3
Spleen	6.27	2.94	2.92	8.2	5.2	5.5
Small intestine total	3.38	3.28	3.28	0.2	1.3	1.5
Small intestine wall	4.37	4.13	4.13	0.5	2.5	2.8
Small intestine content	2.09	2.15	2.16	0.5	1.5	1.6
Large intestine total	4.08	4.13	4.09	1.1	0.2	0.8
Large intestine wall	5.69	5.55	5.48	1.3	1.6	2.5
Large intestine content	2.40	2.65	2.64	0.5	3.8	3.4
Bladder	4.89	660.79	660.70	2.9	41.9	41.9
Vas deferens	8.84	33.19	33.01	2.7	30.8	30.6
Testes	6.67	5.14	5.05	9.4	2.3	1.3
Bones	6.35	5.71	5.60	2.1	5.8	7.0
Brain	4.13	4.66	3.52	12.8	25.1	21.5
Thyroid	6.47	5.73	5.61	2.9	6.5	8.2
Bone marrow	4.15	3.78	3.69	1.7	5.8	6.7
Total body	14.03	14.12	14.14	0.2	0.3	0.4

Table 7. Mouse dose (mGy/MBq) estimates and %CV for 18 F-FTYR using organ harvesting, imaging and hybrid imaging

Target organ	Organ harvesting	Imaging	Hybrid imaging	%CV organ harvesting	%CV imaging	%CV hybrid imaging
Skin	5.16	5.25	5.13	6.3	5.6	7.1
Heart total	7.71	7.43	7.78	9.6	8.7	11.1
Heart tissue	6.54	6.37	6.59	7.8	7.0	9.3
Heart blood	8.14	7.81	8.21	10.1	9.3	11.6
Body	13.95	14.22	13.87	6.9	6.1	7.8
Liver	48.23	46.26	49.28	17.3	15.9	20.2
Gallbladder	17.67	16.98	18.03	16.4	15.0	19.3
Total lung	14.33	11.07	13.74	8.2	7.9	9.3
Right lung	14.39	11.22	13.82	8.1	7.8	9.1
Left lung	14.39	11.05	13.78	8.2	8.0	9.4
Stomach total	3.82	3.60	3.70	7.1	6.2	8.0
Stomach wall	8.17	7.66	7.84	6.5	5.5	7.4
Stomach content	3.09	2.92	3.00	7.3	6.5	8.2
Pancreas	4.71	4.45	4.57	6.6	6.5	5.9
Total kidney	23.90	23.79	25.02	7.8	14.3	8.0
Right kidney	22.89	22.78	23.94	7.3	14.2	8.9
Left kidney	25.04	24.94	26.25	8.2	14.3	7.4
Spleen	17.65	3.02	3.01	10.6	1.4	3.2
Small intestine total	3.25	3.27	3.27	1.0	0.8	1.1
Small intestine wall	4.13	4.16	4.14	1.4	1.2	1.6
Small intestine content	2.10	2.11	2.12	0.3	0.4	0.3
Large intestine total	3.50	3.56	3.51	4.0	3.3	4.9
Large intestine wall	4.79	4.87	4.79	4.7	3.9	5.7
Large intestine content	2.17	2.20	2.18	2.6	2.0	3.2
Bladder	3.84	37.20	37.10	7.1	22.6	22.5
Vas deferens	7.05	8.16	7.97	6.9	5.8	6.3
Testes	9.80	3.82	3.72	5.0	6.6	8.4
Bones	5.50	5.56	5.47	4.0	3.7	4.6
Brain	8.80	9.67	8.73	18.7	16.3	23.8
Thyroid	5.19	5.28	5.16	6.5	5.8	7.3
Bone marrow	3.72	3.77	3.70	2.8	2.5	3.5
Total body	14.23	14.22	14.24	0.4	0.3	0.4

to a reduction in cross-population differences. The remaining differences between organ harvesting and hybrid imaging for both tracers are most likely a consequence of cross-calibrating activities based only on final microPET measurements. PVE in dynamic microPET imaging is a dynamic problem, since it depends on the activity within the region

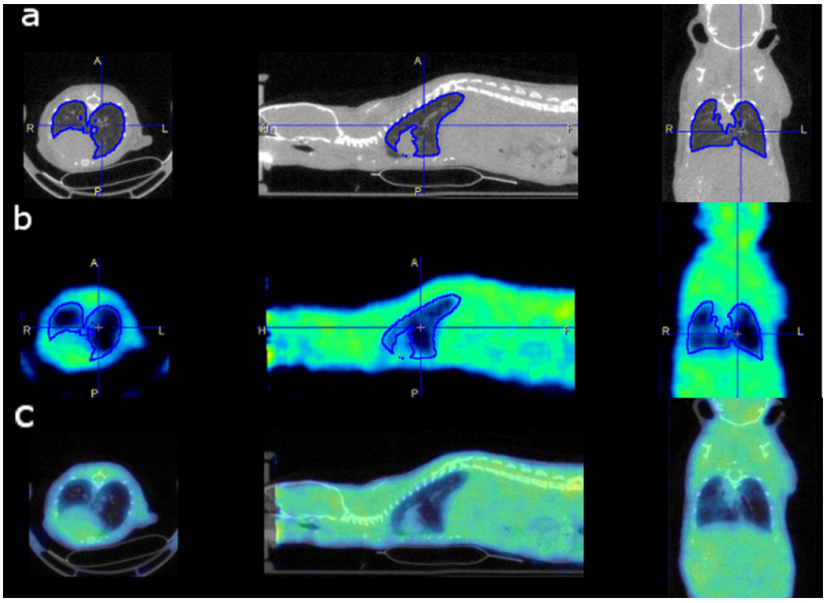

Fig. 3 Co-registered image of microCT and attenuation map of representative subject with lung VOI (from microCT): **a** microCT, **b** attenuation map, **c** overlay of both (transversal, sagittal and coronal image for each).

and the warmth of the background, which changes over time [27]. When comparing major organ absorbed dose estimates for 18 F-FDOPA, hybrid imaging offers increased accuracy compared to conventional imaging (Fig. 4a), with the exception of the absorbed dose in the brain. No general trend for statistical variance (SD) of the dose estimates could be observed and it is not largely increased for imaging. As can be seen in Fig. 4b, hybrid imaging failed to increase accuracy of absorbed dose estimates for 18 F-FTYR in only the heart wall in comparison to imaging only and no trend regarding increase or decrease of statistical variance of dose estimates could be observed. Bland–Altman plots are another bio-statistical technique to examine the agreement between two methods measuring the same quantity [28]. For both tracers, the Bland–Altman plots (Fig. 5) show clearly that the difference between dose estimates as well as the SD of the difference was reduced by applying hybrid imaging compared to imaging.

For human dose estimates with both tracers, a correlation coefficient >0.9950 with $p<0.0001$ between organ harvesting and hybrid imaging was achieved. Considering this high degree of correlation, hybrid dynamic microPET imaging requires far fewer animals compared to the traditional organ harvesting approach. Furthermore, organ harvesting is time-consuming and, depending on the amount of people available for the study, has to be spread over 2 or 3 days, whereas three dynamic microPET scans can easily be executed by a single person in 1 day (data analysis excluded). This in turn decreases the amount of radiopharmaceutical required, making dynamic microPET imaging for radiation dosimetry a more ethical, efficient and cheaper (assuming the equipment to perform microPET imaging is available) way to obtain equivalent results. Using techniques such as parallel scanning of multiple animals in larger bore PET scanners, preclinical dosimetry studies could be performed within a single 2-h dynamic scan [29]. However, due to low *in vivo* contrast in microCT, used to obtain anatomical information for segmentation, fewer organs can be derived from microPET than with organ harvesting and obtaining blood activities is inaccurate (or impossible) due to PVE in small volumes (such as heart chambers and vessels) with microPET. Magnetic resonance imaging may offer a useful alternative for improved segmentation.

When comparing whole organ- and sphere-based segmentation (see supplemental data ESM 1), it becomes clear that whole organ segmentation is redundant, since similar or better results were achieved using hybrid imaging based on sphere segmentation. Particularly when using low contrast microCT imaging for anatomical reference, sphere-based segmentation is far less time-

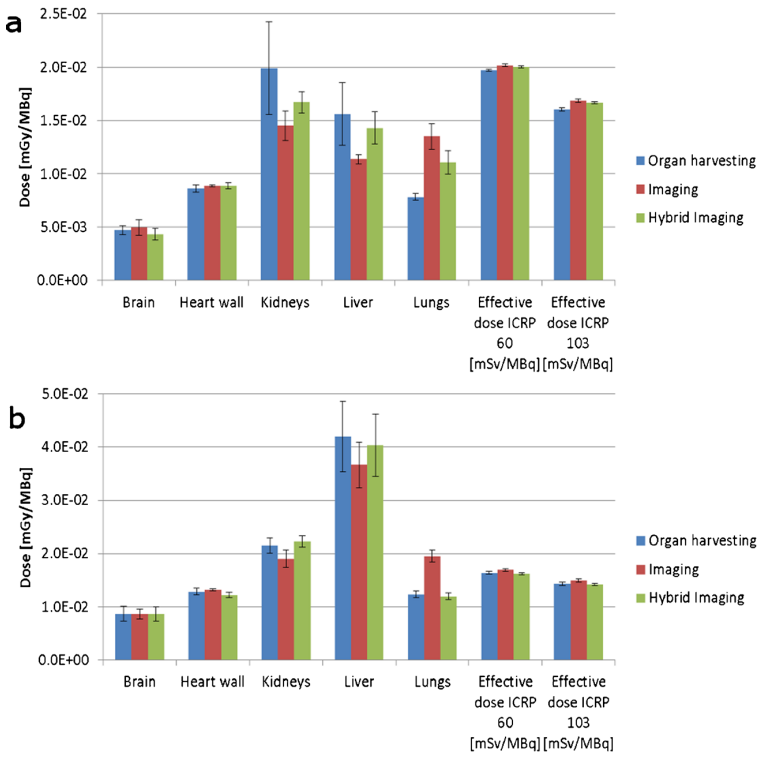

Fig. 4 Human dose comparison 18 F-FDOPA (**a**) and human dose comparison 18 F-FTYR (**b**).

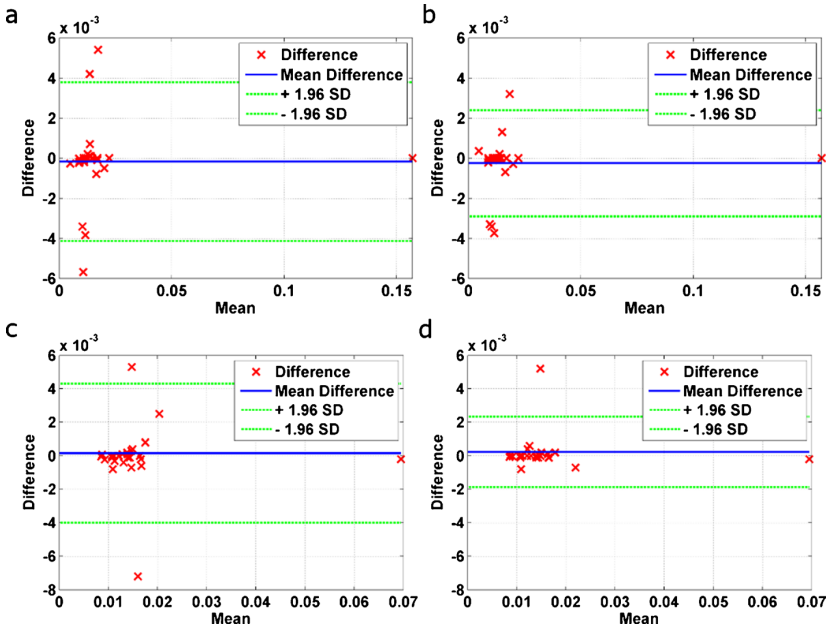

Fig. 5 Bland–Altman plots of derived dosimetry values for 18 F-FDOPA: **a** organ harvesting vs. imaging, **b** organ harvesting vs. hybrid imaging and 18 F-FTYR, **c** organ harvesting vs. imaging, **d** organ harvesting vs. hybrid imaging; *broken green lines* represent confidence interval (mean difference±1.96* SD) or 95 % limits of agreement.

consuming and much less prone to failures in automated organ segmentation due to insufficient soft tissue contrast. However, manual co-registration was applied in this study. Using landmark based co-registration as applied by Warnock et al. [30] might have improved whole organ segmentation as accuracy of registration might be higher.

Table 8. Comparison of mean 18 F-FDOPA dose estimates with literature

Target organ	Organ harvesting	Imaging	Hybrid imaging	Comparison from Brown et al. [mGy/MBq]
Adrenals	1.27E−02	1.25E−02	1.27E−02	1.50E−02
Brain	4.69E−03	4.96E−03	4.34E−03	
Breasts	8.86E−03	9.03E−03	8.96E−03	
Gallbladder wall	1.39E−02	1.32E−02	1.37E−02	
LLI wall	1.68E−02	1.69E−02	1.68E−02	1.60E−02
Small intestine	1.46E−02	1.46E−02	1.46E−02	1.41E−02
Stomach wall	1.24E−02	1.24E−02	1.24E−02	1.21E−02
ULI wall	1.40E−02	1.39E−02	1.40E−02	1.40E−02
Heart wall	8.63E−03	8.87E−03	8.85E−03	
Kidneys	1.99E−02	1.45E−02	1.67E−02	2.74E−02
Liver	1.56E−02	1.14E−02	1.43E−02	1.54E−02
Lungs	7.81E−03	1.35E−02	1.11E−02	1.27E−02
Muscle	1.16E−02	1.16E−02	1.16E−02	8.90E−03
Ovaries	1.69E−02	1.69E−02	1.69E−02	1.41E−02
Pancreas	1.33E−02	1.32E−02	1.33E−02	1.97E−02
Red marrow	1.08E−02	1.08E−02	1.08E−02	1.05E−02
Osteogenic cells	1.69E−02	1.70E−02	1.69E−02	
Skin	8.74E−03	8.77E−03	8.75E−03	8.50E−03
Spleen	8.59E−03	1.20E−02	1.20E−02	1.17E−02
Testes	9.56E−03	1.34E−02	1.33E−02	1.48E−02
Thymus	1.09E−02	1.11E−02	1.10E−02	
Thyroid	1.09E−02	1.10E−02	1.09E−02	1.03E−02
Urinary bladder wall	1.57E−01	1.57E−01	1.57E−01	1.50E−01
Uterus	2.22E−02	2.22E−02	2.22E−02	1.86E−02
Total body	1.17E−02	1.17E−02	1.17E−02	1.05E−02
Effective dose ICRP 60 (mSv/MBq)	1.97E−02	2.02E−02	2.00E−02	1.99E−02
Pearson's *r*	0.9951	0.9929	0.9946	
Significance (*p*)	<0.0001	<0.0001	<0.0001	

Table 8 compares the human radiation dosimetry for 18 F-FDOPA extrapolated from mice to that from human PET scans from Brown et al. [9]. Subjects in their study were pretreated with carbidopa to inhibit peripheral aromatic L-amino acid decarboxylase (AAAD). This allows more 18 F-FDOPA to cross the blood brain barrier in order to increase brain uptake. However, this also slightly alters the biodistribution of 18 F-FDOPA. Nevertheless, most of the absorbed dose estimates derived within this study (extrapolated from animals to humans) are in accordance with the radiation dosimetry derived by Brown et al. and a correlation coefficient >0.99 with $p<0.001$ for all three methods was achieved. In the present study, dosimetry for the urinary bladder wall was based on a theoretical model implemented in OLINDA/EXM, assuming that a fraction of 0.5 of the injected activity was cleared via the urinary pathway. The resulting projected absorbed dose estimate for the urinary bladder wall of 1.57E−02 mGy/MBq closely matched the absorbed dose provided by Brown et al. of 1.50E−02 mGy/MBq. The calculated effective dose deviated by only 1–2 % from that reported in the literature.

To our knowledge, the human dosimetry for 18 F-FTYR was not available in the literature and was derived from preclinical data for the first time in this study. In comparison to 18 F-FDOPA, most of the major organs receive a higher absorbed dose, most likely due to reduced excretion (far less accumulation of activity within the bladder). However, due to the high absorbed dose for the urinary bladder wall, the resulting effective dose is higher for 18 F-FDOPA than for 18 F-FTYR.

A similar pattern was seen in the mouse dosimetry for 18 F-FDOPA and 18 F-FTYR. While for 18 F-FTYR all major organs receive higher absorbed doses, for 18 F-FDOPA the absorbed dose to the bladder is approximately 15 times higher, indicating more rapid excretion and explaining the lack of activity in the remaining organs. For 18 F-FDOPA the calculated absorbed dose for the urinary bladder wall in mice is comparable to the absorbed dose of 543 mGy/MBq to the urinary bladder wall for FDG, as derived by Taschereau and Chatziioannou [31] using a combination of *in vivo* biodistribution and Monte Carlo Simulations on a voxelized mouse phantom. However, the average activity per cc was applied to a small static bladder volume, which might overestimate the resulting activity inside the bladder. When calculating the absorbed doses for the in average injected activity of approximately 10 MBq, organ absorbed doses and total body absorbed dose range from 100 to 400 mGy. The bladder wall absorbed dose for 18 F-FDOPA in the contrary is above 6 Gy for a single scan.

Conclusion

In this study the human radiation dosimetry for both 18 F-FDOPA and 18 F-FTYR was derived from mice using traditional organ harvesting, dynamic microPET imaging and hybrid dynamic imaging (where microPET activities are cross-calibrated with post scan harvested organs to improve quantification). Correlations between organ harvesting and imaging were improved by using hybrid imaging to above $r=0.9950$ ($p<0.0001$). In particular, the error in single organ absorbed doses was reduced, which is of great importance when using preclinical dosimetry data to estimate safe doses for human subjects in clinical trials. Hybrid imaging yields comparable results to traditional organ harvesting with similar statistical variation, yet tends to underestimate single organ absorbed doses slightly compared to organ harvesting. Hybrid imaging also involves fewer resources, radiopharmaceuticals and substantially fewer animals. Additionally, it was shown that the combination of hybrid imaging and segmentation based on spherical VOIs placed in organs leads to more accurate results than laborious organ delineation. The preclinically derived radiation dosimetry for 18 F-FDOPA showed a correlation to literature (human) values of above 0.99 ($p<0.0001$) for all three methods. The effective dose for 18 F-FTYR (not yet available in the literature), was 1.43E−02 mSv/MBq for organ harvesting and 1.42E−02 mSv/MBq for hybrid imaging (based on ICRP 103 tissue weighting factors). Mouse dosimetry showed that the radiation received after an injection of 10 MBq is non-negligible and can reach up to 140 mGy for the total body absorbed dose and several Gy for critical organs.

Acknowledgments. FB is supported by Marie Curie Initial Training Network (MCITN) "Methods in Neuroimaging" under Grant No. #MC-ITN-238593. M.A. Bahri is a "collaborateur logistique" and Alain Plenevaux is a senior research associate from FRS-FNRS Belgium.

Conflict of interest. The authors declare that they have no conflict of interest.

References

1. Lourenco CM, Houle S, Wilson AA, DaSilva JN (2001) Characterization of r-[^{11}C]rolipram for PET imaging of phosphodiesterase-4: *in vivo* binding, metabolism, and dosimetry studies in rats. Nucl Med Biol 28:347–358
2. Harvey J, Firnau G, Garnett ES (1985) Estimation of the radiation dose in man due to 6-[18 F] fluoro-L-dopa. J Nucl Med 26:931–935
3. Lubic SP, Goodwin DA, Meares CF et al (2001) Biodistribution and dosimetry of pretargeted monoclonal antibody 2D12. 5 and Y-Janus-DOTA in BALB/c mice with KHJJ mouse adenocarcinoma. J Nucl Med 42:670–678
4. Rösch F, Herzog H, Stolz B et al (1999) Uptake kinetics of the somatostatin receptor ligand [86 Y] DOTA-d Phe 1-Tyr 3-octreotide ([86 Y] SMT487) using positron emission tomography in non-human primates and calculation of radiation doses of the 90 Y-labelled analogue. Eur J Nucl Med Mol Imaging 26:358–366
5. Tian M, Ogawa K, Wendt R et al (2011) Whole-body biodistribution kinetics, metabolism, and radiation dosimetry estimates of 18 F-PEG6-IPQA in nonhuman primates. J Nucl Med 52:934–941
6. Kurdziel KA, Kiesewetter DO, Carson RE et al (2003) Biodistribution, radiation dose estimates, and *in vivo* Pgp modulation studies of 18 F-paclitaxel in nonhuman primates. J Nucl Med 44:1330–1339
7. Hoffman EJ, Huang SC, Phelps ME (1979) Quantitation in positron emission computed tomography: 1. Effect of object size. J Comput Assist Tomog 3:299–308
8. Kesner AL, Hsueh WA, Czernin J et al (2008) Radiation dose estimates for [18 F] 5-fluorouracil derived from PET-based and tissue-based methods in rats. Mol Imaging Biol 10:341–348

9. Brown WD, Oakes TR, DeJesus OT et al (1998) Fluorine-18-fluoro-L-DOPA dosimetry with carbidopa pretreatment. J Nucl Med 39:1884–1891
10. Segars WP, Tsui BMW, Frey EC et al (2004) Development of a 4-D digital mouse phantom for molecular imaging research. Mol Imaging Biol 6:149–159
11. Mauxion T, Barbet J, Suhard J et al (2013) Improved realism of hybrid mouse models may not be sufficient to generate reference dosimetric data. Med Phys. doi:10.1118/1.4800801
12. Libert L, Franci X, Plenevaux A et al (2013) Production at the Curie level of no-carrier-added 6-^{18}F-fluoro-L-Dopa. J Nucl Med 54:1154–1161
13. Siegel A, Thomas SR, Stubbs JB (1999) MIRD pamphlet no. 16: techniques for quantitative radiopharmaceutical biodistribution data acquisition and analysis for use in human radiation dose estimates. J Nucl Med 40:37S–61S
14. Laforest R, Longford D, Siegel S et al (2007) Performance evaluation of the microPET®—FOCUS-F120. IEEE Trans Nucl Sci 54:42–49
15. Defrise M, Kinahan P, Townsend DW et al (1997) Exact and approximate rebinning algorithms for 3-D PET data. IEEE Trans Med Imaging 16:145–158
16. Bahri MA, Plenevaux A, Warnock G et al (2009) NEMA NU4-2008 image quality performance report for the microPET Focus 120 and for various transmission and reconstruction methods. J Nucl Med 50:1730–1738
17. Feldkamp L, Davis L, Kress J (1984) Practical cone-beam algorithm. Opt Soc Am A Opt Image Sci Vis 1:612–619
18. Kirshner A, Ice R, Beierwaltes W (1975) Radiation dosimetry of 19-iodocholesterol [^{131}I]: the pitfalls of using tissue concentration data (reply). J Nucl Med 16:248–249
19. Eckerman K, Cristy M, Ryman J (1996) The ORNL mathematical phantom series. Oak Ridge National Laboratory, Oak Ridge, TN
20. Stabin MG, Sparks RB, Crowe E (2005) OLINDA/EXM: the second-generation personal computer software for internal dose assessment in nuclear medicine. J Nucl Med 46:1023–1027
21. Cloutier RJ, Smith SA, Watson EE et al (1973) Dose to the fetus from radionuclides in the bladder. Health Phys 25:147–161
22. Protection R (1991) ICRP Publication 60. Annals of ICRP 21:1–3
23. Protection R (2007) ICRP Publication 103. Annals of ICRP 37:2
24. Bretin F, Warnock G, Bahri MA et al (2013) Preclinical radiation dosimetry for the novel SV2A radiotracer [18 F] UCB-H. Eur J Nucl Med Mol Imaging 3:35–42
25. Jan S, Benoit D, Becheva E et al (2011) GATE V6: a major enhancement of the GATE simulation platform enabling modelling of CT and radiotherapy. Phys Med Biol 56:881–901
26. Constantinescu CC, Sevrioukov E, Garcia A et al (2013) Evaluation of [18 F] Mefway Biodistribution and Dosimetry Based on Whole-Body PET Imaging of Mice. Mol Imaging Biol 15:222–229
27. Soret M, Bacharach SL, Buvat I (2007) Partial-volume effect in PET tumor imaging. J Nucl Med 48:932–945
28. Bland JM, Altman DG (1999) Measuring agreement in method comparison studies. Stat Methods Med Res 8:135–160
29. Hsu WL, Chen CL, Wang ZJ et al (2007) Feasibility study of small animal imaging using clinical PET/CT scanner. Nucl Instrum Meth A 571:457–460
30. Warnock G, Turtoi A, Blomme A et al (2013) *In vivo* PET/CT in a human glioblastoma chicken chorioallantoic membrane model: a new tool for oncology and radiotracer development. J Nucl Med 54:1782–1788
31. Taschereau R, Chatziioannou AF (2007) Monte Carlo simulations of absorbed dose in a mouse phantom from 18-fluorine compounds. Med Phys 34:1026–1036

APPENDIX C

Paper III

Absorbed doses to mice for three [^{18}F]-tracers calculated from experimental data and Monte Carlo simulations

Bretin F., Mauxion T., Bahri MA., Luxen A., Plenevaux A., Bardiés M. and Seret A.

Manuscript

Absorbed doses to mice for three [^{18}F]-tracers calculated from experimental kinetic data and Monte Carlo simulations

F. Bretin[1], T. Mauxion[2], M.A. Bahri[1], A. Luxen[1], A. Plenevaux[1], M. Bardiès[2] and A. Seret[1]

[1]University of Liege, Cyclotron Research Centre, Sart Tilman B30, 4000 Liege, Belgium
[2]Inserm UMR 1037 INSERM/UPS, Centre de Recherche en Cancérologie de Toulouse, F-31062 Toulouse, France

Abstract- **In preclinical microPET imaging, small rodents often have to undergo longitudinal studies involving multiple scans combined with microCT imaging to gather anatomical information. The radiation exposure of the animals needs to be addressed since the impact of the radiation might compromise the validity of the results. The aim of the study was to use experimentally obtained kinetic data of three [^{18}F]-tracers and S-values derived by Monte Carlo simulations to calculate absorbed doses in mice and estimate radiation exposure in longitudinal studies.**

The bio-distribution of 6-[^{18}F]fluoro-L-DOPA, 2-[^{18}F]fluoro-L-Tyrosine and [^{18}F]UCB-H was obtained using organ harvesting (OH) at multiple time points, dynamic microPET imaging (DI) and hybrid imaging (HI), where organs are harvested post scan to improve quantification of microPET. Monte Carlo simulations were carried out using GATE v6.1 and the MOBY phantom to determine S-values of multiple source and target organs. Time activity curves were derived from experimental data and residence times for multiple source organs were calculated and used for absorbed dose calculations.

The average total body absorbed dose for all three [^{18}F]-tracers and all methods was almost identical with 14.19 ± 0.10 mGy/MBq. The critical organs for 6-[^{18}F]fluoro-L-DOPA were the kidneys with 23.61 ± 6.34 mGy/MBq for OH and the bladder wall for DI and HM with 660.79 ± 276.57 mGy/MBq and 660.70 ± 276.51 mGy/MBq, respectively. The high derived bladder wall absorbed dose is similar to values provided in literature for bladder wall from [^{18}F]FDG in mice. For 2-[^{18}F]fluoro-L-Tyrosine the highest dose was absorbed by the liver for all three methods with 48.23 ± 8.32 mGy/MBq derived by OH (DI: 46.26 ± 7.35 mGy/MBq; HM: 49.28 ± 9.97 mGy/MBq). For [^{18}F]UCB-H the critical organs were the liver for OH with 65.14 ± 8.47 mGy/MBq and the bladder wall for DI with 57.63 ± 28.36 mGy/MBq.

The calculated absorbed doses derived from the three experimental methods showed good agreement, and correlations between OH and DI were improved by using HI. When assuming multiple injected activities of 10 MBq plus additional radiation from microCT, an accumulated total body absorbed dose of more than 1 Gy and much higher absorbed doses for single organs can be reached possibly introducing stochastic effects. The lethal absorbed dose for a mouse is considered 6 Gy, however, studies have shown that far lower absorbed doses can alter the physiology and compromise results.

Index Terms—**18F-FDOPA, 18F-FTYR, 18F-UCB-H, microPET, mouse dosimetry, quantification, Monte Carlo Simulations**

I. Introduction

In preclinical microPET imaging, small rodents are frequently used as translational models for clinical research, where they have to undergo longitudinal studies involving multiple scans often combined with microCT imaging for anatomical referencing [1-3]. The radiation exposure of animals from each modality needs to be addressed, since multiple studies have shown that even low level exposure might impact on physiological or neurological processes and therefore might compromise the validity of results depending on the type of study [4-7]. A single entrance dose of above 6 Gy is considered lethal to a mouse [8]. However, a study conducted by Detombe et al. found no radiation induced effects on pulmonary or myocardial tissue for a cumulative entrance dose of 5.04 Gy from microCT over six weeks [9]. In general, the biological effects of low-level radiation will vary with the type of radiation, dose delivered, delivery rate, and type of tissue among others [10]. Most studies consider x-ray radiation only regarding biological damage and, especially since the type of radiation, amount and delivery rate differ for microPET, more research needs to be conducted regarding biological damage. In order to quantify the radiation dose from PET imaging, the dynamic biodistribution of the radiopharmaceutical needs to be obtained. Ex vivo measurement of the kinetic data using harvested organs has long been considered the gold-standard technique. Organs are harvested at several time points post administration of the radiopharmaceutical and (for human dosimetry studies) the behaviour of the tracer extrapolated to human data [11-13]. However, organ harvesting is labour intensive and many animals are required to establish the biodistribution. Due to the low time resolution, early blood peaks in organs cannot be detected. Dynamic microPET imaging is a promising technique due to its high time resolution and time efficient procedure. Yet, microPET is prone to partial volume effects (PVE) in small volumes with subsequent quantification errors [14] and hence dosimetry errors. A simple method of correcting for PVE is scaling of the extracted time-activity-curve (TAC). This scaling is based on the ratio between measured activity from PET and the post scan harvested organ activity (measured with a gamma well counter). This method, sometimes referred to as hybrid imaging, was applied in rats by Kesner et al. [15] with a resultant improvement in the correlation between dose estimates (animal data extrapolated

to human data) derived by organ harvesting, imaging and hybrid imaging. PVE and spill-over are size dependent [16] and thus more prevalent in smaller animals (an average mouse weighs approximately ten times less than an average rat). Therefore, the hybrid approach may be of even more value in mice. The aim of this study was to use the experimentally obtained kinetic data of all three methods (organ harvesting, imaging and hybrid imaging) and to calculate the dosimetry in mice using the MOBY phantom [17] and S-factors derived using Monte Carlo Simulations (GATE) [18]. The compounds used in this study were the well-established 6-[^{18}F]fluoro-L-dopa (18F-FDOPA) and 2-[^{18}F]fluoro-L-tyrosine (18F-FTYR), plus the newly developed [^{18}F]UCB-H (18F-UCB-H). The dosimetry results derived by organ harvesting, imaging and hybrid imaging were compared with respect to improvement of quantification of dynamic microPET imaging and to correlation between dosimetry datasets.

II. Materials & Methods

A. Animals

Male C57BL/6 mice were obtained from Charles River Laboratories (Brussels, Belgium) and subsequently bred at the Animal Facility of the GIGA-University of Liege (BE-LA 2610359). All animals were housed under standard 12h:12h light:dark conditions with food and water available ad libitum. All protocols and experimental procedures used in this investigation were reviewed and approved by the Institutional Animal Care and Use Committee of the University of Liege.

B. Radiochemistry

6-[^{18}F]fluoro-L-Dopa was synthesized as described by Libert et al. [19]. 2-[^{18}F]fluoro-L-Tyrosine was prepared using a similar methodology but with 2-formyl-5-methoxy-N,N,N-trimethylbenzenaminium trifluoromethanesulfonate as the starting chemical. The tracers were obtained at the NCA level and therefore with the highest specific activity ever achieved for these tracers (> 540 GBq/µmol). [^{18}F]UCB-H was obtained in a four-step radiosynthesis. Briefly, this consisted of nucleophilic labeling of a pyridine precursor, reductive amination of the labeled product, and internal cyclisation. Specific activity was higher than 500 MBq/µg at the end of synthesis [20].

C. Study protocol

All data acquisition and analysis was performed in accordance to MIRD pamphlet no. 16 [21]. Anaesthesia was induced with 4.5% isoflurane (in oxygen) and maintained after tail vein tracer injection by inhalation of 1-2% isoflurane. After sacrifice by decapitation organs were harvested, weighed (NewClassic ML, Mettler Toledo, Switzerland) and activities were quantified by radioassay using a gamma well counter (Cobra II Auto-Gamma, Perkin-Elmer, USA) resulting in the average activity per g of tissue at each time point.

For 18F-FDOPA, organ harvesting was performed in 30 mice (average weight 23.51 ± 1.75 g) after an average iv bolus of 8.47 ± 1.45 MBq. Five mice per time point were sacrificed by decapitation after 2, 5, 10, 30, 60, and 120 minutes (dissection of: brain, kidney, liver, lung, spleen and testes). Dynamic PET images were acquired for 120 minutes after iv bolus injection of 7.66 ± 1.62 MBq 18F-FDOPA via the tail vein in four separate mice (average bodyweight 22.10 ± 1.21 g). Organs were harvested post scan and activity per gram of tissue was determined as described above.

For 18F-FTYR, dynamic imaging and organ harvesting were performed in the same experiment. 18 mice (average weight 27.63 ± 1.97 g) received 8.08 ± 1.21 MBq and were sacrificed by decapitation after 2, 5, 10, 30, 60 and 120 minutes, with n=3 at each time point (dissection of: brain, kidney, liver, lung, spleen and testes). The three mice to be sacrificed at 120 minutes post injection were also scanned dynamically from injection to sacrifice.

For organ harvesting of 18F-UCB-H, 24 mice (average weight 23.96 ± 1.31 g) were injected with an iv bolus of 6.96 ± 0.81 MBq via the tail vein and were sacrificed by decapitation after 2, 5, 10, 30, 60 and 120 minutes with n=4 at each time point (dissection of: blood, bone, brain, kidney, liver, lung, pancreas, spleen and testes). Dynamic PET images were acquired on 5 mice (average weight 29.72 ± 6.70 g). An average of 9.19 ± 3.40 MBq 18F-UCB-H was administered via the tail vein as bolus. Additionally, an iodine-based contrast agent (1:10 dilution of iobitridol-XENETIX300, Guerbet, Roissy, France) was administered in the peritoneal cavity prior to microCT to aid full organ segmentation. No post scan harvesting was performed for 18F-UCB-H, hence, no hybrid imaging data is available for 18F-UCB-H.

Dynamic microPET images were acquired using a Siemens Concorde Focus 120 microPET (Siemens, Germany) [22] and followed by transmission measurement using the rotating 57Co point source of the scanner. The list-mode data were histogrammed into 3D sinograms using Fourier rebinning [23] and reconstructed using Filtered backprojection (FBP) with a ramp filter cutoff at the Nyquist frequency. Corrections for randoms, dead-time and attenuation were applied but not for scatter, since it was shown that there is no significant improvement by applying the scatter correction for the Focus 120 microPET [24]. A set of 3D images were reconstructed in a 256 x 256 x 95 matrix with a pixel size of 0.4 x 0.4 x 0.8 mm. The dynamic time framing consisted of the following frames: 6x5s, 6x10s, 3x20s, 5x30s, 5x60s, 8x150s, 6x300s, 6x600s and all data were decay corrected to the beginning of each individual frame. Micro-CT images were acquired with an eXplore 120 micro-CT (Gamma Medica, USA / GE Healthcare, UK) to obtain anatomical information for segmentation. All CT images were reconstructed using Feldkamp's Filtered backprojection algorithm [25] with a cut-off at the Nyquist frequency and an isotropic voxel size of 100 µm. In both imaging modalities the MINERVE animal cell bed (Bioscan, USA) was used which provided anaesthesia, physiological control and monitoring of respiration. Micro-CT and microPET images were co-registered using a landmark based approach. Volumes of interest (VOI) were drawn by a single observer (F.B.) on the

micro-CT images using the commercially available research software PMOD (Version 3.306, PMOD Technologies, Switzerland). Spheres of 2 mm radius were placed in organs with sufficient contrast (two VOIs in liver, kidneys and lung, single VOIs otherwise) to decrease the impact of PVE and average activity per volume was derived. MicroPET calibration for conversion of counts/pixel to Bq/ml was performed as recommended by the manufacturer. The accuracy of this calibration has been reported to be better than 2% in our laboratory [24].

For 18F-FDOPA and 18F-FTYR, three different TAC were derived: organ harvesting only (will be referred to as organ harvesting), dynamic PET imaging only (imaging) and hybrid dynamic PET imaging (hybrid imaging), where the activity measured with PET was scaled by a factor derived from the ratio between PET activity at the end of the image acquisition and the quantified post scan activity from harvested organs of the same animal. For 18F-UCB-H organ harvesting and imaging data only is provided.

Organ activities per gram or volume were normalized for injected activity and organ weight or volume, respectively. Organ weights and volumes were taken from the MOBY phantom [17]. For hybrid dynamic PET imaging, the TAC was then scaled as described above. All TACs were interpolated with piecewise cubic Hermite interpolation between time points. In all TACs, physical decay only was assumed after 120 min neglecting any biological clearance from the organs. All numbers of disintegrations in an organ (cumulated activity) were calculated as area under the curve, which is mathematically equal to the residence time, using trapezoidal numerical integration in Matlab.

Since the TACs derived by organ harvesting consist of numerous time points in different animals, every individual time point has its own standard deviation (SD). Hence, the SD of residence times derived by organ harvesting could not be calculated directly and was calculated as follows. Two additional animal TACs were calculated using the mean ± 1SD of each individual time point of the activity measurement and the residence times corresponding to each TAC was computed [20]. This residence time window was expressed as a coefficient of variation in percent (%CV) from the mean value. These residence times (mean ± 1SD) were used to calculate a minimum and maximum absorbed dose for organ harvesting resulting in a best and worst case scenario rather than a real SD. The mean of best and worst case scenario was used as the error for the absorbed dose expressed as %CV of the mean absorbed dose value obtained using the mean TAC. For the statistics of imaging and hybrid imaging every scan was treated separately and mean ± 1SD expressed as %CV were calculated across scans as usual. Correlations between datasets were calculated using Pearson product-moment correlation coefficient in MATLAB.

D. Monte Carlo Simulations

S-factors were derived for the MOBY phantom [17] using GATE v6.1 [26]. The method used to generate the MOBY dataset and S-factors has been previously described [18]. The absorbed doses for organs with derived S-factors and the total body absorbed dose were calculated. Self-radiation could only be accounted for in organs, where the pharmacokinetic data was experimentally determined. Absorbed doses for residual organs were calculated on the basis of cross-radiation from source organs and the remainder only.

III. Results

The biodistribution for both 18F-FDOPA and 18F-FTYR was acquired using organ harvesting, imaging and hybrid imaging, whereas the biodistribution of 18F-UCB-H was acquired using organ harvesting and imaging only. A representative co-registered PET/CT image for each tracer is illustrated in Figure 1. Each CT image was filtered with an isotropic 3D Gaussian kernel of 0.3 x 0.3 x 0.3 mm^3 and the PET image with a 3D Gaussian kernel of 1 x 1 x 2 mm^3. The PET image was averaged over all dynamic frames and scaled from 0 to 1200 kBq/cc.

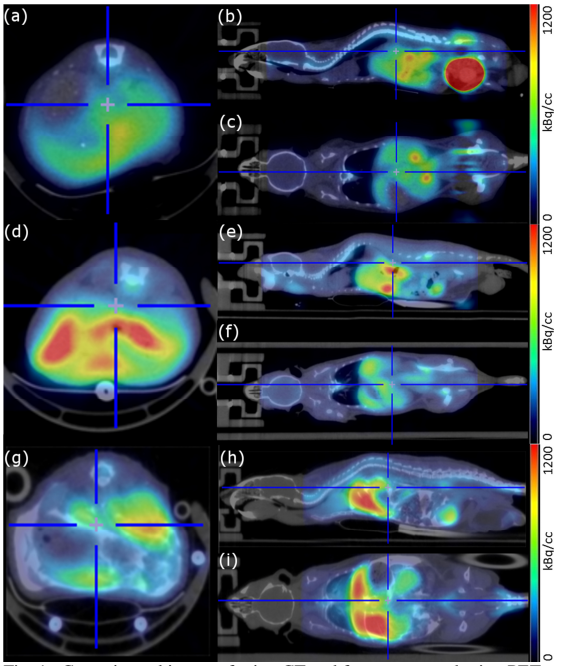

Fig. 1. Co-registered image of microCT and frame-averaged microPET of representative subjects for (a-c) 18F-FDOPA, (d-f) 18F-FTYR and (g-h) 18F-UCB-H with transverse, sagittal and coronal plane each.

Mean TACs, normalized for injected activity and organ weight/size, for all radiopharmaceuticals were calculated for all techniques and are displayed in Figure 2.

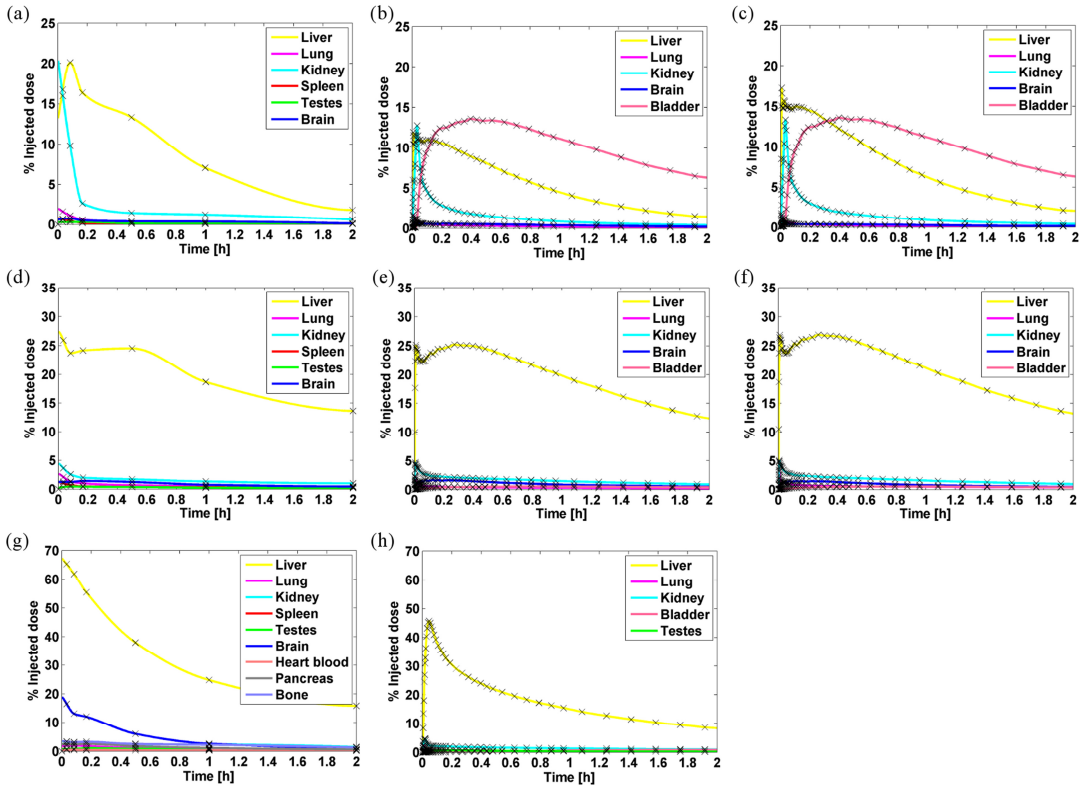

Fig. 2. Mean TACs of (a) 18F-FDOPA Organ harvesting, (b) 18F-FDOPA Imaging, (c) 18F-FDOPA Hybrid Imaging, (d) 18F-FTYR Organ harvesting, (e) 18F-FTYR Imaging, (f) 18F-FTYR Hybrid Imaging, (g) 18F-UCB-H Organ harvesting and (h) 18F-UCB-H Imaging

Residence times based on the TACs for organ harvesting, imaging and hybrid imaging were calculated and are displayed in Table 1 for 18F-FDOPA, Table 2 for 18F-FTYR and Table 3 for 18F-UCB-H. Pearson's product-moment correlation coefficient r and the significance value p for imaging and hybrid imaging to organ harvesting were calculated for the set of residence times obtained with all three approaches.

TABLE I
RESIDENCE TIMES 18F-FDOPA IN h

18F-FDOPA	Organ harvesting	%CV	Imaging	%CV	Hybrid Imaging	%CV
Liver*	2.12E-01	27.6	1.43E-01	7.1	1.98E-01	15.9
Lung*	7.86E-03	13.0	7.90E-03	15.5	5.66E-03	20.9
Kidney*	5.47E-02	31.1	3.81E-02	17.2	3.99E-02	9.5
Spleen	2.66E-03	16.5	-	-	-	-
Bladder	-	-	3.61E-01	36.5	3.61E-01	36.5
Testes	3.16E-03	41.3	-	-	-	-
Brain*	1.03E-02	20.5	1.29E-02	28.0	8.70E-03	26.6
Remainder	2.34E+00	3.4	2.07E+00	5.7	2.02E+00	7.5
Pearson's r	-	-	0.9996	-	0.9985	-
Significance p	-	-	0.0004	-	0.0015	-

* Values used for correlation (derived by all methods)

TABLE II
RESIDENCE TIMES 18F-FTYR IN h

18F-FDOPA	Organ harvesting	%CV	Imaging	%CV	Hybrid Imaging	%CV
Liver*	2.12E-01	27.6	1.43E-01	7.1	1.98E-01	15.9
Lung*	7.86E-03	13.0	7.90E-03	15.5	5.66E-03	20.9
Kidney*	5.47E-02	31.1	3.81E-02	17.2	3.99E-02	9.5
Spleen	2.66E-03	16.5	-	-	-	-
Bladder	-	-	3.61E-01	36.5	3.61E-01	36.5
Testes	3.16E-03	41.3	-	-	-	-
Brain*	1.03E-02	20.5	1.29E-02	28.0	8.70E-03	26.6
Remainder	2.34E+00	3.4	2.07E+00	5.7	2.02E+00	7.5
Pearson's r	-	-	0.9996	-	0.9985	-
Significance p	-	-	0.0004	-	0.0015	-

* Values used for correlation (derived by all methods)

TABLE III
RESIDENCE TIMES 18F-UCB-H IN h

18F-UCB-H	Organ harvesting	%CV	Imaging	%CV
Heart blood	1.27E-02	9.6	-	-
Liver*	9.95E-01	13.5	5.56E-01	6.6
Lung*	3.44E-02	9.3	1.48E-02	14.7
Pancreas	4.30E-02	16.9	-	-
Kidney*	8.26E-02	10.5	5.22E-02	13.3
Spleen	1.06E-02	13.6	-	-
Bladder	-	-	2.94E-02	47.5
Testes*	2.13E-02	12.7	1.32E-02	12.8
Bones	7.71E-02	23.6	-	-
Brain	1.22E-01	18.6	-	-
Remainder	1.23E+00	16.2	1.97E+00	1.7
Pearson's r	-	-	0.9999	-
Significance p	-	-	0.0001	0

* Values used for correlation (derived by all methods)

Mouse absorbed dose estimates for 18F-FDOPA and 18F-FTYR were calculated from organ harvesting, imaging and hybrid imaging and are displayed in Tables 4 and 5. For 18F-UCB-H absorbed dose estimates were only derived by organ harvesting and imaging (Table 6).

TABLE IV
MOUSE ABSORBED DOSES FOR 18F-FDOPA IN mGy/MBq

18F-FDOPA	Organ harvesting	%CV	Imaging	%CV	Hybrid Imaging	%CV
Skin	6.41	2.8	5.79	5.4	5.68	6.9
Heart total	4.74	7.1	3.94	5.6	4.21	3.6
Body	17.64	2.9	16.28	4.4	15.95	6.1
Liver	15.7	23.6	11.08	7.4	14.5	15.3
Gallbladder	6.35	20.2	4.66	6.6	5.85	12.8
Total lung	7.4	7.9	6.72	7.8	6.05	9.3
Stomach total	2.73	4.7	2.33	4.8	2.44	3
Stomach wall	5.99	3.7	5.04	5.7	5.25	3.8
Stomach content	2.18	5.1	1.88	4.4	1.97	2.7
Pancreas	3.6	7.4	3.04	5.5	3.17	3.3
Total kidney	23.61	26.9	17.13	16.9	17.84	9.3
Spleen*	6.27	8.2	2.94	5.2	2.92	5.5
Small intestine total	3.38	0.2	3.28	1.3	3.28	1.5
Small intestine wall	4.37	0.5	4.13	2.5	4.13	2.8
Small intestine content	2.09	0.5	2.15	1.5	2.16	1.6
Large intestine total	4.08	1.1	4.13	0.2	4.09	0.8
Large intestine wall	5.69	1.3	5.55	1.6	5.48	2.5
Large intestine content	2.4	0.5	2.65	3.8	2.64	3.4
Bladder*	4.89	2.9	660.8	41.9	660.7	41.9
Vas deferens*	8.84	2.7	33.19	30.8	33.01	30.6
Testes*	6.67	9.4	5.14	2.3	5.05	1.3
Bones	6.35	2.1	5.71	5.8	5.6	7
Brain	4.13	12.8	4.66	25.1	3.52	21.5
Thyroid	6.47	2.9	5.73	6.5	5.61	8.2
Bone marrow	4.15	1.7	3.78	5.8	3.69	6.7
Total body	14.03	0.2	14.12	0.3	14.14	0.4
Pearson's r	-	-	9.82E-01	-	9.88E-01	-
Significance p	-	-	2.45E-20	-	9.59E-23	-

* Values excluded from correlation, derived by one technique only

For 18F-FDOPA the highest derived absorbed dose from organ harvesting was the kidney with 23.6 ± 6.34 mGy/MBq followed by the remaining body with 17.64 ± 0.52 mGy/Mbq. For imaging and hybrid imaging the highest absorbed dose estimate was for the bladder with 660.79 ± 276.57 (imaging) and 660.70 ± 276.51 (hybrid imaging) mGy/MBq followed by the vas deferens with 33.19 ± 10.24 (imaging) and 33.01 ± 10.11 mGy/MBq (hybrid imaging). The total body absorbed dose was 14.03 ± 0.03 (organ harvesting), 14.12 ± 0.04 (imaging) and 14.14 ± 0.06 mGy/MBq (hybrid imaging). The correlation between dose estimates (after exclusion of values derived by one method only) was

increased from 0.9820 ($p < 0.0001$) to 0.9883 ($p < 0.0001$) by applying hybrid imaging.

TABLE V
MOUSE ABSORBED DOSES FOR 18F-FTYR IN mGy/MBq

18F-FTYR	Organ harvesting	%CV	Imaging	%CV	Hybrid Imaging	%CV
Skin	5.16	10.8	5.25	5.6	5.13	7.1
Heart total	7.71	8.7	7.43	8.7	7.78	11.1
Body	13.95	12	14.22	6.1	13.87	7.8
Liver	48.23	13	46.26	15.9	49.28	20.2
Gallbladder	17.67	12.5	16.98	15	18.03	19.3
Total lung	14.33	8.5	11.07	7.9	13.74	9.3
Stomach total	3.82	6.9	3.6	6.2	3.7	8
Stomach wall	8.17	6.5	7.66	5.5	7.84	7.4
Stomach content	3.09	7.1	2.92	6.5	3	8.2
Pancreas	4.71	14	4.45	6.5	4.57	5.9
Total kidney	23.9	9.6	23.79	14.3	25.02	8
Spleen*	17.65	10.7	3.02	1.4	3.01	3.2
Small intestine total	3.25	1.8	3.27	0.8	3.27	1.1
Small intestine wall	4.13	2.4	4.16	1.2	4.14	1.6
Small intestine content	2.1	0.2	2.11	0.4	2.12	0.3
Large intestine total	3.5	5.6	3.56	3.3	3.51	4.9
Large intestine wall	4.79	6.6	4.87	3.9	4.79	5.7
Large intestine content	2.17	3.5	2.2	2	2.18	3.2
Bladder*	3.84	12.7	37.2	22.6	37.1	22.5
Vas deferens*	7.05	11.3	8.16	5.8	7.97	6.3
Testes*	9.8	8.1	3.82	6.6	3.72	8.4
Bones	5.5	8.4	5.56	3.7	5.47	4.6
Brain	8.8	17.9	9.67	16.3	8.73	23.8
Thyroid	5.19	9.5	5.28	5.8	5.16	7.3
Bone marrow	3.72	8.2	3.77	2.5	3.7	3.5
Total body	14.23	0.4	14.22	0.3	14.24	0.4
Pearson's r	-	-	9.94E-01	-	9.99E-01	-
Significance p	-	-	9.44E-28	-	1.45E-39	-

* Values excluded from correlation, derived by one technique only

For 18F-FTYR the highest absorbed dose derived by organ harvesting was for the liver with 48.23 ± 8.32 mGy/MBq, followed by the kidney with 23.90 ± 1.85 mGy/MBq. For imaging and hybrid imaging the liver was the critical organ as well, with 46.26 ± 7.35 mGy/MBq for imaging and 49.28 ± 9.97 mGy/MBq for hybrid imaging. The second highest radiation was received by the bladder with 37.20 ± 8.40 (imaging) and 37.10 ± 8.33 mGy/MBq (hybrid imaging). The total body absorbed dose was 14.23 ± 0.05 mGy/MBq derived by organ harvesting (Imaging: 14.22 ± 0.05 mGy/MBq / Hybrid imaging 14.24 ± 0.06 mGy/MBq). The correlation between data sets was improved from 0.9943 for imaging to 0.9992 for hybrid imaging (both $p < 0.0001$).

TABLE VI
MOUSE ABSORBED DOSES FOR 18F-UCB-H IN mGy/MBq

18F-UCB-H	Organ harvesting	%CV	Imaging	%CV
Skin	4	10.8	5.58	1.5
Heart total	14.88	8.7	6.67	3.6
Heart tissue	8.99	7.2	5.83	3
Heart blood	16.98	9	6.98	3.7
Body	10.56	12	15.25	1.6
Liver	65.14	13	37.27	6.9
Gallbladder	23.52	12.5	13.85	6.5
Total lung	20.68	8.5	11.25	8.4
Stomach total	4.6	6.9	3.33	2.5
Stomach wall	9.72	6.5	7.14	2.4
Stomach content	3.73	7.1	2.69	2.6
Pancreas	19.49	14	4.17	2.4
Total kidney	34.84	9.6	22.98	12.4
Spleen*	15.23	10.7	3.09	0.8
Small intestine total	3.09	1.8	3.32	0.2
Small intestine wall	3.87	2.4	4.23	0.4
Small intestine content	2.07	0.2	2.12	0.2
Large intestine total	3.1	5.6	3.73	1.2
Large intestine wall	4.14	6.6	5.13	1.2
Large intestine content	2	3.5	2.28	1.1
Bladder*	2.87	12.7	57.63	49.2
Vas deferens*	5.49	11.3	9.89	11.6
Testes*	15.42	8.1	12	9.2
Bones	9.37	8.4	5.66	1
Brain	33.63	17.9	1.25	1.1
Thyroid	4.21	9.5	5.58	1.5
Bone marrow	6.18	8.2	3.66	1
Total body	14.38	0.4	14.17	0.1
Pearson's r	-	-	9.56E-01	-
Significance p	-	-	2.94E-14	-

* Values excluded from correlation, derived by one technique only

For 18F-UCB-H the highest radiation was received by the liver with 65.14 ± 8.47 mGy/MBq derived by organ harvesting and the bladder with 57.63 ± 28.36 mGy/MBq derived by imaging. The second largest absorbed dose for organ

harvesting was the kidney with 34.84 ± 3.34 mGy/MBq and the liver with 37.27 ± 2.59 mGy/MBq for imaging. The total body absorbed dose was 14.38 ± 0.06 mGy/MBq for organ harvesting and 14.17 ± 0.01 mGy/MBq for imaging. The correlation between dose estimates derived by organ harvesting and imaging was 0.9558 ($p < 0.0001$).

IV. Discussion

The biodistribution and mouse radiation dosimetry of 6-[^{18}F]fluoro-L-Dopa, 2-[^{18}F]fluoro-L-Tyrosine were obtained using not only the well-established gold-standard technique of organ harvesting, but also using a conventional imaging technique and the hybrid imaging technique using a cross-calibration between in vivo activities and post scan harvested ex vivo activities. For [^{18}F]UCB-H organ harvesting and conventional imaging data was acquired only. Differences between residence times derived by organ harvesting and conventional imaging were found for all radiopharmaceuticals, most likely resulting from deficiencies in quantification in microPET due to PVE. Constantinescu et al. also reported a poor correlation between post scan harvested organ activities and final microPET measurements [27]. When assuming the organ harvesting residence time to be the reference value, a recovery coefficient defined as the ratio between residence times derived by organ harvesting and imaging can be calculated. These recovery coefficients are shown in Table VII.

TABLE VII
RECOVERY COEFFICIENTS BETWEEN ORGAN HARVESTING AND IMAGING TECHNIQUES

	18F-FDOPA		18F-FTYR		18F-UCB-H	
Organ	Imaging	Hybrid Imaging	Imaging	Hybrid Imaging	Imaging	Hybrid Imaging
Brain	0.80	1.19	0.90	1.01	-	-
Kidney	1.43	1.37	1.00	0.95	1.58	-
Liver	1.48	1.07	1.04	0.98	1.79	-
Lung	0.99	1.39	1.62	1.09	2.33	-

For 18F-FDOPA the hybrid imaging technique improved accuracy of dynamic microPET imaging for the brain, kidney and liver, but slightly decreased it for the lung. For 18F-FTYR, except for the kidney, all derived residence times were improved by applying the hybrid imaging method. Since no post scan harvesting was conducted for 18F-UCB-H, no recovery coefficients for hybrid imaging are available. Additionally, the brain was not in the field of view of the microPET, so no imaging recovery coefficient could be derived for the brain for 18F-UCB-H. All correlation values r (shown in Table I – III) between residence times were above 0.99 (with at least $p < 0.0015$), but were based on four values only. Improved residence time correlations for 18F-FTYR compared to 18F-FDOPA might be an effect of using the same animals for organ harvesting at 120 minutes and dynamic scanning due to a reduction in cross-population differences. The remaining differences between organ harvesting and hybrid imaging for both tracers are most likely a consequence of cross-calibrating activities based only on final microPET measurements. PVE in dynamic microPET imaging is a dynamic problem, since it depends on the activity within the region and the warmth of the background, which changes over time [16]. In other words, early blood peaks, which change conditions between regions, cannot be compensated for using this technique.

When comparing dose estimates derived by the different methods for all three tracers, a high correlation for all estimates (Pearson's $r > 0.95$ with $p < 0.0001$ for imaging; Pearson's $r > 0.98$ with $p < 0.0001$ for hybrid imaging) can be observed. However, since with organ harvesting some residence times could be derived that could not be derived with imaging and vice versa, some dose estimates had to be excluded from the data sets for the computation of the correlation. As the activity accumulation in those organs was significant, the resulting doses were substantially different (highly reducing correlation between datasets) since self-radiation including cross-radiation from other organs was much higher than cross-radiation only. This highlights a limitation of both techniques. Organ harvesting lacks the possibility of quantifying activity of organ contents (i.e. bladder content, stomach content, gallbladder content, blood inside heart chambers), but has the advantage of allowing for the dissection of any organ. However, the technique requires many animals (here at least 18 per tracer) and is time-consuming as well as labour-intensive. Dynamic microPET imaging on the other hand, which requires far fewer animals, allows for the quantification of organ contents (which can be very significant as can be seen for bladder absorbed dose of 18F-FDOPA), but lacks, due to PVE in such small volumes, the accuracy in quantification necessary for dosimetry. The hybrid imaging approach applied here could partially overcome PVE and improved dose estimates derived by imaging. However, due to low in vivo contrast in microCT used to obtain anatomical information for segmentation, fewer organs can be derived from microPET than with organ harvesting. Magnetic resonance imaging (MRI) may offer a useful alternative for improved segmentation. Considering the high degree of correlation achieved and the drawbacks of both techniques, dynamic microPET imaging (with appropriate corrections) is a more ethical and efficient way to obtain equivalent results.

The dosimetry of all three tracers (and all three methods) estimates an average total body dose of approximately 14 mGy/MBq. However, single organ absorbed doses can be much higher depending on the tracer. Especially organs which are part of the urinary excretion pathways (i.e. bladder, kidney and liver) can receive excessive radiation with the urinary bladder wall for 18F-FDOPA being the highest absorbed dose with approx. 660 mGy/MBq (derived by imaging), which is comparable to the urinary bladder wall absorbed dose derived by Taschera u et al. of 543 mGy/MBq from 18F-FDG using a combination of in vivo biodistribution and Monte Carlo Simulations on a voxelized mouse phantom [28].

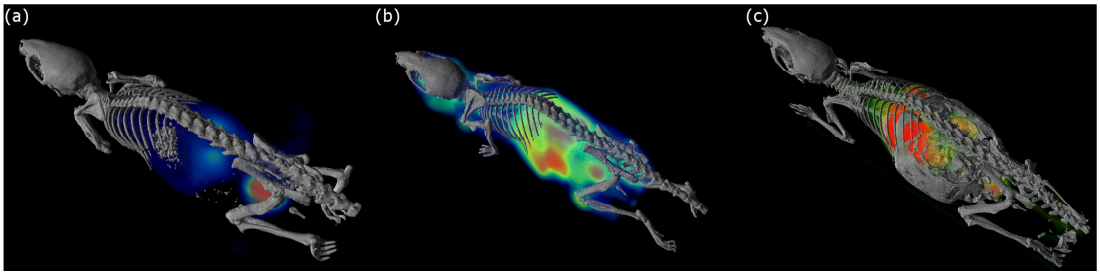

Fig. 3. 3D representation of representative subject's co-registered microCT/microPET images for (a) 18F-FDOPA, (b) 18F-FTYR and (c) 18F-UCB-H. Each CT image was filtered with an isotropic 3D Gaussian kernel of 0.3 x 0.3 x 0.3 mm3 and the PET image with a 3D Gaussian kernel of 1 x 1 x 2 mm3. Threshold based segmentation was performed using the 3D module of PMOD.

For 18F-TYR and 18F-UCB-H the liver was the critical organ with 45 – 50 mGy/MBq and 65 mGy/MBq, respectively.

The 3D representation shown in Fig. 3 also highlights the significant uptake in the critical organs for each tracer in comparison to other organs. When considering an average injection of 10 MBq per scan as routinely done in our institute, single organ absorbed doses can vary between approximately 0.5 Gy up to 6.6 Gy for a single microPET scan, without taking the additional radiation from microCT scanning into account. Delivered doses from microCT highly depend on the machine used and the protocol settings, but can range from several mGy only up to 0.5 Gy per scan [10] further increasing the radiation burden per scan. However, the lethal single entrance total body absorbed dose of 6 Gy [8] will not be exceeded, but organs in the urinary excretion pathways might receive radiations in a range of 1 to 6 Gy. The cumulative organ absorbed doses when assuming longitudinal studies involving several microPET/microCT scans can be much higher depending on the investigated tracer, the injected activity, the number of scans per subject and the used microCT. Nevertheless, investigators should try to keep the radiation burden on animals low by keeping the injected activity as low as possible and using low energy microCT protocols while still obtaining images containing the necessary detail for their study. The use of small animal MRI for anatomical imaging would be beneficial as it would lower the cumulative radiation further. Additionally, using the lowest possible radiation dose reduces the risk of adversely impacting study results.

V. Conclusions

In this study the mouse radiation dosimetry of 18F-FDOPA, 18F-FTYR and 18F-UCB-H was derived using traditional organ harvesting (all tracers), dynamic microPET imaging (all tracers) and hybrid imaging (18F-FDOPA and 18F-FTYR only), where microPET activities are cross-calibrated with post scan harvested organs to improve quantification. Differences in cumulative activity, which can be related to PVE, between organ harvesting and imaging were reduced by using hybrid imaging for most organs and the correlation between dosimetry datasets was improved. Especially, the error in single organ absorbed doses was reduced, which is of great importance in dosimetry to avoid significant over-exposure of subjects. Hybrid imaging yields comparable results to traditional organ harvesting, yet involves substantially fewer animals, less labour and is more time-efficient.

The presented radiation dosimetry of the three 18F-tracers has shown that mice receive a non-negligible amount of radiation with total body absorbed doses of 14 mGy/MBq and single organ absorbed doses ranging from a few mGy/MBq to up to 65 mGy/MBq. Especially urinary bladder wall are critical with an absorbed dose from 18F-FDOPA of 660 mGy/MBq. Assuming single injections of 10 MBq per scan in a longitudinal study setup including additional radiation from microCT scans for anatomical referencing, cumulative total body doses of above 1 - 2 Gy and cumulative single organ absorbed doses between 5 – 10 Gy have to be expected, possibly introducing stochastic effects (depending on number of scans, microCT machine and protocol). Although the amount of radiation will not exceed single entrance lethal limits for mice, studies have shown that far lower doses can alter the physiology. Therefore, keeping the radiation burden on animals as low as possible while still producing the necessary imaging detail should be of concern for any study involving microPET/microCT scans.

Acknowledgment

FB is supported by Marie Curie Initial Training Network (MCITN) "Methods in Neuroimaging" under Grant No. #MC-ITN-238593. M.A. Bahri is a "collaborateur logistique" and Alain Plenevaux is a senior research associate from FRS-FNRS Belgium. TM is supported by the French Ministry of Research as part of the FUI THERANEAN project.

References

1. C. H. Chang, "Longitudinal evaluation of tumor metastasis by an FDG-microPet/microCT dual-imaging modality in a lung carcinoma-bearing mouse model", Anticancer Res., vol. 26, no. 1A, pp. 159-166, Jan. 2006
2. W.K. Hsu, "Characterization of osteolytic, osteoblastic, and mixed lesions in a prostate cancer mouse model using 18F-FDG and 18F-Fluoride PET/CT", J. Nucl. Med., vol. 49, no. 3, pp. 414-421, Mar. 2008
3. C. M. Deroose, "Multimodality imaging of tumor xenografts and metastases in mice with combined small-

animal PET, small-animal CT, and bioluminescence imaging", J. Nucl. Med., vol. 48, no. 2, pp. 295-303, Feb. 2007
4. V. Kersemans, "Micro-CT for anatomic referencing in PET and SPECT: radiation dose, biologic damage, and image quality", J. Nucl. Med., vol. 52, no. 11, pp. 1827-1833, Oct. 2011
5. S. Chen, "Low-dose whole-body irradiation (LD-WBI) changes protein expression of mouse thymocytes: effect of a LD-WBI-enhanced protein RIP10 on cell proliferation and spontaneous or radiation-induced thymocyte apoptosis", Toxicol. Sci., vol. 55, no. 1, pp. 97-106, May. 2000
6. H. Wan, "Effects of low dose radiation on signal transduction of neurons in mouse hypothalamus", Biomed. Environ. Sci., vol. 14, no. 3, pp. 248-255, 2001
7. R. E. J. Mitchel, "Low doses of radiation increase the latency of spontaneous lymphomas and spinal osteosarcomas in cancer-prone, radiation-sensitive trp53 heterozygous mice", Radiat. Res., vol. 159, no. 3 pp. 320-327, Mar. 2003
8. E. L. Ritman, "Micro-computed tomography-current status and developments", Annu. Rev. Biomed. Eng., vol. 6, no. 1, pp. 185-208, Aug. 2004
9. S.A. Detombe, "X-ray dose delivered during a longitudinal micro-CT study has no adverse effect on cardiac and pulmonary tissue in C57BL/6 mice", Acta Radiol., vol. 54, no. 4, pp. 435-441, May 2013
10. S. K. Carlson, "Small animal absorbed radiation dose from serial micro-computed tomography imaging", Mol. Imaging Biol., vol. 9, no. 2, pp. 78-82, Mar. 2007
11. C. M. Lourenco, "Characterization of R-[11C] rolipram for PET imaging of phosphodiesterase-4: in vivo binding, metabolism, and dosimetry studies in rats", Nucl. Med. Biol., vol. 28, no. 4, pp. 347-358, May 2001
12. J. Harvey, "Estimation of the radiation dose in man due to 6-[18F] fluoro-L-dopa." J. Nucl. Med., vol. 26, no. 8, pp. 931-935, 1985
13. S. P. Lubic, "Biodistribution and dosimetry of pretargeted monoclonal antibody 2D12. 5 and Y-Janus-DOTA in BALB/c mice with KHJJ mouse adenocarcinoma", J. Nucl. Med., vol. 42, no. 4, pp. 670-678, April 2001
14. E. J. Hoffman, "Quantitation in positron emission computed tomography: 1. Effect of object size", J. Comput. Assist. Tomog., vol. 3, no. 3, pp. 299-308, June 1979
15. A. L. Kesner, "Radiation Dose Estimates for [18 F] 5-Fluorouracil Derived from PET-Based and Tissue-Based Methods in Rats", Mol. Imaging Biol., vol. 10, no. 6, pp. 341-348, Nov. 2008
16. M. Soret, "Partial-volume effect in PET tumor imaging", J. Nucl. Med., vol. 48, no. 6, pp. 932-945, June 2007
17. W. P. Segars, "Development of a 4-D digital mouse phantom for molecular imaging research", Mol. Imaging Biol., vol. 6, no. 3, pp. 149-159, May 2004
18. T. Mauxion, "Improved realism of hybrid mouse models may not be sufficient to generate reference dosimetric data", Med. Phys., DOI: 10.1118/1.4800801
19. L. Libert, "Production at the Curie Level of No-Carrier-Added 6-18F-Fluoro-L-Dopa", J. Nucl. Med., DOI: 10.2967/jnumed.112.112284
20. F. Bretin, "Preclinical radiation dosimetry for the novel SV2A radiotracer [18F] UCB-H", Eur. J. Nucl. Med. Mol. Imaging, vol. 3, pp.35-42, May 2013
21. A. Siegel, "MIRD pamphlet no. 16: Techniques for quantitative radiopharmaceutical biodistribution data acquisition and analysis for use in human radiation dose estimates", J. Nucl. Med., vol. 40, pp. 37S-61S, April 1998
22. R. Laforest, "Performance evaluation of the microPET®—FOCUS-F120", IEEE. Trans. Nucl. Sci., vol. 54, , no. 1, pp.42-49, Feb. 2007
23. M. Defrise, "Exact and approximate rebinning algorithms for 3-D PET data", IEEE Trans. Med. Imaging, vol. 16, no. 2, pp. 145-158, April 1997
24. M. A. Bahri, "NEMA NU4-2008 image quality performance report for the microPET Focus 120 and for various transmission and reconstruction methods", J. Nucl. Med., vol. 50, no. 10, pp. 1730-1738, Oct. 2009
25. L. Feldkamp, "Practical cone-beam algorithm", Opt. Soc. Am. A. Opt. Image Sci. Vis., vol. 1, no. 6, pp. 612-619, June 1984
26. S. Jan, "GATE V6: a major enhancement of the GATE simulation platform enabling modelling of CT and radiotherapy", Phys. Med. Biol., vol. 56, no. 4, pp. 881-901, Feb. 2011
27. C. C. Constantinescu, "Evaluation of [18F] Mefway Biodistribution and Dosimetry Based on Whole-Body PET Imaging of Mice", Mol. Imaging Biol., vol. 15, no. 2, pp. 222-229, April 2013
28. R. Taschereau, "Monte Carlo simulations of absorbed dose in a mouse phantom from 18-fluorine compounds", Med. Phys., DOI: 10.1118/1.2558115

APPENDIX D

Paper IV

Biodistribution and radiation dosimetry for the novel SV2A radiotracer [^{18}F]UCB-H: First-in-human study

Bretin F., Bahri MA., Bernard C., Warnock G., Aerts J., Mestdagh N., Buchanan T., Otoul C., Koestler F., Mievis F., Giacomelli F., Degueldre C., Hustinx R., Luxen A., Seret A., Plenevaux A.* and Salmon E.*

Manuscript

* Contributed equally

Biodistribution and radiation dosimetry for the novel SV2A radiotracer [^{18}F]UCB-H: First-in-human study

F. Bretin[1], M.A. Bahri[1], C. Bernard[3], G. Warnock[1], J. Aerts[1], N. Mestdagh[2], T. Buchanan[2], C. Otoul[2], F. Koestler[2], F. Mievis[1], F. Giacomelli[1], C. Degueldre[1], R. Hustinx[3], A. Luxen[1], A. Seret[1], A. Plenevaux*[1] and E. Salmon*[1]

[1] - Cyclotron Research Centre, University of Liège, Liège, Belgium

[2] - UCB Pharma, Braine l'Alleud, Belgium

[3] - Nuclear Medicine, CHU, University of Liège, Liège, Belgium

* - These authors contributed equally

Abstract- **[^{18}F]UCB-H is a novel radiotracer with a high affinity for SV2A, a protein expressed in synaptic vesicles. SV2A is the binding site of levetiracetam, a "first in class" antiepileptic drug with a distinct but still poorly understood mechanism of action. The objective of this study was to determine biodistribution and radiation dosimetry in a human clinical trial after injection of [^{18}F]UCB-H and to establish injection limits according to biomedical research guidelines. Additionally, the clinical radiation dosimetry results were compared to estimations in previously published preclinical data. Dynamic whole body PET/CT imaging was performed over approximately 110 minutes on five healthy male volunteers after injection of 144.5 ± 7.1 MBq (range, 139.1 – 156.5 MBq) of [^{18}F]UCB-H. Major organs were delineated on CT images and time-activity curves were obtained from co-registered dynamic PET emission scans. Time-integrated activity coefficients were calculated as area under the curve using trapezoidal numerical integration. A theoretical dynamic bladder model was applied to simulate excretion data and radiation dosimetry was calculated using OLINDA/EXM. The effective dose to the OLINDA/EXM 70 kg standard male was 1.98E-02 ± 1.30E-04 mSv/MBq, with urinary bladder wall, gallbladder wall and the liver receiving the highest absorbed dose. The brain, the tracer's main organ of interest, received an absorbed dose of 1.89E-02 ± 2.66E-03 mGy/MBq. This first human dosimetry study of [^{18}F]UCB-H indicated that the tracer shows similar radiation burdens to widely used common clinical tracers. Single injections of at maximum 321 MBq for USA practice and 505 MBq for European practice keep radiation exposure below recommended limits. Recently published preclinical dosimetry data extrapolated from mice provided satisfactory prediction of total body and effective dose, but showed significant differences in organ absorbed doses compared to human data.**

***Index Terms* — Radiotracer, Human dosimetry, Brain, PET, SV2A, Translational**

I. Introduction

The newly developed radiopharmaceutical [^{18}F]UCB-H shows a nanomolar affinity for the human neuronal synaptic vesicle glycoprotein 2A (SV2A) in the brain. SV2A is critical to proper nervous system function and has been demonstrated to be involved in vesicle trafficking. Levetiracetam, which is a marketed antiepileptic drug, binds to the SV2A protein [1]. However, the specific mechanism of action of this "first in class" drug to treat epilepsy is not yet fully understood [2]. Since [^{18}F]UCB-H targets the SV2A protein in the brain [3], it is a promising candidate for investigating the role of SV2A in central nervous system diseases and to provide a deeper insight into the mechanism of action of levetiracetam.

The intended purpose of this study was to determine in a first clinical trial the whole body distribution of radiation dose following intravenous (iv) injection of [^{18}F]UCB-H in humans and to provide injection limits according to American and European biomedical research guidelines. Additionally, the results of the clinical trial are discussed in relation to the previously reported preclinical radiation dose estimates derived by ex vitro measuring the radioactivity in dissected organs of mice [4].

II. Materials & Methods

A. Subjects and Study design

Five healthy males volunteered to participate in this study. Mean subject characteristics are shown in Table 1. Suitability of subjects for participation in this clinical trial was determined by interview, vital signs and physical examination, clinical blood laboratory tests, 12-lead electrocardiogram and urine drug screening.

TABLE I
SUBJECT CHARACTERISTICS

	Age (y)	Weight (kg)	Height (cm)	BMI (kg/m^2)
Mean	49.5	86.0	180.1	26.4
SD	9.8	15.1	9.4	3.4
Min	42	69	167	22
Max	66	102	190	30

Subjects were males over the age of 65 or over the age of 18 if vasectomised, with a body mass index of 18 to 30 kg/m^2, a height of ≤ 190 cm and vital signs and clinical blood laboratory tests not deviating from any reference ranges. Subjects were excluded if they had previously participated in a study of an investigational medication (or a medical device) within the last 3 months; if they had received any prescription

or over the counter medication within 14 days prior to the study, or had a history of drug abuse within the last 6 months; if they had any medical or psychiatric condition that could compromise the study, or if they had undergone medical imaging involving the application of ionizing radiation in the last 12 months or had such imaging planned in the next 12 months; if they had taken part in any previous research or medical protocol involving radiation (ICRP category IIb: no more than 10 mSv in addition to the natural background radiation in the previous 3 years including the dose from the study [5]);); if they had a family history of cancer (one or more first degree relatives diagnosed before the age of 55 years) or history or presence of any neurological diagnosis. Subjects were furthermore excluded if any medical or surgical condition might alter the metabolism or lead to any risk in regard to the administration of the drug; or if they showed abnormality in 12-lead ECG. The participants were paid to take part in the study, which was approved by the University Hospital Ethic Committee of Liège (Belgium). Subjects provided written informed consent prior to participation. The clinical registration number (EudraCT number) of the study was 2011-003413-42. A single dose microdosing study over a period of 14 days was performed prior to the clinical study in Wistar Han rats using the cold [^{19}F]UCB-H compound. A dose of 0.2 mg/kg was administered as bolus (which is approximately 1000-fold the dose that was administered in humans). No test item treatment-related findings were noted during the study. Therefore, the dose level of 0.2 mg/kg was considered as a "No Observed Effect Level" (NOEL).

B. PET imaging

Data acquisition and analysis were conducted in accordance with MIRD pamphlet no. 16 [6]. Whole body dynamic PET/CT from head to mid-thigh was performed using a Philips GEMINI TF PET/CT (Philips, Amsterdam, Netherlands) [7]. An average of 144.5 ± 7.1 MBq [range, 139.1 - 156.5 MBq] of [^{18}F]UCB-H tracer was injected as iv bolus. Activity remaining in the injection syringe and the attached catheter was quantified and taken into account. The mean and standard deviation of the administered mass of [^{18}F]UCB-H and the specific activity was 0.35 ± 0.18 µg [range, 0.16 – 0.70 µg] and 1022.4 ± 456.6 MBq/µg [range, 410 – 1654 MBq/µg], respectively. The time framing of the dynamic PET scan consisted of six frames with the following duration: 15 s, 30 s, 60 s, 120 s, and twice 180 s. Depending on the height of the subject 11 to 12 bed positions were acquired within each frame, resulting in a total acquisition time of approximately 110 min. All bed positions were decay corrected to the starting time of the individual frame (0.1 min, 5 min, 12 min, 26 min, 66 min, 101 min), which varied slightly from subject to subject due to different amounts of bed positions acquired per frame. The first two subjects were scanned starting at mid-thigh, which was changed to head first for the last three subjects to be able to obtain the peak of the uptake for the upper organs. Prior to the PET scan a whole body spiral CT scan was acquired with 60 – 100 mAs (depending on the subject's weight) for organ segmentation and attenuation correction. All CT images were reconstructed using Feldkamp's Filtered Backprojection [8] with a cut-off at the Nyquist frequency. All PET images were reconstructed using the iterative list mode time-of-flight algorithm [9] and corrections for attenuation, dead-time, random events and scatter were applied. The PET scanner is periodically checked for calibration accuracy as part of quality control according to Belgian rules and has the EARL accreditation [10].

C. Dosimetry analysis

Full organ segmentation was performed by a single observer (FB) on CT images for clearly visible organs (i.e. brain, gallbladder, heart, kidneys, lung, spleen, liver and testes) using PMOD (Version 3.306, PMOD Technologies, Zurich, Switzerland). CT-based volumes of interest (VOI) were used on co-registered PET images to obtain average organ activity per volume in kBq/cc for each frame. Although the bladder was visible in the CT, the volume increase of the organ due to filling with urine throughout the PET emission scan created a misalignment between the location and size of the VOI in CT and PET emission scan. Average activity per volume was applied to organ volumes of the standard 70 kg hermaphroditic phantom [11] implemented in OLINDA/EXM (Version 1.1) [12] and normalized for injected activity. Heart wall and heart blood pool could not be separated in the images due to insufficient contrast and were summarized as heart wall. Time-activity curves (TAC) were linearly interpolated between time points (0.1 min, 5 min, 12 min, 26 min, 66 min, 101 min) and physical decay only was assumed after the last time point up to 10 h post injection. Biological clearance of activity from organs after 2h was neglected assuming the activity was trapped inside the organ. Time-integrated activity coefficients, which are mathematically equal to the number of disintegrations occurring within the source organ, were calculated from these TACs by trapezoidal numerical integration as proposed in literature [6, 13] using MATLAB software version 7.12.0 (Mathworks, Natick, USA). Since CT-based segmentation was not feasible for the urinary bladder and only a limited number of time points were available, urinary excretion scenarios with voiding every 4 h and a biological half-life of 3 h equal to those used in the preclinical study were modeled [4]. Additionally, pre-voiding of subjects was simulated by decreasing the voiding interval to 2 h for the same scenarios. PET-based VOI were created to estimate the activity present in the bladder content (using the 5 highest activity pixel inside the VOI), but were not used for dose calculations due to the limited number of time points and the low accuracy. Activity of organs that could not be clearly delineated was together with all unaccounted for activity assigned to the remainder of the body. The calculated time-integrated activity coefficients were used for dosimetry calculations with OLINDA/EXM software to obtain total absorbed dose and the effective dose based on tissue weighting factors from ICRP publication 60 [14] for the standard 70 kg adult male model. Newer tissue weighting factors exist, which were published in ICRP publication 103 [15], however, they are phantom specific and no appropriate

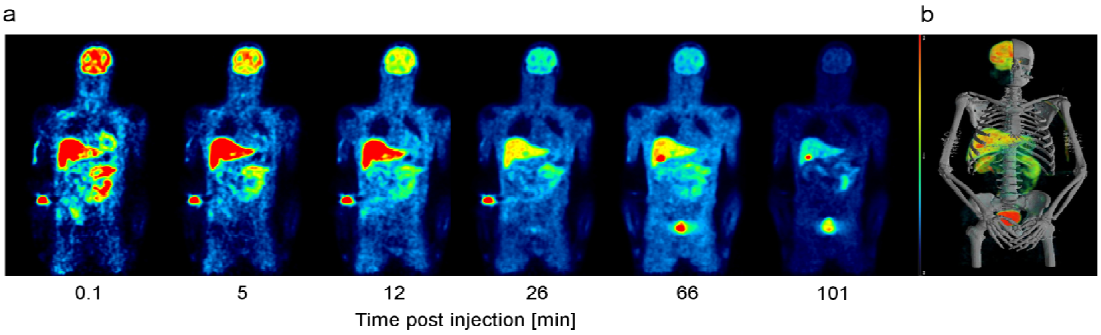

Fig. 2a) Whole body coronal image of representative subject at different time points post administration of [^{18}F]UCB-H (same slice and activity scale, filtered with Gaussian kernel of 8 mm isotropic, injection equipment removed after fourth frame for quantification of remaining activity) and b) 3D representation of PET/CT image averaged over all frames

S-factors for dose calculations are available as of yet [16]. Standard deviations (sample for injected dose, mass of drug and subject statistics; population for time-integrated activity coefficients and doses) across subjects were calculated using Excel (Excel 2010, Microsoft, Redmond, USA) and expressed as coefficients of variation (in percentage) for time-integrated activity coefficients and doses. Minimum and especially maximum values were displayed, since these are of special interest in dosimetry. Correlations between datasets were calculated using Pearson product-moment correlation coefficient in Matlab.

III. Results

The biodistribution over time of [^{18}F]UCB-H was determined for major organs in the five human male volunteers and is presented in percentage of injected activity, normalized to organ volumes of the 70 kg phantom in Fig. 1.

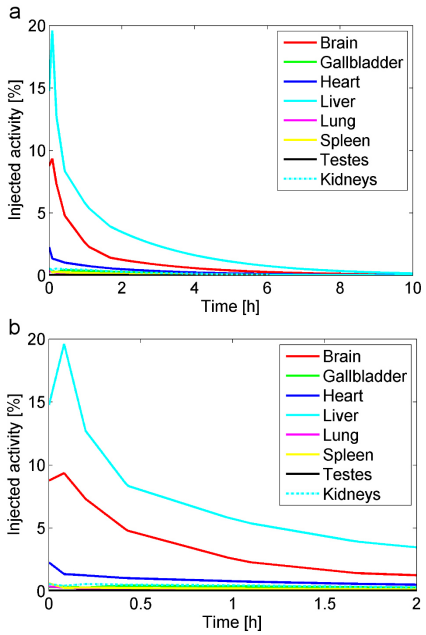

Fig. 1. a) Average interpolated TAC including physical decay in % of injected activity over 10 h b) Zoom on first 2 h

The highest uptake was observed within the liver with an initial value of 19% of injected activity after 5 minutes followed by a rapid washout phase to 3.5% after 2 h. The brain showed an average uptake of 9.4% after 5 min with a washout phase to 1.2% after 2 h. The other significant uptake was in the heart with 2.3% after 1 minute and 0.5% after 2 h. The gallbladder was characterized by a low uptake compared to other organs but showed very slow clearance to increase of activity over the scan duration depending on the subject.

Time-integrated activity coefficients of segmented organs were calculated and are shown in Table 2. The highest number of disintegrations per organ occurred in the bladder with an average time-integrated activity coefficient of 3.08E-01 h (voiding interval of 4 h, excretion fraction of 0.5) followed by the liver (2.28E-01 h) and the brain (1.01E-01 h).

TABLE II
AVERAGE TIME-INTEGRATED ACTIVITY COEFFICIENTS (h)
*derived theoretically

Organ	Mean (n=5)	%CV	Minimum	Maximum
Brain	1.01E-01	16.0	8.25E-02	1.15E-01
Gallbladder	1.37E-02	52.0	4.28E-03	2.22E-02
Heart	2.98E-02	13.5	2.57E-02	3.58E-02
Kidneys	3.21E-02	16.8	2.35E-02	3.61E-02
Lung	5.95E-03	24.4	4.23E-03	7.93E-03
Spleen	7.51E-03	18.8	6.44E-03	9.90E-03
Liver	2.28E-01	10.7	1.93E-01	2.54E-01
Testes	1.28E-03	16.1	1.04E-03	1.47E-03
Bladder*	3.08E-01	0.0	3.08E-01	3.08E-01
Remainder	1.91E+00	2.3	1.86E+00	1.97E+00

Fig. 2a illustrates whole body coronal plane images of a representative subject at different time points post administration of [^{18}F]UCB-H and a 3D representation of the segmented CT image overlaid with the corresponding frame-averaged PET image in Fig. 2b. Half of the skull in the CT images was removed for display purposes. The high initial uptake in the liver and in the brain can be observed as well as the prolonged uptake within the gallbladder.

The average absorbed dose statistics across all subjects are shown in Table 3 including the standard deviation expressed as coefficient of variation (%CV) and the minimum and maximum value obtained. The highest absorbed dose was

received by the urinary bladder wall with 1.56E-01 ± 0.00E+00 mGy/MBq followed by the gallbladder wall with 3.66E-02 ± 1.13E-02 mGy/MBq and the liver with 3.26E-02 ± 3.01E-03 mGy/MBq. The absorbed dose to the brain, which is the tracer's main target of interest, was 1.89E-02 ± 2.07E-04 mGy/MBq. The effective dose calculated using the tissue weighting factors from ICRP publication 60 was 1.98E-02 ± 1.30E-0.4 mSv/MBq.

TABLE III
ABSORBED DOSE ESTIMATES (mGy/MBq) FOR 70KG STANDARD MALE PHANTOM (BLADDER FRACTION 0.5)

Organ	Mean (n=5)	%CV	Minimum	Maximum
Adrenals	1.34E-02	1.6	1.31E-02	1.36E-02
Brain	1.89E-02	14.1	1.59E-02	2.13E-02
Breasts	8.28E-03	1.0	8.21E-03	8.41E-03
Gallbladder Wall	3.66E-02	30.7	2.16E-02	5.00E-02
LLI Wall	1.54E-02	1.5	1.51E-02	1.57E-02
Small Intestine	1.37E-02	1.2	1.35E-02	1.39E-02
Stomach Wall	1.19E-02	0.9	1.18E-02	1.20E-02
ULI Wall	1.35E-02	1.3	1.33E-02	1.37E-02
Heart Wall	2.33E-02	9.6	2.10E-02	2.67E-02
Kidneys	2.67E-02	12.6	2.14E-02	2.93E-02
Liver	3.26E-02	9.2	2.83E-02	3.56E-02
Lungs	7.13E-03	4.6	6.75E-03	7.56E-03
Muscle	1.08E-02	1.1	1.06E-02	1.09E-02
Ovaries	1.55E-02	1.2	1.53E-02	1.58E-02
Pancreas	1.38E-02	1.5	1.35E-02	1.40E-02
Red Marrow	1.03E-02	0.7	1.02E-02	1.04E-02
Osteogenic Cells	1.56E-02	1.5	1.53E-02	1.59E-02
Skin	8.05E-03	1.3	7.93E-03	8.20E-03
Spleen	1.39E-02	10.3	1.28E-02	1.63E-02
Testes	1.30E-02	6.0	1.22E-02	1.38E-02
Thymus	1.03E-02	0.8	1.02E-02	1.04E-02
Thyroid	9.99E-03	1.6	9.83E-03	1.02E-02
Urinary Bladder Wall	1.56E-01	0.0	1.56E-01	1.56E-01
Uterus	2.08E-02	1.1	2.05E-02	2.11E-02
Total Body	1.18E-02	0.0	1.18E-02	1.18E-02
Effective Dose ICRP 60 (mSv/MBq)	1.98E-02	0.7	1.97E-02	2.00E-02

Since the urinary bladder wall data was modeled, different bladder scenarios were implemented to clarify the impact on the bladder dose and the effective dose. Three different fractions of injected activity being cleared via the urinary excretion system were assigned and the absorbed dose for the urinary bladder wall and the effective total body dose are shown in Fig. 3. The urinary bladder wall absorbed dose decreased from 1.56E-01 mGy/MBq to 9.83E-02 mGy/MBq, when reducing the excretion fraction from 0.5 to 0.3. However, the assumption of a urinary excretion fraction of 0.5, meaning that half of the injected activity is cleared via the urinary pathway, is a rather conservative approach and might be an overestimation. By pre-scan hydration of the patient the voiding interval could be decreased to 2 h, which would result in a decreased urinary bladder wall absorbed dose of 9.37E-02 mGy/MBq for an excretion fraction of 0.5 (6.10E-02 mGy/MBq for excretion fraction of 0.3). Activity data derived from PET based segmentation showed that an average of 4.32 ± 1.16 % of injected activity was present inside the urinary bladder across subjects after 110 minutes (data based on 5 hottest pixel applied in kBq/cc to the urinary bladder content of 203 cc of the OLINDA phantom).

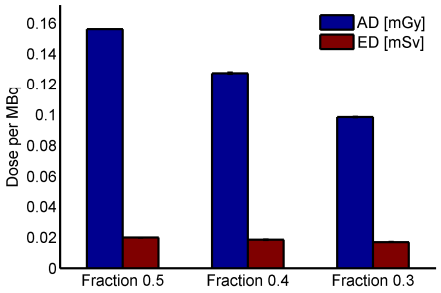

Fig. 3. Impact of assigned excretion fraction on urinary bladder wall dose and effective dose (voiding interval of 4 h); AD = Absorbed dose, ED = Effective dose based on ICRP 60

Regarding the clinical safety assessment, two out of 5 subjects reported treatment-emergent adverse events (viral infection and headache in 1 subject each) a few hours after study drug administration. The Investigator considered the adverse events to be mild in intensity and not to be related to the study drug. Both adverse events resolved and did not lead to premature discontinuation of the study. There were no clinically significant trends in any laboratory, vital sign, or ECG parameters following single iv bolus administration of [^{18}F]UCB-H. There were no clinically relevant increases from baseline in the QTcB or QTcF electrocardiographic interval.

IV. Discussion

This study is the first clinical trial to directly assess the biodistribution and whole body radiation dose given to humans by the compound [^{18}F]UCB-H. The urinary bladder wall, whose dose was derived theoretically, received the highest absorbed dose followed by gallbladder, liver and kidneys. The highest %CV (30.7%) was obtained for the gallbladder, which is a result of different filling states of the organ across subjects. The significant uptake of [^{18}F]UCB-H in the brain shows its potential for investigating the expression of SV2A in the normal or pathological central nervous system. If comparing the effective dose received by the OLINDA/EXM 70 kg adult male phantom to that of one of the most widely used PET tracers [^{18}F]FDG, [^{18}F]UCB-H with 1.98E-02 mSv/MBq stays below the effective dose reported in literature for [18F]FDG, i.e. 2.1E-02 to 2.9E-02 mSv/MBq [17] and below limit recommendations of 10 mSv provided by the ICRP [5]. Additionally, guidelines of the Society of Nuclear Medicine propose for [^{18}F]FDG brain PET scans an

injected activity of 185 – 740 MBq depending on equipment limitations, specific application and patient compliance [18]. Assuming a similar use of [^{18}F]UCB-H in brain PET scans for displacement studies, the high activity reaching the brain suggests that an injected activity of 200 MBq would be sufficient for the purpose of the tracer, which was confirmed by preliminary kinetic modelling studies performed in our lab. Therefore, the absorbed doses of organs as well as the effective dose will stay significantly below those of [^{18}F]FDG for routine use in clinic. The herein used urinary excretion scenario with voiding every 4h and a fraction of 0.5 (0.5 to 0.3 shown in Fig. 3) of total injected activity leaving via urinary excretion pathways within 6h results in an absorbed dose of 1.56E-01 ± 0.00E+00 mGy/MBq to the urinary bladder wall. When comparing this theoretical estimation to derived absorbed doses in humans for [^{18}F]FDG by Deloar et al. [17] using MRI/PET with 3.1E-01 ± 1.9E-01 mGy/MBq (only voiding post scan at approx. 80 min, physical decay assumed after), the radiation dose to the bladder from [^{18}F]UCB-H remains below this value. However, the scenarios are different and whether speed of accumulation and amount of activity excreted via urinary pathways are similar is unknown. The average of 4.32 ± 1.16 % of injected activity present in the urinary bladder suggests that the assumed fraction of 0.5 is a conservative approach. Nonetheless, due to the limited amount of time points available and inaccurate PET based segmentation, the conservative approach should be used for calculating first injection doses in order to avoid over-exposure of patients.

For biomedical research in the USA the Food and Drug Administration (FDA) defined maximum exposures for single injections (SI) and annual total injections (ATI) limiting the dose received by whole body, active blood-forming organs, lens of the eye, and gonads to 30 mSv for single injection and 50 mSv for annual exposure [19]. For other organs the limits are 50 mSv and 150 mSv, respectively. In accordance with these FDA dose limits the maximum single and annual injection dose of [^{18}F]UCB-H is 321 MBq and 962 MBq, respectively, with the urinary bladder being the critical organ. For a urinary excretion fraction of 0.3 (as presented in Fig. 3) the urinary bladder wall remains the dose limiting organ with a maximum injected dose of 508 MBq (SI) and 1525 MBq (ATI).

In Europe different guidelines exist for tracers depending on their societal benefit [5]. [^{18}F]UCB-H is classified as a tracer with moderate societal benefit (Category IIb) due to its potential for "increases in knowledge leading to health benefit". The maximum effective dose for ICRP category IIb is 10 mSv per single injection. This limit would be exceeded based on the ICRP 60 tissue weighting factors for an injection of 505 MBq for a urinary excretion fraction of 0.5 or 592 MBq for an excretion fraction of 0.3.

However, when performing dual modality studies with PET/CT, the CT dose should be considered and the sum of both exposures should be kept as low as possible while still producing diagnostically useful images. When hypothesizing an administered activity of 200 MBq for a brain study, the average effective dose of the PET scan amounts to 3.96 mSv. In a typical brain PET study involving a single head scan for attenuation correction the CT exposure most likely stays below 1 mSv (depending on equipment and protocol), which keeps the total exposure of the patient far below radiation limits.

A. Comparison of preclinical data (derived by organ harvesting in mice) and clinical data

When comparing data derived by organ harvesting in mice [4] and the data derived from this study in humans large differences can be observed in lung, liver and brain regarding time-integrated activity coefficient as shown in Fig. 4. The preclinically determined time-integrated activity coefficient of the lung was overestimated by a factor of 10 compared to the clinical value, that of the liver by a factor of 1.9 and that of the brain by 1.7.

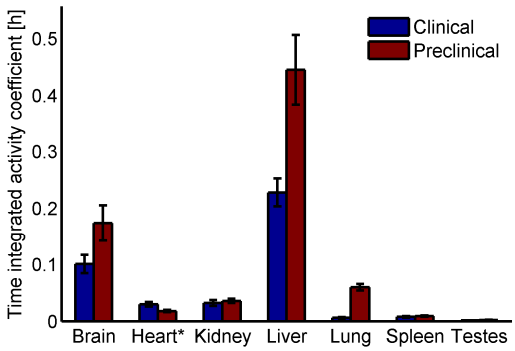

Fig. 4. Comparison of mean animal (organ harvesting in mice) derived time-integrated activity coefficients and mean human derived time-integrated activity coefficients (±SD) (*Heart wall only)

A comparison of the preclinical and clinical dose estimates is presented in Fig. 5. The Pearson's correlation coefficient between the mean animal derived dose estimates and mean human derived dose estimates was 0.969 with p-value ≤ 0.0001 (based on all 27 values).

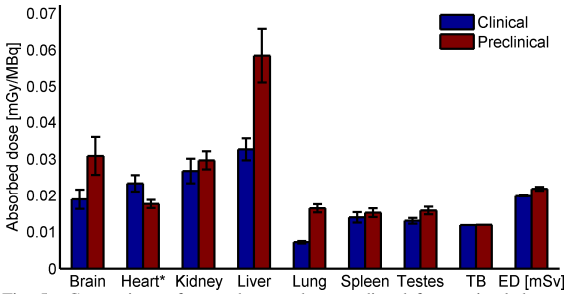

Fig. 5. Comparison of mean human dose predicted from animal data and mean derived human dose (±SD) for major organs (both for 70kg adult standard male, urinary excretion fraction 0.5); TB = total body, ED = Effective dose based in ICRP 60

Several explanations can be given for differences between human data predicted on the basis of animal data and real human data. The most general is the fact that the interspecies

extrapolation method used does not account for differences in metabolism; it is only based on the ratio between organ to body weight in both species. The organs with the largest difference in time-integrated activity coefficients (brain, liver and lung) also have the largest difference in organ to body weight ratio indicating that the assumptions made for interspecies extrapolation after Kirshner [20] should be treated carefully. Moreover, these organs are highly perfused and when considering the activity injected per kg body weight (approx. 285 MBq/kg in mice vs. 2 MBq/kg in humans) it is clear that the activity remaining in the blood is higher in animals increasing the activity in organs. This is not the case for the human heart wall value derived from animal data, because prior to activity quantification with a gamma well counter the blood was removed from the heart chambers of the animals. Additionally, blood content and heart wall could not be separated in the human study leading to a higher value for the heart wall in the human study. Furthermore, the impact of anaesthesia on the animal's metabolism for that specific tracer is unclear and it has been previously shown that e.g. in the case of [^{18}F]FDG the type of anaesthesia can significantly alter the uptake of the tracer in the myocardium in mice [21].

V. Conclusions

The novel radiotracer [^{18}F]UCB-H meets standard criteria with regard to whole body distribution of radiation doses for human application. The maximum single injection dose was determined to be 321 MBq for practice in the USA and 587 MBq in Europe. For both guidelines of biomedical research involving radiopharmaceuticals the urinary bladder wall followed by the liver and the gallbladder were the limiting organs. Due to the high uptake of the tracer in its target organ, the brain, an injection of 200 MBq (effective dose of 3.96 mSv) is considered to be sufficient for brain studies investigating the role of SV2A in central nervous system diseases. Based on this consideration repeated scans in displacement studies are feasible with [^{18}F]UCB-H. Depending on the radiation dose from the attenuation scan and as a function of which research guideline has to be followed, two to three consecutive scans keep radiation exposure below recommended limits.

The comparison of previously published preclinical data derived from organ harvesting in mice for [^{18}F]UCB-H and of human data suggests that, although the effective dose was overestimated by only 10% in animal data, precautions should be taken when using animal data to predict injection limits. Absorbed doses of single organs were significantly different between the studies. However for this tracer, most of the values were overestimated in data derived from animals therefore minimizing the risk of an overexposure in humans in this case.

Acknowledgment

This work was funded by the Walloon Region Public Private Partnership NEUROCOM, with University of Liège and UCB Pharma as partners. F. Bretin is supported by Marie Curie Initial Training Network (MCITN) "Methods in Neuroimaging" under Grant No. #MC-ITN-238593. M.A. Bahri is a "collaborateur logistique" and A. Plenevaux is a senior research associate from FRS-FNRS Belgium.

References

1. B. A. Lynch, "The synaptic vesicle protein SV2A is the binding site for the antiepileptic drug levetiracetam", P. Natl. Acad. Sci. USA, vol. 101, no. 26, pp. 9861-9866, May 2004.
2. . Patsalos, "Pharmacokinetic profile of levetiracetam: toward ideal characteristics", Pharmacol. Therapeut., vol. 85, no. 2, pp. 77-85, Feb. 2000.
3. G. I. Warnock, "Evaluation of 18F-UCB-H as a Novel PET Tracer for Synaptic Vesicle Protein 2A in the Brain", J. Nucl. Med., vol. 55, no. 5, pp. 1336-1341, Aug. 2014.
4. F. Bretin, "Preclinical radiation dosimetry for the novel SV2A radiotracer [18F] UCB-H", Eur. J. Nucl. Med. Mol. I. Res., vol. 3, pp. 35-42, Oct. 2013.
5. A. Verbruggen, "Guideline to regulations for radiopharmaceuticals in early phase clinical trials in the EU," Eur. J. Nucl. Med. Mol. I., vol. 35, no. 11, pp. 2144-2151, Nov. 2008.
6. J. A. Siegel, "MIRD pamphlet no. 16: Techniques for quantitative radiopharmaceutical biodistribution data acquisition and analysis for use in human radiation dose estimates", J. Nucl. Med., vol. 40, pp. 37S-61S, 1999.
7. S. Surti, "Performance of Philips Gemini TF PET/CT scanner with special consideration for its time-of-flight imaging capabilities," J. Nucl. Med., vol. 48, no. 3, pp. 471-480, Mar. 2007.
8. L. Feldkamp, "Practical cone-beam algorithm", J. Opt. Soc. Am. A., vol. 1, no. 6, pp. 612-619, June 1984.
9. W. Wang, "Systematic and distributed time-of-flight list mode PET reconstruction", IEEE Nucl. Sci. Conf. R., vol. 3, pp. 1715-1722, Nov. 2006.
10. R. Boellaard, "EARL FDG-PET/CT accreditation program: Feasibility, overview and results of first 55 successfully accredited sites", Society of Nuclear Medicine Annual Meeting Abstracts, vol. 54, Supplement 2, p. 2052, May 2013.
11. K. Eckerman, "The ORNL mathematical phantom series", Oak Ridge, TN: Oak Ridge National Laboratory, 1996.
12. M. G. Stabin, "OLINDA/EXM: the second-generation personal computer software for internal dose assessment in nuclear medicine", J. Nucl. Med., vol. 46, no. 6, pp. 1023-1027, June 2005.
13. M. G. Stabin, "Fundamentals of Nuclear Medicine Dosimetry", Springer, 2008.
14. International Committee on Radiological Protection, "ICRP Publication 60", Annals of ICPR, vol. 21, 1990.
15. International Committee on Radiological Protection, "ICRP Publication 103", Annals of ICPR, vol. 37, 2007.
16. U. Eberlein, "Biokinetics and dosimetry of commonly used radiopharmaceuticals in diagnostic nuclear medicine–a review", Eur. J. Nucl. Med. Mol. I., vol. 38, no. 12, pp. 2269-2281, Dec. 2011.
17. H. M. Deloar, "Estimation of absorbed dose for 2-[F-18] fluoro-2-deoxy-D-glucose using whole-body positron

emission tomography and magnetic resonance imaging", Eur. J. Nucl. Med. Mol. I., vol. 25, no. 6, pp. 565-574, June 1998.
18. A. D. Waxman, "Society of Nuclear Medicine Procedure Guideline for FDG PET Brain Imaging", Society of Nuclear Medicine, 2009.
19. C. o. F. Regulations, "Drugs for human use, Title 21, Volume 5," in *http://www.accessdata.fda.gov/scripts/cdrh/cfdocs/cfcfr/CFRSearch.cfm?fr=361.1*, FDA, Ed., ed, (Rev. 01/04/12).
20. A. Kirshner, "Radiation dosimetry of 19-iodocholesterol [I31I]: The pitfalls of using tissue concentration data (reply)", J. Nucl. Med., vol. 16, pp. 248-249, 1975.
21. B. J. Fueger, "Impact of animal handling on the results of 18F-FDG PET studies in mice", J. Nucl. Med., vol. 47, no. 6, pp. 999-1006, June 2006.

APPENDIX E

Paper V

Performance evaluation and x-ray dose quantification for various scanning protocols of the GE eXplore 120 micro-CT

Bretin F., Warnock G., Luxen A., Plenevaux A., Seret A. and Bahri MA.

IEEE Transactions on Nuclear Science 5(60):3235-3241, 2013

IEEE TRANSACTIONS ON NUCLEAR SCIENCE, VOL. 60, NO. 5, OCTOBER 2013 3235

Performance Evaluation and X-ray Dose Quantification for Various Scanning Protocols of the GE eXplore 120 Micro-CT

Florian Bretin, Geoffrey Warnock, André Luxen, Alain Plenevaux, Alain Seret, and Mohamed Ali Bahri

***Abstract*—The aim of this paper was to evaluate the performance of the General Electric eXplore 120 micro-CT regarding image quality and delivered dose of several protocols. Image quality (resolution, linearity, uniformity, and geometric accuracy) was assessed using the vmCT phantom developed for the GE eXplore Ultra, the QRM low contrast, and the QRM Bar Pattern Phantom. All dose measurements were performed using a mobileMOSFET dose verification system, and the CTDI_{100} and the multiple-scan average dose (MSAD) were determined with a custom-built PMMA phantom. Additionally, *in vivo* scans in sacrificed rats with different weights were acquired to assess dose, contrast, and resolution variation due to X-ray absorption in surrounding tissue. The spatial resolution was determined as between 95 and 138 μm with a geometric accuracy of 0.1%. The system has a highly linear response to the iodine concentrations (0.937–30 mg/ml) for all protocols. The calculated CTDI_{100} ranged from 20.15 to 56.79 mGy, and the MSAD from 27.98 to 77.45 mGy. The results were confirmed by *in vivo* scans in rats with different weights, and no impact of body weight on delivered dose could be observed. However, body weight had a slight impact on image contrast and resolution.**

***Index Terms*—Dosimetry, performance evaluation, X-ray tomography.**

I. Introduction

MICRO-COMPUTED tomography (micro-CT) is a scaled-down CT-imaging modality for small animals. Increased interest in *in vivo* preclinical imaging has promoted huge technical developments, making micro-CT a useful tool to study tissue morphology and disease status in small animals such as rodents. Most of the current micro-CT scanners provide a set of scanning protocols designed to meet the image quality requirements for particular study types, such as characterization of bone structure and density in osteoporosis and osteoarthritis, study of microvasculature anatomy, and tumor or tissue visualization [1], [2]. These protocols mainly differ in tube voltage and current, exposure time, binning of the detector elements, and the number of projections. In order to reach the high resolution (typically 50–100 μm) needed when imaging small animals, the X-ray dose delivered must be high compared to clinical scanners in order to improve signal-to-noise ratio, which is achieved by increasing the tube current and the exposure time per projection [3]. Since longitudinal studies, often combined with other ionizing imaging modalities like positron emission tomography or single photon emission tomography, are increasingly used in preclinical imaging [4], [5], it is important to quantify the radiation delivered to the animals to rule out any influence of the irradiation on the outcome of the study [6]. A dose of 6 Gy is considered lethal to a mouse [7], however some studies report that even low doses can affect protein expressions [8] and alter signal transduction of neurons in mouse hypothalamus [9]. On the other hand, a study conducted by Detombe *et al.* found no radiation-induced effects on pulmonary or myocardial tissue for a cumulative entrance dose of 5.04 Gy over six weeks [10].

The aim of the present paper was to evaluate the performance of the General Electric (GE) eXplore 120 micro-CT regarding image quality and resulting X-ray dose for various protocols to provide support in choosing the appropriate protocol to meet requirements of a study type. Image quality was assessed using the same methodology and image quality assurance vmCT phantom developed by Du [11] for the GE eXplore Ultra. The Quality Assurance in Radiology and Medicine (QRM) low contrast [12] and Bar Pattern phantoms [13] were also used to assess the contrast and resolution. The dose delivered by the protocols that are used for live animal scans, which were also part of the performance evaluation, was quantified by measuring dose profiles and computing the CT dose index (CTDI), which is routinely used in clinics [14] and has been shown to be a promising parameter for quality assurance and dose assessment in micro-CT [15]. The multiple-scan average dose (MSAD) was computed, and it was, along with the CTDI, compared to experimentally obtained *in vivo* dosimetry data in rats. Weight and size of the rats were varied in order to investigate dose deviations due to body weight. Additionally, the QRM Bar Pattern phantom was used to evaluate resolution degradation due to X-ray absorption in rats with different weights.

II. Materials and Methods

A. Micro-CT

The eXplore CT 120 is the latest generation micro-CT from General Electric (GE Healthcare, Amersham, U.K. /GammaMedica, Northridge, CA, USA). The scanner is

Manuscript received May 23, 2013; revised July 25, 2013; accepted August 08, 2013. Date of publication October 01, 2013; date of current version October 09, 2013. This work was supported by the Marie Curie Initial Training Network (MC-ITN) "Methods in Neuroimaging" under Grant No. MC-ITN-238593.

The authors are with the Cyclotron Research Center, University of Liege, 4000 Liege, Belgium (e-mail: Florian.Bretin@ulg.ac.be; geoffwarnock@gmail.com; aluxen@ulg.ac.be; alain.plenevaux@ulg.ac.be; aseret@ulg.ac.be; M.Bahri@ulg.ac.be).

Color versions of one or more of the figures in this paper are available online at http://ieeexplore.ieee.org.

Digital Object Identifier 10.1109/TNS.2013.2279180

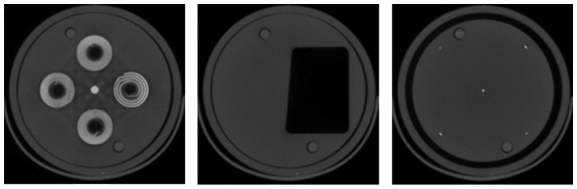

(a) (b) (c)

Fig. 1. Micro-CT images of (a) coil, (b) slanted edge, and (c) geometric accuracy sections.

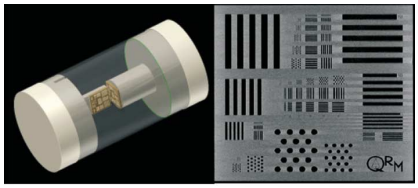

(a) (b)

Fig. 2. QRM Bar Pattern phantom. (a) Full view and (b) structural chip close-up [13].

equipped with a mammography X-ray tube and a CCD detector, fiber-optically coupled to a phosphor screen, designed for high-resolution (80 μm resolution as stated by the manufacturer) and rapid high-contrast scanning in small animals. The X-ray source is a high-power rotating-anode tube with 5 kW peak source power and a focal spot of 300 μm and is able to provide tube voltages between 70–120 kVp with a typical current range from 20 to 50 mA. The only filtration used is the inherent filtration of the tube housing (equivalent to about 1.5 mm Al). The CCD detector consists of 3500×2300 pixel elements covering an active area of 110×75 mm^2. The source and the detector, positioned opposite to each other at a fixed distance of 450 mm, rotate on a gantry around a fixed carbon fiber bed. Two beds were designed to cater for mouse (25 mm width) and rat (75 mm width). The maximum axial field of view (FOV) per rotation is 55 mm with a transaxial length of 85 mm. With overlapping FOVs and stitching of images, a maximum axial scan length of 250 mm can be achieved [16]. The system operates with three different detector binning modes (1×1, 2×2, and 4×4). No scatter or beam hardening correction is implemented for the eXplore 120. Feldkamp's filtered backprojection algorithm [17] is used to reconstruct a 3-D volume image. The image matrix size and the isotropic voxel size (25/50/100 μm) depend on the selected number of FOVs and the binning mode.

B. Phantoms

The design of the vmCT phantom (Fig. 1) and the associated methodology are fully described by Du *et al.* [11] and Bahri *et al.* [16]. Briefly, the vmCT is a single phantom consisting of six separate modular sections (resolution coils, slanted edge, geometric accuracy, CT number evaluation, linearity, and uniformity and noise) each designed to evaluate one aspect of image quality. The sections are held together inside an acrylic tube (inner diameter: 63 mm; outer diameter: 70 mm; length: 54 mm). The phantom fits within the scanners' field of view, allowing all quantitative information to be obtained from a single scan.

The QRM low-contrast phantom is a resin cylinder (diameter: 32 mm; length: 40 mm). It contains small cylindrical inserts (diameters: 1 and 2.5 mm; length: 40 mm) at a specified low contrast with respect to the background. The contrast-to-noise ratio was measured for the four inserts. The QRM Bar Pattern phantom [13], which consists of two silicon chips containing bar and point patterns of 5–150 μm in diameter/line thickness embedded in resin, was used to visually evaluate the spatial resolution and is displayed in Fig. 2 [18].

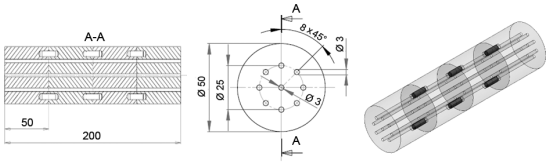

(a) (b) (c)

Fig. 3. PMMA phantom with (a) side view, (b) cut in front view, and (c) isometric view.

TABLE I
PROTOCOL SETTINGS

	Projections (views)	Gantry rotation (°)	Exposure time per projection (ms)	Detector binning mode	Voltage (kV)	Current (mA)	Voxel size (μm)
Fast scan 220 (P1)*	220	192	16	4x4	70	32	100
Fast scan 360 (P2)*	360	360	16	4x4	70	32	100
Soft tissue fast scan (P3)*	220	192	32	2x2	70	50	50
Soft tissue step & shoot (P4)*	220	192	16	4x4	80	32	100
Low Noise (P5)	720	360	20	2x2	100	50	50
In Vivo bone scan (P6)	360	360	20	2x2	100	50	50

*used for dosimetry

For dosimetry measurements, a cylindrical poly(methyl methacrylate) (PMMA; the most widely used material for phantoms in dosimetry for CT [15], [19], [20]) phantom was custom made. It was 200 mm in length with a diameter of 50 mm and had nine longitudinal boreholes with a diameter of 3 mm, of which eight were radially distributed (every 45°) at distances of 12.5 mm around the center hole as can be seen in Fig. 3. The diameter of 50 mm was chosen to represent a standard rat as in the NEMA NU42–2008 rat-like phantom. For ease of manufacturing, the whole phantom was split into 4×50-mm parts, which were connected with two PMMA pins at each interface to prevent any movement as displayed in Fig. 3 [21].

C. Measurements

Six standard scanning protocols regularly used in our laboratory (Table I) were studied using the three image quality phantoms (vmCT and QRM). A set of bright- and dark-field images were collected for each scan to correct for individual detector gain and offset in the raw projection data. Projections were reconstructed into 3-D volume images with a voxel size of $100 \times 100 \times 100$ μm^3. Resolution section data from the vmCT phantom were also reconstructed with a voxel size of $50 \times 50 \times 50$ μm^3 for protocols P3, P5, and P6. These three protocols have a detector-binning mode of 2×2, which allows reconstruction

of the projections at either 50 or 100 μm. The data acquired with the other protocols were recorded with the 4×4 detector-binning mode and could only be reconstructed with the largest voxel size. Data analysis was performed using PMOD software, version 3.3 (PMOD Technologies Ltd., Zurich, Switzerland), and MATLAB software, version 7.7 (http://www.mathworks.com).

1) Spatial Resolution: The spatial resolution was evaluated qualitatively and quantitatively by computing the modulation transfer function (MTF) from the coil and slanted edge section [see Fig. 1(a) and (b)] of the vmCT phantom as described by Du *et al.* [11]. The MTF is calculated for each aluminum coil by the standard deviation (SD) inside regions of interest (ROIs) placed on the coil, which is corrected by the SD inside the uniform region of the phantom, and the mean absolute difference CT values of aluminum and plastic. From averaged slices and therefore a noise reduced image of the slanted edge, an edge spread function (ESF) was generated, which is the integral of the line spread function (LSF). Calculating the modulus of the Fourier transform of the LSF gives the presampled MTF of the detector [16].

2) Geometric Accuracy: In the geometric accuracy section of the vmCT phantom [Fig. 1(c)], four beads were positioned at 35 mm distance in an ideal square, with one additional in the center (24.75 mm from every other). Distance in number of pixels between the centers of the beads was measured, and the true physical pixel size was calculated by dividing the known distance by numbers of pixels. The axial pixel spacing was measured on the image of the geometric accuracy section, removed from the phantom and scanned with its diameter toward the axial direction.

3) Linearity: The linearity of the system was determined by linear regression of the relation between signal intensity and iodine concentration (0.9375, 1.875, 3.75, 7.5, 15, and 30 mg/mL) inside vials placed in the vmCT phantom.

4) CT Number: Measured CT numbers for air and eight different materials (cortical bone-equivalent tissue-mimic, a silicone-based vascular contrast compound, polytetrafluoroethylene, high-density polyethylene, fat-mimicking epoxy resin, muscle-mimicking epoxy resin, polymethyl methacrylate plastic, and water-equivalent epoxy resin) were compared to the protocol specific values provided by the manufacturer. For details on materials, see [11].

5) Uniformity: The variation of the signal intensity and the average SD of a central and four peripheral ROIs in the uniform region of the vmCT phantom was assessed. The uniformity-to-noise ratio was calculated by dividing the average difference in signal intensity from center to periphery and the average SD noise.

6) Dosimetry: All dosimetric measurements [only for protocols used for live animal scans: P1 to P4 (Table I)] were carried out with a mobileMOSFET Dose Verification System (Best Medical Canada, Canada) with standard-sensitivity MOSFET sensors (14 mV/cGy for 40–120 kVp, isotropic response with $\pm 3\%$ over 360°) and calibration factors provided by the manufacturer. At each of the nine transaxial positions of the phantom (Fig. 3), the dose was measured (center $\mathrm{n} = 4$, other $\mathrm{n} = 2$) from -50 to $+50$ mm longitudinally around the center of an axial scan to be able to calculate the CTDI_{100}. Between -50 to -20 mm and 20 to 50 mm, measurements were made every 5 mm, whereas between -20 and 20 mm around the scan center, the dose was measured every 2.5 mm. The phantom remained fixed throughout all measurements on the microCT bed; only the bed was moved in axial direction with respect to the gantry. Using the axial dose profiles obtained, the CTDI_{100} [15] [19] [20] was computed as follows:

$$\mathrm{CTDI}_{100} = \frac{1}{N \cdot T} \sum_{i=-50}^{50} D(i) \tag{1}$$

where $D(i)$ equals the axial dose profile along the scanner axis z. $N \cdot T$ is defined in clinical scanners as the nominal beamwidth at the axis of rotation with N as the number of simultaneously acquired slices and the width of each slice T [15]. The acquired FOV for a single acquisition is 55 mm for the eXplore 120, which was set equal to the nominal beamwidth. The $\mathrm{CTDI}_{100}/\mathrm{mAs}$ was computed based on the central dose profile.

The experimentally acquired center dose profiles were used to construct theoretical dose profiles for multiple field-of-view (mFOV) scans for all protocols. When mFOVs are acquired with the eXplore 120, an overlap of 15 mm exist between each single field of view (sFOV), which is used to stitch images together after reconstruction. Therefore, the first and the last sFOV have an overlap region of 15 mm, and the inner sFOVs a total overlap region of 30 mm. The MSAD was computed for all protocols used for dosimetry, which represents the average dose over one scan interval (I) in the central portion of a multiple-scan (N) dose profile. It was computed from the theoretically constructed mFOV dose profiles $D_N(t)$ as follows [20]:

$$\mathrm{MSAD} = \frac{1}{I} \sum_{t=-I/2}^{+I/2} D_N(t). \tag{2}$$

The center scan interval has a width of 55 mm, and the number of acquired sFOV assumed was five (total scan length of 155 mm) [21]. The dose length product (DLP) was not provided, as it is a more appropriate unit for clinical systems that do not acquire sFOVs with an overlap to obtain an mFOV scan.

D. In Vivo Measurements

To quantify the *in vivo* X-ray dose delivered to animals, the MOSFET sensors were placed in three sacrificed rats of 272, 415, and 610 g body weight. All animals were part of other studies, which were reviewed and approved by the Institutional Animal Care and Use Committee of the University of Liège, Liège, Belgium, and were sacrificed after completion of the studies. The weight was varied to show the variation of the delivered dose due to attenuation inside matter. Four MOSFET sensors were placed inside the skull, chest cavity, abdomen (intestines), and the anal cavity above the testes as illustrated in Fig. 4.

Each location of the sensors was scanned twice as an sFOV in each animal with the four protocols used for the phantom dosimetry scan. For each protocol and each animal, an mFOV

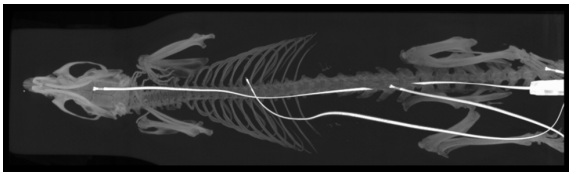

Fig. 4. Maximum intensity projection of exemplary rat including MOSFET sensors.

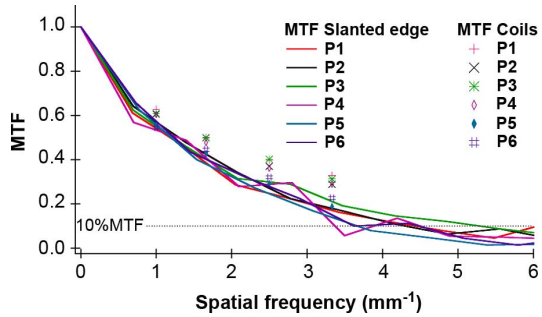

Fig. 5. MTF for all protocols measured from the slanted edge and resolution coil sections. The dotted line represents the 10% MTF.

scan covering all sensors was acquired to assess the increase of dose in mFOV scans. Additionally, after conducting the dosimetry evaluation, the QRM Bar Pattern phantom was inserted into the abdomen of each animal. An sFOV scan was acquired centered on the phantom with the same four protocols to visually inspect the impact of scatter and reduced X-ray transmitted intensity onto the image contrast and resolution *in vivo*.

III. Results

A. Spatial Resolution

The MTF of the system was determined over a frequency range from 0 to 6 mm^{-1} based on the analysis of the reconstructed images of the coil and slanted edge sections for all protocols (Fig. 5). The MTF obtained by the coil method agreed well with the slanted edge results. The 10% MTF for the slanted edge was in the range 3.6–4.8 mm^{-1} (P1 & P2 $= 4.2$; P3 & P4 $= 4.8$; P5 $= 3.6$; and P6 $= 3.8$), corresponding to a spatial resolution between 95 and 138 μm. Due to their size, the coils did not allow assessment of the 10% MTF. The spatial resolution of the system was not measured in the z-direction because the vmCT phantom was not designed for this measurement. The QRM Bar Pattern phantom confirmed the results, as the smallest visible objects were those of 100 μm (the other objects in this phantom have a size above 150 μm or below 50μm).

B. Geometric Accuracy

The nominal pixel spacing both in-plane and axial was within 0.1% of the manufacturer's specification. For protocol-specific nominal pixel spacing, see Table I.

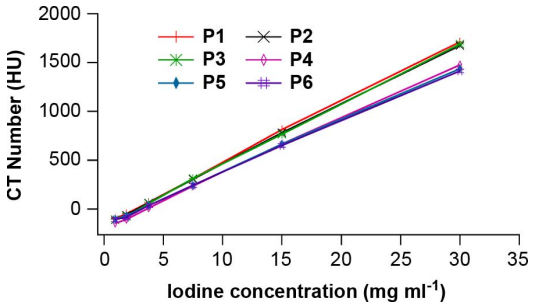

Fig. 6. Plot of the CT number measured in each vial versus the iodine concentration.

TABLE II
Uniformity

	P1	P2	P3	P4	P5	P6
Uniformity to noise ratio	0.5811	0.7658	0.2384	0.7665	0.4501	0.2331

C. Linearity and CT Number

A highly linear relationship between measured CT number and iodine concentration (average $\mathrm{R}^2 = 0.9995 \pm 0.00025$) was observed with a tube voltage dependent slope (Fig. 6). The same behavior was also observed for the CT number evaluation section for measured versus expected CT number with an average $\mathrm{R}^2 = 0.9984 \pm 0.00075$.

D. Uniformity

The central region of the polycarbonate uniformity section always exhibited a lower CT number and a higher noise than peripheral regions. This cupping effect was masked by the noise when the images were reconstructed with the largest voxel size (100 μm) except for protocols designed for low noise (P3, P5, and P6). At 50 μm voxel size, the noise was greatly increased, and the uniformity-to-noise ratio decreased, emphasizing the cupping effect. The uniformity-to-noise ratios for all protocols (from reconstructed images with protocol-specific voxel size) are shown in Table II.

E. Contrast

The contrast-to-noise ratio (CNR) measured with the QRM low-contrast phantom decreased with the diameter and true contrast of the insert (Fig. 7). The best contrast discrimination (highest CNR values) was observed for the P2 and P5 protocols.

F. Dosimetry

Axial dose profiles for all nine transaxial positions were obtained for protocols P1–P4. The dose distribution in x-, y-, and z-direction is displayed in Fig. 8 for P1 and P2. In contrast to the 360° gantry rotation protocol P2, 192° rotation (P1) resulted in a nonhomogeneous dose distribution across transaxial positions.

The CTDI_{100} of all transaxial positions was calculated, and the central position including the transaxial average is shown in

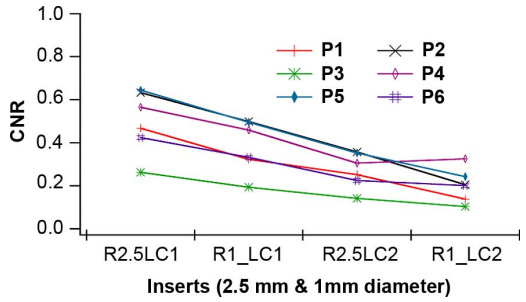

Fig. 7. CNR plots measured for all contrast inserts and for all protocols. (RxLCn: x is the diameter of the insert in millimeters, $n = 1$ for the highest true contrast and $n = 2$ for the lowest true contrast).

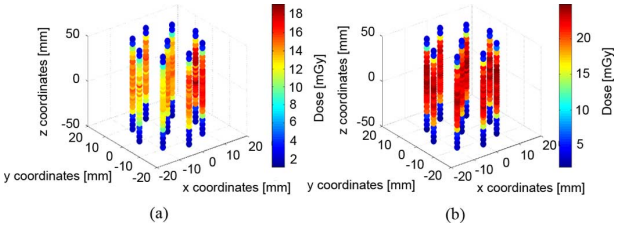

Fig. 8. Spatial dose distributions as measured for (a) P1 and (b) P2.

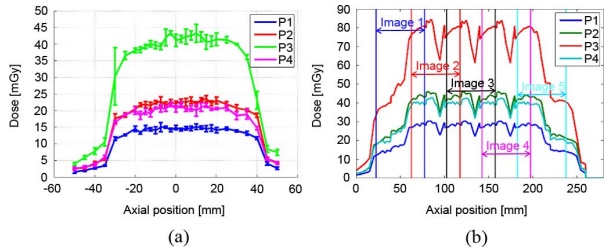

Fig. 9. Dose profiles of (a) transaxial center position and (b) calculated mFOV scan dose profiles of transaxial center position.

TABLE III
CTDI_{100} SUMMARY

	CTDI_{100} center (mGy)	CTDI_{100} transaxial average (mGy)	CTDI_{100}(center)/mAs
P1	20.25 ± 0.14	20.15 ± 1.81	0.1798
P2	30.90 ± 0.38	31.18 ± 0.47	0.1676
P3	55.81 ± 1.41	56.79 ± 4.98	0.1586
P4	28.56 ± 0.25	28.64 ± 3.04	0.2535

Table III. The CTDI_{100} (center) per mAs of the X-ray tube was also calculated for all protocols.

The dose profiles of the transaxial center position for all assessed protocols are shown in Fig. 9(a). Collimation of the beam was observed at -35 to $+45$ mm along the z-axis around the center of the scan.

In Fig. 9(b), the theoretically obtained mFOV scan dose (5 sFOVs) profiles at the center of the dosimetry phantom are displayed. Each image plane is marked by vertical lines and horizontal arrows. Overlap between images for stitching of

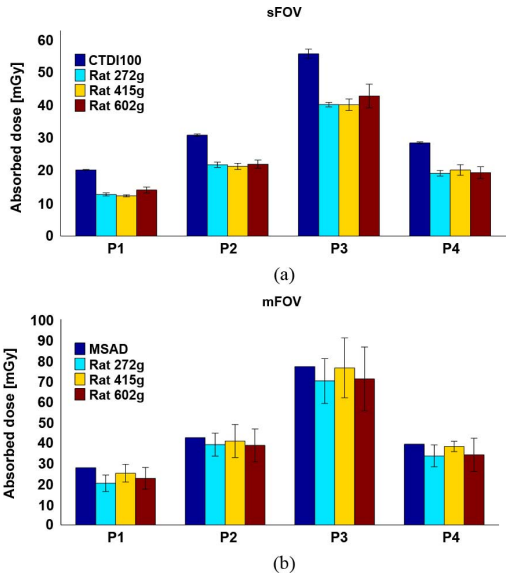

Fig. 10. *In vivo* dose measurement summary for (a) single-field-of-view and (b) multiple-fields-of-view scans; MSAD is a theoretical value, no SD.

TABLE IV
MSAD INCLUDING PEAK VALUE FOR CENTER POSITION IN PMMA PHANTOM

	MSAD (mGy)	Peak value (mGy)
P1	27.98	30.41
P2	42.67	45.95
P3	77.45	84.5
P4	39.47	42.9

reconstructed images was taken into account, and the falling edges outside of the imaging field of view are displayed.

In Table IV, the calculated MSAD of mFOV scans using theoretically obtained mFOV scan dose profiles is shown. Peak values are included for comparison to *in vivo* whole-body scan data in rats.

G. In Vivo Dosimetry

The averaged measured *in vivo* dose for all protocols for sFOV and mFOV scans is shown in Fig. 10. Doses for specific protocols were averaged across sensor position for each rat as the position did not impact significantly on the measured dose. The CTDI_{100} for sFOV measurements and the MSAD for mFOV measurements were added for comparison.

Standard deviations for mFOV measurements proved to be higher due to a less homogenous dose profile along the z-axis. Overbeaming resulted in a difference between CTDI, MSAD, and the respective point *in vivo* measurements.

H. In Vivo Bar Pattern Phantom

In Fig. 11, exemplary *in vivo* images using P2 [Fig. 11(a) and (b)] and P3 [Fig. 11(c) and (d)] are displayed with the QRM Bar Pattern phantom inside the abdomen of rat 1 [Fig. 11(a) and (c)] and rat 3 [Fig. 11(b) and (d)]. For comparison, an image acquired using P3 of the phantom in air is provided [Fig. 11(e)]. When using P2, *in vivo* line structures below 150 μm cannot be resolved independently of the amount

(a) (b) (c) (d) (e)

Fig. 11. *In vivo* bar pattern scan of (a) rat 1 using P2, (b) rat 3 using P2, (c) rat 1 using P3, and (d) rat 3 using P3, and (e) *ex vivo* in air using P3; all images from −500 to 2000 HU.

of attenuating tissue surrounding. In the images acquired with P3, which uses a higher tube current and a longer exposure time, lines with a thickness of 100 μm are visible inside the 200-g-rat scan and point structures with a diameter of 150 μm in both scans. For both protocols, the amount of surrounding tissue influences the contrast between the metal plate and the rest of the phantom and therefore impacts on the calculated X-ray density of the materials.

IV. Discussion

In this study, the vmCT phantom, with related performance tests, and two QRM phantoms were used to evaluate the performance of the eXplore CT 120 scanner for various scanning protocols. Image quality parameters that were evaluated using the vmCT phantom in a single acquisition per protocol included: spatial resolution, geometric accuracy, CT number evaluation, linearity, and uniformity and noise. The results calculated with the slanted edge indicate a 10% of MTF in the range 3.6–4.8 mm^{-1} corresponding to effective spatial resolution between 95 and 138 μm. The QRM Bar Pattern phantom confirmed these results, as the smallest visible objects were those of 100 μm in *ex vivo* scans. The MTF values provided by the coils method at the four spatial frequencies (0.15, 0.2, 0.3, and 0.5 mm) agreed well with the slanted edge, although the values were slightly higher. The sensitivity of the slanted edge method toward the noise and orientation [16] could explain the difference in the MTF values between protocols as well as between methods.

The geometric accuracy of the system in both transaxial and axial directions was evaluated, and the nominal pixel spacing was shown to be within 0.1% for all tested protocols. The eXplore CT 120 demonstrated a highly linear response over the range of iodine solutions used. The same behavior was also observed for the CT evaluation section. The signal uniformity and noise were evaluated for all protocols. A cupping effect was observed, which is masked by noise for protocols with a voxel size of 100 μm. The noise and the uniformity-to-noise ratio were voxel-size (binning mode) dependent. The high level of the noise may also explain the low values of CNR measured with the QRM low-contrast phantom. The implementation of beam-hardening corrections to improve the uniformity of the system over the entire field of view would be a valuable improvement for this system. Du *et al.* [11], who used the vmCT phantom to evaluate the performance of the GE eXplore Ultra (GE Healthcare, London, ON, Canada), reported a 10% MTF of 2.5 line pairs per millimeter (equal to a resolution of 200 μm). The eXplore CT120 demonstrated a better resolution. However, the GE eXplore Ultra showed better results for signal uniformity [11].

The CTDI_{100} was measured using a custom-built PMMA phantom with MOSFET sensors for protocols P1–P4. All calculated CTDI_{100} showed standard deviations below 3%, with the exception of two positions in the P3 for which deviations were higher (8%–11%). This may be attributed to slight positioning errors of the micro-CT bed at the falling edges of the dose profiles. This can be seen in Fig. 9(a) in the P3 data, where deviations are higher on the collimated edges of the beam. Furthermore, it was observed that the collimation of the beam had an offset of 5 mm in the positive z-direction relative to the center of the axial scan. This might be the result of inaccurate calibration of the micro-CT table with respect to the detector. Since the acquired FOV (55 mm) is smaller than the collimated beam (80 mm), large overbeaming takes place, increasing the CTDI_{100} compared to the dose throughout the real beam width [as can be seen in Fig. 10(a)]. The average dose over the full collimated beamwidth can be obtained by multiplying the CTDI_{100}, shown in Table III, with the factor of 0.6875.

The P1–P3 showed a deviation of 8%–9% in the cross-sectional average CTDI_{100}. This is likely due to limitation to 192° rotation, leading to a transaxial gradient in the dose measured as can be seen in Fig. 8(a) where the dose is highest on the lower right side of the phantom. When the CTDI_{100} was analyzed per mAs, a deviation of 5% across 70-kVp protocols was found, with an average of 0.1686 ± 0.009 mGy/mAs.

When comparing the result to different studies using other microCT systems, it shows that the GE eXplore CT 120 delivers a comparably low dose to the animals. Willekens *et al.* [22], who investigated the radiation dose of the Skyscan 1178 (SkyScan, Kontich, Belgium), measured a CTDI_{100} of 6.6 mGy/mAs in a 2.7-cm-diameter water container (at 50 kV, 615 μA and 121 s image acquisition). They derived average organ doses around 400 mGy, which is approximately 10 times higher than using the GE eXplore 120. However, by decreasing resolution, scan time, and number of projections, they achieved a dose of 1.2 mGy/mAs. Hupfer [15], using a TomoScope microCT (CT Imaging GmbH, Erlangen, Germany), reported a CTDI_{100} inside a 32-mm cylindrical phantom of approximately 2.2 mGy/mAs (40 kV, 23 mAs). Kersemans [6], using a Bioscan nanoSPECT/CT, measured a CTDI inside a 60-mm-diameter cylindric PMMA phantom of 7.7 mGy/mAs (35 kV, 50 μA, 400 ms, 180 projections) to 3.7 mGy/mAs (65 kV, 123 μA, 2 s, and 360 projections). When comparing literature values of dose output, it should be noted that the size of the phantom as well as the material have an impact on the measurement. Additionally, the actual mAs used in a protocol should be considered, as it determines the resulting dose received by the scan subject.

Using the experimentally obtained dose profiles inside the center position of the PMMA phantom, the MSAD for the central image plane of a five-fields-of-view scan was theoretically computed. In comparison to an sFOV, the average dose in the center of an mFOV scan using the GE eXplore 120 is approximately doubled with steeply falling edges in the dose profile. The results were confirmed by *in vivo* measurements in three different rats, where sFOV scans centered on sensors in skull, chest, abdomen, and anal cavity were performed including an

mFOV scan with each protocol. Although the weight of the animals varied from 272 to 602 g, little deviation of the sFOV doses could be observed. Standard deviations for mFOV scans were higher due to a less homogenous dose profile as can be seen in Fig. 9(b), which increases the sensitivity of the measurement toward sensor placement across subjects. Due to the large overbeaming when only considering the acquired FOV of 55 mm, the CTDI_{100} and the MSAD predict a higher dose than measured in single-dose point measurements. However, when correcting the CTDI_{100} with the previously provided factor to the whole beamwidth, agreement between sFOV measurements and the CTDI_{100} is satisfactory.

When visually inspecting the *in vivo* scans of the QRM Bar Pattern phantom inserted into the abdomen of rats with different weights, a clear impact of the amount of surrounding tissue and the different protocols can be observed on contrast and resolution. The protocol depositing more energy (P3) could confirm *ex vivo* results and achieve a resolution of approximately 100 μm *in vivo*, whereas low-energy protocols (P1, P2, and P4) only can resolve structures of 150 μm. However, for all low-energy protocols, the images appeared blurred. The amount of surrounding tissue decreased the contrast between the plate inside the phantom and the filling material of the phantom perceivably. Thus, a tradeoff between resolution/contrast and dose delivered must be made when planning experiments. Smaller animals seem to be more suitable for experiments where resolution/contrast is of high importance. However, if high resolution is not necessary and the contrast achieved is sufficient, low-energy protocols should be used for the sake of dose reduction.

In conclusion, the eXplore CT 120 achieved a mean effective spatial resolution in the range 95–138 μm (10% MTF). The system was shown to be linear and geometrically accurate. The major difference between the protocols was the noise level, which limits the detectability of low contrasts. The average dose delivered by the protocols used for *in vivo* imaging ranged from 20.15 to 56.79 mGy for single-field-of-view scans and 27.98 to 77.45 mGy for multiple-fields-of-view scans depending on tube settings. The high dose delivered especially by protocol P3 should be taken into account when planning multimodality scans in a longitudinal setup, where radiation effects might compromise the study. However, doses delivered by the GE eXplore 120 are equal to or lower than doses of other microCT systems reported in the literature.

References

[1] M. J. Paulus, "High resolution X-ray computed tomography: an emerging tool for small animal cancer res," *Neoplasia*, vol. 2, no. 1-2, pp. 62–70, Jan. 2000.

[2] N. M. D. Clerck, "High-resolution X-ray microtomography for the detection of lung tumors in living mice," *Neoplasia*, vol. 6, no. 4, pp. 374–379, Jul. 2004.

[3] N. Ford, "Fundamental image quality limits for microcomputed tomography in small animals," *Med. Phys.*, vol. 30, no. 11, pp. 2869–2877, Oct. 2003.

[4] L. O. T. Gainkam, "Comparison of the biodistribution and tumor targeting of two 99mTc-labeled anti-EGFR nanobodies in mice, using pinhole spect/micro-CT," *J. Nucl. Med.*, vol. 49, no. 5, pp. 788–795, Apr. 2008.

[5] C. H. Chang, "Longitudinal evaluation of tumor metastasis by an FDG-microPet/microCT dual-imaging modality in a lung carcinoma-bearing mouse model," *Anticancer Res.*, vol. 26, no. 1A, pp. 159–166, Jan. 2006.

[6] V. Kersemans, "Micro-CT for anatomic referencing in PET and SPECT: radiation dose, biologic damage, and image quality," *J. Nucl. Med.*, vol. 52, no. 11, pp. 1827–1833, Oct. 2011.

[7] E. L. Ritman, "Micro-computed tomography-current status and develop," *Annu. Rev. Biomed. Eng.*, vol. 6, no. 1, pp. 185–208, Aug. 2004.

[8] S. Chen, "Low-dose whole-body irradiation (LD-WBI) changes protein expression of mouse thymocytes: Effect of a LD-WBI-enhanced protein Rip10 on cell proliferation and spontaneous or radiation-induced thymocyte apoptosis," *Toxicol. Sci.*, vol. 55, no. 1, pp. 97–106, May 2000.

[9] H. Wan, "Effects of low dose radiation on signal transduction of neurons in mouse hypothalamus," *Biomed. Environ. Sci.*, vol. 14, no. 3, pp. 248–255, 2001.

[10] S. A. Detombe, "X-ray dose delivered during a longitudinal micro-CT study has no adverse effect on cardiac and pulmonary tissue in C57BL/6 mice," *Acta Radiol.*, vol. 54, no. 4, pp. 435–441, May 2013.

[11] L. Y. Du, "A quality assurance phantom for the performance evaluation of volumetric micro-CT systems," *Phys. Med. Biol.*, vol. 52, no. 23, pp. 7087–7108, Nov. 2007.

[12] W. Kalender, "Comparative evaluation: Acceptance testing and constancy testing for micro-CT scanners," *Biomed. Tech.*, vol. 50, no. 2, pp. 1192–1193, 2005.

[13] O. Langner, "Bar and point test patterns generated by dry-etching for measurement of high spatial resolution in micro-CT," in *Proc. IFMBE*, 2009, pp. 428–431.

[14] M. M. Rehani, "Managing patient dose in computed tomography," *Ann. ICRP*, vol. 30, no. 4, pp. 7–45, Oct. 2000.

[15] M. Hupfer, "Dosimetry concepts for scanner quality assurance and tissue dose assessment in micro-CT," *Med. Phys.*, vol. 39, no. 2, pp. 658–670, Jan. 2012.

[16] M. A. Bahri, "Performance evaluation of the general electric eXplore ct 120 micro-CT using the vmCT phantom," *Nucl. Instrum. Methods Phys. Res. A*, vol. 648, pp. S181–S185, Aug. 2011.

[17] L. Feldkamp, "Practical cone-beam algorithm," *J. Opt. Soc. Amer. A*, vol. 1, no. 6, pp. 612–619, Jun. 1984.

[18] M. A. Bahri, "Performance evaluation of the GE eXplore CT 120 micro-CT for various scanning protocols," in *Proc. IEEE NSS/MIC*, 2012, pp. 3783–3785, M21-18.

[19] K. Jessen, "Dosimetry for optimisation of patient protection in computed tomography," *Appl. Radiat. Isot.*, vol. 50, no. 1, pp. 165–172, Jan. 1999.

[20] J. A. Bauhs, "CT dosimetry: Comparison of measurement techniques and Devices1," *Radiographics*, vol. 28, no. 1, pp. 245–253, Jan. 2008.

[21] F. Bretin, "X-ray dose quantification for various scanning protocols with the GE eXplore 120 micro-CT," in *Proc. IEEE NSS/MIC*, 2012, pp. 3775–3777.

[22] I. Willekens, "Evaluation of the radiation dose in microCT with optimization of the scan protocol," *Contrast Media Mol. Imag.*, vol. 5, no. 4, pp. 201–207, Jul. 2010.

APPENDIX F

Paper VI

Monte Carlo Simulations of the dose from imaging with GE eXplore 120 micro-CT using GATE

Bretin F., Bahri MA., Luxen A., Phillips C., Plenevaux A. and Seret A.

Manuscript

Monte Carlo simulations of the dose from imaging with GE eXplore 120 micro-CT using GATE

F. Bretin, M.A. Bahri, A. Luxen, C. Phillips, A. Plenevaux, and A. Seret

University of Liege, Cyclotron Research Centre, Sart Tilman B30, 4000 Liege, Belgium

Abstract- **Small animals are increasingly used as translational models in preclinical imaging studies involving microCT in which the subjects can be exposed to significant amounts of radiation. While the radiation levels are generally sublethal, studies have shown that low level radiation can change physiological parameters in mice. In order to rule out any influence of the radiation on the outcome of the experiments, or resulting deterministic effects in the subjects, involved radiation levels need to be addressed. The aim of this study was to investigate the radiation dose delivered by the GE eXplore 120 microCT non-invasively using Monte Carlo simulations in GATE and to compare results to previously obtained experimental values. Tungsten x-ray spectra were simulated at 70, 80 and 100 kVp using an analytical tool and their half-value layers were simulated for spectra validation against experimentally measured values of the real x-ray tube. A Monte Carlo model of the microCT system was set up and four protocols that are regularly applied to live animal scanning were implemented. The CTDI inside a PMMA phantom was derived and multiple field of view acquisitions were simulated using a PMMA phantom, a representative mouse and rat. Simulated half value layers agreed with experimentally obtained results within a 7% error window. The CTDI ranged from 20 to 56 mGy and closely matched experimental values. Derived organ doses in mice reached 459 mGy in bones and up to 200 mGy in soft tissue organs using the highest energy protocol. Dose levels in rats were lower due to the increased mass of the animal compared to mice. Monte Carlo simulations proved a valuable tool to investigate the 3D dose distribution in animals from microCT. Small animals, especially mice due to their small volume, receive significant amounts of radiation from the GE eXplore 120 microCT, which might alter physiological parameters in a longitudinal study setup.**

***Index Terms*—microCT, Monte Carlo Simulations, small animal dosimetry, X-ray quantification**

I. Introduction

Small animal imaging techniques, such as micro Computed Tomogrpahy (microCT) and micro Positron Emission Tomography (microPET), have gained significant importance in preclinical studies, since small animals are increasingly used as translational models for clinical disease and treatment research [1]. Both imaging techniques can deliver, especially in a longitudinal study setup, extensive amounts of radiation. In microPET imaging of mice the injected activity per kg can be 100 times higher than in humans in a clinical setup resulting in far higher absorbed doses in animals [2, 3]. In microCT imaging, since it is used for anatomical referencing or disease staging in longitudinal studies, the needed resolution is typically between 50 – 100 µm. To achieve such a high resolution with an adequate signal-to-noise ratio, the photon flux of the X-ray tube has to be high leading to a significant radiation burden. While the absorbed dose distribution (or the S-factors for calculations of absorbed doses) of several isotopes in small animal microPET imaging have been derived in literature [3-5] and can be applied to every microPET scan, the dose distribution resulting from microCT imaging is machine dependent and needs to be addressed for every machine. Most studies investigate dose point measures in vivo experimentally using TLD chips in or in the vicinity of organs [6-9]. Monte Carlo simulations (MCS) are a valuable tool to quantify the 3D absorbed dose distribution in microCT non-invasively [10, 11], especially in locations or organs that are difficult to assess in vivo accurately due to large sensor geometries. Experimentally, bone doses can only be investigated using surface entrance doses with sensors being placed on top of the bone. With MCS however, it is possible to obtain the spatial dose distribution within the bone. The aim of the study was to simulate the microCT GE eXplore 120 and quantify the computed tomography dose index over 100 mm ($CTDI_{100}$) inside a PMMA phantom and the dose delivered to rats and mice by several protocols that are regularly applied to live animals. The results will be compared to values experimentally obtained in our lab available in literature [12].

II. Materials & Methods

All simulations of the GE eXplore 120 microCT were performed using GATE v6.1 [13]. Since CT imaging and dose calculations involve low energy radiation, the simulations were performed using the low energy Penelope package for physics processes and interaction models (check http://geant4.web.cern.ch/geant4/G4UsersDocuments/UsersGuides/PhysicsReferenceManual/html/node64.html for details and all cross-sections) [14]. The following physical processes were implemented in all performed simulations: Photoelectric effect, Compton scattering, Rayleigh scattering, Electron Ionization, Bremsstrahlung and multiple electron scattering. For details on the implemented GE eXplore 120 microCT the reader is referred to [12, 15], only information relevant to dosimetry simulations will be repeated here. The inbuilt X-ray source of the GE eXplore 120 microCT is a Dunlee PX1483GS (Subdivision of Philips Healthcare, Amsterdam, Netherlands). Its rotating anode is made of tungsten and rhenium and has a focal spot with a diameter of 300 µm. The

tube has a 5 kW peak source power and can provide tube voltages between 70-120 kVp with a tube current range from 20 to 50 mA. Its inherent filtration is equivalent to 1.5 mm Aluminium. The CCD detector of the system is positioned on a rotating gantry opposite of the tube at a fixed distance of 450 mm with a carbon fibre bed designed to cater for mouse (25 mm width) or rats (75 mm width) in the centre of rotation. The maximum axial field of view (FOV) per rotation is 55 mm (85 mm in transaxial direction). Via overlapping FOV's (15 mm on each side of the FOV) and stitching of images the maximum axial field of view can be extended to 250 mm. The axial dose profile (collimation of the X-ray beam) was experimentally determined to have a full width half max (FWHM) of 74.5 mm at the centre of rotation [12].

A. *Simulation geometry*

The X-ray tube was reduced for simplicity to its focal spot and was modelled as a circular disk with a radius of 150 µm. The opening angle of the X-ray beam was determined via trigonometric calculation to be 18.8008° using the experimentally determined FWHM of the axial dose profile (74.5 mm) and the distance of the tube to the centre of rotation (225 mm). A detector was modelled at the distance of 450 mm to the X-ray source. Since no images had to be reconstructed from simulated data and large numbers of small detectors are computationally expensive, the detector was not subdivided and was modelled as a single continuous element for the purpose of verifying spectra only.

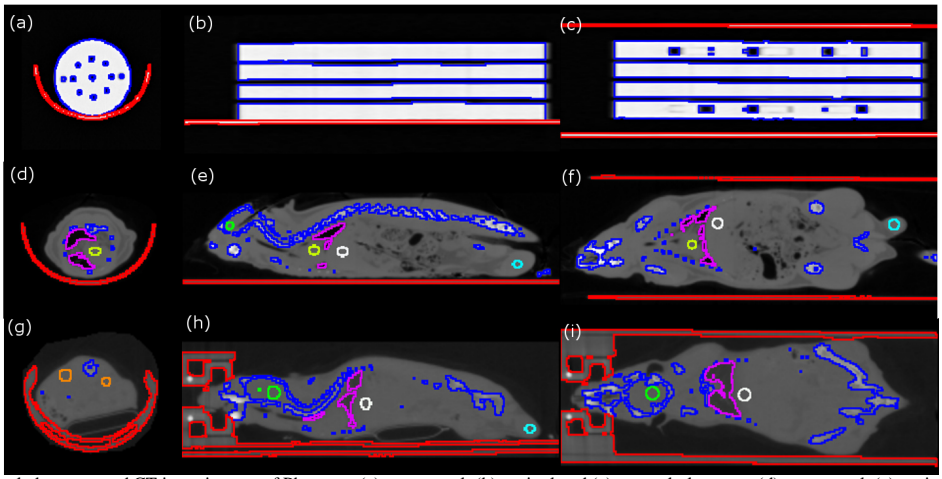

Fig. 1. Down-sampled, segmented CT input images of Phantom: (a) transversal, (b) sagittal and (c) coronal plane; rat: (d) transversal, (e) sagittal and (f) coronal plane; and mouse: (g) transversal, (h) sagittal and (i) coronal plane

B. *X-ray spectra and half-value layer*

For the simulation of the X-ray spectrum at 70, 80 and 100 kVp the spectrum simulator provided by Siemens on their website (https://w9.siemens.com/cms/oemproducts/Home/X-rayToolbox/spektrum/Pages/radIn.aspx) based on an algorithm by Boone et al. [16] was used. The algorithm was developed for Tungsten spectra only between 30 and 140 kV. Input parameters were 70, 80 and 100 kV peak voltages, air kerma of 0.1 Gy and 1.5 mm equivalent Al filtration according to the filtration of the microCT.

In order to validate the spectra, the half value layer (HVL) was simulated and experimentally determined. The HVL represents the thickness of a material reducing the intensity of radiation by absorption and scattering by one half. In radiology it is usually measured using aluminium (Al) for beam quality control purposes. For the determination of the HVL using simulations, a 60 mm x 60 mm box of Al was inserted into the beam path at 60 mm distance to the X-ray source with varying thickness (0 – 6.5 mm, depending on kVp). An ideal single lead detector at a distance of 225 mm with a size of 80 mm x 80 mm x 1 mm was used for stopping and counting photons. For each simulation a total amount of 6E+07 photons were simulated to determine the HVL of spectra at 70, 80 and 100 kVp.

The HVL of the PX1483GS at 70, 80 and 100 kVp was experimentally determined with the X-ray quality control device Black Piranha of RTI Electronics (RTI AB, Mölndal, Sweden). The sensor was placed at the center of rotation of the gantry on the carbon fiber bed with the x-ray tube in stationary top position above the sensor. The tube was triggered with a tube current of 50 mA and an exposure time of 100 ms at the respective tube voltage with 5 measurements per tube voltage setting.

C. *Phantoms*

CT images in Analyze7.5 format were implemented into the rotational centre between source and detector and were rotated instead of the source-detector geometry according to the settings of the simulated protocol, which are displayed in Table 1. The images included the microCT bed as the attenuation inside the bed decreases the amount of X-ray quanta reaching the subject on the table. Three images shown in Figure 1 were used for dose calculations, which were down-sampled for computational speed: the custom build phantom used in [12] (0.7109 mm x 0.7019 mm x 3.1999 mm voxel

size), a representative mouse (0.3996 mm x 0.3996 mm x 0.3996 mm voxel size) and a representative rat (0.7992 mm x 0.7992 mm x 0.7992 mm voxel size). Images were segmented and the ranges of arbitrary pixel values (PV) of segmented structures were related to either existing materials or newly implemented materials in the material database of GATE. Since the soft tissue contrast between organs (apart from lung) in mouse and rat was poor, organs were not fully segmented but spheres were manually placed in the centre of organs. The PV ranges inside the spheres in the respective organ were derived and the spheres were used for dose readouts from the dose maps of the simulations.

TABLE I
PROTOCOL SETTINGS

	Voltage (kV)	Current (mA)	Exposure time (ms)	Projections (Views)	Gantry rotation (°)
Fast scan 220 (P1)	70	32	16	220	192
Fast scan 360 (P2)	70	32	16	360	360
Soft tissue fast scan (P3)	70	50	32	220	192
Soft tissue step & shoot (P4)	80	32	16	220	192

D. *Dose simulations*

Four different acquisition protocols (P1 to P4), which were also experimentally investigated in [12], were implemented and simulated using all three above mentioned phantoms (PMMA, mouse, rat). In the starting position (0° rotation) of each simulation the X-ray source was located in the top position over the various phantoms. The phantoms were then rotated anti-clockwise during the simulation according to protocol settings. A total amount of 6E+07 photons/sec were simulated in each simulation. The output of simulations was a co-registered Analyze7.5 image of the spatial dose distribution with the same size and resolution as the original input CT image. Single field of view (sFOV) acquisitions and multiple fields of view (mFOV) acquisitions were simulated. The mFOV simulations consisted of several independently performed sFOV simulations with the source translated in axial direction according to machine settings of the GE eXplore 120 microCT. The overlap between images of 15 mm on each side used for stitching images together was taken into account. The dose maps of all sFOV building the mFOV acquisition were then added up numerically to one dose map. For the PMMA phantom one sFOV simulation was performed with each protocol and one mFOV consisting of 5 sFOV simulations using P1. Due computer memory issues, the resolution of the image of the PMMA phantom had to be decreased to a voxel size of 1.4218 mm x 1.4218 mm x 3.1999 mm for simulations using P2. For rodent simulations mFOV scans were performed with 3 sFOV for mice and 5 sFOV for rats. Organ doses in mice were derived for all protocols (P1 to P4) and for rat P1 and P3 were used.

E. *Scaling of dose maps and CTDI/MSAD calculation*

Since only a fraction of the real amount of photons emitted by the X-ray source was simulated to decrease simulation time, the resulting dose maps were scaled using experimentally obtained data. Eight axial dose profiles D(i) along the scanner axis z were extracted from the unscaled dose map of the PMMA phantom around the centre hole inside the phantom, which were averaged and then used to compute the CTDI analogue to [12]:

$$CTDI_{100} = \frac{1}{N \cdot T} \sum_{i=-50}^{50} D(i) \tag{1}$$

N · T is usually defined as the nominal beam width, but was set equal to the width of the acquired FOV of 55 mm as in [12]. The dose map was then scaled by the ratio between the computed $CTDI_{sim}$ based on simulated data and the experimentally obtained $CTDI_{exp}$ available in [12] in the same centre position, similar to Taschereau et al. [10]. The obtained scaling factors f_s were applied to all simulations of the respective protocol.

$$f_s = \frac{CTDI_{\exp}}{CDTI_{sim}} \tag{2}$$

For all sFOV simulations of the PMMA phantom the CTDI was computed in 9 transaxial positions as described above. Additionally, the FWHM of all extracted dose profiles was determined. The MSAD of P1 was calculated using the mFOV acquisition dose profile $D_N(t)$as follows:

$$MSAD = \frac{1}{I} \sum_{t=-\frac{I}{2}}^{+\frac{I}{2}} D_N(t) \tag{3}$$

where I equals the width of the central sFOV of 55 mm. Organ and bone doses were derived from the scaled dose maps of mice and rats using the co-registered VOIs of the input images shown in Figure 1.

III. Results

A. *Simulated X-ray spectra*

In Figure 4 the X-ray spectra at 70, 80 and 100 kVp tube voltage simulated using the Siemens X-ray tool are displayed. The spectra were simulated for a pure Tungsten anode, characteristic emission peaks can be observed for 80 and 100 kVp.

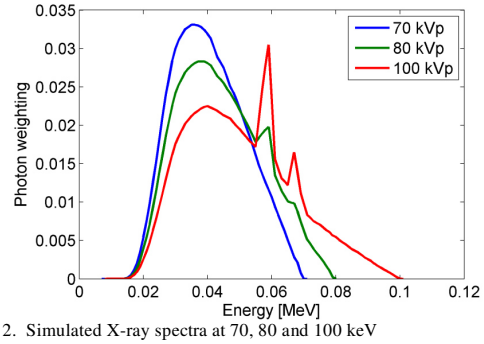

Fig. 2. Simulated X-ray spectra at 70, 80 and 100 keV

B. Half-value layer

The half value layer of the spectra of the x-ray tube PX1483GS was measured experimentally and the results are displayed in Table 2. The tube current and the exposure were kept constant at I = 50 mA and Exp = 100 ms.

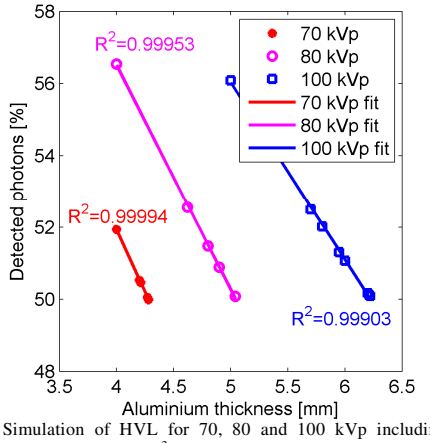

Fig. 3. Simulation of HVL for 70, 80 and 100 kVp including fit and coefficient of determination (R^2)

TABLE II
EXPERIMENTAL MEASUREMENT OF HVL

Tube voltage (kVp)	70	80	100
Measured tube voltage (kVp)	70.60 ± 0.06	79.92 ± 0.07	96.99 ± 0.08
Measured exposure (ms)	93.93 ± 1.50	94.64 ± 0.42	94.84 ± 0.55
Measured dose (mGy)	0.51 ± 0.01	0.73 ± 0.00	1.22 ± 0.01
Measured HVL (mm Al)	4.22 ± 0.02	4.88 ± 0.01	5.80 ± 0.01

The half layer value at 70 kVp was determined by simulation to be 4.28 mm Al, 5.04 mm Al at 80 kVp and 6.22 mm Al at 100 kVp. The simulation of the HVL showed a highly linear relation between the percentage of detected photons of all emitted photons and the thickness of the aluminium box inside the beam path with $R^2 > 0.999$ for all tube voltages (as can be seen in Fig. 3). The differences between experimentally obtained values and simulated values amounted to 1.33% for 70 kVp, 3.21% for 80 kVp and 6.69% for 100 kVp.

C. Dose simulation

In Table 3 the PV of materials inside the phantoms obtained by segmentation of the Analyze7.5 input images are displayed along with the assigned materials of the material database of GATE. PV of all organs (apart from lung) overlapped and were summarized as soft tissue. Bone structures could not be resolved due to the limited resolution of the images and the whole skeleton was summarized as bone. A material definition from the MOBY phantom [17] of lung tissue was assigned to the lung pixel value range of mouse and rat. All other material compositions were taken from the material database of GATE.

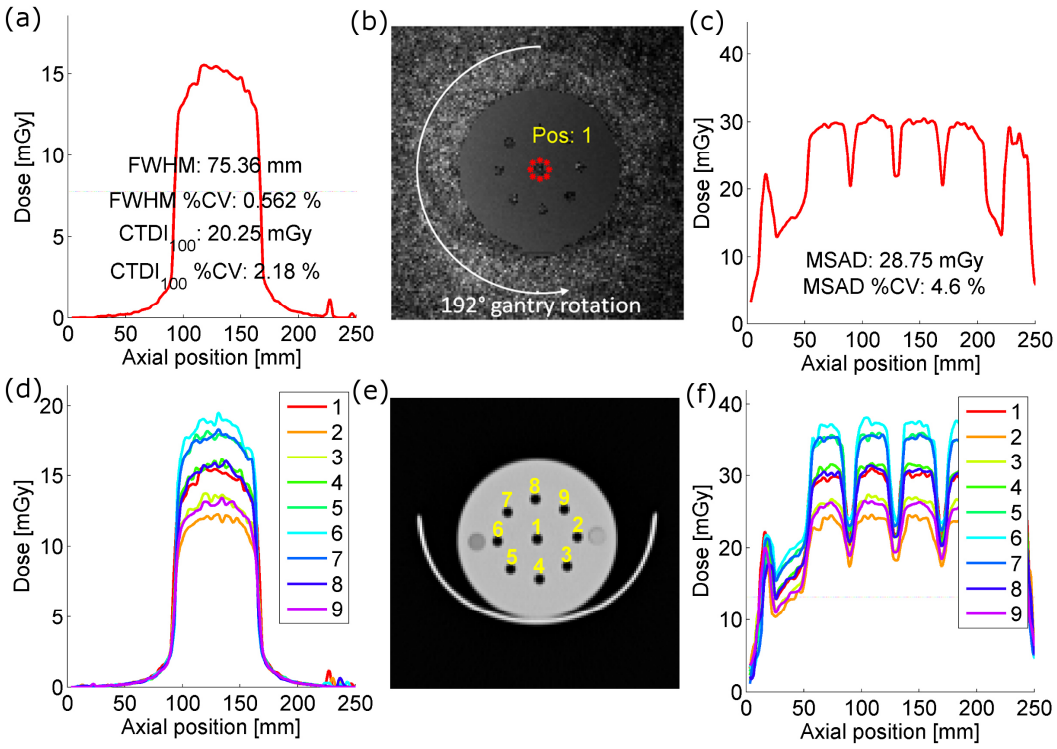

Fig. 4. Simulated average dose profiles of P1 in PMMA phantom with (a) Center position sFOV, (b) simulated dose map including positions for data extraction for centre CTDI calculation, (c) simulated mFOV, (d) all transaxial positions sFOV, (e) CT input image with data extraction locations, (f) all transaxial positions mFOV

TABLE III
PIXEL VALUES OF MATERIALS IN PHANTOMS

	PV PMMA phantom	PV rat phantom	PV mouse phantom	Material*
Air	-32768 to 624	-15750 to -13607	-17579 to -9380	Air
Lung tissue	-	-13607 to -5835	-9380 to -3888	Lung Moby
PMMA	624 to 20295	-	-3888 to -1000	PMMA
Carbon Fiber	20295 to 32768	-5835 to -1712	-	Carbon Fiber
Soft tissue	-	-1712 to 2107	-1000 to 1500	Soft tissue
Bone	-	2107 to 32767	1500 to 32767	Spine bone

*from GATE material database

In Table 4 the scaling factors fs (ratio between experimentally derived $CTDI_{100}$ and the $CTDI_{100}$ obtained from unscaled simulated dose maps), the scaled and averaged $CTDI_{100}$ of the center position including the transaxial average for P1 to P4 are displayed. The averaged MSAD including the transaxial average was only simulated for P1. The highest radiation was delivered by P3, followed by P2. Standard deviation for 192° gantry rotation in the transaxial average $CTDI_{100}$ is increased compared to the 360° rotation protocols.

TABLE IV
SCALING FACTOR, $CTDI_{100}$ AND MSAD DERIVED BY SIMULATION IN PMMA PHANTOM

	P1	P2	P3	P4
Scaling factor f_s	9816.1	12642	13547.8	14228.1
$CTDI_{100}$ center (mGy)	20.25 ± 0.44	30.09 ± 0.29	55.81 ± 0.48	28.56 ± 7.41
$CTDI_{100}$ transaxial (mGy)	20.12 ± 2.59	30.94 0.19	55.58 ± 7.82	28.13 ± 3.71
MSAD center (mGy)	28.75 ± 1.32	-	-	-
MSAD transaxial (mGy)	28.76 ± 4.05	-	-	-

In Figure 4 simulated dose profiles inside the PMMA phantom of P1 are displayed. The $CTDI_{100}$ was determined to be 20.25 ± 0.44 mGy and the MSAD (5 sFOV acquisition) was 28.75 ± 1.32 mGy. Peak dose point value in the mFOV acquisition was 37.9 mGy. Dose profiles in positions on the left side of the phantom (position 4 to 8) showed higher maximum dose values due to the limited 192° anti-clockwise rotation of the gantry for sFOV and mFOV acquisitions.

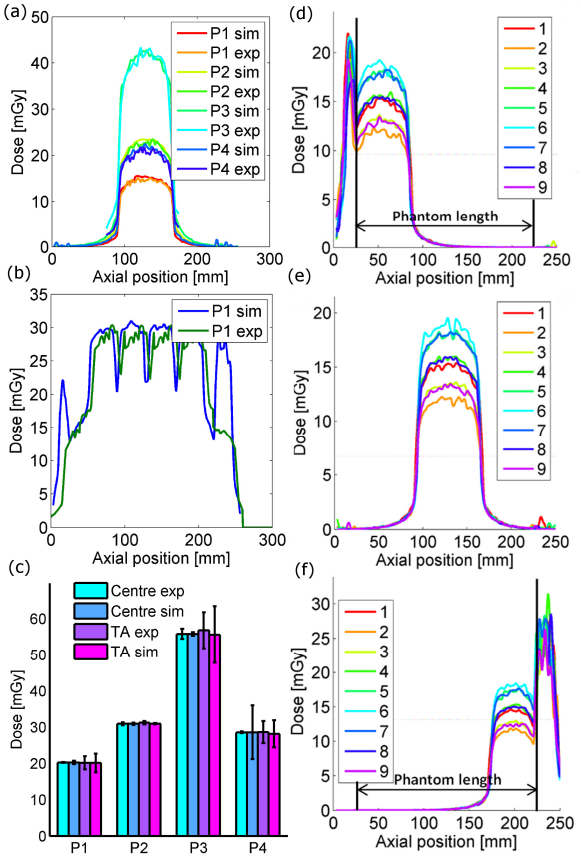

Fig. 5. Experimental (exp) and simulated (sim) data of (a) center position inside PMMA phantom for all protocols and sFOV, (b) mFOV using P1 and (c) CTDI of all protocols for centre position and the transaxial average (TA), – sFOV average dose profiles in transaxial center position inside PMMA phantom extracted from mFOV acquisition of P1 with (d) leftmost acquisition, (e) center acquisition and (f) rightmost acquisition; for positions 1 to 9 see Figure 4e

In Figure 5a and 5b a comparison of sFOV (P1 to P4) and mFOV (P1) dose profiles of the center position inside the PMMA phantom derived experimentally taken from [12] and by simulations is presented. In Figure 5c the $CTDI_{100}$ of all protocols obtained experimentally and by simulations are displayed for the centre position and the transaxial average. All derived values agreed within an error range of 2%. Figure 5d to 5f display dose depositions outside the phantom boundaries in air that were observed in mFOV acquisitions.

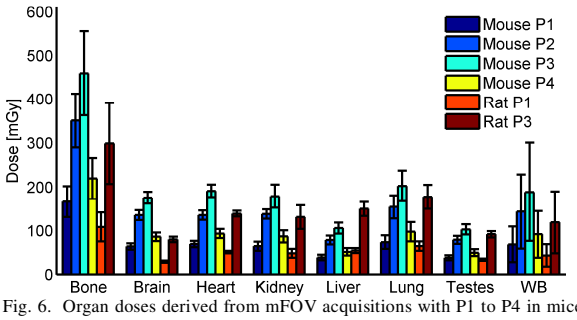

Fig. 6. Organ doses derived from mFOV acquisitions with P1 to P4 in mice (3 sFOV) and with P1and P3 in rats (5 sFOV), WB=whole body

In Figure 6 organ doses including the whole-body dose simulated in the mouse phantom using P1 to P4 and the rat phantom using P1 and P3 are displayed. Analogue to the phantom results, P3 delivered the highest amount of radiation. The largest dose was received by the bones with an average of 459.13 ± 96.37 mGy from P3 in mice (166.37 ± 35.49 mGy from P1, 351.00 ± 61.29 mGy from P2, 219.43 ± 46.49 mGy from P4). The average whole body dose in mice was 188.70 ± 112.05 mGy from P3 (68.39 ± 40.89 mGy P1, 143.80 ± 84.91 mGy from P2, 91.28 ± 53.55 mGy from P4). Doses absorbed by rats are slightly lower compared to mice and the total body dose from P1 was 43.07 ± 25.79 mGy and 118.89 ± 71.09 mGy from P3 (highest dose in bones of 108.20 ± 33.32 mGy for P1 and 298.69 ± 91.87 mGy for P3).

IV. Discussion

In this study we investigated the radiation dose delivered by the GE eXplore 120 microCT using Monte Carlo simulations. X-ray spectra for a tungsten anode were simulated with a publicly available tool provided by Siemens based on an algorithm by Boone et al. [16] and validated with experimental measurements and simulations of the HVL. Although the x-ray source PX1483GS contains tungsten and rhenium and the simulated x-ray spectra at 70, 80 and 100 kVp tube voltage were based on data for tungsten anodes only, the experimentally obtained HVL and simulated data agreed closely. Differences in the HVL of 1.33% at 70 kVp, 3.21% at 80 kVp and 6.69% at 100 kVp could be observed, which is in the range of the inaccuracy of ± 10% or ± 0.2 mmAl provided by the manufacturer of the sensor for 70 and 80 kVp. Yet, the error between experimental data and simulated data increased with tube voltage for two reasons. First, the simulated x-ray spectra are for tungsten anodes only, and the material characteristic peaks in an x-ray spectrum become more apparent at higher tube voltages as can be seen in Figure 2. The peaks characteristic for rhenium are slightly different than for tungsten explaining the larger difference at higher tube voltages. Second, the experimentally measured output tube voltage at 100 kVp was 96.99 ± 0.08 kVp with a sensor inaccuracy of ± 1.5%, while the simulated spectrum was simulated for 100 kVp possibly causing a further mismatch at 100 kVp between experimentally obtained HVL and simulated data. However, since no experimental data for 100 kVp protocols was available, no scaling factor could be derived and consequently the radiation dose at 100 kVp could not be investigated but will be part of future studies.

Deriving pixel value ranges of structures or organs inside the low-contrast microCT images by segmentation proved challenging. Many structures contained similar pixel values and overlapped. All segmented organs apart from the lung had to be summarized as soft tissue inside the image. All bone structures including the bone marrow were assigned the same material composition due to overlapping pixel values and the low resolution of the down-sampled phantoms. The material composition of spine bone, which is implemented in the material database of GATE, was assigned to the whole skeleton, since its density of 1.42 g/cm^3 represented an approximate average of all bone densities implemented in GATE. Analytical phantoms instead of voxelized phantoms, such as the MOBY and ROBY phantom [18], would have enabled to differentiate between more structures, but are commercial products nowadays and were not available to us.

The derived $CTDI_{100}$ values inside the PMMA phantom (see Table IV) confirmed experimentally obtained values available in [12]. Although the center $CTDI_{100}$ could not be different to the experimental value due to scaling of the dose maps to that particular value, the transaxial averages of 192° and 360° rotation protocols agreed as well (see Figure 5c) proving that the simulated dose deposition inside the phantom reflects the measured situation. Standard deviations were slightly higher in the simulated transaxial averages compared to experimental transaxial averages, which could be related to noise originating from simulating only a fraction of the total amount of photons emitted and scaling afterwards. Simulations with the real photon flux of the x-ray tube might improve results due to a higher signal-to-noise ratio; however, long computation times are to be expected. The simulated mFOV dose profile of protocol P1 in the center position of the PMMA phantom matched the experimentally determined dose profile from [12] closely. The experimentally obtained dose profile was derived by measuring a sFOV dose profile using MOSFET sensors inside the PMMA phantom, which was then used to theoretically construct the mFOV dose profile by superposition and shifting of the sFOV dose profile. The agreement between both mFOV dose profiles confirmed the assumptions of the additive nature of the dose profiles inside the homogenous medium and makes phantom measurements and simulations of mFOV acquisitions in phantoms redundant, since the mFOV dose profile can be obtained by simple superposition of sFOV dose profiles. The calculated MSAD based on simulations in the center FOV consequently matched the experimental value within an error range of 5%. It is to be expected, that simulated mFOV acquisitions would produce similarly accurate results for all other protocols due to the very close agreement of sFOV dose profiles of all protocols. The mFOV acquisitions of protocols P2 to P4 were therefore not simulated to save computation time. However, the simulated mFOV dose profile of protocol P1 showed dose deposition peaks on either side of the profile outside of the phantom boundaries in air (see Figure 5b). They originate from the first

and last sFOV acquisition in axial scanner direction (translation of the source in axial direction of ±8 cm), where the beam is directed at the boundary between air and PMMA as can be seen in Figure 5d and 5f. Even when the source is located in the center (corresponding dose profile in Figure 5e) dose is deposited in air outside of the phantom boundaries. The artifacts could be related to edge effects on material boundaries and scatter from inside the phantom. There was no impact from the artifacts on the calculation of the MSAD, since the MSAD was calculated in the central portion (central sFOV) of the dose profile.

The derived doses from the animal phantoms of mouse and rat showed that significant doses are inflicted on both species in a typical microCT acquisition. Especially smaller animals, such as mice, receive a large amount of radiation due to their small volume with bone doses of 459.13 ± 96.37 mGy (P3). The whole body received a total amount of radiation of 68.39 ± 40.89 mGy (mouse, P1) and 43.07 ± 25.79 mGy (rat, P1), which is far more than predicted by the MSAD for P1 (3 sFOV for mouse: 28.49 ± 1.36 mGy; 5 sFOV for rat: 28.75 ± 1.32 mGy). This is related to the difference in volume between the PMMA phantom, the mouse and the rat. The PMMA phantom has a total volume of 392.69 ccm, the rat 258.18 ccm and the mouse 18.76 ccm. Boone et al. [19] performed Monte Carlo simulations with a homogenous small animal model of different diameters (5 to 40 mm) and also found that the dose increases with a decreasing animal diameter. Derived rat organ doses are therefore closer to the MSAD due to the more similar volume. The average soft tissue organ dose in mice was 159.42 ± 43.91 mGy and 128.02 ± 36.67 mGy using P3. High energy protocols such as P3 with longer exposure and a larger tube current compared to P1 result in higher radiation burdens. The large standard deviations in all derived organ doses might be a result of the 192° gantry rotation only, which results in higher doses on one side of the animal (analogue to dose profiles in the PMMA phantom for P1 shown in Figure 4d). Another factor might be simulating only a fraction of the photons and scaling afterwards, which results in a higher signal-to-noise ratio as if the real number of photons would have been simulated. Analytical animal models, where different material compositions can be easily assigned to different organs, might improve the accuracy of the results and they should be implemented for future studies.

When comparing the herein derived mouse doses for the 360° rotation protocol P2 to data of a 70 kVp protocol (2 mm Al filtration, 360 x 0.5s exposures and 0.5 mA) derived by Taschereau et al. [10] for another microCT, absolute total body doses delivered by the GE eXplore 120 microCT are slightly larger, but the dose per mAs is lower (total body dose of 0.78 mGy/mAs vs. 1.03 mGy/mAs from Taschereau et al.). The protocols are different and the GE eXplore uses a much higher current while the exposure per projection is much shorter compared to the machine simulated by Taschereau et al.. The higher absolute doses might be also a result of the soft beam of the GE eXplore as it has 0.5 mm Al less filtration.

In future studies an analytical small animal model should be used to be able to assign different material compositions to all organs and to derive more organ doses, especially to the radiosensitive bone marrow. Simulations with the appropriate photon flux of the respective x-ray tube might increase the signal-to-noise ratio in dose maps and produce more accurate results.

In conclusion, we established a valid Monte Carlo simulation model of the GE explore 120 microCT for tube voltages of 70, 80 and 100 kVp. Simulated dose profiles and consequently the $CTDI_{100}$ and MSAD in a PMMA phantom agreed closely with published experimentally derived results. Monte Carlo simulations proved a valuable tool to derive non-invasively organ doses in rats and mice. Researchers using the GE eXplore 120 microCT can expect significant radiation doses in mice from a single acquisition with total body doses of 189 mGy using P3. Especially bones in mice are exposed to high radiation burdens of up to 459 mGy. The additional radiation from microCT in longitudinal dual modality studies should always be taken into account in order to avoid overexposures of animals that might compromise the outcome of the study.

ACKNOWLEDGMENT

FB is supported by Marie Curie Initial Training Network (MCITN) “Methods in Neuroimaging” under Grant No. #MC-ITN-238593. M.A. Bahri is a “collaborateur logistique” and Alain Plenevaux is a senior research associate from FRS-FNRS Belgium. Special thanks to Francoise Malchair for providing us with the Black Piranha device and conducting the measurement with us.

REFERENCES

1. W. Koba, "MicroPET/SPECT/CT imaging of small animal models of disease", Am. J. Pathol., vol. 182, no. 2, pp. 319-324, Feb. 2013
2. P. Zanotti-Fregonara, "Suggested pathway to assess radiation safety of 18F-labeled PET tracers for first-in-human studies", Eur. J. Nucl. Med. Mol. I., vol. 40, no. 11, Oct. 2013
3. R. Taschereau, "Monte Carlo simulations of absorbed dose in a mouse phantom from 18-fluorine compounds", Med. Phys., vol. 34, no. 3, p. 1026, Feb. 2007
4. M. G. Stabin, "Voxel-based mouse and rat models for internal dose calculations", J. Nucl. Med., vol. 47, no. 4, pp. 655-659, Apr. 2006.
5. E. Larsson, "Mouse S-factors based on Monte Carlo simulations in the anatomical realistic Moby phantom for internal dosimetry", Cancer Biother. Radio., vol. 22, no. 3, pp. 438-442, June 2007.
6. V. Kersemans, "Micro-CT for anatomic referencing in PET and SPECT: radiation dose, biologic damage, and image quality", J. Nucl. Med., vol. 52, no. 11, pp. 1827-1833, Nov. 2011.
7. S. D. Figueroa, "TLD assessment of mouse dosimetry during microCT imaging", Med. Phys., vol. 35, no. 9, pp. 3866-3874, Aug. 2008.

8. S. K. Carlson, "Small animal absorbed radiation dose from serial micro-computed tomography imaging", Mol. Imaging Biol., vol. 9, no. 2, pp. 78-82, Feb. 2007.
9. I. Willekens, "Evaluation of the radiation dose in microCT with optimization of the scan protocol", Contrast Media Mol. I., vol. 5, no. 4, pp. 201-207, July 2010.
10. R. Taschereau, "Monte Carlo simulations of dose from microCT imaging procedures in a realistic mouse phantom", Med. Phys., vol. 33, no. 1, pp. 216-224, Dec. 2006.
11. M. Hupfer, "Dosimetry concepts for scanner quality assurance and tissue dose assessment in micro-CT", Med. Phys., vol. 39, no. 2, p. 658-670, Jan. 2012.
12. F. Bretin, "Performance Evaluation and X-ray Dose Quantification for Various Scanning Protocols of the GE eXplore 120 Micro-CT", IEEE T. Nucl. Sci., vol. 60, no. 5,pp. 3235-3241, Oct. 2013.
13. S. Jan, "GATE V6: a major enhancement of the GATE simulation platform enabling modelling of CT and radiotherapy", Phys. Med. Biol., vol. 56, no. 4, p. 881, Feb. 2011.
14. F. Salvat, "PENELOPE-2006: A code system for Monte Carlo simulation of electron and photon transport", Workshop Proceedings, vol. 4, p. 7, July 2006.
15. M. A. Bahri, "Performance evaluation of the General Electric eXplore CT 120 micro-CT using the vmCT phantom", Nucl. Instrum. Meth. A, vol. 648, pp. S181-S185, Aug. 2011.
16. J. M. Boone "An accurate method for computer-generating tungsten anode x-ray spectra from 30 to 140 kV", Med. Phys., vol. 24, no. 11, pp. 1661-1670, Aug. 1997.
17. W. P. Segars, "Development of a 4-D digital mouse phantom for molecular imaging research", Mol. Imaging Biol., vol. 6, no. 3, pp. 149-159, May 2004.
18. M. A. Keenan, "RADAR realistic animal model series for dose assessment", J. Nucl. Med., vol. 51, no. 3, pp. 471-476, March 2010.
19. J. M. Boone, "Small-animal X-ray dose from micro-CT", Mol. Imaging, vol. 3, no. 3, pp. 149-158, June 2004.

References

[1] G. Warnock, et al. (2013). In vivo PET/CT in a human glioblastoma chicken chorioallantoic membrane model: a new tool for oncology and radiotracer development. *Journal of Nuclear Medicine*, **54** (10): 1782–1788.

[2] Z.-C. Li, et al. (2011). Small-animal PET/CT assessment of bone microdamage in ovariectomized rats. *Journal of Nuclear Medicine*, **52** (5): 769–775.

[3] C. Schiepers, et al. (2011). Molecular imaging in oncology: the acceptance of PET/CT and the emergence of MR/PET imaging. *European radiology*, **21** (3): 548–554.

[4] V. Bettinardi, et al. (2011). Integrated PET/CT systems: State of the art and Clinical Applications. *Nuclear Physics B-Proceedings Supplements*, **215** (1): 31–33.

[5] S. Vallabhajosula, et al. (2011). A broad overview of positron emission tomography radiopharmaceuticals and clinical applications: what is new? In *Seminars in nuclear medicine*, volume 41, pages 246–264. Elsevier.

[6] E. Brianzoni, et al. (2005). Radiotherapy planning: PET/CT scanner performances in the definition of gross tumour volume and clinical target volume. *European journal of nuclear medicine and molecular imaging*, **32** (12): 1392–1399.

[7] E. Deshayes, et al. (2014). Myocardial Perfusion Imaging with 82Rb Cardiac PET/CT. In *Atlas of PET/CT in Pediatric Patients*, pages 253–258. Springer.

[8] M. F. Di Carli, et al. (2007). Clinical myocardial perfusion PET/CT. *Journal of Nuclear Medicine*, **48** (5): 783–793.

[9] V. Berti, et al. (2011). PET/CT in diagnosis of dementia. *Annals of the New York Academy of Sciences*, **1228** (1): 81–92.

[10] V. Garibotto, et al. (2014). PET/CT in the Clinical Evaluation of Pediatric Epilepsy. In *Atlas of PET/CT in Pediatric Patients*, pages 181–185. Springer.

[11] V. Berti, et al. (2011). PET/CT in diagnosis of movement disorders. *Annals of the New York Academy of Sciences*, **1228** (1): 93–108.

[12] P. M. Matthews, et al. (2013). Technologies: preclinical imaging for drug development. *Drug Discovery Today: Technologies*, **10** (3): e343–e350.

[13] W. Koba, et al. (2013). MicroPET/SPECT/CT imaging of small animal models of disease. *The American journal of pathology*, **182** (2): 319–324.

[14] L. O. T. Gainkam, et al. (2008). Comparison of the biodistribution and tumor targeting of two 99mTc-labeled anti-EGFR nanobodies in mice, using pinhole SPECT/micro-CT. *Journal of Nuclear Medicine*, **49** (5): 788–795.

[15] C.-H. Chang, et al. (2006). Longitudinal evaluation of tumor metastasis by an FDG-microPet/microCT dual-imaging modality in a lung carcinoma-bearing mouse model. *Anticancer research*, **26** (1A): 159–166.

[16] V. Kersemans, et al. (2011). Micro-CT for anatomic referencing in PET and SPECT: radiation dose, biologic damage, and image quality. *Journal of Nuclear Medicine*, **52** (11): 1827–1833.

[17] M. G. Stabin (2008). *Fundamentals of nuclear medicine dosimetry*. Springer.

[18] P. Khong, et al. (2013). ICRP publication 121: radiological protection in paediatric diagnostic and interventional radiology. *Annals of the ICRP*, **42** (2): 1–63.

[19] B. J. McParland (2010). *Nuclear medicine radiation dosimetry: advanced theoretical principles*. Springer.

[20] ICRP (2007). ICRP Publication 103. *Annals of the ICRP*, **37** (2.4): 2.

[21] ICRP (1977). ICRP Publication 26. *Annals of the ICRP*, **1**.

[22] ICRP (1990). ICRP Publication 60. *Annals of the ICRP*, **21** (1-3).

[23] H. Menzel, et al. (2008). ICRP Publication 110. Realistic reference phantoms: an ICRP/ICRU joint effort. A report of adult reference computational phantoms. *Annals of the ICRP*, **39** (2): 1–164.

[24] U. Eberlein, et al. (2011). Biokinetics and dosimetry of commonly used radiopharmaceuticals in diagnostic nuclear medicine–a review. *European journal of nuclear medicine and molecular imaging*, **38** (12): 2269–2281.

[25] K. Khamwan, et al. (2010). The determination of patient dose from 18F-FDG PET/CT examination. *Radiation protection dosimetry*, **141** (1): 50–55.

[26] S. Senthamizhchelvan, et al. (2010). Human biodistribution and radiation dosimetry of 82Rb. *Journal of Nuclear Medicine*, **51** (10): 1592–1599.

[27] J. Hirvonen, et al. (2010). Human biodistribution and radiation dosimetry of 11C-(R)-PK11195, the prototypic PET ligand to image inflammation. *European journal of nuclear medicine and molecular imaging*, **37** (3): 606–612.

[28] J. Schwarzenberg, et al. (2011). Human biodistribution and radiation dosimetry of novel PET probes targeting the deoxyribonucleoside salvage pathway. *European journal of nuclear medicine and molecular imaging*, **38** (4): 711–721.

[29] Y. Kimura, et al. (2014). Biodistribution and radiation dosimetry in humans of [11C] FLB 457, a positron emission tomography ligand for the extrastriatal dopamine D2 receptor. *Nuclear medicine and biology*, **41** (1): 102–105.

[30] J. W. Poston (1993). Application of the effective dose equivalent to nuclear medicine patients. the mird committee. *Journal of nuclear medicine: official publication, Society of Nuclear Medicine*, **34** (4): 714.

[31] C. Martin (2014). Effective dose: how should it be applied to medical exposures? *British Journal of Radiology*, **80** (956).

[32] I. Pantos, et al. (2014). Adult patient radiation doses from non-cardiac CT examinations: a review of published results. *British Journal of Radiology*, **84** (1000).

[33] F. A. Mettler Jr, et al. (2008). Effective Doses in Radiology and Diagnostic Nuclear Medicine: A Catalog 1. *Radiology*, **248** (1): 254–263.

[34] G. Brix, et al. (2005). Radiation exposure of patients undergoing whole-body dual-modality 18F-FDG PET/CT examinations. *Journal of Nuclear Medicine*, **46** (4): 608–613.

[35] B. Huang, et al. (2009). Whole-body PET/CT scanning: estimation of radiation dose and cancer risk 1. *Radiology*, **251** (1): 166–174.

[36] R. Taschereau, et al. (2006). Monte Carlo simulations of dose from microCT imaging procedures in a realistic mouse phantom. *Medical physics*, **33** (1): 216–224.

[37] R. Taschereau, et al. (2007). Monte carlo simulations of absorbed dose in a mouse phantom from 18-fluorine compounds. *Medical physics*, **34** (3): 1026–1036.

[38] N. Ford, et al. (2003). Fundamental image quality limits for microcomputed tomography in small animals. *Medical physics*, **30** (11): 2869–2877.

[39] P. Zanotti-Fregonara, et al. (2013). Suggested pathway to assess radiation safety of 18F-labeled PET tracers for first-in-human studies. *European journal of nuclear medicine and molecular imaging*, **40** (11).

[40] A. Verbruggen, et al. (2008). Guideline to regulations for radiopharmaceuticals in early phase clinical trials in the EU. *European journal of nuclear medicine and molecular imaging*, **35** (11): 2144–2151.

[41] A. L. Kesner, et al. (2008). Radiation dose estimates for [18F] 5-fluorouracil derived from PET-based and tissue-based methods in rats. *Molecular Imaging and Biology*, **10** (6): 341–348.

[42] ICRP (1992). ICRP Publication 62: Radiological Protection in Biomedical Research. *Annals of the ICRP*, **22** (3).

[43] J. van der Aart, et al. (2012). Radiation dose estimates for carbon-11-labelled PET tracers. *Nuclear medicine and biology*, **39** (2): 305–314.

[44] FDA (2013). Drugs for human use. *Code of Federal Regulations*, **5** (21D): http://www.accessdata.fda.gov/scripts/cdrh/cfdocs/cfcfr/CFRSearch.cfm?fr=361.1.

[45] T. G. Turkington (2001). Introduction to PET instrumentation. *Journal of nuclear medicine technology*, **29** (1): 4–11.

[46] F. R. Wrenn, et al. (1951). The use of positron-emitting radioisotopes for the localization of brain tumors. *Science*, **113** (2940): 525–527.

[47] L. I. Araujo, et al. (1991). Noninvasive quantification of regional myocardial blood flow in coronary artery disease with oxygen-15-labeled carbon dioxide inhalation and positron emission tomography. *Circulation*, **83** (3): 875–885.

[48] P. Valk, et al. (2006). *Positron Emission Tomography: Clinical Practice*. Springer.

[49] P. Kinahan, et al. (1998). Attenuation correction for a combined 3D PET/CT scanner. *Medical physics*, **25** (10): 2046–2053.

[50] W. Wang, et al. (2006). Systematic and distributed time-of-flight list mode PET reconstruction. In *Nuclear Science Symposium Conference Record, 2006. IEEE*, volume 3, pages 1715–1722. IEEE.

[51] L. Jødal, et al. (2012). Positron range in PET imaging: an alternative approach for assessing and correcting the blurring. *Physics in medicine and biology*, **57** (12): 3931.

[52] T. K. Lewellen (2008). Recent developments in PET detector technology. *Physics in medicine and biology*, **53** (17): R287.

[53] M. Soret, et al. (2007). Partial-volume effect in PET tumor imaging. *Journal of Nuclear Medicine*, **48** (6): 932–945.

[54] E. J. Hoffman, et al. (1979). Quantitation in positron emission computed tomography: 1. Effect of object size. *Journal of computer assisted tomography*, **3** (3): 299–308.

[55] G. N. Hounsfield (1973). Computerized transverse axial scanning (tomography): Part 1. Description of system. *The British journal of radiology*, **46** (552): 1016–1022.

[56] T. M. Buzug (2008). *Computed tomography: from photon statistics to modern cone-beam CT*. Springer.

[57] L. Feldkamp, et al. (1984). Practical cone-beam algorithm. *JOSA A*, **1** (6): 612–619.

[58] W. E. Bolch, et al. (2009). MIRD pamphlet no. 21: a generalized schema for radiopharmaceutical dosimetry-standardization of nomenclature. *Journal of Nuclear Medicine*, **50** (3): 477–484.

[59] F. H. Attix (2008). *Introduction to radiological physics and radiation dosimetry*. John Wiley & Sons.

[60] W. Hendee (2010). Radiation Physics for Medical Physicists-2nd ed. *Medical Physics*, **37** (9): 5148–5148.

[61] H. Zaidi (1999). Relevance of accurate Monte Carlo modeling in nuclear medical imaging. *Medical Physics*, **26** (4): 574–608.

[62] D. Raeside (1976). Monte carlo principles and applications.

[63] F. James (1980). Monte Carlo theory and practice. *Reports on Progress in Physics*, **43** (9): 1145.

[64] J. Turner, et al. (1985). A Monte Carlo primer for health physicists. *Health physics*, **48** (6): 717–733.

[65] A. M. Ferrenberg, et al. (1992). Monte Carlo simulations: Hidden errors from "good" random number generators. *Physical Review Letters*, **69** (23): 3382–3384.

[66] F. James (1990). A review of pseudorandom number generators. *Computer Physics Communications*, **60** (3): 329 – 344.

[67] S. Jan, et al. (2004). GATE: a simulation toolkit for PET and SPECT. *Physics in medicine and biology*, **49** (19): 4543.

[68] S. Jan, et al. (2011). GATE V6: a major enhancement of the GATE simulation platform enabling modelling of CT and radiotherapy. *Physics in medicine and biology*, **56** (4): 881.

[69] S. Agostinelli, et al. (2003). GEANT4-a simulation toolkit. *Nuclear instruments and methods in physics research section A: Accelerators, Spectrometers, Detectors and Associated Equipment*, **506** (3): 250–303.

[70] M. G. Stabin, et al. (2005). OLINDA/EXM: the second-generation personal computer software for internal dose assessment in nuclear medicine. *Journal of Nuclear Medicine*, **46** (6): 1023–1027.

[71] K. F. Eckerman, et al. (1996). The ORNL mathematical phantom series. *Oak Ridge, TN: Oak Ridge National Laboratory*.

[72] M. G. Stabin, et al. (2003). Physical models and dose factors for use in internal dose assessment. *Health physics*, **85** (3): 294–310.

[73] W. P. Segars, et al. (2004). Development of a 4-D digital mouse phantom for molecular imaging research. *Molecular Imaging & Biology*, **6** (3): 149–159.

[74] T. Mauxion, et al. (2013). Improved realism of hybrid mouse models may not be sufficient to generate reference dosimetric data. *Medical physics*, **40** (5): 052501.

[75] J. A. Siegel, et al. (1999). MIRD pamphlet no. 16: techniques for quantitative radiopharmaceutical biodistribution data acquisition and analysis for use in human radiation dose estimates. *Journal of Nuclear Medicine*, **40**: 37S–61S.

[76] M. Stabin, et al. (1999). Radiation dosimetry in nuclear medicine. *Applied radiation and isotopes*, **50** (1): 73–87.

[77] S. Shanehsazzadeh, et al. (2009). Determination of human absorbed dose of 67GA-DTPA-ACTH based on distribution data in rats. *Radiation protection dosimetry*, **134** (2): 79–86.

[78] J. S. Lewis, et al. (2000). Comparative dosimetry of copper-64 and yttrium-90-labeled somatostatin analogs in a tumor-bearing rat model. *Cancer biotherapy & radiopharmaceuticals*, **15** (6): 593–604.

[79] R. Laforest, et al. (2005). Dosimetry of 60/61/62/64Cu-ATSM: a hypoxia imaging agent for PET. *European journal of nuclear medicine and molecular imaging*, **32** (7): 764–770.

[80] F. Bretin, et al. (2013). Preclinical radiation dosimetry for the novel SV2A radiotracer [18 F] UCB-H. *EJNMMI Res*, **3**: 35.

[81] R. A. Comley, et al. (2012). Biodistribution and radiation dosimetry of the serotonin 5-HT6 ligand [11C] GSK215083 determined from human whole-body PET. *Molecular Imaging and Biology*, **14** (4): 517–521.

[82] H. Herzog, et al. (2008). Biodistribution and radiation dosimetry of the A1 adenosine receptor ligand 18F-CPFPX determined from human whole-body PET. *European journal of nuclear medicine and molecular imaging*, **35** (8): 1499–1506.

[83] H. Vesselle, et al. (2003). 18F-Fluorothymidine radiation dosimetry in human PET imaging studies. *Journal of Nuclear Medicine*, **44** (9): 1482–1488.

[84] K. A. Kurdziel, et al. (2003). Biodistribution, radiation dose estimates, and in vivo Pgp modulation studies of 18F-paclitaxel in nonhuman primates. *Journal of Nuclear Medicine*, **44** (8): 1330–1339.

[85] M. Tian, et al. (2011). Whole-body biodistribution kinetics, metabolism, and radiation dosimetry estimates of 18F-PEG6-IPQA in nonhuman primates. *Journal of Nuclear Medicine*, **52** (6): 934–941.

[86] N. Seneca, et al. (2005). Whole-body biodistribution, radiation dosimetry estimates for the PET norepinephrine transporter probe (S, S)-[18F] FMeNER-D2 in non-human primates. *Nuclear medicine communications*, **26** (8): 695–700.

[87] D. Tipre, et al. (2004). Radiation dosimetry estimates for the PET serotonin transporter probe 11C-DASB determined from whole-body imaging in non-human primates. *Nuclear medicine communications*, **25** (1): 81–86.

[88] C. C. Constantinescu, et al. (2013). Evaluation of [18F] Nifene biodistribution and dosimetry based on whole-body PET imaging of mice. *Nuclear medicine and biology*, **40** (2): 289–294.

[89] A. Kirshner, et al. (1975). Radiation dosimetry of 19-iodocholesterol [I31I]: the pitfalls of using tissue concentration data (reply). *J Nucl Med*, **16**: 248–249.

[90] C. C. Constantinescu, et al. (2013). Evaluation of [18F] Mefway biodistribution and dosimetry based on whole-body PET imaging of mice. *Molecular Imaging and Biology*, **15** (2): 222–229.

[91] C. M. Lourenco, et al. (2001). Characterization of R-[11C] rolipram for PET imaging of phosphodiesterase-4: in vivo binding, metabolism, and dosimetry studies in rats. *Nuclear medicine and biology*, **28** (4): 347–358.

[92] M. Sakata, et al. (2013). Direct comparison of radiation dosimetry of six PET tracers using human whole-body imaging and murine biodistribution studies. *Annals of nuclear medicine*, **27** (3): 285–296.

[93] P. Luoto, et al. (2010). Human Dosimetry of Carbon-11 Labeled N-butan-2-yl-1-(2-chlorophenyl)-N-methylisoquinoline-3-carboxamide Extrapolated from Whole-body Distribution Kinetics and Radiometabolism in Rats. *Molecular Imaging and Biology*, **12** (4): 435–442.

[94] N. I. Escobar, et al. (1998). Pharmacokinetics, biodistribution and dosimetry of 99m Tc-labeled anti-human epidermal growth factor receptor humanized monoclonal antibody R3 in rats. *Nuclear medicine and biology*, **25** (1): 17–23.

[95] J. Toyohara, et al. (2009). Preclinical and the first clinical studies on [11C] CHIBA-1001 for mapping $\alpha 7$ nicotinic receptors by positron emission tomography. *Annals of nuclear medicine*, **23** (3): 301–309.

[96] R. Sparks, et al. (1999). Comparison of the effectiveness of some common animal data scaling techniques in estimating human radiation dose. In *Sixth International Radiopharmaceutical Dosimetry Symposium*, pages 705–716.

[97] R. Loeevinger, et al. (1968). A schema for absorbed-dose calculations for biologically-distributed radionuclides. *Journal of nuclear medicine: official publication, Society of Nuclear Medicine*, pages Suppl–1.

[98] T. B. Shope, et al. (1981). A method for describing the doses delivered by transmission x-ray computed tomography. *Medical physics*, **8** (4): 488–495.

[99] J. A. Bauhs, et al. (2008). CT Dosimetry: Comparison of Measurement Techniques and Devices 1. *Radiographics*, **28** (1): 245–253.

[100] K. Jessen, et al. (1999). Dosimetry for optimisation of patient protection in computed tomography. *Applied Radiation and isotopes*, **50** (1): 165–172.

[101] S. D. Figueroa, et al. (2008). TLD assessment of mouse dosimetry during microCT imaging. *Medical physics*, **35** (9): 3866–3874.

[102] A. J. Einstein, et al. (2010). Radiation Dose from Single-Heartbeat Coronary CT Angiography Performed with a 320–Detector Row Volume Scanner. *Radiology*, **254** (3): 698–706.

[103] C. H. McCollough, et al. (2011). CT dose index and patient dose: they are not the same thing. *Radiology*, **259** (2): 311–316.

[104] G. I. Warnock, et al. (2014). Evaluation of 18F-UCB-H as a Novel PET Tracer for Synaptic Vesicle Protein 2A in the Brain. *Journal of Nuclear Medicine*, pages jnumed–113.

[105] B. A. Lynch, et al. (2004). The synaptic vesicle protein SV2A is the binding site for the antiepileptic drug levetiracetam. *Proceedings of the National Academy of Sciences of the United States of America*, **101** (26): 9861–9866.

[106] R. J. Cloutier, et al. (1973). Dose to the fetus from radionuclides in the bladder. *Health Physics*, **25** (2): 147–161.

[107] H. M. Deloar, et al. (1998). Estimation of absorbed dose for 2-[F-18] fluoro-2-deoxy-D-glucose using whole-body positron emission tomography and magnetic resonance imaging. *European journal of nuclear medicine*, **25** (6): 565–574.

[108] F. Bretin, et al. (2014). Hybrid MicroPET Imaging for Dosimetric Applications in Mice: Improvement of Activity Quantification in Dynamic MicroPET Imaging for Accelerated Dosimetry Applied to 6-[18 F] Fluoro-l-DOPA and 2-[18 F] Fluoro-l-Tyrosine. *Molecular Imaging and Biology*, **16** (3): 383–394.

[109] W. D. Brown, et al. (1998). Fluorine-18-fluoro-L-DOPA dosimetry with carbidopa pretreatment. *Journal of Nuclear Medicine*, **39**: 1884–1891.

[110] C. M. Deroose, et al. (2007). Multimodality imaging of tumor xenografts and metastases in mice with combined small-animal PET, small-animal CT, and bioluminescence imaging. *Journal of Nuclear Medicine*, **48** (2): 295–303.

[111] E. L. Ritman (2004). Micro-computed tomography-current status and developments. *Annu. Rev. Biomed. Eng.*, **6**: 185–208.

[112] S. K. Carlson, et al. (2007). Small animal absorbed radiation dose from serial micro-computed tomography imaging. *Molecular Imaging and Biology*, **9** (2): 78–82.

[113] F. Bretin, et al. (2013). Performance Evaluation and X-ray Dose Quantification for Various Scanning Protocols of the GE eXplore 120 Micro-CT.

[114] O. Langner, et al. (2009). Bar and point test patterns generated by dry-etching for measurement of high spatial resolution in micro-CT. In *World Congress on Medical Physics and Biomedical Engineering, September 7-12, 2009, Munich, Germany*, pages 428–431. Springer.

[115] M. Hupfer, et al. (2012). Dosimetry concepts for scanner quality assurance and tissue dose assessment in micro-CT. *Medical physics*, **39** (2): 658–670.

[116] J. M. Boone, et al. (1997). An accurate method for computer-generating tungsten anode x-ray spectra from 30 to 140 kV. *Medical physics*, **24** (11): 1661–1670.

[117] J. M. Boone, et al. (2004). Small-animal X-ray dose from micro-CT. *Molecular imaging*, **3** (3): 149–158.

[118] S. Chen, et al. (2000). Low-dose whole-body irradiation (LD-WBI) changes protein expression of mouse thymocytes: effect of a LD-WBI-enhanced protein RIP10 on cell proliferation and spontaneous or radiation-induced thymocyte apoptosis. *Toxicological Sciences*, **55** (1): 97–106.

[119] H. Wan, et al. (2001). Effects of low dose radiation on signal transduction of neurons in mouse hypothalamus. *Biomedical and environmental sciences: BES*, **14** (3): 248–255.

[120] S. Štolc, et al. (2011). Body distribution of 11C-methionine and 18FDG in rat measured by microPET. *Interdisciplinary toxicology*, **4** (1): 52–55.

[121] O. G. Rousset, et al. (1998). Correction for partial volume effects in PET: principle and validation. *Journal of Nuclear Medicine*, **39** (5): 904–911.

[122] B. J. Fueger, et al. (2006). Impact of animal handling on the results of 18F-FDG PET studies in mice. *Journal of Nuclear Medicine*, **47** (6): 999–1006.

[123] P. Zanotti-Fregonara, et al. (2012). Suggested pathway to assess radiation safety of 11 C-labeled PET tracers for first-in-human studies. *European journal of nuclear medicine and molecular imaging*, **39** (3): 544–547.

[124] M. Cristy, et al. (1987). Specific absorbed fractions of energy at various ages from internal photon sources. vi. newborn. *ORNL/TM-8381*, **6**.

[125] M. Lassmann, et al. (2011). EANM Dosimetry Committee guidance document: good practice of clinical dosimetry reporting. *European journal of nuclear medicine and molecular imaging*, **38** (1): 192–200.

[126] C. L. Efferson, et al. (2010). Downregulation of Notch pathway by a γ-secretase inhibitor attenuates AKT/mammalian target of rapamycin signaling and glucose uptake in an ERBB2 transgenic breast cancer model. *Cancer research*, **70** (6): 2476–2484.

[127] W. K. Hsu, et al. (2008). Characterization of osteolytic, osteoblastic, and mixed lesions in a prostate cancer mouse model using 18F-FDG and 18F-fluoride PET/CT. *Journal of Nuclear Medicine*, **49** (3): 414–421.

[128] R. E. J. Mitchel, et al. (2003). Low doses of radiation increase the latency of spontaneous lymphomas and spinal osteosarcomas in cancer-prone, radiation-sensitive Trp53 heterozygous mice. *Radiation research*, **159** (3): 320–327.